Reactions of Small Molecules Facilitated by Metal–Acceptor Interactions

Thesis by

Daniel Leif Migdow Suess

In Partial Fulfillment of the Requirements for the degree

of

Doctor of Philosophy

CALIFORNIA INSTITUTE OF TECHNOLOGY

Pasadena, California

2013

(Defended May 17, 2013)

Acknowledgements

I am immensely grateful to have had Jonas as my PhD advisor. I especially admire his academic approach to research, scientific rigor, and ability to inspire those around him. Nothing can make me more excited about my research than discussing it with Jonas. I also appreciate that he gave me the freedom and support to write a thesis that I can be truly proud of. Jonas has also built an outstanding research group, and I thank all current and former members of the group for making the lab such an invigorating place to study. In particular, Hill Harman and Marc-Etienne Moret have taught me a tremendous amount about bonding in main group elements and transition metals, and they were also very encouraging and helpful in allowing me to carve out my own niche in projects they started. Charlene Tsay and I coauthored a paper, and working with her was ideal in every aspect. I genuinely looked forward to the yearly meetings with my thesis committee (John Bercaw, Sarah Reisman, and Theo Agapie) and thank them for their support and feedback. I also appreciate the advice and mentorship I've received over the years from Kit Cummins and Dianne Newmann. Both Caltech and MIT have tremendous staff and facilities; I am particularly grateful to Larry Henling and Peter Müller for teaching me X-ray crystallography. In addition, Dave VanderVelde and George Rossman assisted with NMR and Raman spectroscopic experiments, respectively. My research has been generously funded by several sources, including an MIT Presidential Fellowship, the NSF (GRFP, CHE-0750234, CHE-0802907, and CHE-0947829), the NIH (GM070757), the Gordon and Betty Moore Foundation, and the Beckman Institute. Lastly, I thank my friends and family for their unwavering support and encouragement of my graduate school work.

Abstract

The role of metal-acceptor interactions arising from M–BR_3 and M–PR_3 bonding is discussed with respect to reactions between first-row transition metals and N_2, H_2, and CO. Thermally robust, $S = {}^1/_2$ (TPB)Co(H_2) and (TPB)Co(N_2) complexes (TPB = tris(2-(diisopropylphosphino)phenyl)borane) are described and the energetics of N_2 and H_2 binding are measured. The H_2 and N_2 ligands are bound more weakly in the (TPB)Co complexes than in related (SiP_3)M(L) complexes (SiP_3 = tris(2-(diisopropylphosphino)phenyl)silyl). Comparisons within and between these two ligand platforms allow for the factors that affect N_2 (and H_2) binding and activation to be delineated. The characterization and reactivity of (DPB)Fe complexes (DPB = bis(2-(diisopropylphosphino)phenyl)phenylborane) in the context of N_2 functionalization and E–H bond addition (E = H, C, N, Si) are described. This platform allows for the one-pot transformation of free N_2 to an Fe hydrazido(-) complex *via* an Fe aminoimide intermediate. The principles learned from the N_2 chemistry using (DPB)Fe are applied to CO reduction on the same system. The preparation of (DPB)Fe($CO)_2$ is described as well as its reductive functionalization to generate an unprecedented Fe dicarbyne. The bonding in this highly covalent complex is discussed in detail. Initial studies of the reactivity of the Fe dicarbyne reveal that a CO-derived olefin is released upon hydrogenation. Alternative approaches to uncovering unusual reactivity using metal-acceptor interactions are described in Chapters 5 and 6, including initial studies on a new π-accepting tridentate diphosphinosulfinyl ligand and strategies for designing ligands that undergo site-selective metallation to generate heterobimetallic complexes.

Table of Contents

List of Charts

Chapter 1

Chapter 2 Weak N_2 and H_2 Binding at an $S = {}^1/_2$ Co Center

Chapter 4 An Fe Dicarbyne that Releases Olefin upon Hydrogenation

Chapter 5 Late Metal Diphosphinosulfinyl S(O)P_2 Pincer-Type Complexes

List of Figures

Chapter 1 Introduction to Metal-Acceptor Interactions

Chapter 2 Weak N_2 and H_2 Binding at an $S = {}^1/_2$ Co Center

Chapter 3 Dinitrogen Functionalization *via* E–H Addition to Fe–B Bonds

Chapter 4 An Fe Dicarbyne that Releases Olefin upon Hydrogenation

Chapter 6 Ligand Design for the Site-Selective Installation of Pd and Pt Centers to Generate Homo- and Heteropolymetallic Motifs

List of Schemes

Chapter 1 Introduction to Metal-Acceptor Interactions

Chapter 2 Weak N_2 and H_2 Binding at an $S = {}^1/_2$ Co Center

Chapter 3 Dinitrogen Functionalization *via* E–H Addition to Fe–B Bonds

Chapter 4 An Fe Dicarbyne that Releases Olefin upon Hydrogenation

Chapter 5 Late Metal Diphosphinosulfinyl S(O)P_2 Pincer-Type Complexes

Chapter 6 Ligand Design for the Site-Selective Installation of Pd and Pt Centers to Generate Homo- and Heteropolymetallic Motifs

List of Tables

Chapter 1

Chapter 2 Weak N_2 and H_2 Binding at an $S = {}^1/_2$ Co Center

Chapter 3 Dinitrogen Functionalization *via* E–H Addition to Fe–B Bonds

Chapter 4 An Fe Dicarbyne that Releases Olefin upon Hydrogenation

Chapter 1 Introduction to Metal-Acceptor Interactions

1.1 Motivation

Dinitrogen reduction reactions typically employ electron-releasing transition metals that backbond into the N–N π^* orbitals. This results in a weakened N–N bond with a corresponding increase in M–N bond order, as is elegantly illustrated by Cummins's report of the bimetallic cleavage of N_2 by two tris(amido) Mo^{III} complexes to form two tris(amido) Mo^{VI} nitrides.[1] Group IV and V metals have been shown to bind N_2 by a variety of modes, and the reactions of these highly activated N_2 complexes with protons, other electrophiles, and E–H bonds have been described.[2] Monometallic N_2 functionalization reactions have been most thoroughly developed using group VI complexes[3] in which M–N π-backbonding renders Nβ susceptible to electrophilic attack. In general, this mode of activation is more challenging for mononuclear mid- to late-first-row metal complexes due to their relatively contracted d orbitals. The diminished π-backbonding capabilities of these metals has been addressed by generating highly reduced, anionic N_2 complexes that react with strong electrophiles.[4,5] However, such complexes necessarily have high 3d electron counts with partly (or even fully) populated antibonding orbitals. As such, the development of strategies for the stabilization of these species is of high interest.

One approach is to incorporate covalent acceptor functionalities into the primary sphere of the metal in order to impart favorable bonding character to otherwise antibonding orbitals. For example, in the TBP $[(SiP_3)Fe(N_2)][Na(12\text{-crown-}4)_2]$ complex,[4b] four electrons occupy the degenerate d_{xy} and $d_{x^2-y^2}$ orbitals which are σ-antibonding with respect

to the phosphine donors. If not for the π-accepting properties of the phosphines, this complex would likely be exceptionally reactive. Ancillary ligands with hard donors can also serve as acceptors if the metal can backbond through an accessible π^* orbital, as illustrated by late-metal complexes of bis(imino)pyridine ligands such as Chirik's $(PDI)Fe(CO)_2$.[6] The Fe center in this complex is formally zero-valent and is therefore somewhat unusual given the presence of three hard N donors. However, one of the occupied Fe 3d orbitals is strongly conjugated with a ligand π^* orbital; this covalent interaction stabilizes the electron-rich Fe much like a phosphine. More striking is Burger's report of a thermally stable, formally Ir^{III} nitride complex in a square planar geometry (Chart 1.1). This geometry would typically require occupation of a filled $Ir–N_{nitride}$ π^*

Chart 1.1 Selected complexes stabilized by metal-acceptor interactions

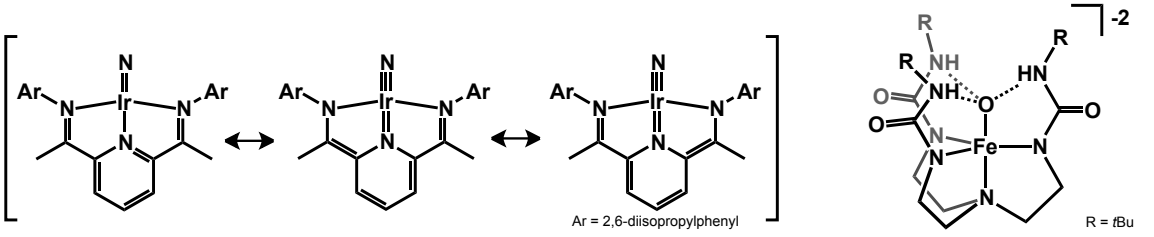

(PDI)Ir(N): Burger (2009)

$[(H_3buea)Fe(O)]^{2-}$: Borovik (2000)

orbital, thereby obliterating one of the $Ir–N_{nitride}$ π bonds and likely rendering such a complex highly reactive. However, similarly to Chirik's $(PDI)Fe(CO)_2$ complex, the supporting PDI ligand is a competent π-acceptor and forms a bonding interaction with the Ir–N π^* orbital (as represented by the Ir^V resonance structures in Chart 1.1), thereby conferring greater stability to this species.

One alternative approach for stabilizing species with high electron counts is through the use of secondary coordination sphere acceptor interactions. For example, Borovik has described tris(ureato)amine ligands that feature three hydrogen bond donors in the cavity of the open coordination site.[7] Several unusual species have been generated using this ligand platform, including a high-spin, trigonal bipyramidal Fe^{III} oxido complex that has one electron in each of three formally Fe–O antibonding orbitals (Chart 1.1).[8] The presence of three hydrogen bond donors compensates for the diminished Fe–O bond order in this complex. Although secondary coordination sphere interactions are not the primary focus of this thesis, in Chapter 6 I present strategies for synthesizing heterobimetallic motifs in this context. The role of primary sphere, covalent metal-acceptor interactions (particularly those mediated by M–PR_3 and M–BR_3 bonds) in stabilizing electron-rich complexes is of central importance to the work presented in Chapters 2, 3, 4, and 5.

1.2 Metal-borane bonding

The nucleus of this thesis involves complexes of the neutral L_3Z-type TPB and DPB ligands, each of which were originally described by Bourissou.[9] These ligands incorporate a borane as a σ-accepting group and three or two phosphines, respectively, as σ-donating, π-accepting ligands (Chart 1.2). The DPB ligand class also features a polyhaptic phenyl group that can participate in σ donation and π backbonding. The primary aim in this thesis is to present some discoveries and principles pertaining to the use of M–BR_3 and M–PR_3 acceptor interactions in the reactions of N_2, CO, and substrates with E–H bonds. An important aspect of this chemistry is that M–P and M–B bonds are highly flexible and can adjust to the electronic requirements of the metal, thereby providing access to a range of

Chart 1.2 General forms of (TPB)MX and (DPB)MX complexes

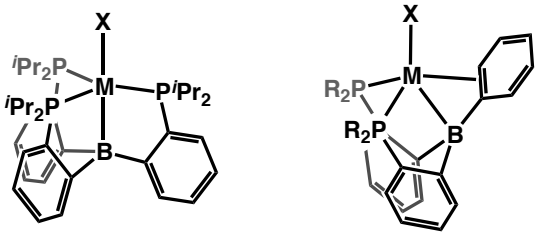

(TPB)MX (DPB)MX

electronic structures including highly reduced metal species. In addition, *trans*-disposed $M–BR_3$ bonds can facilitate binding of weakly σ-donating ligands such as N_2 and H_2, which will be a topic of discussion in Chapter 2. In Chapters 3 and 4, I will show how the M–B and M–P bonds in highly reduced N_2 and CO complexes can serve as electron reservoirs, whereby reaction of these species with electrophiles results in substantial electron transfer from the M–B and M–P bonds to M–N and M–C multiple bonds. I will also present ways in which M–B bonds can participate in E-H bond activations for delivery of the E fragment to N_2-derived ligands.

Each chapter includes background on specific topics of relevance. Of central importance to Chapters 2, 3, and 4 are matters pertaining to $M–BR_3$ bonding, so this topic is the focus of the remainder of this introduction. Although the π-accepting properties of phosphines are well appreciated in coordination chemistry,[10] σ-accepting ligands such as boranes are less understood. The first structurally characterized complex with an $M–BR_3$ bond was an Ru complex reported by Hill[11] in 1999 and the number of complexes of this type has since grown.[12] The discussion in this chapter will focus on published, structurally

characterized, first-row-metal complexes of C_3-symmetric ligands and simple models for understanding their bonding.

For first-row complexes, there are only three ligands that have been reported to bridge B and M to give C_3-symmetric metallaboratrane structures (Chart 1.3). The $B(mim^{tBu})_3$ and

Chart 1.3 General forms of C_3-symmetric metallaboratranes

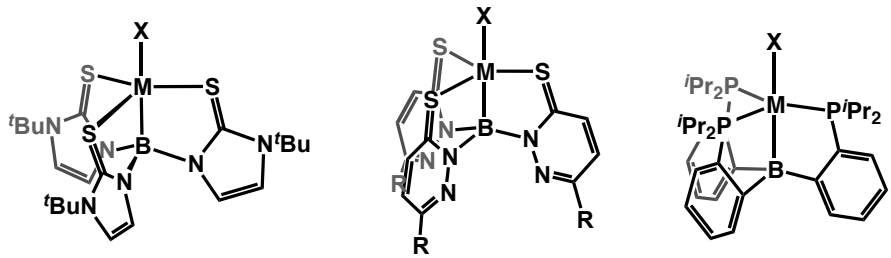

$B(Pn^R)_3$ ligands are quite similar in that both bind the transition metal with three sulfur donors and the borane with three nitrogen donors. Structurally characterized Fe, Co, Ni, and Cu complexes[13] show consistently short M–B distances and high degrees of pyramidalization at B (Table 1.1), suggesting significant M–B interactions that seem to be consistent regardless of the identity and spin state of M. (It is impossible to thermodynamically quantify the strength of an M–BR_3 interaction in these complexes because they are all bound in cage structures. To date, no complex featuring an unsupported M–BR_3 bond has been structurally characterized for any transition metal.) The Pauling electronegativities and valence atomic orbital ionization energies (Table 1.2) for B (2s + 2p) are well matched with those values for late first row metals (3d + 4s), suggesting that the M–BR_3 bond should be highly covalent. Based on the structural

Table 1.1 Structural metrics of C_3-symmetric metallaboratranes

Ligand	M	X	Spin	M–B (Å)	Σ∠(C–B–C) (˚)	Ref	Notes
B(mim^{t}Bu)$_3$	Fe(CO)	CO	0	2.108	327	13b	
	Co^+	PPh_3	1	2.131	328	13a	
	Ni	Cl	$^1/_2$	2.107	332	13c	
	Ni	Cl	$^1/_2$	2.110	331	13d	
	Ni	NCS	$^1/_2$	2.079	332	13d	
	Ni	N_3	$^1/_2$	2.092	331	13d	
	Ni	OAc	$^1/_2$	2.113	330	13d	
B(Pn^R)$_3$	Co	Cl	1	2.068	329	13e	R = ^{t}Bu
	Co	Pn	?	2.004	326	13e	R = ^{t}Bu
	Co	Pn	?	1.984	326	13e	R = Ph
	Ni	Cl	$^1/_2$	2.034	331	13e	R = Me
	Ni	Cl	$^1/_2$	2.015	327	13e	R = ^{t}Bu
	Cu	Cl	0	2.060	330	13f	R = ^{t}Bu
TPB	Fe	Br	$^3/_2$	2.458	342	14	
	Fe	OH	$^3/_2$	2.444	337	15	
	Fe	NH_2	$^3/_2$	2.449	340	15	
	Fe	Me	$^3/_2$	2.523	341	15	
	Fe^+	—	$^3/_2$	2.217	347	15	
	Fe^+	NH_3	$^3/_2$	2.434	341	15	
	Fe^+	N_2H_4	$^3/_2$	2.392	339	15	
	Fe	N_2Na	$^1/_2$	2.311	330	14	
	Fe^-	N_2	$^1/_2$	2.293	331	14	
	Fe	$NNSiMe_3$	$^1/_2$	2.435	338	4c	
	Fe	NAr	0	2.589	338	14	Ar = *p*-OMe-C_6H_4
	Co	Br	1	2.463	342	16	
	Co	N_2	$^1/_2$	2.319	339	16	
	Co	H_2	$^1/_2$	2.280	336	16	
	Ni	—	0	2.168	339	17	
	Cu	Cl	0	2.508	347	17	
	Cu^+	—	0	2.495	355	18	
	Cu	—	$^1/_2$	2.289	347	18	
	Cu^-	—	0	2.198	339	18	

Table 1.2 Selected Pauling electronegativity and atomic orbital ionization energy values.

	Electronegativity	2s	2p	3s	3p	3d	4s	4p
B	2.04	14.0	8.3					
C	2.55	19.5	10.7					
N	3.04	25.5	13.1					
O	3.44	32.3	15.9					
F	3.98	46.4	18.7					
Al	1.61			11.3	5.95			
Si	1.90			15.0	7.81			
P	2.19			18.7	10.2			
S	2.58			20.7	11.7			
Cl	3.16			25.3	13.8			
Sc	1.36					4.71	5.70	3.22
Ti	1.54					5.58	6.07	3.35
V	1.63					6.32	6.32	3.47
Cr	1.66					7.19	6.57	3.47
Mn	1.55					7.93	6.82	3.59
Fe	1.83					8.68	7.07	3.72
Co	1.88					9.42	7.32	3.84
Ni	1.91					10.0	7.56	3.84
Cu	1.90					10.7	7.69	3.97

metrics of the $B(mim^{tBu})_3$ and $B(Pn^R)_3$ complexes as well as the Pauling electronegativity and atomic orbital ionization values for their constituent atoms, there appears to be little difference between M–BR_3 and M–SiR_3 bonding.

However, this bonding description is clearly not appropriate for TPB complexes which exhibit large variations in their M–B distances and degrees of pyramidalization at B. For example, (TPB)Ni displays a short Ni–B bond of 2.168 Å and a pyramidalized B center as indicated by $\Sigma\angle$(C–B–C) = 339°.[17] Both structural parameters, as well as an upfield-shifted ^{11}B NMR signal (16 ppm), indicate significant Ni–B bonding. On the other hand, the isoelectronic complex [(TPB)Cu][BAr^F_4] has greatly diminished Cu–B bonding based on the longer Cu–B distance (2.495 Å), nearly planar B ($\Sigma\angle$(C–B–C) = 355°), and downfield-

shifted ^{11}B NMR signal (67 ppm).[18] This pair of complexes suggests that simply decreasing the basicity of the metal by substituting Ni(0) for Cu(I) and/or increasing the molecular charge can obliterate M–B bonding. Thus, the comparison of an M–BR_3 interaction to an M–SiR_3 bond is not generally valid because it does not capture the greater flexibility (and probable weakness) of M–BR_3 bonds compared with the stronger, more rigid M–SiR_3 bonds. The reason for the comparatively weaker bonding is that a BR_3 ligand can decoordinate to give a very stable BR_3 fragment whereas decoordination of an SiR_3 ligand results in a relatively unstable silyl cation, silyl radical, or silyl anion. Given the differences in M–B bonding between complexes of TPB, B(mim$^{t\text{Bu}}$)$_3$, and B(Pn$^{t\text{Bu}}$)$_3$, a general bonding description for M–BR_3 bonds must address the large dependence on substituent effects, the large range of M–B covalency, and the (likely) inherent weakness of the interaction.

Current descriptions of M–BR_3 bonds are all problematic, and complications may arise when descriptions of chemical bonding are conflated with formalisms for electron counting. Parkin, building on Green's Covalent Bond Classification method ("CBC method"),[19] argues that borane coordination to a metal results in an M–BR_3 bonding orbital (which is considered a ligand-based orbital) and an M–BR_3 antibonding orbital (which is designated as a metal-based orbital).[20] Therefore, the metal contributes two of its d electrons to a M–BR_3 bond which decreases the d^n electron count by two. One problem with Parkin's formulation of M–BR_3 bonding is that the polarity of the bond may be highly dependent on a number of factors including the identity of the metal, the molecular charge, and the other ligands on both M and B. Thus, the electrons cannot always be reliably assigned either to M or to B. As such, Hill has advocated for describing the electron count of an "*(M–B)*^{n}" unit, akin to the Enemark-Feltham notation for describing [M–NO] electron

counts.[21] His formalism acknowledges the ambiguity inherent to M–BR_3 bonding (especially in cage structures) and therefore provides an unambiguous formalism for counting electrons in these complexes. Importantly, this formalism makes no distinction between M–BR_3 bonding and any other type of covalent metal–ligand bonding (e.g. M–SiR_3).

In response to Hill's *(M–B)*^{n} model, Parkin has argued that the CBC method already achieves Hill's stated goal: if coordination of a borane is always assumed to decrease the d^n electron count by two, then there is no ambiguity in the metal's electron count, which renders Hill's formalism redundant. Of course, the opposite assumption about M–BR_3 bonding—that borane coordination to a metal has *no effect* on the d electron count—would similarly provide an unambiguous method for counting electrons in M–BR_3 complexes (and may be a more appropriate description of the bonding in some cases). Thus, Parkin's retort is only correct if one concedes that the CBC method provides merely a means for electron counting and offers no formulation of M–BR_3 bonding. That is, to the extent that the CBC method makes claims about the bonding in M–BR_3 complexes (e.g. strength, polarity, effect on d electron count), Hill's formulism serves a purpose that is distinct from the CBC method.

However, Parkin does in fact make important arguments about M–BR_3 bonding, which I will summarize and expand upon in this chapter. Central to the Parkin's application of the CBC method to a description of *bonding* (as opposed to electron counting) is Haaland's distinction between "normal covalent" and "dative covalent" bonds.[22] Through mostly empirical observations about the bonding in main group elements, Haaland makes several convincing connections between the nature of a bond in a molecule and the minimum-

energy pathway by which it would rupture (either in the gas phase or in an innocent solvent). In Haaland's classification scheme, normal covalent bonds (e.g. the C–C bond in ethane) fragment homolytically in the gas phase whereas dative covalent bonds (e.g. the B–N bond in ammonia borane) fragment heterolytically. Of course, one may argue that a bond does not have any "knowledge" of the fragments from which it is derived, however Haaland and others[23] argue that it in fact does: normal covalent bonds tend to have deep, narrow potential wells with correspondingly higher bond strengths while dative covalent bonds tend to have wider, more shallow potential wells with correspondingly lower bond strengths. Dative covalent bonds are more variable in bond length and often longer than normal covalent bonds. In addition, the length and strength of dative covalent bonds are much more sensitive to molecular charge and inductive effects. Thus, Haaland argues that if one can confidently predict the minimum-energy rupture pathway of a bond between main group elements, one can make powerful predictions about the nature of the bond in the molecule.

Haaland's ideas may be applied to transition metals, albeit with added caution. The notion of minimum-energy rupture is particularly complicated for first-row-metal complexes because of the variety of electronic structures the metal fragment may adopt before and after the hypothetical bond rupture. To illustrate, a two-electron M–BR_3 bond may be reasonably broken to give $M:^{n}$ + BR_3, $M\cdot^{(n+1)}$ + $\cdot BR_3^-$, or $M^{(n+2)}$ + $:BR_3^{2-}$ (Chart 1.4); the types of bonds that would give rise to these minimum-energy rupture pathways are inverse dative covalent, normal covalent, and dative covalent, respectively. In the same way, an M–SiR_3 bond could be broken to give $M:^-$ + SiR_3^+, M· + $\cdot SiR_3$, or M^+ + $:SiR_3^-$. In

Chart 1.4 Representations of M–BR_3 and M–SiR_3 bonds that are distinguished by their minimum-energy rupture pathways

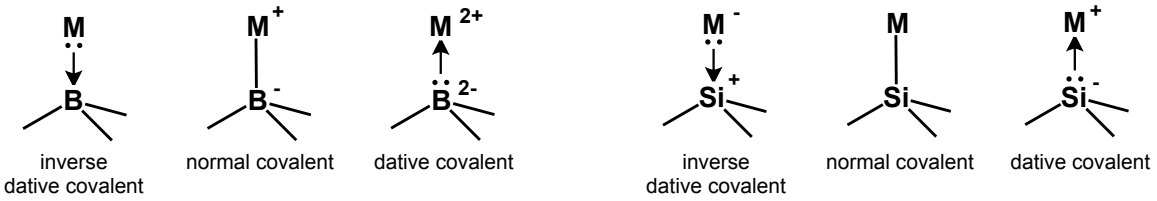

the latter case, none of the SiR_3 fragments are particularly stable (unlike a neutral BR_3 fragment) so one would expect M–SiR_3 bonds in general to have narrower potential wells and be less variable in distance than M–BR_3 bonds.

Without explicitly considering minimum-energy rupture pathways for transition-metal complexes, Parkin makes a simple and elegant link between Haaland's bond classifications and the CBC method's ligand classifications in order to describe their bonding:[20, 24] L-type ligands participate in dative covalent bonds, X-type ligands participate in normal covalent bonds, and Z-type ligands participate in dative covalent bonds.[i] Although there are several problems with pairing bond types and ligand types as defined by the CBC method (especially with respect to the implications of the bond classification on the d^n electron count (*vide supra*)), this approach offers a convenient starting point for describing covalent bonds with a high degree of predictive power.

[i] Parkin and Green make no distinction between "inverse" dative bonds and regular dative bonds since the selection of which species functions as the ligand and which functions as the metal is arbitrary. However, I use this terminology in order to distinguish between the two very different minimum-energy rupture pathways available to inverse and regular dative M–BR_3 and M–SiR_3 bonds (Chart 1.4).

1.3 Metal-borane bonding in (TPB)M complexes

The TPB ligand is distinguished from both $B(mim^{tBu})_3$ and $B(Pn^{tBu})_3$ by its ability to allow for a wide range of M–BR_3 interactions. Chapter 2 presents unusual $S = {}^1/_2$ (TPB)Co complexes with weakly bound N_2 and H_2 ligands and includes a discussion of how issues pertaining to the M–BR_3 bonding in these and related complexes impacts the binding of σ-donor ligands. As such, additional discussion is warranted with respect to the bonding in (TPB)M complexes as well as experimental methods for probing it.

For the purposes of this discussion, an M–B interaction may be considered a "strong interaction" (as for $B(mim^{tBu})_3$ and $B(Pn^{tBu})_3$ complexes and perhaps some TPB complexes), a "non-interaction" (as for [(TPB)Cu][BAr^F_4]), or a "weak interaction" (Figure 1.1). Stronger interactions should be favored by more diffuse metal orbitals (such as those in

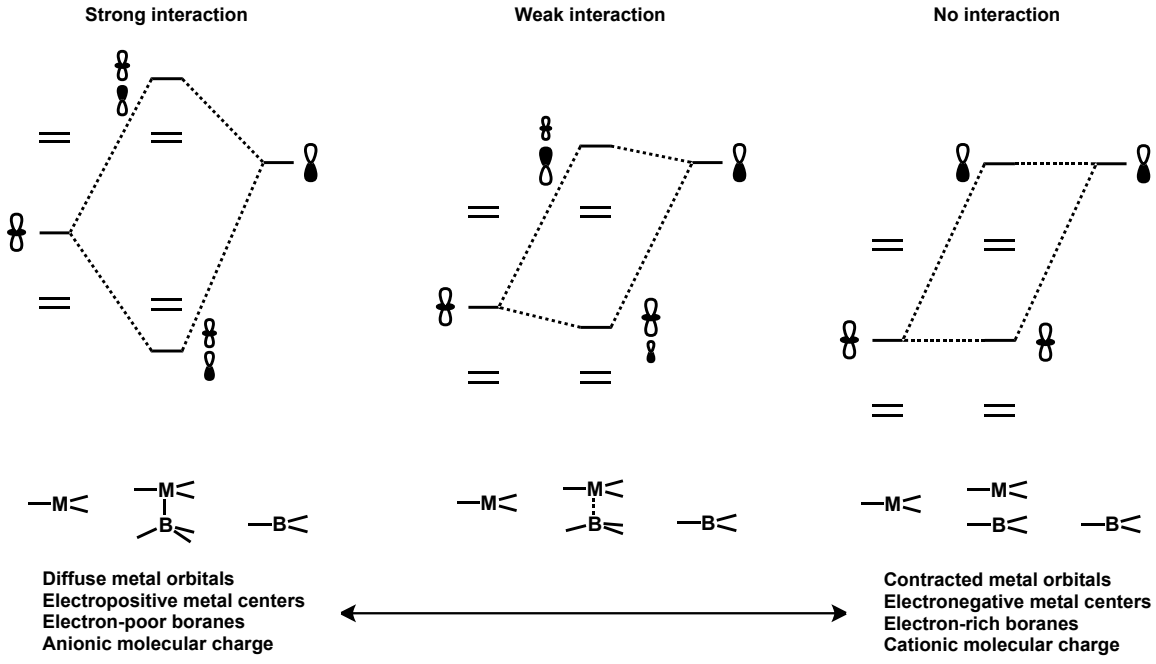

Figure 1.1 Simplified MO representation of M–BR_3 bonding.

second- and third-row-transition metals), more electropositive metals, more electron-poor boranes (as for $B(mim^{tBu})_3$ and $B(Pn^{tBu})_3$), and anionic molecular charges. These features should be experimentally manifested in shorter M–B distances, more pyramidalized B centers, and upfield-shifted ^{11}B NMR signals (only for diamagnetic complexes). For an $S = {}^1/_2$ complex, the B-character of an M–BR_3 bond can be examined by the magnitude of hyperfine coupling to ^{11}B in its EPR spectrum so long as the unpaired spin resides in the M–B bonding orbital. As such, neither NMR spectroscopy nor EPR spectroscopy is a general method for probing M–B bonding. Boron K-edge XAS (in conjunction with metal K- and L-edge XAS) has never been utilized to measure the degree of M–B charge transfer and covalency in M–BR_3 bonds but could in principle be a very powerful tool for these purposes. As such, I initiated a collaboration with Prof. Stephen Cramer at the Advanced Light Source at Lawrence Berkeley National Lab to record the low-energy B K-edge spectra of several TPB complexes. Unfortunately, in preliminary experiments we were not able to record spectra that gave sufficient signal due to the low spectroscopic concentration of B in these complexes. Thus, XRD analysis is currently the most general method for probing M–B bonding, but there are significant limitations to interpreting these data (*vide infra*).

The structural data for most TPB complexes (Table 1.1) indicate weak M–BR_3 interactions. However, ambiguity about the relative strength of an M–BR_3 bond can arise not only when metrics such as bond length and boron pyramidalization adopt intermediate values. Since most M–BR_3 bonds should have shallow potential wells, there may be a relatively low dependence of the strength of the interaction on the M–BR_3 distance. For example, (TPB)FeNAr (Ar = *p*-OMe-C_6H_4)[14] adopts a pseudotetrahedral geometry at Fe as

expected for a divalent Fe imide complex.[25] As such, it has a long Fe–B distance of 2.589 Å. By comparison, the Cu–B distance in [(TPB)Cu][BAr^F_4]—a complex that very likely has little or no Cu–B interaction—is 0.1 Å shorter.[18] Based on this metric, it would be reasonable to assume that the Fe and B atoms in (TPB)Fe(NAr) do not interact. However, the B atom in the latter complex is rather significantly pyramidalized ($\Sigma\angle$(C–B–C) = 338°), and DFT calculations suggest that the Fe $3d_{z^2}$ orbital has some degree of σ bonding with B. Therefore it seems that there may be some degree of Fe–B bonding in (TPB)Fe(NAr) even at such a long distance. On the other hand, the pyramidalization at B could simply be due to strain in the cage structure imposed by steric or electronic factors. In contrast to (TPB)Fe(NAr), the $S = {}^3/_2$ [(TPB)Fe][BAr^F_4] complex has a relatively short Fe–B distance of 2.217 Å and a more planar B ($\Sigma\angle$(C–B–C) = 347°).[15] DFT studies on this molecule suggest little Fe–B bonding in spite of the short distance. These examples illustrate that even though XRD analysis is currently the most general experimental approach for assessing M–BR_3 bonding, caution must be exercised when using structural data to assess M–B bonding.

The discussion thus far has assumed that M–BR_3 bonding for first row metals occurs by overlap of a filled d orbital (often though not necessarily $3d_{z^2}$) with an unfilled B $2p_z$ orbital. Although this is a good foundational model for thinking about M–BR_3 bonding, an M–BR_3 interaction need not be mediated by the metal's d orbitals. This is most clearly illustrated by [(TPB)Cu][K(benzo-15-crown-5)$_2$] which features a Cu–B bond that is highly polarized toward B.[18] The bonding in this complex may be best regarded as a B lone pair donating into an empty Cu $4p_z$ orbital; the Cu $3d_{z^2}$ orbital is not involved in bonding to B. Although this type of bonding is permitted because the empty Cu $4p_z$ orbital is sufficiently

low in energy to interact with B and because the Cu $3d_{z^2}$ does not interact with B, it is not strictly limited to Cu(I) or other main group elements. For example, mixing of Fe 3d and 4p atomic orbitals may be important for backbonding to B (as well as CO ligands) in several of the highly reduced complexes described in Chapter 4.

1.4 Metal-borane bonding in (DPB)M complexes

The discussion of M–BR_3 bonding has thus far been limited to C_3-symmetric ligands in which the M–BR_3 interactions are thought to occur exclusively along the M-BR_3 internuclear bond. However, the N_2 and CO functionalization chemistry described in Chapters 3 and 4 involves metal complexes of the C_S-symmetric DPB ligand. Aside from the new compounds described in this thesis, complexes of DPB ligands have been reported with Ni,[26] Cu,[27] Rh,[9a, 28] Pd,[28a] Pt,[28a] and Au[29] metal centers. For Rh, Pd, Pt, and Au, the ligands are always found to bind in a κ^3-PBP fashion wherein the BPh group binds only through B. For all Ni and Cu complexes, the BPh group binds either in an η^2-BC or an η^3-BCC mode. These and several other coordination modes are observed in the work presented herein (Chart 1.5). As such, the M–BR_3 bonding in DPB complexes is

Chart 1.5 Potential BPh binding modes in (DPB)M complexes

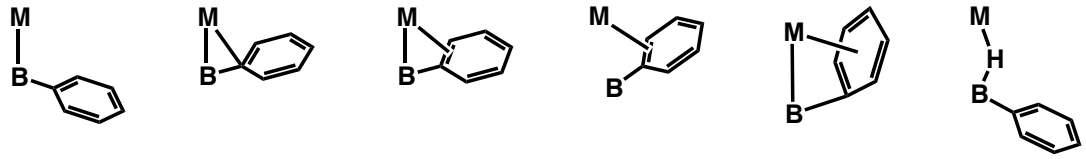

η^1-B η^2-BC η^3-BCC η^2-CC η^7-BPh (μ–H)-B

substantially more complicated than that in TPB complexes owing to the variable hapticity of the BPh group as well as significant π delocalization between B and its phenyl

substituent. Nevertheless, it is worthwhile to consider the orbitals that may participate in M–BPh bonding. The calculated molecular orbitals of phenylborane are shown in Figure 1.2 (Gaussian09, M06L/6-31+g(d)). Of the seven π molecular orbitals, the

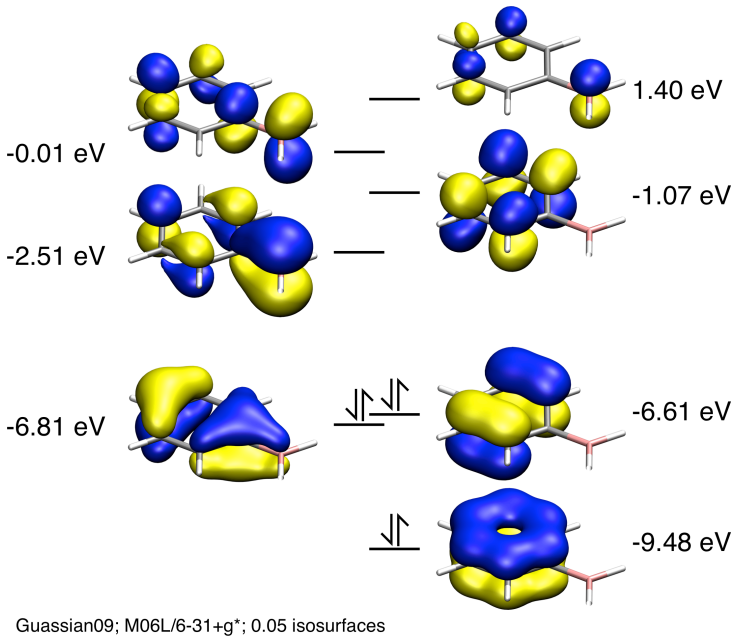

Figure 1.2 Frontier MOs of $PhBH_2$.

LUMO has the greatest B $2p_z$ character. Additional mixing between B $2p_z$ and phenyl π orbitals can be seen in LUMO+2 and HOMO-1. Thus, metal coordination to any of the seven atoms in the BPh group could indicate M–L bonding, M–L backbonding, or some combination thereof. Backbonding into conjugated BPh π orbitals would not necessarily result in pyramidalization at B, so this metric is not a reliable indicator of the strength of the M–B interaction. In addition, the orientation of the B $2p_z$ orbital with respect to the metal can vary, leading to "bent" bonds of varying curvature. As such, the M–B distance is also a flawed indicator of the relative degrees of M–B bonding. However, the extent of

backbonding to the phenyl ring can be qualitatively assessed by examining the C–C bond lengths for elongation.

1.5 H–H bond addition facilitated by M–BR_3 bonds

For every example of a M–BR_3 complex that is *not* based on TPB or DPB, the M–BR_3 bond is formed by addition of an hydridoborate bond to the metal center. The reverse reaction—hydride storage in a M–BR_3 bond—has been the subject of recent interest.[12b] Owen has reported a Rh–BR_3 complex that reacts with H_2 to generate a Rh(H)–H–BR_3 species,[8] and this type of reactivity has also been observed for a sterically pressured (^{Ph}DPB^{Mes})Ni complex (Scheme 1.1).[26] The latter result is particularly noteworthy because

Scheme 1.1 H_2 addition to (DPB)Ni and (TPB)Ni complexes

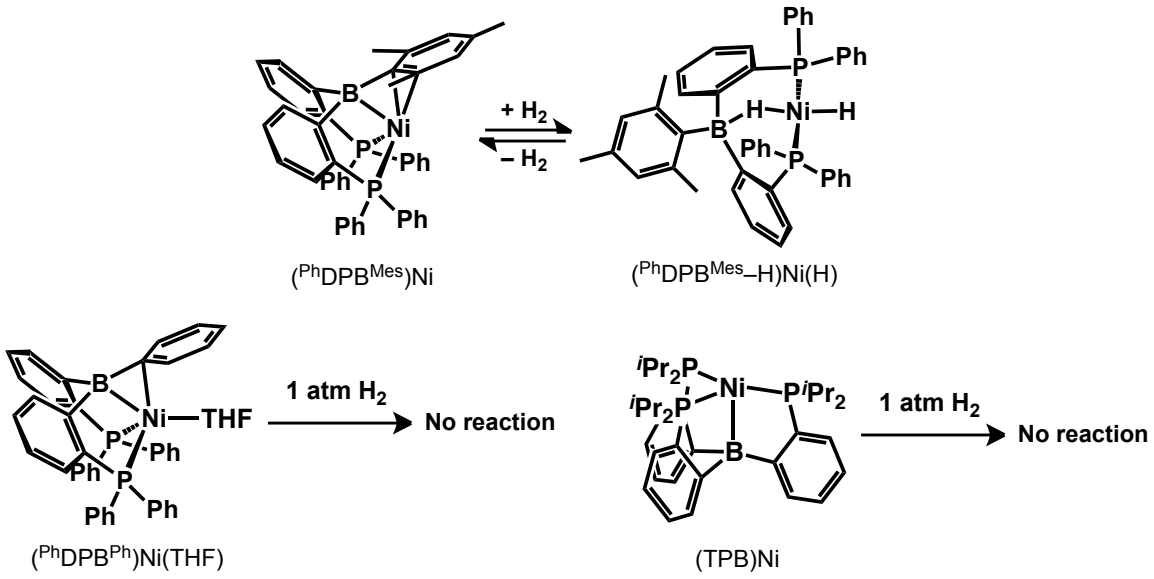

oxidative addition of H_2 at a related mononuclear Ni complexes without the presence of a borane is thought to be thermodynamically unfavorable.[30] In contrast, neither of the isoelectronic (^{Ph}DPB^{Ph})Ni(THF) nor (TPB)Ni complexes reacts with H_2,[26, 31] underscoring

the importance of hemilability for one of the three donors in these systems. These results suggest that DPB complexes may be expected to be generally more reactive toward E–H bonds than TPB complexes due to the greater hemilability of the BPh group compared with that of the third phosphine in the TPB ligand. Therefore, although it has been shown that (TPB)Fe(N_2) reacts with H_2 to give first (TPB–H)Fe(H)(N_2) followed by (TPB–H)Fe(H)(H_2) (Scheme 1.2),[32] a (DPB)Fe motif was identified as a more desirable synthetic target for realizing N_2 and CO functionalization with E–H bonds (see Chapters 3 and 4).

Scheme 1.2 H_2 addition to (TPB)Fe(N_2)

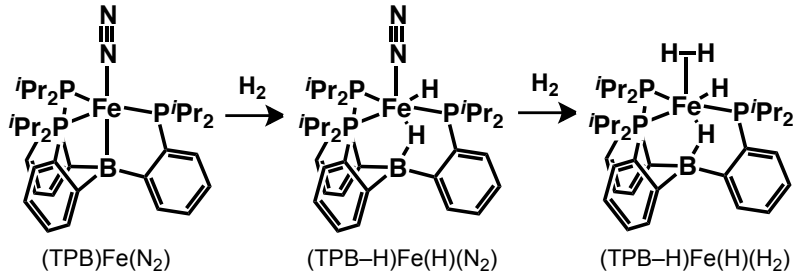

(TPB)Fe(N_2) (TPB–H)Fe(H)(N_2) (TPB–H)Fe(H)(H_2)

(1) (a) Laplaza, C. E.; Cummins, C. C. *Science,* **1995,** *268*, 861; (b) Laplaza, C. E.; Johnson, M. J. A.; Peters, J. C.; Odom, A. L.; Kim, E.; Cummins, C. C.; George, G. N.; Pickering, I. J. *J. Am. Chem. Soc.,* **1996,** *118*, 8623; (c) Peters, J. C.; Cherry, J.-P. F.; Thomas, J. C.; Baraldo, L.; Mindiola, D. J.; Davis, W. M.; Cummins, C. C. *J. Am. Chem. Soc.,* **1999,** *121*, 10053.
(2) (a) Manriquez, J. M.; Bercaw, J. E. *J. Am. Chem. Soc.,* **1974,** *96*, 6229; (b) Manriquez, J. M.; Sanner, R. D.; Marsh, R. E.; Bercaw, J. E. *J. Am. Chem. Soc.,* **1976,** *98*, 3042; (c) Chirik, P. J. *Dalton Trans.,* **2006**, 16; (d) Fryzuk, M. D. *Acc. Chem. Res.,* **2009,** *42*, 127; (e) Hirotsu, M.; Fontaine, P. P.; Zavalij, P. Y.; Sita, L. R. *J. Am. Chem. Soc.,* **2007,** *129*, 12690; (f) Gambarotta, S. *J. Organomet. Chem,* **1995,** *500*, 117.
(3) (a) Hidai, M.; Mizobe, Y. *Chem. Rev.,* **1995,** *95*, 1115; (b) Chatt, J.; Heath, G. A.; Richards, R. L. *J. Chem. Soc., Chem. Commun.,* **1972**, 1010; (c) Arashiba, K.; Miyake, Y.; Nishibayashi, Y. *Nature Chem.,* **2010,** *3*, 120; (d) Yandulov, D. V.; Schrock, R. R. *J. Am. Chem. Soc.,* **2002,** *124*, 6252; (e) Chatt, J.; Dilworth, J. R.; Richards, R. L. *Chem. Rev.,* **1978,** *78*, 589.
(4) (a) Betley, T. A.; Peters, J. C. *J. Am. Chem. Soc.,* **2003,** *125*, 10782; (b) Lee, Y.; Mankad, N. P.; Peters, J. C. *Nat. Chem.,* **2010,** *2*, 558; (c) Moret, M.-E.; Peters, J. C. *J. Am. Chem. Soc.,* **2011,** *133*, 18118; (d) Suess, D. L. M.; Peters, J. C. *J. Am. Chem. Soc.,* **2013,** *135*, 4938.
(5) Indeed, each example of well-defined Nβ functionalization of an Fe or Co N_2 complexes uses either Na/Hg amalgam or Mg.
(6) (a) Bart, S. C.; Chłopek, K.; Bill, E.; Bouwkamp, M. W.; Lobkovsky, E.; Neese, F.; Wieghardt, K.; Chirik, P. J. *J. Am. Chem. Soc.,* **2006,** *128*, 13901; (b) Tondreau, A. M.; Milsmann, C.; Lobkovsky, E.; Chirik, P. J. *Inorg. Chem.,* **2011,** *50*, 9888.
(7) Borovik, A. S. *Acc. Chem. Res.,* **2005,** *38*, 54.
(8) Tsoureas, N.; Kuo, Y.-Y.; Haddow, M. F.; Owen, G. R. *Chem. Commun.,* **2010,** *47*, 484.
(9) (a) Bontemps, S.; Gornitzka, H.; Bouhadir, G.; Miqueu, K.; Bourissou, D. *Angew. Chem. Int. Ed.,* **2006,** *45*, 1611; (b) Bontemps, S.; Bouhadir, G.; Dyer, P. W.; Miqueu, K.; Bourissou, D. *Inorg. Chem.,* **2007,** *46*, 5149.
(10) (a) Marynick, D. S. *J. Am. Chem. Soc.,* **1984,** *106*, 4064; (b) Dunne, B. J.; Morris, R. B.; Orpen, A. G. *J. Chem. Soc., Dalton Trans.,* **1991**, 653; (c) Lyne, P. D.; P Mingos, D. M. *J. Organomet. Chem,* **1994,** *478*, 141.
(11) Hill, A. F.; Owen, G. R.; White, A. J.; Williams, D. J. *Angew. Chem. Int. Ed.,* **1999,** *38*, 2759.
(12) (a) Braunschweig, H.; Dewhurst, R. D. *Dalton Trans.,* **2010,** *40*, 549; (b) Owen, G. R. *Chem. Soc. Rev.,* **2012,** *41*, 3535.
(13) (a) Mihalcik, D. J.; White, J. L.; Tanski, J. M.; Zakharov, L. N.; Yap, G. P. A.; Incarvito, C. D.; Rheingold, A. L.; Rabinovich, D. *Dalton Trans.,* **2004**, 1626; (b) Figueroa, J. S.; Melnick, J. G.; Parkin, G. *Inorg. Chem.,* **2006,** *45*, 7056; (c) Senda, S.; Ohki, Y.; Hirayama, T.; Toda, D.; Chen, J.-L.; Matsumoto, T.; Kawaguchi, H.; Tatsumi, K. *Inorg. Chem.,* **2006,** *45*, 9914; (d) Pang, K.; Tanski, J. M.; Parkin, G. *Chem. Commun.,* **2008**, 1008; (e) Nuss, G.; Saischek, G.; Harum, B. N.; Volpe, M.; Gatterer, K.; Belaj, F.; Mösch-Zanetti, N. C. *Inorg. Chem.,* **2011,** *50*, 1991; (f) Nuss, G.; Saischek, G.; Harum, B. N.; Volpe, M.; Belaj, F.; Mösch-Zanetti, N. C. *Inorg. Chem.,* **2011,** *50*, 12632.
(14) Moret, M.-E.; Peters, J. C. *Angew. Chem. Int. Ed.,* **2011,** *50*, 2063.

(15) Anderson, J. S.; Moret, M.-E.; Peters, J. C. *J. Am. Chem. Soc.,* **2013,** *135*, 534.
(16) Suess, D. L. M.; Tsay, C.; Peters, J. C. *J. Am. Chem. Soc.,* **2012,** *134*, 14158.
(17) Sircoglou, M.; Bontemps, S.; Bouhadir, G.; Saffon, N.; Miqueu, K.; Gu, W.; Mercy, M.; Chen, C.-H.; Foxman, B. M.; Maron, L.; Ozerov, O. V.; Bourissou, D. *J. Am. Chem. Soc.,* **2008,** *130*, 16729.
(18) Moret, M.-E.; Zhang, L.; Peters, J. C. *J. Am. Chem. Soc.,* **2013,** *135*, 3792.
(19) Green, M. L. H. *J. Organomet. Chem.,* **1995,** *500*, 127.
(20) Parkin, G. *Organometallics,* **2006,** *25*, 4744.
(21) Hill, A. F. *Organometallics,* **2006,** *25*, 4741.
(22) Haaland, A. *Angew. Chem. Int. Ed.,* **1989,** *28*, 992.
(23) Frank Weinhold, C. R. L., *Valency and Bonding: A Natural Bond Orbital Donor-Acceptor Perspective*. Cambridge University Press: Cambridge, 2005.
(24) Parkin, G.; Crabtree, R. H.; Mingos, D., Classification of organotransition metal compounds. In *Comprehensive Organometallic Chemistry 3rd Edn.*, 2007; Vol. 1.
(25) Saouma, C. T.; Peters, J. C. *Coord. Chem. Rev.,* **2011,** *255*, 920.
(26) Harman, W. H.; Peters, J. C. *J. Am. Chem. Soc.,* **2012,** *134*, 5080.
(27) Sircoglou, M.; Bontemps, S.; Mercy, M.; Miqueu, K.; Ladeira, S.; Saffon, N.; Maron, L.; Bouhadir, G.; Bourissou, D. *Inorg. Chem.,* **2010,** *49*, 3983.
(28) (a) Bontemps, S.; Sircoglou, M.; Bouhadir, G.; Puschmann, H.; Howard, J. A. K.; Dyer, P. W.; Miqueu, K.; Bourissou, D. *Chem. Eur. J.,* **2008,** *14*, 731; (b) Conifer, C. M.; Law, D. J.; Sunley, G. J.; White, A. J. P.; Britovsek, G. J. P. *Organometallics,* **2011,** *30*, 4060.
(29) Sircoglou, M.; Bontemps, S.; Mercy, M.; Saffon, N.; Takahashi, M.; Bouhadir, G.; Maron, L.; Bourissou, D. *Angew. Chem. Int. Ed.,* **2007,** *46*, 8583.
(30) Flener Lovitt, C.; Frenking, G.; Girolami, G. S. *Organometallics,* **2012,** *31*, 4122.
(31) Tsay, C.; Peters, J. C. *Chem. Sci.,* **2012,** *3*, 1313.
(32) Fong, H.; Moret, M.-E.; Lee, Y.; Peters, J. C. *Organometallics,* **2013,** *32*, 3053.

Chapter 2 Weak N_2 and H_2 Binding at an $S = {}^1/_2$ Co Center

2.1 Background

The relationship between N_2 and H_2 as ligands for coordination compounds has been appreciated since the first non-classical H_2 complex was characterized by Kubas.[1] Both ligands are σ donors and π acceptors and are thought to bond with transition metals according to the Dewar-Chatt-Duncanson model. While diamagnetic H_2 complexes of the late transition metals are relatively rare, reports of paramagnetic H_2 complexes are scant for all metals.[2] This chapter presents the synthesis and characterization of $S = {}^1/_2$ (TPB)Co(N_2) and (TPB)Co(H_2) complexes[3] as well as a discussion of their electronic structures. These complexes are novel in their own right but are also interesting in relationship to isostructural complexes of the TPB and SiP_3 ligands. In this context, the (TPB)Co complexes described herein help elucidate fundamentals of H_2 and N_2 binding and activation—particularly the distinction between strong binding and high degrees of activation—as well as aspects of the relationship between M–BR_3 and M–SiR_3 bonding.

From a broader perspective, Co-based coordination compounds are active catalysts for a number of H_2-producing and -consuming reactions, including H^+ reduction,[4] H_2 storage,[5] and hydroformylation.[6] In each of these processes, non-classical Co(H_2) complexes are probable intermediates and H_2 binding (or release) is likely an elementary mechanistic step. For example, interest in developing earth-abundant catalysts for H^+ reduction has prompted mechanistic investigations of several Co-based catalysts.[7] The three most plausible mechanisms (Scheme 2.1) invoke H_2 release from a transient Co(H_2) complex formed by

Scheme 2.1 Proposed mechanisms for Co-mediated H^+ reduction

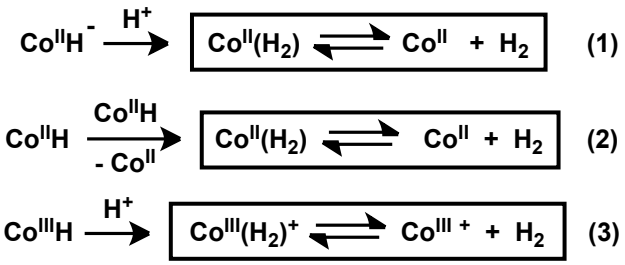

protonation of a $Co^{II}H$ species (1), bimolecular coupling of two $Co^{II}H$ species (2), or protonation of a $Co^{III}H$ species (3). Although mechanisms (1) and (2) invoke an $S = {}^1/_2$ $Co(H_2)$ complex, such a complex has never been observed. There are a few reports of closed-shell $Co(H_2)$ complexes[8] as well as some $Co(H_2)(H)$ complexes[9] (Chart 2.1); in each

Chart 2.1 Previously described $Co(H_2)$ and $Co(H_2)H$ complexes

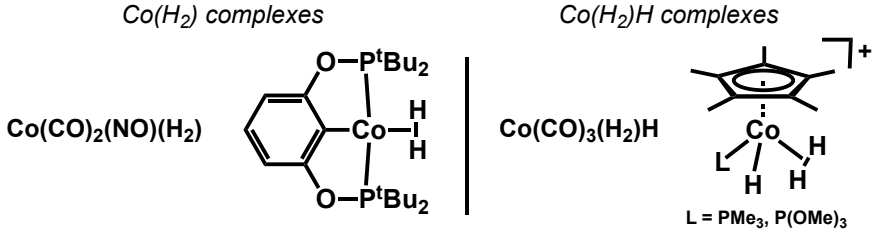

case, the complexes' thermal instability called for *in situ* characterization at low temperature. In addition, the energetics of H_2 binding to Co in any spin state or to any homogenous open-shell metal complex have not been experimentally ascertained. Given the broad scope of current research interest in the H_2 chemistry of Co, the development of model systems that fill this void is of high interest. The $S = {}^1/_2$ (TPB)$Co(H_2)$ complex described below is first example of such a model complex.

2.2 Results

Installation of Co into TPB was accomplished by metallation with $CoBr_2$ in the presence of excess Co powder (Scheme 2.2). Orange-brown (TPB)CoBr has a solution

Scheme 2.2 Synthetic entry to (TPB)Co complexes

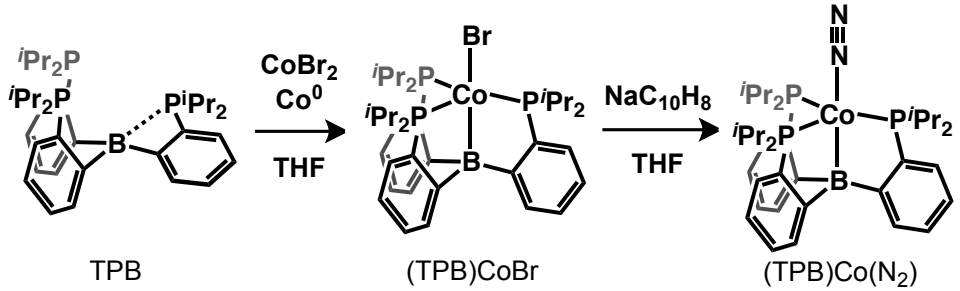

TPB (TPB)CoBr (TPB)Co(N_2)

magnetic moment of μ_{eff} = 3.0 μ_B (298 K), indicating an S = 1 spin state. Its solid-state geometry is in between tetrahedral and trigonal bipyramidal (TBP) with a Co–B distance of 2.4629(8) Å (Figure 2.1). The average Co–P distance is 2.34 Å which is consistent with its high-spin state. Thus, (TPB)CoBr can be viewed on one hand analogously to known $(PPh_3)_3CoX$ complexes that lack a σ acceptor interaction, and on another hand similarly to Thomas's Co-Zr heterobimetallic complexes supported by phosphinoamide ligands.[10]

Reduction of (TPB)CoBr with 1 equiv $NaC_{10}H_8$ under N_2 yields yellow, S = $^1/_2$ (TPB)Co(N_2) (μ_{eff} = 1.5μ_B, 298 K). Its EPR spectrum shows a nearly axial signal (g = [2.561, 2.077, 2.015]) (Figure 2.2, top). Due to the broadness of the features, no reliable hyperfine coupling information may be gleaned. In the solid state, (TPB)Co(N_2) adopts a trigonal bipyramidal geometry with a Co–B bond length of 2.319(1) Å (Figure 2.3). The presence of one wide P–Co–P angle (128.81° vs. 107.87° and 112.21°) in conjunction with

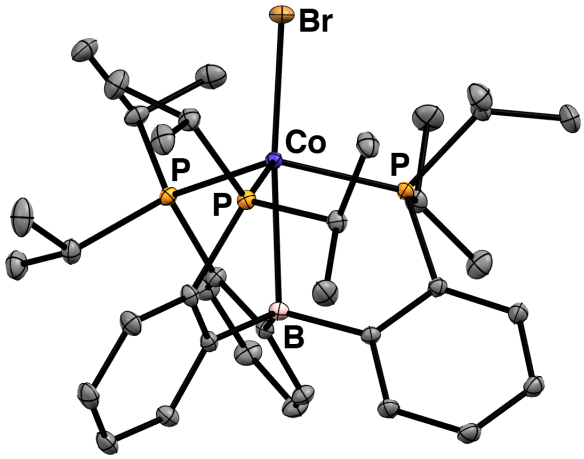

Figure 2.1 Displacement ellipsoid (50%) representation of (TPB)CoBr. H atoms omitted for clarity. Selected distances and angles: Co–B = 2.4629(8) Å; Co–P = 2.3140(3) Å, 2.3498(2) Å, 2.3533(2) Å; Co–Br = 2.3810(2) Å; ∠(P–Co–P) = 116.69(1)°, 113.13(1)°, 112.43(1)°; Σ∠(C–B–C) = 342°.

the pseudoaxial EPR spectrum indicates that the unpaired spin density resides in the plane containing the Co and P atoms since a triply-occupied, degenerate set of $d_{xy}/d_{x^2-y^2}$ orbitals is subject to a Jahn-Teller distortion. Similar EPR features and geometric distortions from C_3 symmetry have been observed for the valence isoelectronic compounds $(SiP_3)Fe(N_2)$ and $[(SiP_3)Co(PMe_3)][BAr^F{}_4]$ (*vide infra*). An intense $\nu_{(N\text{-}N)}$ stretch is observed by IR spectroscopy at 2089 cm^{-1}. A similar $\nu_{(N\text{-}N)}$ stretch (2,081 cm^{-1}) has been recently reported for an isostructural and topologically related cobalt alumatrane complex.[11]

The cyclic voltammagram of $(TPB)Co(N_2)$ shows a broad feature corresponding to an oxidation process at 0.2 V vs. Fc/Fc^+ and a quasi-reversible reduction wave at -2.0 V vs. Fc/Fc^+ (Figure 2.4). The broadness of the oxidation wave may be a result of decoordination of N_2 and/or binding of THF on the electrochemical time scale. These results prompted me to pursue one-electron chemical oxidation and reduction. Further reduction of $(TPB)Co(N_2)$

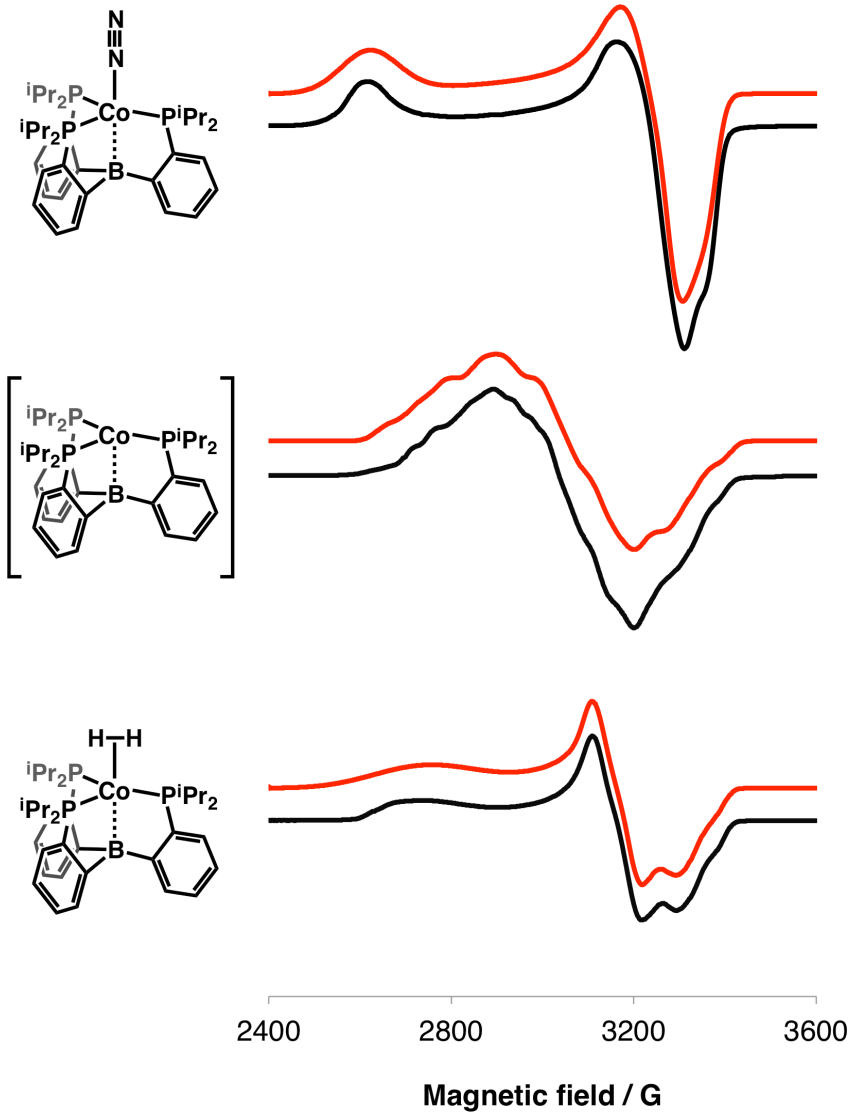

Figure 2.2 EPR spectra of (TPB)Co(N_2) (top), "(TPB)Co" (middle), and (TPB)Co(H_2) (bottom) recorded in toluene glass at 10 K and 9.38 GHz. Black traces: experiment; red traces: simulation.

with 1 equiv $NaC_{10}H_8$ and encapsulation with 2 equiv 12-crown-4 generates red, closed-shell [(TPB)Co(N_2)][Na(12-crown-4)$_2$] (Scheme 2.3). The $\nu_{(N\text{-}N)}$ stretch of 1978 cm^{-1} is significantly lower that of (TPB)Co(N_2). Its solid-state structure (Figure 2.5) shows contracted Co–B, Co–P, and Co–N distances compared with those of (TPB)Co(N_2),

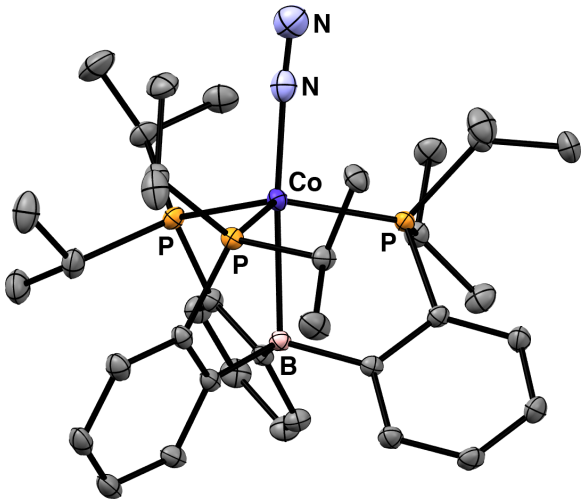

Figure 2.3 Displacement ellipsoid (50%) representation of (TPB)Co(N_2). H atoms omitted for clarity. Selected distances and angles: Co–B = 2.3203(12) Å; Co–P = 2.2600(3) Å, 2.2654(3) Å, 2.3290(3) Å; Co–N = 1.8621(12) Å; N–N = 1.0623(18) Å; ∠(P–Co–P) = 107.87(1)°, 112.21(1)°, 128.81(1)°; Σ∠(C–B–C) = 339°.

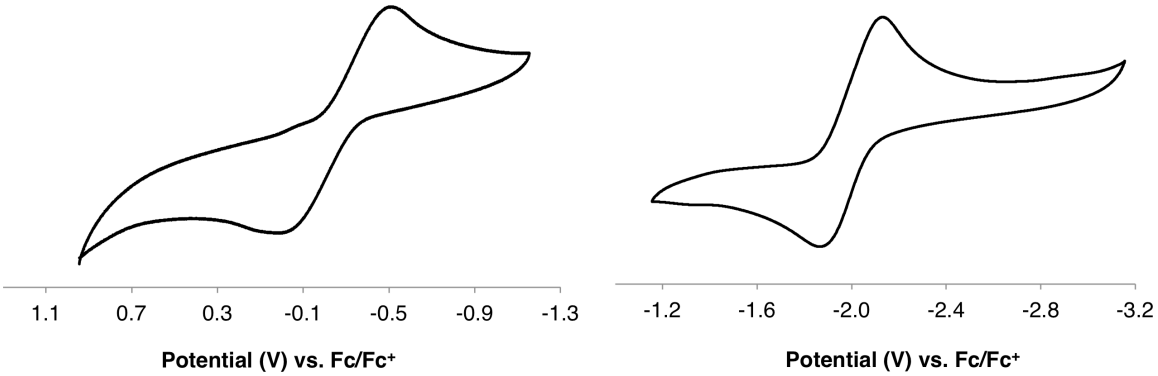

Figure 2.4 Cyclic voltammagram of (TPB)Co(N_2) scanning oxidatively (left) and reductively (right) at 100 mV/sec in THF with 0.1 M $TBAPF_6$ electrolyte.

consistent with increased backbonding to each of these atoms. In addition, the Co center is nearly perfectly C_3-symmetric as would be expected for a closed-shell complex. The electronic structure of [(TPB)Co(N_2)][Na(12-crown-4)$_2$] and related complexes will be discussed later in the chapter.

Scheme 2.3 Oxidation and reduction of (TPB)Co(N_2)

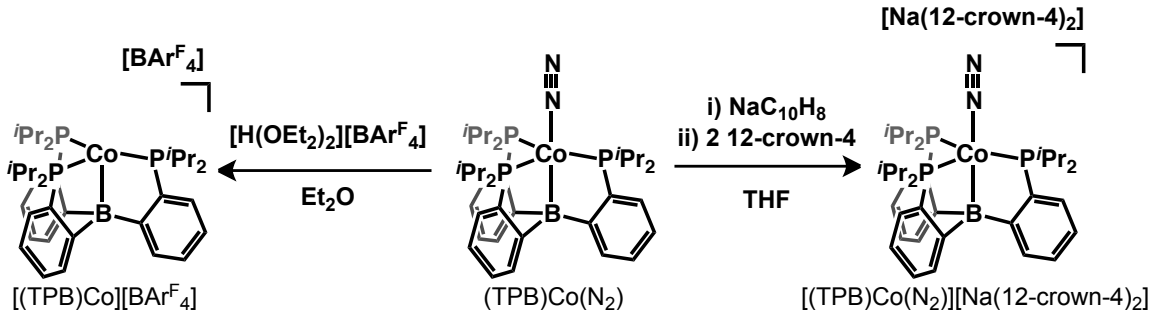

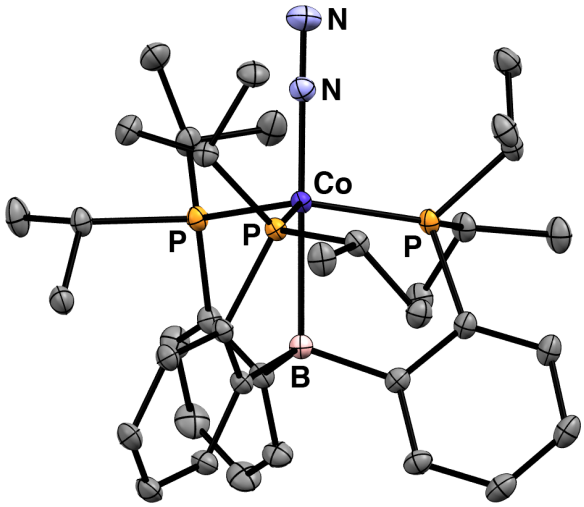

Figure 2.5 Displacement ellipsoid (50%) representation of [(TPB)Co(N_2)][Na(12-crown-4)$_2$]. Countercation, solvent molecules, and H atoms omitted for clarity. Selected distances and angles: Co–B = 2.300(3) Å; Co–P = 2.1872(8) Å, 2.1878(7) Å, 2.1918(8) Å; Co–N = 1.792(3) Å; N–N = 1.130(4) Å; ∠(P–Co–P) = 117.33(1)°, 117.64(1)°, 118.03(1)°; Σ∠(C–B–C) = 331°.

Oxidation of (TPB)Co(N_2) can be achieved by addition of 1 equiv [H·(OEt$_2$)$_2$][BAr$^F_4$] to generate red-purple [(TPB)Co][BAr$^F_4$]. SQUID magnetometry measurements indicate that the complex adopts a high spin state in the solid state (Figure 2.6) with no evidence for spin crossover. The ^{1}H NMR spectrum in C_6D_6/Et$_2$O is C_3-symmetric and structure (Figure 2.7) confirms that [(TPB)Co][BAr$^F_4$] does not bind N_2. There are many structural

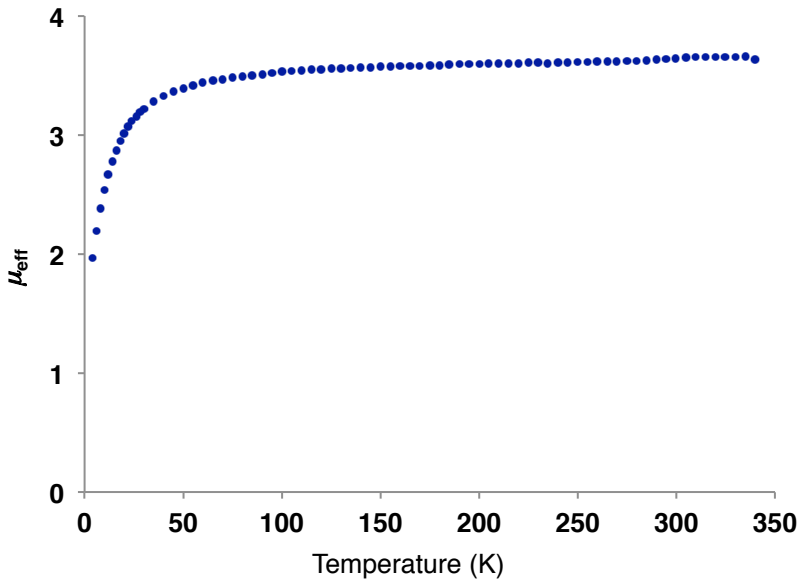

Figure 2.6 Temperature dependence of the magnetic susceptibility of [(TPB)Co][BAr^F_4] as measured by SQUID magnetometry.

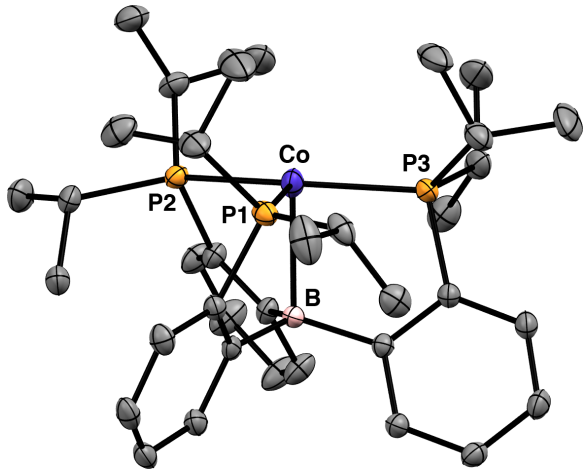

Figure 2.7 Displacement ellipsoid (50%) representation of [(TPB)Co][BAr^F_4]. Counteranion and H atoms omitted for clarity. Selected distances and angles: Co–B = 2.2559(16) Å; Co–P1 = 2.3473(5) Å, 2.3406(5) Å, 2.3031(5) Å; ∠(P1–Co–P2) = 111.90(2)°; ∠(P1–Co–P3) = 110.35(2)°; ∠(P2–Co–P3) = 136.57(2)°; Σ∠(C–B–C) = 388°.

similarities between [(TPB)Co][BAr^F_4] and the reported [(TPB)Fe][BAr^F_4] complex:[12] both display a M–B distance that is shorter and a B center that is less pyramidalized than

that in the corresponding (TPB)MBr complexes. For [(TPB)Fe][BAr^F_4], this apparent discrepancy was rationalized by there being little or no Fe–B bonding such that the Fe–B distance is a reflection of the geometrical constrains imposed by the cage structure.[12] This explanation is equally plausible for [(TPB)Co][BAr^F_4]. In addition, both complexes display one wide P–M–P angle, which may also be attributed to the cage structure.

Application of vacuum to a toluene solution of (TPB)Co(N_2) results in formation of a new species. Dark brown "(TPB)Co" absorbs more strongly than (TPB)Co(N_2) in the entire visible region, with the former having characteristic absorption bands at 510 nm and 806 nm (ε = 640 and 690 M^{-1} cm^{-1}, respectively). This transformation can be observed by ^{1}H NMR spectroscopy; (TPB)Co(N_2) and "(TPB)Co" show different sets of ten paramagnetically-shifted signals, indicating that both species are C_3-symmetric in solution (Figure 2.8). The EPR spectrum of (TPB)Co (Figure 2.2, middle) shows the disappearance of the signal corresponding to (TPB)Co(N_2) as well as a new signal (g = [2.372, 2.166, 2.089]). Although this spectrum has more features than that of (TPB)Co(N_2), hyperfine coupling cannot be rigorously simulated due to the large number of spin-active nuclei and the broadness of the signal. Attempts to grow single crystals of "(TPB)Co" under Ar or vacuum have been unsuccessful.

There are several reasonable structures of "(TPB)Co:" (i) a dicobalt bridging N_2 complex of the form (TPB)Co-(μ-1,2-N_2))-Co(TPB); (ii) a cyclometallated species under rapid exchange in which a ligand C–H bond has been intramolecularly activated; (iii) a trigonal pyramidal species with a vacant site *trans* to the B atom; (iv) a complex with either a weak intramolecular agostic interaction or bound solvent molecule. The solution

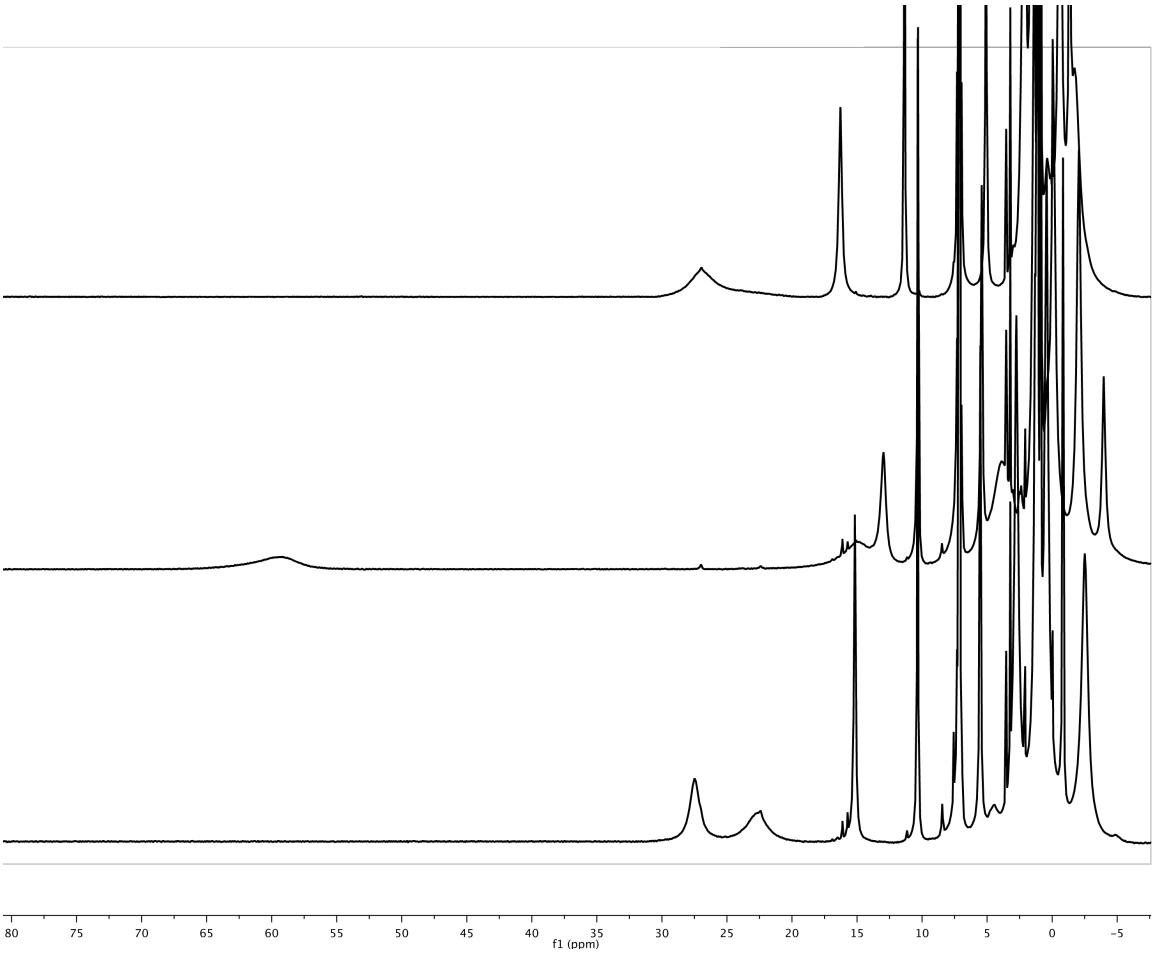

Figure 2.8 ^{1}H NMR spectra of (TPB)Co(N_2) under 1 atm N_2 (top), "(TPB)Co" under vacuum (middle), and (TPB)Co(H_2) under 1 atm H_2 (bottom) recorded in C_6D_6 at RT.

Raman spectrum of "(TPB)Co" does not display any resonances between 1,700 and 2,300 cm^{-1}, the region in which $\nu_{(N\text{-}N)}$ and $\nu_{(Co\text{-}H)}$ stretches are anticipated. This leads me to favor structural possibilities (iii) or (iv) rather than (i) or (ii). Additionally, "(TPB)Co" may be formed in arene (benzene and toluene) as well as more weakly coordinating solvents (pentane and HMDSO); this leads me to disfavor a model that invokes solvent binding. Structure type (iii) has been previously observed for the related trigonal pyramidal complexes of (SiP_3)[13] and (TPB).[12, 14] The optimized geometry of "(TPB)Co" (B3LYP/6-

31g(d)) reveals a trigonal pyramidal geometry of structure type (iii) and a short Co–B distance of 2.14 Å; attempts to locate a minimum geometry with an intramolecular C–H agostic interaction resulted in convergence to structure type (iii).

Addition of 1 atm H_2 to solutions of "(TPB)Co" results in new spectroscopic features that are most consistent with formation of the non-classical H_2 complex (TPB)Co(H_2). In solution under 1 atm H_2, the UV/vis spectrum of (TPB)Co(H_2) is similar to that of (TPB)Co(H_2). The ^{1}H NMR spectrum of (TPB)Co(H_2) under 1 atm H_2 consists of ten paramagnetically-shifted signals, indicating that (TPB)Co(H_2) is C_3-symmetric on the NMR time scale. In addition, no peak corresponding to free H_2 is observed at room temperature, suggesting that H_2 is interacting rapidly with "(TPB)Co" (a sharp peak corresponding to free H_2 is not observed above -90 °C in toluene-d_8). The EPR spectra of (TPB)Co(H_2) and (TPB)Co(N_2) are similar, with the former exhibiting somewhat greater rhombicity as displayed by its more pronounced splitting of g_2 and g_3 (Figure 2.2, bottom; g = [2.457, 2.123, 2.029]). The EPR spectra of (TPB)Co(H_2) and (TPB)Co(D_2) are identical and broad; as a result, no ^{1}H hyperfine coupling can be gleaned. Raman spectra of (TPB)Co(H_2) and (TPB)Co(D_2) (in both solution and solid states) are identical; this observation precludes the presence of Co-H(D) bonds in (TPB)Co(H_2)/(D_2) which are expected to have observable stretches that are subject to isotopic shifts approximated by the harmonic oscillator model. In contrast to M–H(D) stretches, H–H and D–D stretches often are too weak to observe or are obscured by resonances attributed to the other ligands.[2c, 2e]

Orange single crystals of (TPB)Co(H_2) were grown by slowly cooling a saturated solution of (TPB)Co(H_2) under 1 atm H_2. The sample diffracted strongly to 0.58 Å, and the

final solution (not including the H_2 ligand) fits the data very satisfactorily. The (TPB)Co frameworks of (TPB)Co(N_2) and (TPB)Co(H_2) are similar, with the latter exhibiting slightly contracted Co–P and Co–B bonds and more uniform P–Co–P angles (Figure 2.9).

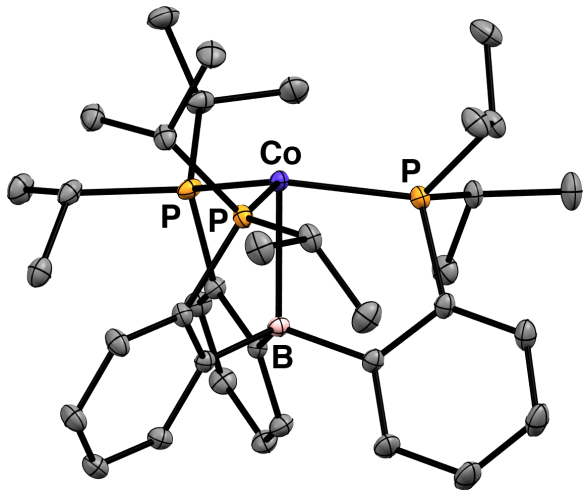

Figure 2.9 Displacement ellipsoid (50%) representation of (TPB)Co(H_2). H atoms omitted for clarity. Selected distances and angles: Co–B = 2.2800(10) Å; Co–P = 2.2412(3) Å, 2.2650(3) Å, 2.2749(3) Å; ∠(P–Co–P) = 110.97(1)°, 119.00(1)°, 124.50(1)°; Σ∠(C–B–C) = 336°.

A globular disc of residual positive electron density *trans* to the B atom is observed (Figure 2.10) which may be assigned to the H–H internuclear electron density. Subjecting this same analysis to the previously published (SiP_3)Fe(H_2) complex[2e] as well as the concurrently published (SiP_3)Co(H_2) complex[3] give rise to strikingly similar images. Further discussion of these isostructural complexes is undertaken later in the chapter.

The non-H atom locations of (TPB)Co(H_2) provide further support of formulating (TPB)Co(H_2) as an H_2 complex rather than a dihydride. In particular, an octahedral *cis*-dihydride is expected to exhibit one wide P–Co–P angle to accommodate a bisecting hydride ligand. The widest P–Co–P angle in (TPB)Co(H_2) is 124.50(1)° which is

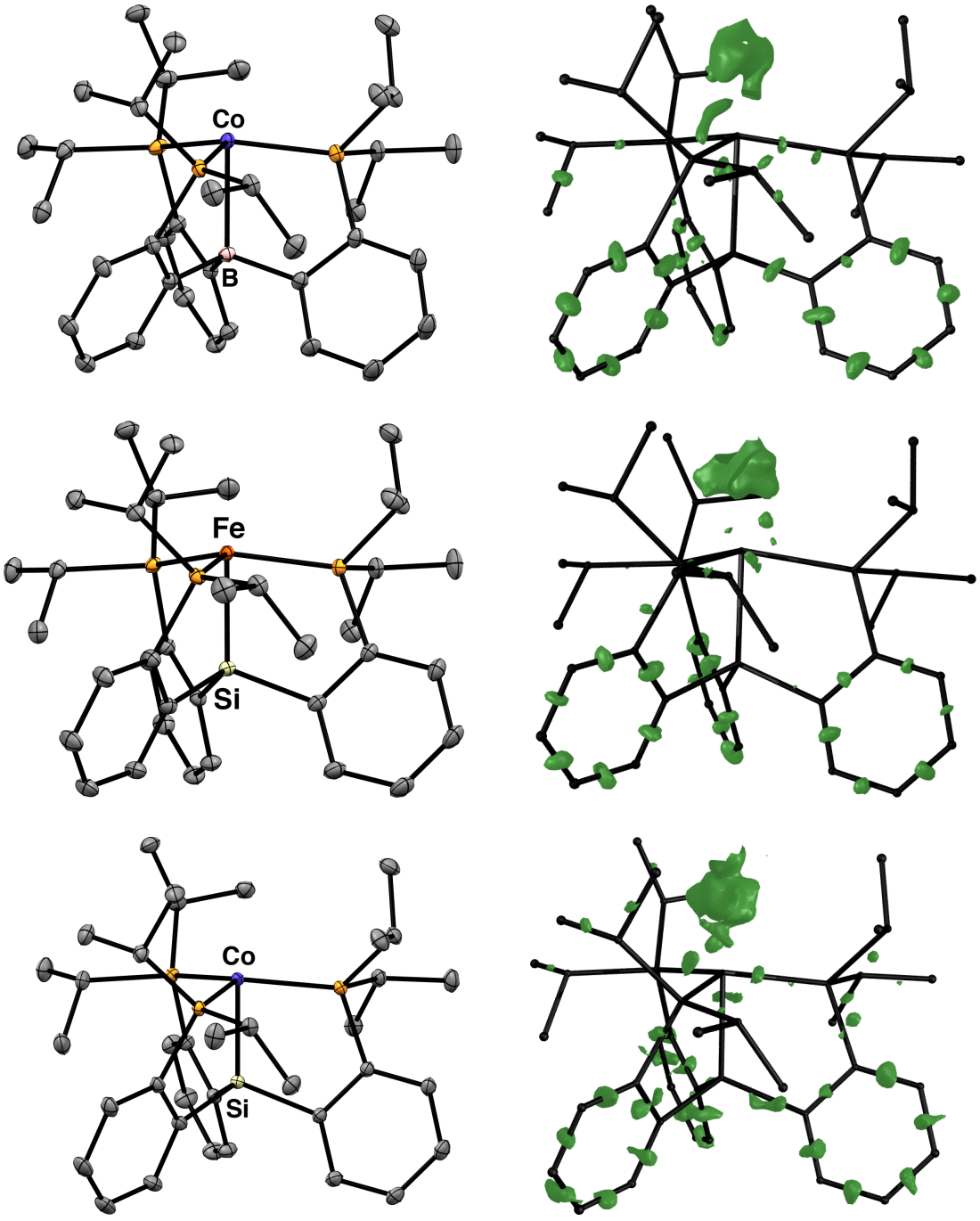

Figure 2.10 Displacement ellipsoid (50%) representations (left) and positive residual electron density maps (right, 0.47 e^- $Å^{-3}$ isosurface) of (TPB)Co(H_2) (top), (SiP_3)Fe(H_2) (middle), and (SiP_3)Co(H_2) (bottom).

significantly narrower than would be expected. Alternatively, if the H-H bond is cleaved in (TPB)Co(H_2) to give a trigonal bipyramidal species of the form Co(H)(TPB-H), the boron in (TPB)Co(H_2) would be expected to be tetrahedral with nearly linear B-H-Co bonding; this isomer would have a significantly longer Co-B distance than that which is observed. The non-H atom positions in the DFT-optimized structure are consistent with the X-ray structure; the intact H_2 ligand in the optimized structure is not significantly elongated compared with free H_2 (0.82 and 0.74 Å, respectively). Although the spectroscopic and computational data support the formulations of (TPB)Co(H_2) as a non-classical H_2 complex, it remains possible that dihydride structures and/or a hydride-borohydride structure for (TPB)Co(H_2) are thermally accessible. Reversible H_2 activation across an M–B bond in related Ni and Fe systems to form a (B–H)M(H) motifs has been observed.[15] (TPB)Co(H_2) facilitates scrambling of HD to give H_2, D_2, and HD; although this process may be mediated by transient hydrido species, it may also be accomplished by other conceivable mechanisms such as Lewis acidic H_2 activation and deprotonation by trace exogenous base.

The UV/vis spectra of (TPB)Co(N_2) and (TPB)Co(H_2) (1 atm N_2 or H_2, toluene, RT) show a small quantity of "(TPB)Co" which is readily identified by its characteristic band at 806 nm. This subtle feature suggested that the thermochemistry of H_2 and N_2 binding to "(TPB)Co" could be determined by UV/vis spectroscopy. Gratifyingly, the temperature dependence of K_{H2} could be extracted by monitoring the concentration of "(TPB)Co" by UV/vis spectroscopy in the range 24.2–81.7 °C (toluene, 1 atm H_2; Figure 2.11). A van't Hoff analysis reveals the energetics of H_2 binding to"(TPB)Co:" ΔH° =

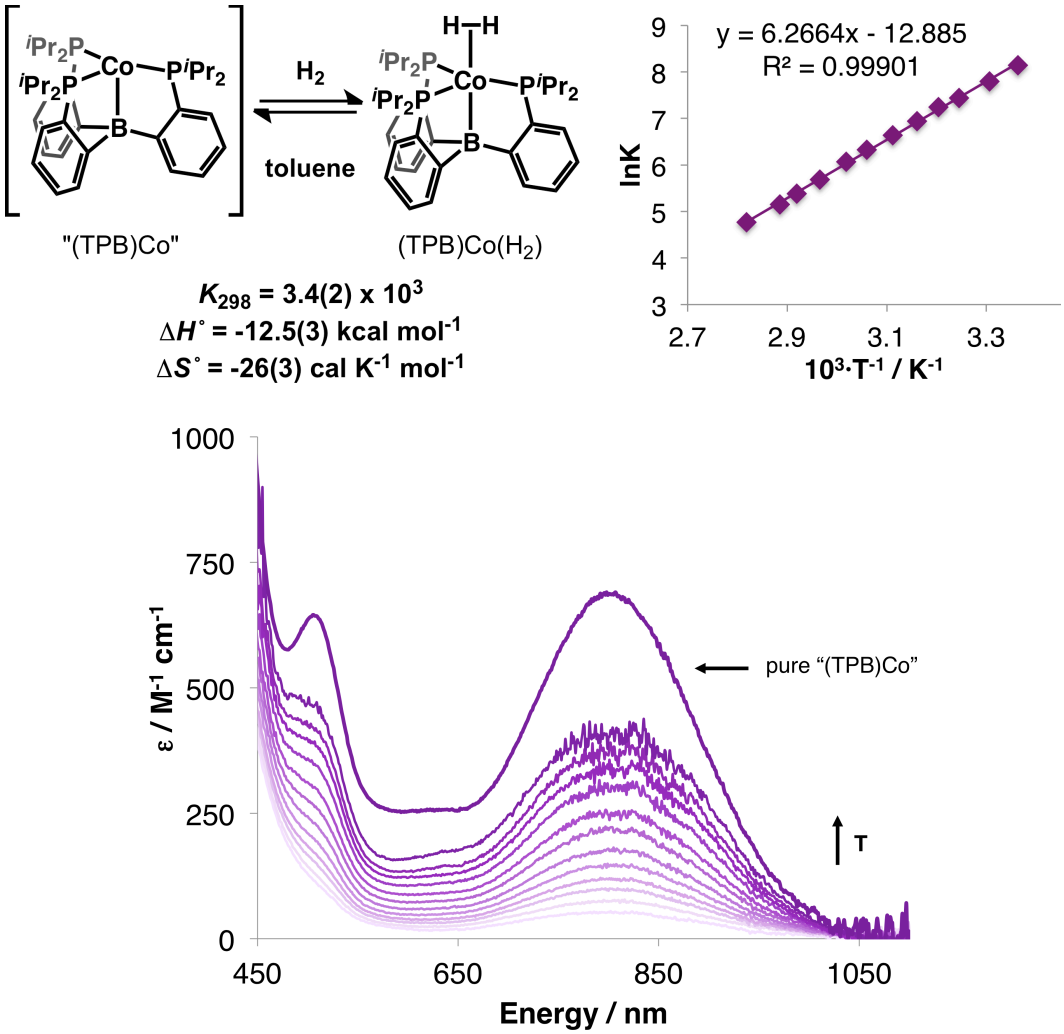

Figure 2.11 Temperature-dependent UV/vis study of the thermodynamics of H_2 binding to "(TPB)Co." The top trace in the UV/vis spectrum corresponds to pure "(TPB)Co." Darker traces correspond to higher concentrations of (TPB)Co(H_2). Van't Hoff plots were derived by monitoring the concentration of "(TPB)Co" as indicated by the absorbance at 740 nm where the signal does not become saturated at any temperature in this experiment.

-12.5(3) kcal mol^{-1} and $\Delta S°$ = -26(3) cal K^{-1} mol^{-1}. These values may include contributions from a weak agostic interaction or interaction with solvent, depending on the solution structure of "(TPB)Co" (*vide supra*). This work is, to my knowledge, the first time the energetics of H_2 binding to a homogeneous Co complex have been determined

experimentally. These values are in line with representative examples of H_2 binding energetics for other homogeneous metal complexes ($\Delta H°$: -6.5 to -18 kcal mol^{-1}; $\Delta S°$: -19 to -44 cal K^{-1} mol^{-1}).[16] Caution should be exercised in directly comparing these thermodynamic values since the standard states may be defined differently. The standard states for all thermodynamic studies in this chapter are defined as 1 M in all species in toluene at RT.

An analogous study of N_2 binding to "(TPB)Co" was undertaken between 30.2–86.3 °C (toluene, 1 atm N_2; Figure 2.12), and the energetics of N_2 binding to "(TPB)Co" were determined to be $\Delta H°$ = -13.9(7) kcal mol^{-1} and $\Delta S°$ = -32(5) cal K^{-1} mol^{-1}. Compared with N_2, binding H_2 is slightly less favorable enthalpically and less *dis*favorable entropically. The more negative value of $\Delta S°$ for N_2 binding is in part due to the higher absolute entropy of free N_2. Similar observations have been made for Cr, Mo, and W complexes.[16a, 16b, 16f]

2.3 Discussion

The properties of (TPB)Co(N_2) and (TPB)Co(H_2) are particularly interesting in the context of related isostructural (TPB) and (SiP_3) complexes. Through an analysis of the data presented in this chapter and that published elsewhere, I aim to delineate what factors are most important in dictating the strength of N_2 (and H_2) binding and the degree of N_2 activation. First, it is notable that no "vacant" Fe, Co, or Ni complexes of the form (SiP_3)M with any molecular charge have been observed; in all cases, these fragments bind N_2 in the absence of a better ligand.[17] The remarkable penchant for N_2 binding by

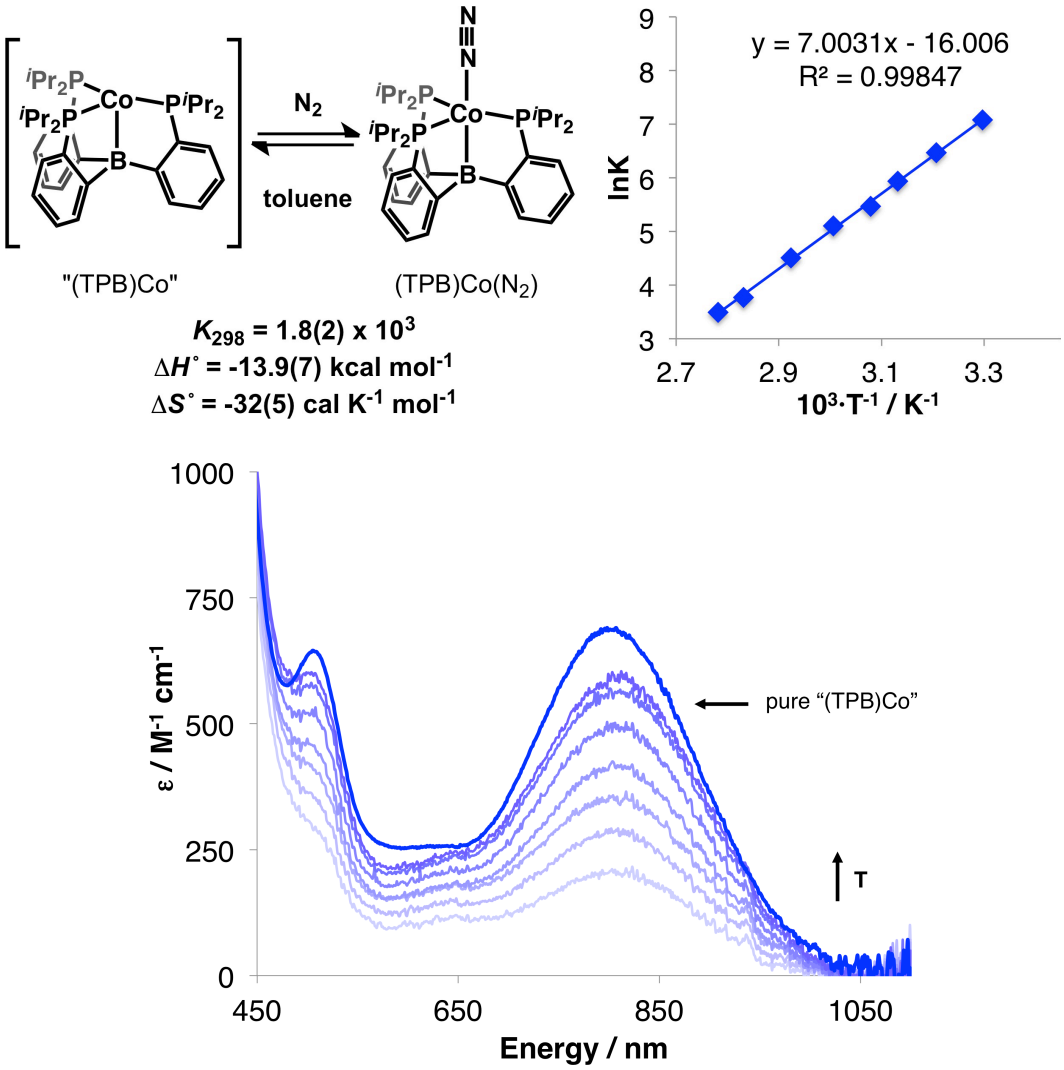

Figure 2.12 Temperature-dependent UV/vis study of the thermodynamics of H_2 binding to "(TPB)Co." The top trace in the UV/vis spectrum corresponds to pure "(TPB)Co." Darker traces correspond to higher concentrations of (TPB)Co(N_2). Van't Hoff plots were derived by monitoring the concentration of "(TPB)Co" as indicated by the absorbance at 740 nm where the signal does not become saturated at any temperature in this experiment.

these systems is exemplified by [(SiP_3)Ni(N_2)][BAr^F_4] which, in spite of its extremely high $\nu_{(N-N)}$ value of 2223 cm^{-1}, binds N_2 fully at RT even under vacuum.[17c] The strong N_2 binding for this system has been attributed to the σ-accepting properties of the complex (rather than π back-donation).[17c] This high Lewis acidity can be rationalized by

considering the Ni center either as a formally low-coordinate, Ni^{II} center that is partially stabilized by an anionic :SiR_3 donor or, alternatively, as a formally Ni^0 center with an extremely electrophilic *trans* cationic SiR_3 acceptor. Of course, neither formulation is appropriate given the high covalency of the Ni–SiR_3 bond (see Chapter 1), however they represent reasonable models for the observed Lewis acidity.

The fact that (TPB)Ni—which should be a stronger π-backbonding fragment than $[(SiP_3)Ni]^+$ due to its neutral charge—does not bind N_2 or H_2 under the same conditions (RT and 1 atm) supports the importance of σ-donotation for N_2 binding.[17c] If the silyl and borane ligands are considered σ-accepting fragments, then SiR_3^+ should be a better σ-acceptor than BR_3 and would therefore render the Ni more Lewis acidic in the *trans* site. On the other hand, if the ligands are considered as two-electron donors, then it follows that :BR_3^{2-} should be a stronger donor than :SiR_3^- and would therefore render the Ni less Lewis acidic in the *trans* site. Both formalisms account for the stronger N_2 and H_2 binding by $[(SiP_3)Ni]^+$ compared with (TPB)Ni. Alternatively, one can consider a simple MO model in which the lone pair on N forms a dative bond with the empty Ni–SiR_3 or Ni–BR_3 antibonding orbital. Since Si is less electronegative than B and an SiR_3 ligand forms a normal covalent bond with Ni (whereas a BR_3 ligand forms a more polarized dative covalent bond), one would expect the empty Ni–ER_3 orbital to be more localized on Ni in an Ni–SiR_3 complex compared with an Ni–BR_3 complex. This model would suggest that $[(SiP_3)Ni]^+$ binds N_2 more strongly than (TPB)Ni because of the better orbital overlap in the former. Support for this model would require a detailed theoretical treatment.

If a metal complex can bind N_2 strongly but with little activation (such as $[(SiP_3)Ni(N_2)][BAr^F_4]$) then it follows that it should be possible to design a complex that binds N_2 weakly but with a greater degree of activation. The lower N_2 stretch and lower N_2 binding constant of $(TPB)Co(N_2)$ in comparison with $[(SiP_3)Ni(N_2)][BAr^F_4]$ demonstrate this hypothesis. Based on the preceding discussion, the (TPB)Co fragment is expected to be a poorer σ-acceptor than the $[(SiP_3)Ni]^+$ fragment; the former should also be a better π donor because of its neutral charge and the identity of the metal center because earlier metals have more diffuse orbitals.

In order to develop a more thorough understanding of the effects of electron count, metal identity, and charge on the degree of N_2 activation, I will make a series of comparisons that vary one of these parameters at a time. First, since it is clear that the identities of the both the transition metal and the apical main group metal are important with respect to N_2 binding and activation in these complexes, it is useful to consider the [M–E] unit when determining the electron count (

Table 2.1 and Table 2.2). In this regard, $(SiP_3)Fe$ and (TPB)Co complexes of the same molecular charge may be considered to be valence isoelectronic. Compared with $[(SiP_3)Fe(N_2)][Na(12\text{-crown-}4)_2]$, $[(TPB)Co(N_2)][Na(12\text{-crown-}4)_2]$ imparts a lower degree of N_2 activation as judged by its higher $\nu_{(N-N)}$ value (1978 vs. 1920 cm^{-1}), yet its reduction potential is only modestly more anodic (-2.0 vs. -2.2 V vs. Fc/Fc^+). Importantly, this difference in N_2 activation is manifested in the reactivity of these complexes with electrophiles. Whereas Nβ in $[(SiP_3)Fe(N_2)Na(THF)_x]$ can be functionalized with silyl electrophiles such as TMSCl to give, for example, $(SiP_3)Fe(NNSiMe_3)$, my attempts to take advantage of the nucleophilicity of Nβ in

[(TPB)Co(N_2)Na(THF)$_x$] were met with no success: I only observed net one- and two-electron oxidation. Although it is possible that N_2 functionalization was achieved in the reactions with [(TPB)Co(N_2)Na(THF)$_x$] but that the product was too unstable to be observed, this reactivity pattern is at least anecdotally consistent with the spectroscopic and electrochemical differences between the two systems. Thus, the following conclusions can be tentatively drawn: for an initial functionalization of N_2 in which a single metal site imparts nucleophilicity to Nβ for reaction with an electrophile, Fe is expected to be more effective than Co owing to the greater π basicity of the former. Although the constituent atoms of a [Co–B] unit are more electronegative than those of an [Fe–Si] unit—and therefore might be expected to undergo underdesired oxidation reactions more slowly—its attenuated π basicity may render it less suitable for at least an initial N_2 functionalization reaction.

Each of the N_2 complexes based on the SiP_3 and TPB platforms adopts a nearly TBP geometry and has a total [M–E] electron count of at least eight. As such, the differences in [M–E] electron counts reflect only differences in the occupation of the d_{xy} and $d_{x^2-y^2}$ orbitals, neither of which are involved in N_2 binding or activation. Thus, these electron counts are not expected to be very consequential for N_2 binding and activation except to the extent that they affect the molecular charge. Indeed, the differences in $\nu_{(N-N)}$ between [(SiP_3)Fe(N_2)][Na(12-crown-4)$_2$] and [(TPB)Fe(N_2)][Na(12-crown-4)$_2$] (1920 vs. 1905 cm^{-1}), (SiP_3)Fe(N_2) and (TPB)Fe(N_2) (2003 vs. 2011 cm^{-1}), and (SiP_3)Co(N_2) and (TPB)Co(N_2) (2063 vs. 2089 cm^{-1}) are small and do not follow a clear trend even though the molecules in each pair differ by one valence electron. On the other hand, the

Table 2.1 Comparisons of (TPB)Fe and (SiP_3)Fe complexes

M	Fe					
E	B			Si		
Name	$[(TPB)Fe]^+$	$(TPB)Fe(N_2)$	$[(TPB)Fe(N_2)]^-$	$[(SiP_3)Fe(N_2)]^+$	$(SiP_3)Fe(N_2)$	$[(SiP_3)Fe(N_2)]^-$
Charge	+1	0	-1	+1	0	-1
[M-E] count	7	8	9	8	9	10
S	$^3/_2$	1	$^1/_2$	1	$^1/_2$	0
N_2 binding [a]	-	fully	fully	fully	fully	fully
M–N	-	?	1.781(2)	1.914(2)	1.819(15)	1.795(3)
N–N	-	?	1.144(3)	1.091(3)	1.125(2)	1.132(4)
$\nu_{(N-N)}$ (KBr)	-	2011	1905	2143	2003	1920
$\nu_{(N-N)}$ (solution)	-	-	1918	-	-	-
$\nu_{(N-N)}$ (thin film)	-	-	-	-	-	-
$E_{1/2}$ [b]	-	-1.5	-2.19	-	-1	-2.2
M–E	2.2167(15)	?	2.293(3)	2.2978(7)	2.2713(6)	2.236(1)
M–P (avg.)	2.38	?	2.25	2.39	2.29	2.2
Ref.	12	18	18	17b	17a, 17b	17b

Table 2.2 Comparisons of (TPB)M and (SiP_3)M complexes (M = Ni, Co)

M	Co				Ni	
E	B			Si	B	Si
Name	$[(TPB)Co]^+$	$(TPB)Co(N_2)$	$[(TPB)Co(N_2)]^-$	$(SiP_3)Co(N_2)$	(TPB)Ni	$[(SiP_3)Ni(N_2)]^+$
Charge	+1	0	-1	0	0	+1
[M-E] count	8	9	10	10	10	10
S	1	$^1/_2$	0	0	0	0
N_2 binding [a]	-	partially	fully	fully	-	fully
M–N	-	1.8623(12)	1.792(3)	1.813(2)	-	1.905(2)
N–N	-	1.0618(19)	1.130(4)	1.123(3)	-	1.083(3)
$\nu_{(N-N)}$ (KBr)	-	-	-	-	-	-
$\nu_{(N-N)}$ (solution)	-	-	-	2063	-	-
$\nu_{(N-N)}$ (thin film)	-	2089	1978	-	-	2223
$E_{1/2}$ [b]	-	-0.2	-2	?	?	?
M–E	2.2559(16)	2.2800(10)	2.301(3)	2.2327(7)	2.168(2)	2.2451(9)
M–P (avg.)	2.33	2.29	2.19	2.23	2.2	2.32
Ref.	-	3	-	17a	14a	17c

[a] 1 atm N_2 at RT in solution. [b] Oxidation potential. Distances given in Å, energies in cm^{-1}, and potentials in V vs. Fc/Fc^+ in THF with $TBAPF_6$ electrolyte.

molecular charge appears to be a critical factor for the degree of N_2 activation: the three pairs of N_2 complexes in Table 2.1 and Table 2.2 that differ by molecular charge and not electron count or M identity ((TPB)Fe(N_2) and [(SiP_3)Fe(N_2)][BAr^F_4]; [(TPB)Fe(N_2)][Na(12-crown-4)$_2$] and (SiP_3)Fe(N_2); [(TPB)Co(N_2)][Na(12-crown-4)$_2$] and (SiP_3)Co(N_2)) show a lower $\nu_{(N-N)}$ for the anionic species by an average of 105 cm^{-1}. Similarly, the four pairs of N_2 complexes that differ by molecular charge and not by the identities of M or E ([(SiP_3)Fe(N_2)][BAr^F_4] and (SiP_3)Fe(N_2); (SiP_3)Fe(N_2) and [(SiP_3)Fe(N_2)][Na(12-crown-4)$_2$]; (TPB)Fe(N_2) and [(TPB)Fe(N_2)][Na(12-crown-4)$_2$]; (TPB)Co(N_2) and [(TPB)Co(N_2)][Na(12-crown-4)$_2$]) show an average decrease in $\nu_{(N-N)}$ of 110 cm^{-1} upon addition of one electron.

2.4 Summary

In conclusion, the series of (TPB)M and (SiP_3)M N_2 and H_2 complexes allow for a systematic comparison of the factors that affect N_2 and H_2 binding and activation in highly covalent late metal complexes of three-fold symmetry. These experimental comparisons are enabled by the thermal robustness of these unusual complexes. The weak N_2 (and H_2) binding to (TPB)Co makes clear the important distinction between the strength of binding and the degree of activation. In general, the TPB ligand renders the metal a poorer σ-accepter than the SiP_3 ligand, which is the primary factor that contributes to the weaker N_2 binding in TPB complexes. On the other hand, the degree of N_2 activation is primarily dictated by the molecular charge and identity of the transition metal; the identity of the axial main group atom and the overall electron count have little effect on N_2 activation for complexes of this geometry.

2.5 Experimental

*General Considerations***.** All manipulations were carried out using standard Schlenk or glovebox techniques under an atmosphere of dinitrogen. Solvents were degassed and dried by sparging with N_2 gas and passage through an activated alumina column. Deuterated solvents were purchased from Cambridge Isotopes Laboratories, Inc. and were degassed and stored over activated 3 Å molecular sieves prior to use. Reagents were purchased from commercial vendors and used without further purification unless otherwise noted. (TPB)[19] was synthesized according to literature procedures. Elemental analyses were performed by Midwest Microlab (Indianapolis, IN).

*Spectroscopic measurements***.** ^{1}H, ^{13}C, and ^{31}P NMR spectra were collected at room temperature, unless otherwise noted, on Varian 300 MHz and 400 MHz NMR spectrometers. ^{1}H and ^{13}C spectra were referenced to residual solvent resonances. ^{31}P spectra were referenced to external 85% phosphoric acid (δ = 0 ppm). EPR spectra were recorded on a Bruker EMS spectrometer at ca. 1 mM concentrations. IR measurements were obtained in KBr pellets using a Bio-Rad Excalibur FTS 3000 spectrometer with Varian Resolutions Pro software or as thin films formed by evaporation using a Bruker Alpha Platinum ATR spectrometer with OPUS software. Solution-state Raman spectra were acquired using a coherent Innova 70 5-W Ar-ion laser, a Spex 750M spectrograph with a 1200 gr/mm grating, and a Horiba Jobin Yvon Synapse TE cooled CCD detector. Solid-state Raman spectra were acquired on a Renishaw M1000 Micro Raman spectrometer system using an Ar ion laser and 514.5 nm excitation.

X-ray Crystallography. X-ray diffraction studies were carried out at the Caltech Division of Chemistry and Chemical Engineering X-ray Crystallography Facility on a Bruker three-circle SMART diffractometer with a SMART 1K CCD detector. Data was collected at 100K using Mo Kα radiation (λ = 0.71073 Å). Structures were solved by direct or Patterson methods using SHELXS and refined against F^2 on all data by full-matrix least squares with SHELXL-97.[20] All non-hydrogen atoms were refined anisotropically. All hydrogen atoms were placed at geometrically calculated positions and refined using a riding model. The isotropic displacement parameters of all hydrogen atoms were fixed at 1.2 (1.5 for methyl groups) times the Ueq of the atoms to which they are bonded.

Computational Details. All calculations were performed using the Gaussian03 suite.[21] The geometry optimizations were done without any symmetry restraints using the B3LYP hybrid functional. The 6-31g(d) basis set was used for all atoms. Minimized structures were verified with frequency calculations. The starting coordinates for the metal and ligand were taken from the crystal structures. To model H_2 adducts, hydrogen atoms were initially placed in the apical binding site at an arbitrary initial distance of 1.5 Å from the metal and 0.9 Å from each other. To model dihydrides, hydrogen atoms were initially placed orthogonal to one another (one in the apical site and one bisecting a P–M–P angle) at a distance of 1.4 Å from the metal.

Preparation of (TPB)CoBr: A Schlenk tube was charged with TPB (502.0 mg, 0.8500 mmol), $CoBr_2$ (185.9 mg, 0.8500 mmol), Co powder (249.6 mg, 4.250 mmol), THF (20 mL), and a magnetic stirbar. The green solution was heated at 90 ˚C for two days. After cooling, the residue was transferred to a 500 mL filter flask in a glovebox. The solvent was removed from the resulting deep yellow-green solution *in vacuo* to give a dark

residue. Residual THF was removed by adding benzene (5 mL) to the residue and evaporating to dryness under vacuum. Pentane (200 mL) was added and stirred vigorously for 5 min. This resulted in formation of a yellow solution with blue precipitate. The solution was decanted from the solids and filtered through a pad of Celite on a scintered glass frit. The remaining solids were extracted with pentane (60 mL portions) until the extracts were colorless (four times); the extracts were filtered and combined with the first batch. Removal of the solvent in vacuo provided a yellow-brown solid that was dissolved in benzene (5 mL) and lyophilized to give an orange-brown solid (435 mg, 0.596 mmol, 70%). Single crystals were grown by slow evaporation of an Et_2O solution into HMDSO. ^{1}H NMR (400 MHz, C_6D_6) δ 111.76, 29.58, 16.71, 15.99, 4.59, -0.03, -0.20, -1.01, -2.66, -8.34. Elemental analysis for $C_{36}H_{54}BBrCoP_3$: calc. C 59.28 H 7.46, found C 58.90 H 7.17.

Preparation of (TPB)Co(N_2): A solution of $NaC_{10}H_8$ was prepared by stirring naphthalene (34.3 mg, 0.277 mmol) and sodium (23.7 mg, 1.03 mmol) in THF (3 mL) for 4 hr. The resulting deep green solution was filtered and added dropwise to a stirring solution of (TPB)CoBr (149.4 mg, 0.2056 mmol) in THF (2 mL). The resulting dark red-brown solution was allowed to stir for 6 hr. Solvent was removed *in vacuo* and the resulting dark red-brown residue was dissolved in benzene (2 mL). Solvent was again removed *in vacuo* and the resulting solid was stirred in benzene (3 mL) for five min. The brown solution was filtered through a pad of Celite and lyophilized to give dark brown "(TPB)Co". Solid samples of "(TPB)Co" stored under N_2 turned bright yellow over several days, giving (TPB)Co(N_2) (106.0 mg, 0.1566 mmol, 76%). Single crystals were

grown by slow evaporation of an Et_2O solution into HMDSO. ^1H NMR (400 MHz, C_6D_6) δ 26.95, 23.82, 16.28, 11.35, 5.09, 2.15, 1.56, -0.60, -1.35, -1.73. Elemental analysis shows low values for N which is consistent with the observed lability of the N_2 ligand.

Preparation of [(TPB)Co(N_2)][Na(12-crown-4)$_2$]: To a -78 ˚C solution of (TPB)CoBr (70.5 mg, 0.0967 mmol) in THF (2 mL) was added a freshly prepared solution of $NaC_{10}H_8$ (23.5 mg $C_{10}H_8$, 0.222 mmol) in THF (3 mL). The solution was brought to RT and allowed to stir for six hours. Addition of 12-crown-4 (51.1 mg, 0.290 mmol) and removal of solvent in vacuo provided a dark red solid. Et_2O was added and subsequently removed in vacuo. The residue was suspended in C_6H_6 and filtered and the solids were washed with C_6H_6 (2 x 2 mL) and pentane (2 x 2 mL) to furnish a red solid (68.8 mg, 0.0660 mmol, 68%). Single crystals were grown by vapor diffusion of pentane onto a THF solution of the title compound that had been layered with Et_2O. NMR peaks are somewhat broadened likely owing to the presence of a small amount of (TPB)Co(N_2). ^1H NMR (400 MHz, THF-d_8) δ 7.41 (3H), 6.94 (3H), 6.66 (3H), 6.44 (3H), 3.64 (32H), 2.29 (br), 1.37 (6H), 1.20 (6H), 0.93 (6H), -0.26 (6H). ^{11}B NMR (128 MHz, THF-d_8) δ 9.32. ^{31}P NMR (162 MHz, THF-d_8) δ 62.03.

Preparation of [(TPB)Co][BAr$^F_4$]: To a -78 ˚C solution of (TPB)Co(N_2) (91.5 mg, 0.135 mmol) in Et_2O (2 mL) was added solid [H(OEt_2)$_2$][BAr$^F_4$] (134.0 mg, 0.132 mmol). The reaction was brought to RT and vented to allow for the escape of H_2. The purple-brown solution was stirred for 1 hr. The solution was layered with pentane (5 mL) and stored at -35 ˚C to furnish red-purple single crystals of the title compound (162.9 mg,

0.0952 mmol, 82%) which were washed with pentane (3 x 2 mL). ^{1}H NMR (400 MHz, C_6D_6) δ 26.25, 23.80, 8.64, 8.44 ([BAr^F_4]), 7.88 ([BAr^F_4]), 6.33, -2.16, -3.68.

Generation of "(TPB)Co:" A yellow solution of (TPB)Co(N_2) in C_6D_6 was subjected to three freeze-pump-thaw cycles which resulted in formation of a dark brown solution. The transformation is clean by ^{1}H NMR and reversible by exposure to N_2 atmosphere to reform (TPB)Co(N_2). ^{1}H NMR (400 MHz, C_6D_6) δ 59.33, 14.93, 12.96, 10.31, 5.42, 3.88, 1.38, -0.10, -2.05, -3.97. Elemental analysis was not obtained due to the compound's propensity to bind atmospheric N_2.

Generation of (TPB)Co(H_2): A dark brown solution of "(TPB)Co" under vacuum was exposed to 1 atm H_2, resulting in immediate formation of a yellow solution. The transformation is clean by ^{1}H NMR and reversible by subjecting the solution to three freeze-pump-thaw cycles to reform "(TPB)Co". Single crystals were grown by slowly cooling a saturated solution (1:1 HMDSO:methylcyclohexane) of (TPB)Co(H_2) from 80 °C to RT. ^{1}H NMR (400 MHz, C_6D_6) δ 27.48, 22.60, 15.17, 10.34, 5.52, 2.75, 1.21, 0.43, -0.84, -2.51. Elemental analysis was not obtained because the compound is only stable to H_2 loss under H_2 atmosphere.

Measurement of K(H_2) as a function of temperature: A 0.00390 M solution of (TPB)Co(N_2) (23.8 mg, 0.0351 mmol) in toluene (9.00 mL) was generated in a glovebox. A two-necked glass tube with a 24/40 joint on top and a side arm with a 14/20 joint was charged with the solution and a stirbar. The 24/40 joint was equipped with a dip probe

(Hellma Worldwide, 10mm, 661.302-UV model) and the 14/20 joint was fitted with a rubber septum. The septum was pierced with a hole that allowed for introduction of a thermocouple into the solution. The sealed apparatus was removed from the glovebox and connected to a Schlenk line. The solution was frozen, evacuated, and refilled with H_2. This was repeated an additional two times. The UV/vis spectrum was recorded at twelve temperatures, allowing for at least 2 min. to equilibrate at each temperature: 24.2, 29.3, 35.0, 39.0, 43.2, 48.2, 53.7, 58.1, 64.1, 69.4, 73.4, and 81.7 ˚C (see Figure 2.11 in the main text). The concentration of "(TPB)Co" was calculated from the absorbance at 740 nm based on the known extinction coefficient of a pure sample of "(TPB)Co" at 740 nm (see Figure 2.11). This wavelength (740 nm) was selected instead of the peak's maximum (806 nm) because of signal saturation around 800 nm that arises from a strong absorbance in the background. The binding constant $K(H_2)$ was calculated at each temperature using the equation:

$$K(H_2) = [(TPB)Co(H_2)]/([H_2][\text{“(TPB)Co”}])$$

$$\text{where } [(TPB)Co(H_2)] = 0.0351/V(tol) - [\text{“(TPB)Co”}]$$

The temperature dependence of $[H_2]$ in toluene[22] and the density of toluene were taken from the literature.[23] An identical procedure was undertaken to measure the N_2 binding data using 6.7 mg $(TPB)Co(N_2)$ and $[N_2]$ in toluene from the literature.[24]

This chapter was reproduced in part with permission from

Suess, D. L. M.; Tsay, C.; Peters, J. C. *J. Am. Chem. Soc.* **2012**, *134*, 14158–14164.

(1) (a) Kubas, G. J.; Ryan, R.; Swanson, B.; Vergamini, P.; Wasserman, H. *J. Am. Chem. Soc.,* **1984,** *106*, 451; (b) Kubas, G. J.; Ryan, R.; Wrobleski, D. A. *J. Am. Chem. Soc.,* **1986,** *108*, 1339; (c) Morris, R. H.; Earl, K. A.; Luck, R. L.; Lazarowych, N. J.; Sella, A. *Inorg. Chem.,* **1987,** *26*, 2674.
(2) (a) Bart, S. C.; Lobkovsky, E.; Chirik, P. J. *J. Am. Chem. Soc.,* **2004,** *126*, 13794; (b) Baya, M.; Houghton, J.; Daran, J.-C.; Poli, R.; Male, L.; Albinati, A.; Gutman, M. *Chem. Eur. J.,* **2007,** *13*, 5347; (c) Hetterscheid, D. G. H.; Hanna, B. S.; Schrock, R. R. *Inorg. Chem.,* **2009,** *48*, 8569; (d) Kinney, R. A.; Hetterscheid, D. G. H.; Hanna, B. S.; Schrock, R. R.; Hoffman, B. M. *Inorg. Chem.,* **2010,** *49*, 704; (e) Lee, Y.; Kinney, R. A.; Hoffman, B. M.; Peters, J. C. *J. Am. Chem. Soc.,* **2011,** *133*, 16366.
(3) Suess, D. L. M.; Tsay, C.; Peters, J. C. *J. Am. Chem. Soc.,* **2012,** *134*, 14158.
(4) (a) Losse, S.; Vos, J. G.; Rau, S. *Coord. Chem. Rev.,* **2010,** *254*, 2492; (b) Wang, M.; Chen, L.; Sun, L. *Energy Environ. Sci.,* **2012,** *5*, 6763.
(5) (a) Dincă, M.; Long, J. R. *Angew. Chem. Int. Ed.,* **2008,** *47*, 6766; (b) Suh, M. P.; Park, H. J.; Prasad, T. K.; Lim, D.-W. *Chem. Rev.,* **2012,** *112*, 782.
(6) Hebrard, F. d. r.; Kalck, P. *Chem. Rev.,* **2009,** *109*, 4272.
(7) Dempsey, J. L.; Brunschwig, B. S.; Winkler, J. R.; Gray, H. B. *Acc. Chem. Res.,* **2009,** *42*, 1995.
(8) (a) Gadd, G. E.; Upmacis, R. K.; Poliakoff, M.; Turner, J. J. *J. Am. Chem. Soc.,* **1986,** *108*, 2547; (b) Bianchini, C.; Mealli, C.; Meli, A.; Peruzzini, M.; Zanobini, F. *J. Am. Chem. Soc.,* **1988,** *110*, 8725; (c) Heinekey, D.; Liegeois, A.; van Roon, M. *J. Am. Chem. Soc.,* **1994,** *116*, 8388; (d) Heinekey, D.; vanRoon, M. *J. Am. Chem. Soc.,* **1996,** *118*, 12134; (e) Hebden, T. J.; St John, A. J.; Gusev, D. G.; Kaminsky, W.; Goldberg, K. I.; Heinekey, D. M. *Angew. Chem. Int. Ed.,* **2010,** *50*, 1873.
(9) (a) Sweany, R. L.; Russell, F. N. *Organometallics,* **1988,** *7*, 719; (b) Doherty, M. D.; Grant, B.; White, P. S.; Brookhart, M. *Organometallics,* **2007,** *26*, 5950.
(10) Greenwood, B. P.; Forman, S. I.; Rowe, G. T.; Chen, C.-H.; Foxman, B. M.; Thomas, C. M. *Inorg. Chem.,* **2009,** *48*, 6251.
(11) Rudd, P. A.; Liu, S.; Gagliardi, L.; Young, J., Victor G; Lu, C. C. *J. Am. Chem. Soc.,* **2011,** *133*, 20724.
(12) Anderson, J. S.; Moret, M.-E.; Peters, J. C. *J. Am. Chem. Soc.,* **2013,** *135*, 534.
(13) Tsay, C.; Mankad, N. P.; Peters, J. C. *J. Am. Chem. Soc.,* **2010,** *132*, 13975.
(14) (a) Sircoglou, M.; Bontemps, S.; Bouhadir, G.; Saffon, N.; Miqueu, K.; Gu, W.; Mercy, M.; Chen, C.-H.; Foxman, B. M.; Maron, L.; Ozerov, O. V.; Bourissou, D. *J. Am. Chem. Soc.,* **2008,** *130*, 16729; (b) Moret, M.-E.; Zhang, L.; Peters, J. C. *J. Am. Chem. Soc.,* **2013**, 130304112449007.
(15) (a) Harman, W. H.; Peters, J. C. *J. Am. Chem. Soc.,* **2012,** *134*, 5080; (b) Fong, H.; Moret, M.-E.; Lee, Y.; Peters, J. C. *Organometallics,* **2013,** *32*, 3053.
(16) (a) Gonzalez, A. A.; Zhang, K.; Nolan, S. P.; Lopez de la Vega, R.; Mukerjee, S. L.; Hoff, C. D.; Kubas, G. J. *Organometallics,* **1988,** *7*, 2429; (b) Gonzalez, A. A.; Hoff, C. D. *Inorg. Chem.,* **1989,** *28*, 4295; (c) Hauger, B. E.; Gusev, D.; Caulton, K. G. *J. Am. Chem. Soc.,* **1994,** *116*, 208; (d) Heinekey, D.; Voges, M. H.; Barnhart, D. M. *J. Am. Chem. Soc.,* **1996,** *118*, 10792; (e) Shen, J.; Haar, C. M.; Stevens, E. D.; Nolan, S. P. *J. Organomet. Chem.,* **1998,** *571*, 205; (f) Grills, D. C.; van Eldik, R.; Muckerman, J. T.; Fujita, E. *J. Am. Chem. Soc.,* **2006,** *128*, 15728.

(17) (a) Whited, M. T.; Mankad, N. P.; Lee, Y.; Oblad, P. F.; Peters, J. C. *Inorg. Chem.,* **2009,** *48*, 2507; (b) Lee, Y.; Mankad, N. P.; Peters, J. C. *Nat. Chem.,* **2010,** *2*, 558; (c) Tsay, C.; Peters, J. C. *Chem. Sci.,* **2012,** *3*, 1313.
(18) Moret, M.-E.; Peters, J. C. *Angew. Chem. Int. Ed.,* **2011,** *50*, 2063.
(19) Bontemps, S.; Bouhadir, G.; Dyer, P. W.; Miqueu, K.; Bourissou, D. *Inorg. Chem.,* **2007,** *46*, 5149.
(20) G. M. Sheldrick, SHELXTL 2000, Universität Göttingen: Göttingen, Germany, 2000.
(21) M. J. Frisch, G. W. T., H. B. Schlegel, G. E. Scuseria, M. A. Robb, J. R. Cheeseman, J. A. Montgomery, Jr., T. Vreven, K. N. Kudin, J. C. Burant, J. M. Millam, S. S. Iyengar, J. Tomasi, V. Barone, B. Mennucci, M. Cossi, G. Scalmani, N. Rega, G. A. Petersson, H. Nakatsuji, M. Hada, M. Ehara, K. Toyota, R. Fukuda, J. Hasegawa, M. Ishida, T. Nakajima, Y. Honda, O. Kitao, H. Nakai, M. Klene, X. Li, J. E. Knox, H. P. Hratchian, J. B. Cross, V. Bakken, C. Adamo, J. Jaramillo, R. Gomperts, R. E. Stratmann, O. Yazyev, A. J. Austin, R. Cammi, C. Pomelli, J. W. Ochterski, P. Y. Ayala, K. Morokuma, G. A. Voth, P. Salvador, J. J. Dannenberg, V. G. Zakrzewski, S. Dapprich, A. D. Daniels, M. C. Strain, O. Farkas, D. K. Malick, A. D. Rabuck, K. Raghavachari, J. B. Foresman, J. V. Ortiz, Q. Cui, A. G. Baboul, S. Clifford, J. Cioslowski, B. B. Stefanov, G. Liu, A. Liashenko, P. Piskorz, I. Komaromi, R. L. Martin, D. J. Fox, T. Keith, M. A. Al-Laham, C. Y. Peng, A. Nanayakkara, M. Challacombe, P. M. W. Gill, B. Johnson, W. Chen, M. W. Wong, C. Gonzalez, and J. A. Pople. *Gaussian 03, Revision B.01*, Gaussian Inc.: Wallingford, CT, 2004.
(22) Brunner, E. *J. Chem. Eng. Data,* **1985,** *30*, 269.
(23) McLinden, M. O.; Splett, J. D. *J. Res. Natl. Inst. of Stand. and Technol.,* **2008,** *113*.
(24) Jabłoniec, A.; Horstmann, S.; Gmehling, J. *Ind. Eng. Chem. Res.,* **2007,** *46*, 4654.

Chapter 3 Dinitrogen Functionalization *via* E–H Addition to Fe–B Bonds

3.1 Background

The complex mechanisms of industrial, biological, and synthetic N_2 reduction processes continue to spur research on the coordination chemistry and reactivity of N_2 by a variety of conceptually distinct approaches.[1] For example, models of potential intermediates can be synthesized from well-defined metal precursors and fine chemicals (e.g. N_2H_4) in order to study their reactivity and spectroscopic features. Alternatively, precatalysts can be screened for the fixation of N_2 to reduced nitrogen-containing products (e.g. NH_3 or N_2H_4) and further studied under optimized conditions. My goal in this chapter is to delineate well-defined, elementary N_2 functionalization reactions that can be performed at a single Fe site.

The limiting pathways for any N_2 reduction process that occurs at a single metal site are the so-called distal (or "Chatt") and alternating mechanisms (Scheme 3.1).[2] Early metals that make strong M–N π bonds are well-suited for distal-type N_2 reduction mechanisms wherein strong M–Nα π–backbonding weakens the N–N bond, thereby rendering Nβ susceptible to protonation. Many reports have examined the catalytic and stoichiometric functionalization of N_2 using group VI metals, and in all cases distal-type mechanisms and intermediates are invoked.[3] Although both Mo- and V-dependent nitrogenases require Mo and/or V for their function, mounting evidence suggests that biological N_2 reduction occurs at one or more Fe centers in FeMoco and it is reasonable to assume that this is also the case for the V-dependent enzymes.[1a] Previous members of the Peters group have generated

terminal, multiply-bonded Fe–N model complexes, thereby demonstrating the electronic feasibility of species invoked on a distal pathway.[4] Most saliently, it has been shown that the $(BP_3)Fe$ platform can accommodate an N_2 ligand—a π-accepting ligand—as well as a terminal nitride—a strongly π-donating ligand.[5]

Scheme 3.1 Limiting mechanisms of single-site N_2 reduction

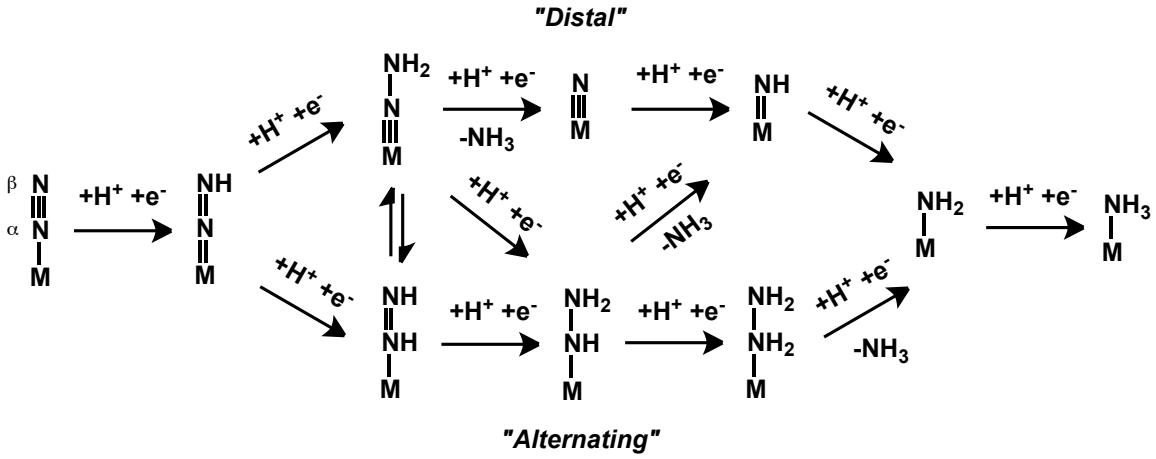

Of course, the feasibility of multiply-bonded Fe–N species in an N_2 reduction scheme has no implications for the actual mechanism of any N_2 reduction catalyst based on Fe. In addition, intermediates on a distal pathway may be converted to intermediates on an alternating pathway and vice versa, so the two pathways need not be distinct. For example, after protonation of Nβ in a terminal N_2 complex to form a diazenido species (a reasonable first step in a mononuclear N_2 reduction scheme), the distal and alternating mechanisms can then diverge, generating an aminoimide complex in the former or a hydrazine complex in the latter. These species are isomers and could conceivably interconvert, thereby switching between alternating and distal mechanisms. Another example is the hypothetical protonation of Nα in an aminoimide complex to give a hydrazido complex. There are of

course myriad possible ways to complicate these two limiting pathways, especially if one invokes the participation of other atoms in the cofactor or amino acid residues.

In addition to the ligand field considerations that lend plausibility to a distal mechanism based on Fe, such a mechanism also holds appeal because synthetic complexes have been demonstrated to model several of these reactions. Similarly to early-metal complexes, an electron-rich terminal Fe–N_2 complex could have a sufficiently π-basic metal to render Nβ susceptible to one or more protonations. This acid/base chemistry has been demonstrated in reactions between anionic Fe–N_2 model complexes and formally electrophilic reagents.[i] Former members of the Peters group have developed this class of reactivity in three different systems: $(BP_3)Fe$,[6] $(SiP_3)Fe$,[7] and (TPB)Fe.[8] I will briefly summarize the findings with the (TPB)Fe system since they represent the furthest extent of well-defined N_2 reduction at Fe prior to the work described in this chapter (Scheme 3.2). Successive reductions and silylations of $(TPB)Fe(N_2)$ give $(TPB)Fe(N_2)(Na(THF)_x)$, $(TPB)Fe(NNSiMe_3)$, and $(TPB)Fe(NNSiMe_3)Na(THF)$. Although the latter species does not undergo further functionalization with Me_3SiCl, a related species, $(TPB)Fe(NNSi_2)$, may be prepared that features a less sterically-encumbering disilylazacyclopentane ring (Scheme 3.3). Each subsequent reduction and silylation decreases N–N π bonding character and increases Fe–N π bonding character as shown by Fe–N and N–N distances as well as DFT studies.

[i] Although an anionic Fe–N_2 complex and an electrophilic reagent such as TMSCl may react as a nucleophile and electrophile, respectively, they may alternatively function as a reductant and oxidant if one-electron transfer processes are operable. The mechanistic details of these reactions are not known.

Scheme 3.2 Stepwise N_2 reduction at (TPB)Fe

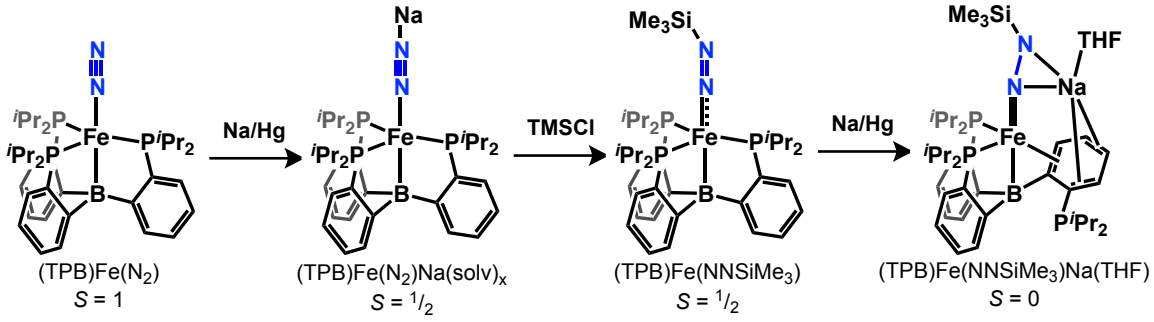

Scheme 3.3 Preparation of (TPB)Fe($NNSi_2$)

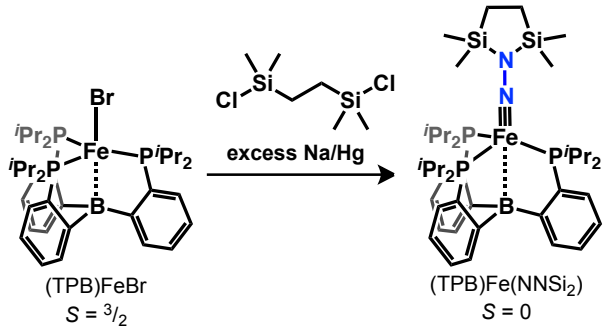

For complexes that model a distal N_2 reduction pathway based on Fe, the formation of (TPB)Fe($NNSi_2$) represents the state of the art. However, the field's understanding of Nα functionalization—which is central to an alternating pathway—remains less developed. In fact, prior to the work described in this chapter, there were no examples of Nα functionalization at a mononuclear metal complex based on any metal. Some of the challenges for realizing Nα functionalization can be seen by considering protonation reactions (Scheme 3.1). Direct protonation of Nα in an N_2 complex, a diazenido complex, or an aminoimide complex would be an entrance to an alternating mechanism. However, this may be challenging to achieve in a synthetic system because, in each case, Nβ is likely more basic than Nα; in fact, Nα may exhibit some degree of electrophilic character.

Furthermore, protonation could occur at Fe which, at least in synthetic systems and also possibly in nitrogenase, could lead to facile H_2 elimination.[7, 9] The organometallic N_2 chemistry at Fe is not sufficiently developed to reliably predict the regioselectivities of such protonation reactions.

The fact that there have been no reports of Nα functionalization is highly problematic if an alternating pathway (in whole or in parts) is considered a viable mechanism for N_2 reduction at a single Fe site.[9] The approach for Nα functionalization described in this chapter is to generate an Fe aminoimide from N_2 (such as (TPB)Fe($NNSi_2$)) and to subsequently add non-polar E–H bonds (E = Si or H) across the Fe–NNR_2 linkage (Scheme 3.4). This is distinct from previous work that entails reaction of a nucleophilic Fe fragment

Scheme 3.4 Nα and Nβ functionalization of N_2 at a single Fe site

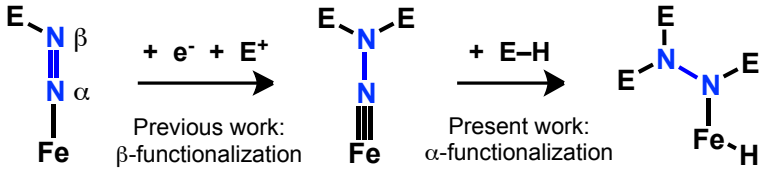

with an electrophilic reagent, which, as discussed in the context of protonation reactions, may not result in Nα functionalization. In contrast, an E–H bond addition reaction would almost certainly precede at the metal, leaving Nβ untouched at least initially. Indirect support for this approach is derived from reports of the partial and complete hydrogenolysis of terminal Fe imide complexes.[10] It should be noted that N_2 functionalization with non-polar E–H bonds has rich precedent with early metals.[11] The only example of such reactivity using Fe was reported by Holland wherein reductive cleavage of N_2 forms a triiron bis-μ-nitride complex which undergoes hydrogenolysis to release NH_3.[12] This builds

on earlier reports of the hydrogenolysis of bridging nitrides that were generated from synthetic sources.[13]

I anticipated that the aminoimide complex (TPB)Fe($NNSi_2$) would be an appropriate species for testing this hypothesis not only because it was the only such complex to be derived from N_2, but also because the Fe–B bond could participate in the E–H activation step (Chapter 1).[14] Unfortunately, the desired Nα functionalization was not realized with (TPB)Fe($NNSi_2$). Addition of 1 atm H_2 or 1 equiv $PhSiH_3$ at RT results in no observable reaction; at higher temperatures, (TPB)Fe($NNSi_2$) decomposes and no tractable products were identified in the presence of H_2 or $PhSiH_3$. Given the increased E–H bond addition reactivity of (DPB)Ni systems compared with the (TPB)Ni systems, I decided to target Fe aminoimides supported by DPB ligands and to study their subsequent reactivity with E–H bonds. Several points of caution arose from the outset:

- Can the DPB ligand stabilize low-coordinate, electron-rich Fe complexes? Will the ligand be stable under strongly reducing conditions?
- Will a (DPB)Fe fragment bind and activate N_2 sufficiently to enable Nβ functionalization (in order to generate an Fe aminoimide)? The BCC fragment in DPB is expected to be less electron-releasing than its counterpart in TPB (a phosphine donor) which may make N_2 activation more challenging for the former system.
- Can an Fe aminoimide complex be supported by DPB? The stability of the aminoimide intermediate requires a pseudotetrahedral geometry about Fe with a strong-field tripodal donor in order to impart a low-spin $S = 0$ configuration with an Fe≡N triple bond.[15] If the BCC fragment is not sufficiently strong-field to meet these

electronic requirements, an Fe aminoimide based on the DPB ligand would not be expected to be stable.

Clearly, the central hypothesis of this chapter—that E–H bond addition to an N_2-derived (DPB)Fe aminoimide is a viable strategy for Nα functionalization—rests on issues related to the coordination chemistry of (DPB)Fe complexes. As such, the molecular and electronic structures of these complexes will also be of high interest.

3.2 Preparation of (DPB)Fe synthons

Metallation with Fe of TPB proceeds in high yield by comproportionation of $FeBr_2$ and Fe powder in refluxing THF to give (TPB)FeBr.[16] Given the similarity between the isopropyl-substituted DPB ligand and TPB, these metallation conditions were among the first attempted for the DPB system. Unfortunately, all attempts to metallate DPB under these conditions led to intractable mixtures. Likewise, stirring a THF solution of DPB with $FeBr_2$ and 1 equiv Na/Hg afforded Fe metal and unreacted DPB. In this solvent, it is likely that there is a high speciation of unligated $FeBr_2(THF)_x$ which, upon reduction, gives Fe metal. However, it was found that DPB and $FeBr_2$ form a yellow solution in C_6H_6, indicating a high degree of complex formation. As such, a successful metallation procedure was developed wherein DPB and $FeBr_2$ are stirred in THF until all of the $FeBr_2$ dissolves. The volatiles are removed *in vacuo* and Et_2O is added in order to remove residual THF. Replacement of Et_2O with C_6H_6 affords a yellow solution that turns brown after stirring over 1 equiv Na/Hg for several hours. This procedure allows (DPB)FeBr to be isolated in 84% yield (Scheme 3.5).

Scheme 3.5 Synthesis of (DPB)FeBr

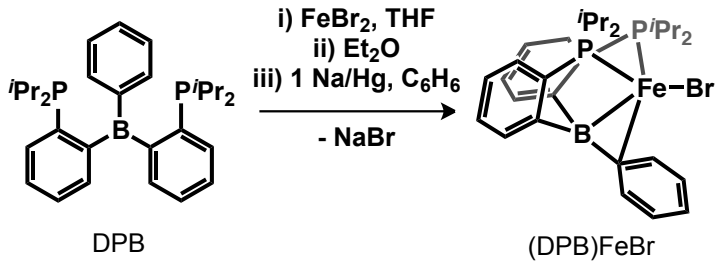

DPB (DPB)FeBr

(DPB)FeBr is brown with a low-energy electronic transition at 922 nm (ε = 590 in toluene). The solution magnetic moment value of 3.8 μ_B (RT, C_6D_6) is indicative of an S = 3/2 state. The ^{1}H NMR spectrum contains thirteen paramagnetically-shifted resonances between 185 and -58 ppm, indicating that the complex is C_S-symmetric in solution. The solid-state structure was determined by XRD analysis (Figure 3.1) and shows Fe in a pseudotetrahedral geometry with moderately close Fe–B and Fe–C_{ipso} interactions (2.3242(11) and 2.2605(9) Å, respectively). The closest Fe–C_{ortho} distance is negligibly long at 2.5483(11) Å. Given the solid-state structure, high-spin state, and C_s symmetry in solution, the η^2-BC_{ipso} ligand may be formulated as a donor *via* a filled π-arene orbital and an acceptor via the empty p orbital on B.

Further reduction of (TPB)FeBr with 1 equiv Na/Hg under atm N_2 results in formation of the dinuclear, bridging N_2 complex [(DPB)Fe]$_2$(μ-1,2-N_2) (Scheme 3.6). Alternatively, [(DPB)Fe]$_2$(μ-1,2-N_2) may be generated on a preparative scale directly by metallation of DPB with 2 equiv Na/Hg in 66% yield. The paramagnetically-shifted ^{1}H NMR spectrum of [(DPB)Fe]$_2$(μ-1,2-N_2) has thirteen resonances between 172 and -76 ppm, indicating that each Fe is equivalent and has local C_s symmetry. Solution- and solid-state IR spectra of

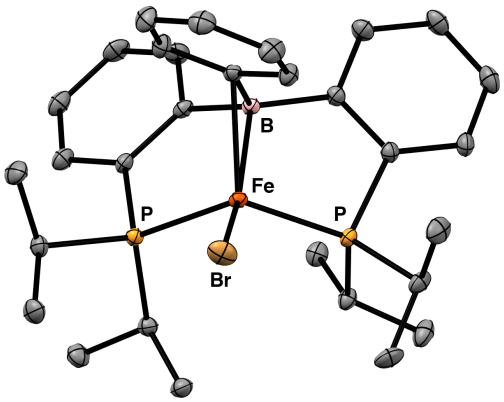

Figure 3.1 Displacement ellipsoid (50%) structure of (DPB)FeBr. H atoms are omitted for clarity. Selected distances and angles: Fe–B = 2.3242(11) Å; Fe–C_{ipso} = 2.2605(9) Å; Fe–P = 2.3785(4) Å, 2.3835(5) Å; Fe–Br = 2.3870(3) Å; ∠(P–Fe–P) = 106.61(1)°; Σ∠(C–B–C) = 353°.

Scheme 3.6 Preparation of [(DPB)Fe]$_2$(μ-1,2-N_2).

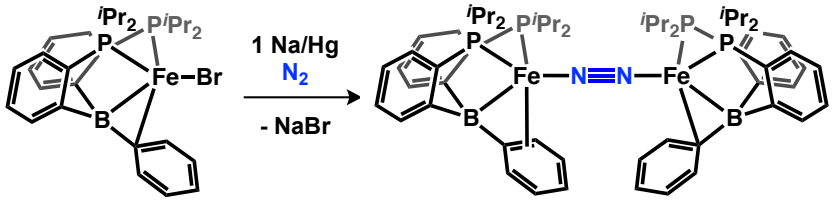

[(DPB)Fe]$_2$(μ-1,2-N_2) lack an N–N stretch, suggesting that the complex maintains its pseudocentrosymmetric, dinuclear structure in solution. The RT solution magnetic moment is 4.6 μ_B, somewhat higher than the spin-only value of 4.0 μ_B expected for two uncoupled S = 1 Fe centers.

The two pseudo-tetrahedral Fe centers in [(DPB)Fe]$_2$(μ-1,2-N_2) have different local geometries in the solid state (Figure 3.2). The geometry about one of the Fe centers (Fe_A) is distinguished by a short Fe–C_{ortho} contact (2.2714(7) Å) and relatively long Fe–B and Fe–C_{ispo} distances (2.3739(7) and 2.2516(6) Å, respectively; Table 3.1). The other Fe center

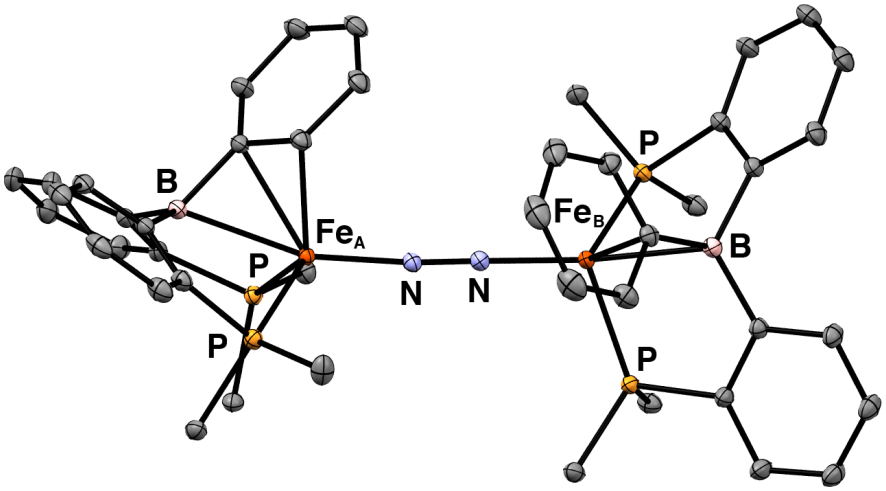

Figure 3.2 Displacement ellipsoid (50%) structure of [(DPB)Fe]$_2$(μ-1,2-N$_2$). P^{i}Pr$_2$ groups are truncated and H atoms are omitted for clarity. See Table 3.1 for selected bond lengths and angles.

Table 3.1 Selected bond lengths (Å) and angles (˚) of [(DPB)Fe]$_2$(μ-1,2-N$_2$).

	Fe–N	N–N	Fe–B	F–C$_{ipso}$	Fe–C$_{ortho}$	Fe–P (avg.)	Σ∠(C–B–C)
Fe$_A$	1.8261(5)	1.1705(8)	2.3739(7)	2.2517(6)	2.2714(7)	2.347	352
Fe$_B$	1.8382(6)		2.3136(7)	2.2133(6)	2.6642(7)	2.341	351

(Fe$_B$) displays somewhat shorter Fe–B and Fe–C$_{ipso}$ distances (2.3136(7) and 2.2133(6) Å, respectively) and a negligible Fe–C$_{ortho}$ interaction (2.6642(7) Å). The phenyl ring bound to Fe$_A$ exhibits alternating C–C bond lengths (Table 3.2 and Table 3.3) whereas this asymmetry is negligible for the phenyl ring bound to Fe$_B$; these metrics indicate that back-donation to the arene ring is more significant for Fe$_A$ and back-donation to the B atom is more significant for Fe$_B$. Since Fe$_A$ and Fe$_B$ are equivalent in solution, the Fe–BCC interaction must be highly flexible and the solid-state bond metrics reflect the large range of local geometries available to the Fe centers.

Table 3.2 Fe-BCC distances in select (DPB)Fe(L) complexes

L	Fe-B	Fe-C1	Fe-C2
Br	2.3234(11)	2.2608(9)	2.5486(11)
N_2 (site A)	2.3739(7)	2.2517(6)	2.2714(7)
N_2 (site B)	2.3136(7)	2.2133(6)	2.6642(7)
$[N_2]^-$	2.244(2)	2.055(2)	2.327(2)
($NNSi_2$) (mol. 1)	2.3768(6)	2.1493(5)	2.3405(6)
($NNSi_2$) (mol. 2)	2.4288(7)	2.1440(6)	2.2266(6)

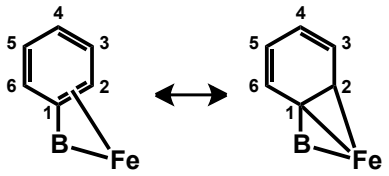

Table 3.3 C–C distances of the bound arene in select (DPB)Fe(L) complexes.

L	C1-C2	C2-C3	C3-C4	C4-C5	C5-C6	C6-C1
Br	1.4191(14)	1.3891(18)	1.3977(15)	1.3935(18)	1.3880(16)	1.4212(15)
N_2 (site A)	1.4211(10)	1.4185(10)	1.3711(12)	1.4124(12)	1.3785(10)	1.4303(10)
N_2 (site B)	1.4167(10)	1.3987(11)	1.3839(14)	1.3944(15)	1.3890(12)	1.4184(10
$[N_2]^-$	1.429(3)	1.426(3)	1.379(4)	1.408(4)	1.383(3)	1.442(3)
($NNSi_2$) (mol. 1)	1.4231(7)	1.4238(8)	1.3681(9)	1.4196(10)	1.3690(8)	1.4324(7)
($NNSi_2$) (mol. 2)	1.4285(9)	1.4357(9)	1.3645(13)	1.4223(13)	1.3648(9)	1.4372(9)

Interestingly, the 5 K Mössbauer spectrum of crushed microcrystalline powders of [(DPB)Fe]$_2$(μ-1,2-N_2) (Figure 3.3 and Figure 3.4) displays two doublets in a 1:1 ratio which can be fit either assuming similar values for $|\Delta E_q|$ (1.63 and 1.59 mm s^{-1}) and very different values for δ (0.58 and 0.78 mm s^{-1}) (Figure 3.3) or assuming very different values for $|\Delta E_q|$ (1.39 and 1.81 mm s^{-1}) and similar values for δ (0.69 and 0.67 mm s^{-1}) (Figure 3.4). Both sets of parameters fit the data satisfactorily and thus cannot be distinguished on

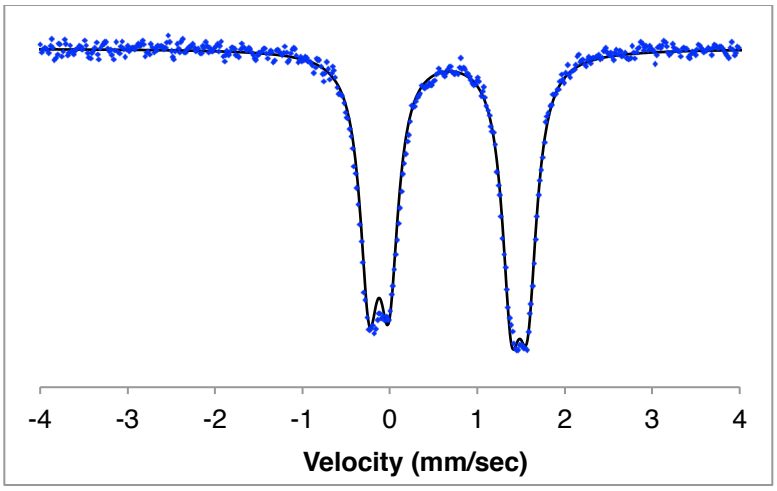

Figure 3.3 Mössbauer spectrum of $[(DPB)Fe]_2(\mu\text{-}1,2\text{-}N_2)$ recorded at 5 K and fit using the following parameters. Site 1: $\delta = 0.58$ mm s^{-1}, $|\Delta E_q| = 1.63$ mm s^{-1}; site 2: $\delta = 0.78$ mm s^{-1}, $|\Delta E_q| = 1.59$ mm s^{-1}.

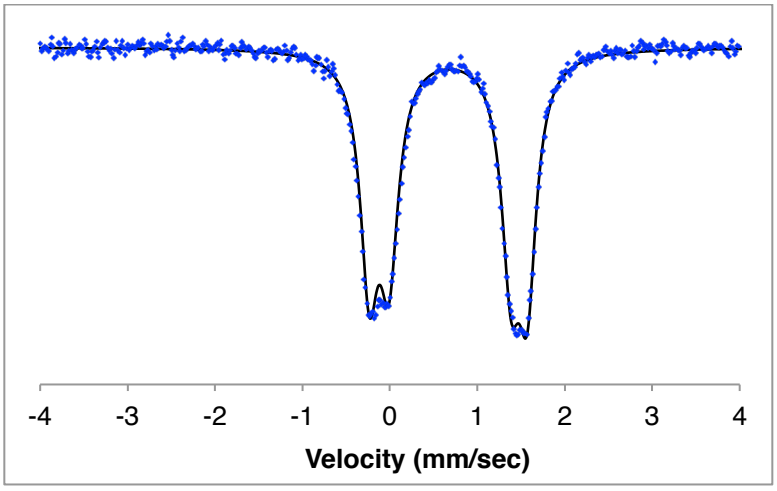

Figure 3.4 Mössbauer spectrum of $[(DPB)Fe]_2(\mu\text{-}1,2\text{-}N_2)$ recorded at 5 K and fit using the following parameters. Site 1: $\delta = 0.69$ mm s^{-1}, $|\Delta E_q| = 1.39$ mm s^{-1}; site 2: $\delta = 0.67$ mm s^{-1}, $|\Delta E_q| = 1.81$ mm s^{-1}.

the basis of this experiment. Nonetheless, it is interesting to observe that Mössbauer spectroscopy—like XRD analysis—can be used as a sensitive technique for distinguishing between two Fe centers that are unique in the solid state but equivalent in solution. Thus,

differences in the Mössbauer spectra of two chemically distinct compounds should not be overinterpretted since relatively large differences can arise from chemically identical species.

3.3 C–H and N–H Bond Activation by [(DPB)Fe]$_2$(μ-1,2-N$_2$)

Having gained synthetic entry to (DPB)Fe complexes, it was prudent to explore the reactivity of this system toward E–H bond activation, particularly as a means of comparison with the (TPB)Fe system. Exposure of (TPB)Fe(N_2) to 1 atm H_2 results in H–H bond activation to give (TPB–H)Fe(H)(H_2) (Chapter 1).[17] On the other hand, [(DPB)Fe]$_2$(μ-1,2-N_2) decomposes rapidly at RT under 1 atm H_2 to give a variety of diamagnetic and paramagnetic products as judged by ^{1}H and ^{31}P NMR spectroscopy. Although this result was somewhat disappointing, it does point to the greater reactivity of (DPB)M complexes with E–H bonds in comparison with their (TPB)M counterparts.

Given the stability of E–H bond addition products using the (DPB)Ni systems (with varying substituents on B and P), I thought that similarly stable Fe complexes may be accessed by using a directing group that could contribute two addition electrons to the system. For these purposes, I initially tested the reactivity of [(DPB)Fe]$_2$(μ-1,2-N_2) with benzo(*h*)quinoline and 2-phenylpyridine. Accordingly, heating C_6D_6 solutions of 0.5 equiv [(DPB)Fe]$_2$(μ-1,2-N_2) and either benzo[*h*]quinoline or 2-phenylpyridine to 70 ˚C for several hours results in clean conversion to $S = 0$ C–H activation products: magenta (DPB–H)Fe(benzo[*h*]quinolin-10-yl) or maroon (DPB–H)Fe(2-(pyridin-2-yl)phenyl), respectively (Scheme 3.7). No intermediates are observed in these reactions; incomplete mixtures

Scheme 3.7. Bond activation reactions of $[(DPB)Fe]_2(\mu\text{-}1,2\text{-}N_2)$.

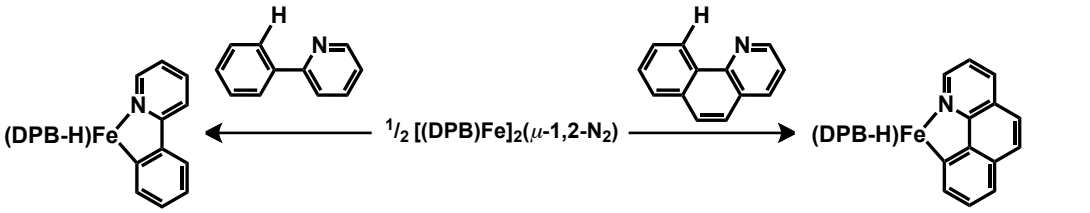

(DPB–H)Fe(2-(pyridin-2-yl)phenyl) (DPB–H)Fe(benzo[*h*]quinolin-10-yl))

contain only $[(DPB)Fe]_2(\mu\text{-}1,2\text{-}N_2)$ and the C–H activated product. This suggests that ligand substitution of N_2 by the substrate is rate-determining.

Both C-H activation products are C_s-symmetric in solution as evidenced by their ^{1}H NMR spectra, however their very broad ^{31}P signals indicate that the coalescence temperature is near RT. In addition, their ^{1}H NMR spectra contain a single broad hydride resonance at -22.8 and -21.1 ppm, respectively, indicating the presence of an Fe–H–B functional group rather than a terminal Fe–H. Sharp ^{11}B NMR signals at -7.3 and -8.5 ppm, respectively, lend further support to this conclusion. The solid-state structures of both (DPB–H)Fe(benzo[*h*]quinolin-10-yl) and (DPB–H)Fe(2-(pyridin-2-yl)phenyl) are very similar and the geometrical features about Fe are highly conserved (Figure 3.5). In addition to confirming the presence of the Fe–H–B group and establishing the stereochemistry of C–H addition (N *trans* to H), the structures show the presence of a long Fe–arene interaction that completes the octahedral coordination sphere, thereby allowing a low-spin configuration to be achieved.

There is some precedent (albeit limited) for directed[18] and undirected[19] C–H activation by zero-valent, low-coordinate Fe complexes, and these stoichiometric reactions have

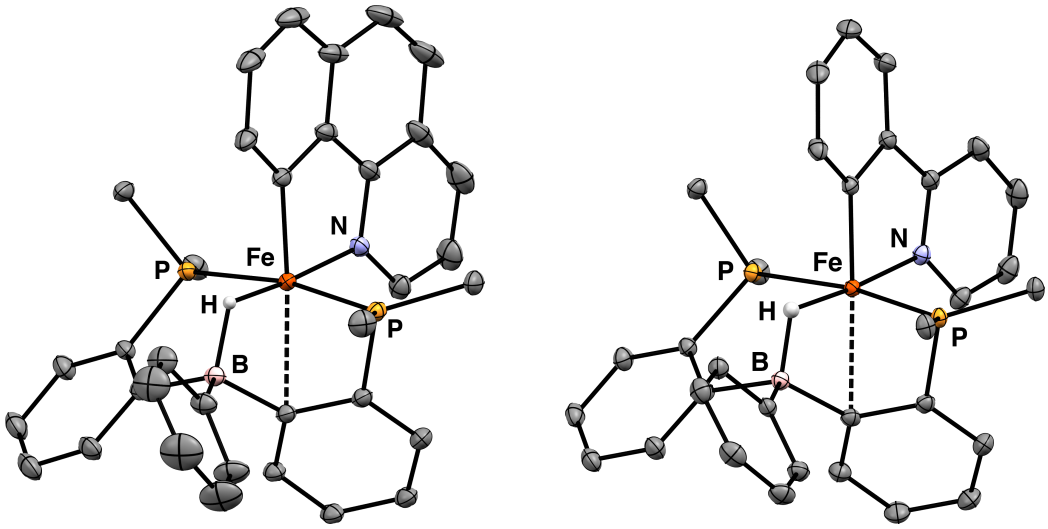

Figure 3.5 Displacement ellipsoid (50%) structures of (DPB–H)Fe(benzo[*h*]quinolin-10-yl) (left) and (DPB–H)Fe(2-(pyridin-2-yl)phenyl) (right). P^{i}Pr$_2$ groups are truncated and H atoms and solvent molecules are omitted for clarity. Selected distances and angles for (DPB)Fe(benzo[*h*]quinolin-10-yl): Fe–N = 1.9682(8) Å; Fe-C_{aryl} = 1.9286(8) Å; Fe-C_{aryl} = 2.3739(8) Å; Fe–P = 2.2189(3) Å, 2.2665(3) Å; Fe–B = 2.3342(9) Å; ∠(P–Fe–P) = 169.59(1)°; ∠(C–Fe–C) = 160.39(4)°; Σ∠(C–B–C) = 335°. Selected distances and angles for (DPB)Fe(2-(pyridin-2-yl)phenyl): Fe–N = 1.9547(9) Å; Fe-C_{aryl} = 1.9193(10) Å; Fe-C_{aryl} = 2.3555(10) Å; Fe–P = 2.2125(3) Å, 2.2731(3) Å; Fe–B = 2.3175(11) Å; ∠(P–Fe–P) = 170.85(1)°; ∠(C–Fe–C) = 161.56(4)°; Σ∠(C–B–C) = 337°.

found application in catalytic transformations.[20] As such, the observed reactivity of [(DPB)Fe]$_2$(μ-1,2-N_2) is not surprising. On the other hand, oxidative addition of N–H bonds by Fe is less common and appears to be limited to relatively acidic amides.[21] Addition of 8-aminoquinoline to 0.5 equiv [(DPB)Fe]$_2$(μ-1,2-N_2) in C_6D_6 at RT gives a red-orange solution within an hour. The ^{1}H NMR spectrum contains a pattern of more than thirty paramagnetically-shifted and -broadened signals, suggesting that the reaction mixture contains either a single C_1-symmetric species or two C_s-symmetric species.

Single crystals of the product are twinned to varying extents based on screening several crystals. One of the least-twinned crystals was studied by XRD analysis and showed the desired N–H activated product (DPB–H)Fe(8-amidoquinoline) (Figure 3.6). Although there

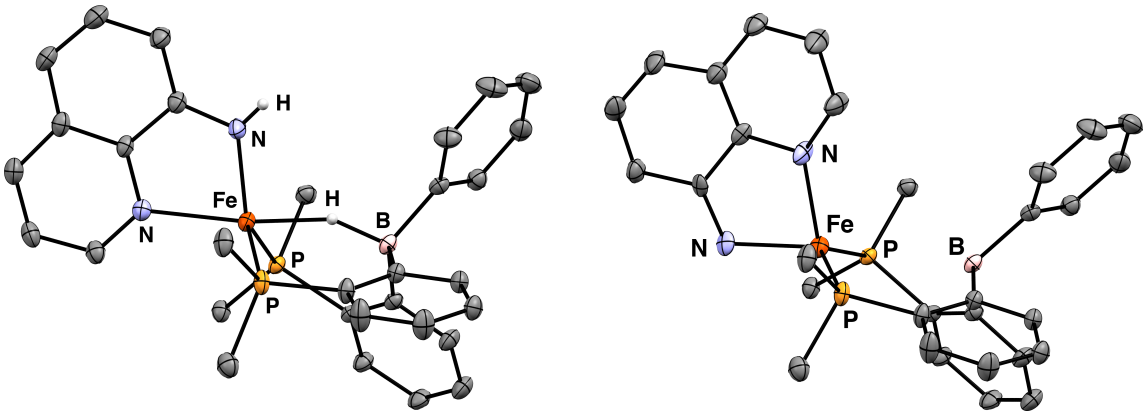

Figure 3.6 Displacement ellipsoid (50%) structure of the major (90%, left) and minor (10%, right) components of a twinned crystal of (DPB–H)Fe(8-amidoquinoline). P^iPr_2 groups are truncated and H atoms are omitted for clarity. Selected distances and angles for the major component: Fe–B = 2.967(2) Å; Fe-N_{amido} = 1.958(2) Å; Fe-N_{quin} = 2.192(2) Å; Fe–P = 2.4324(5) Å, 2.4552(5) Å; ∠(P–Fe–P) = 122.55(2)°; Σ∠(C–B–C) = 335°.

is only one molecule per asymmetric unit, the molecule is disordered between two isomers: one with the amido *cis* to the borohydride (90%) and one with the amido *trans* to the borohydride (10%). Since the "*trans*" isomer is a minor component of the speciation in this crystal, its bond metrics are not reliable. The major component shows the presence of a borohydride moiety and long Fe–P distances which suggests that N–H activation of 8-aminoquinoline furnishes an $S = 2$ addition product. The Fe–B distance is long (nearly 3 Å) which indicates that the borohydride ligand is a weaker donor than that in the C–H addition products (e.g. (DPB–H)Fe(benzo[*h*]quinolin-10-yl)). In a limiting sense, the former may be

considered hydridoborate ligand while the latter may be considered a borane-capped Fe–H.

Given the XRD data, the simplest explanation for the solution NMR data is that the reaction mixture consists of two isomers of (DPB–H)Fe(8-amidoquinoline) that co-crystallize. The solution magnetic moment of 5.2 μ_B (C_6D_6, RT) is consistent with the presence of two $S = 2$ isomers of the appropriate molecular weight. These isomers may be at thermodynamic equilibrium, or they may arise from different pathways for N–H addition that are trapped as two stereoisomers. Further experimentation is required to distinguish between these two possibilities. Regardless of how the two isomers of (DPB–H)Fe(8-amidoquinoline) are generated, the high-spin ground state structure of the products is notable in comparison to that of the low-spin C–H addition products. Although (DPB–H)Fe(8-amidoquinoline) could conceivably adopt a pseudo-octahedral, low-spin structure, the amido donor is apparently not sufficiently strong-field for this configuration. In order to have an $S = 2$ ground state, the Fe–H bond lengthens so that it resembles more of a weak-field borohydride than a strong-field hydride. On the other hand, the strong-field aryl ligands in the C–H-activated products impart a low-spin configuration. The major geometrical requirements for this configuration are a sixth ligand (in this case an arene donor) and a tighter Fe–H interaction. These results delineate the ways that the DPB ligand can stabilize low-spin and high-spin configurations upon E–H addition reactions and suggest that a variety of spin manifolds should be considered when designing new stoichiometric and catalytic applications based on this reactivity.

3.3 N_2 functionalization using the (DPB)Fe platform

A simple way to compare the degree of N_2 activation imparted by the (DPB)Fe platform with that imparted by the (TPB)Fe platform is to compare the solid-state structures and $\nu_{(N-N)}$ values for their N_2 complexes. Unfortunately, the (TPB)Fe(N_2) complex has not been structurally characterized owing to problems arising from twinned crystals.[16] Furthermore, the analogous (DPB)Fe complex exists as the dinuclear bridging complex [(DPB)Fe]$_2$(μ-1,2-N_2). As such, I sought to prepare a mononuclear [(DPB)Fe(N_2)]$^-$ complex to compare with the reported [(TPB)Fe(N_2)][Na(12-crown-4)$_2$].[16] Addition of two equiv KC_8 to [(DPB)Fe]$_2$(μ-1,2-N_2) followed by encapsulation with benzo-15-crown-5 results in formation of the red-brown, mononuclear [(DPB)Fe(N_2)][K(benzo-15-crown-5)$_2$] complex (Scheme 3.8). The solid-state structure (Figure 3.7) reveals its pseudotetrahedral geometry with an especially close Fe–C_{ipso} distance of 2.055(2) Å. The Fe–N and N–N distances (1.792(2) and 1.135(3) Å, respectively) indicate modestly attenuated N_2 activation in comparison with those of the analogous [(TPB)Fe(N_2)][Na(12-crown-4)$_2$] system (1.781(2) and 1.144(3) Å, respectively). This interpretation is supported by a slightly higher value of $\nu_{(N-N)}$ for the

Scheme 3.8 Preparation of [(DPB)Fe(N_2)][K(benzo-15-crown-5)$_2$]

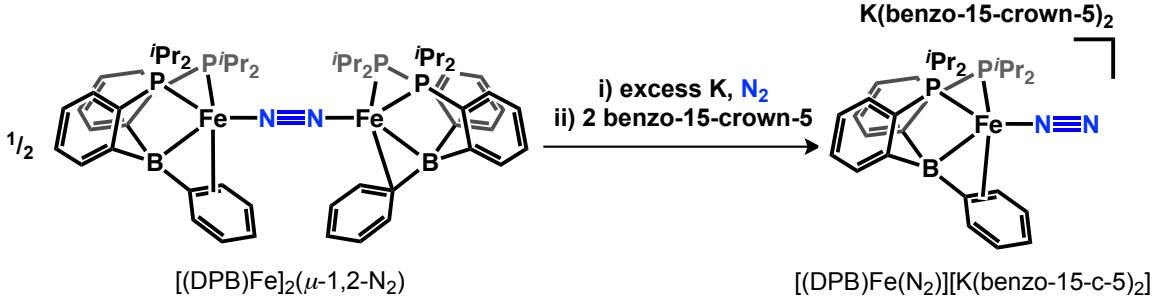

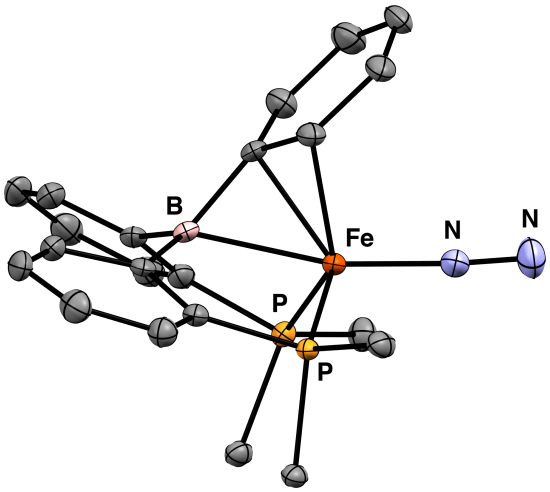

Figure 3.7 Displacement ellipsoid (50%) structure of [(DPB)Fe(N_2)][K(benzo-15-crown-5)$_2$]. P^{i}Pr$_2$ groups are truncated and H atoms, the counteraction, and solvent molecules are omitted for clarity. Selected distances and angles: Fe–N = 1.792(2) Å; N–N = 1.135(3) Å; Fe–B = 2.244(2) Å; Fe-C_{ipso} = 2.055(2) Å; Fe-C_{ortho} = 2.327(2) Å; Fe–P = 2.2178(7) Å, 2.2268(7) Å; ∠(P–Fe–P) = 109.46(3)°; Σ∠(C–B–C) = 353°.

DPB-ligated complex compared with the TPB-ligated complex (1935 vs. 1918 cm^{-1}). Importantly, these results establish that the (DPB)Fe platform is robust under strongly reducing conditions and that replacement of one phosphine of TPB with an aryl donor in DPB does not result in significantly attenuated N_2 activation.

Having established the viability of the (DPB)Fe platform for N_2 activation, I sought to take advantage of the presumably basic Nβ for its disilylation as has been previously demonstrated for the (TPB)Fe platform.[16] Accordingly, the green, diamagnetic Fe aminoimide complex (DPB)FeNNSi$_2$ may be accessed by stirring (DPB)FeBr with 1.1 equiv 1,2-bis(chlorodimethylsilyl)ethane and 3.1 equiv Na/Hg in THF under 1 atm N_2 (Scheme 3.9). Alternatively, 0.5 equiv [(DPB)Fe]$_2$(μ-1,2-N_2) may be employed as a starting material in conjunction with 2.1 equiv Na/Hg. The ^{1}H and ^{31}P NMR spectra of

Scheme 3.9 Preparation of (DPB)Fe(NNSi$_2$)

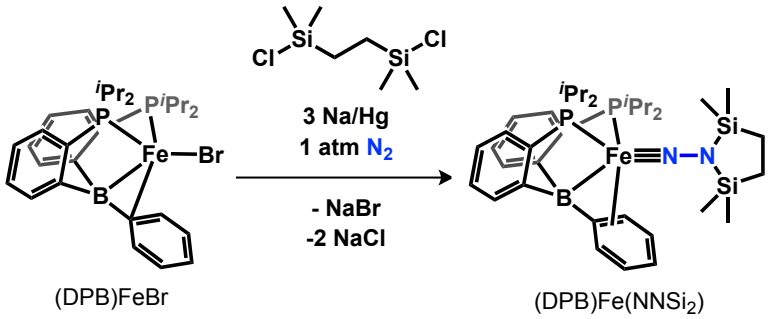

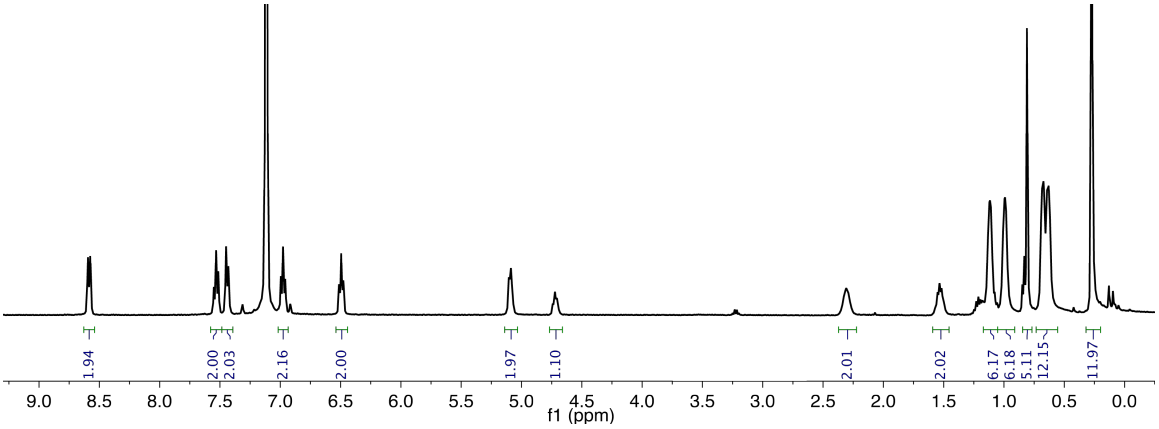

Figure 3.8 ^{1}H NMR spectrum of (DPB)Fe(NNSi$_2$).

(DPB)Fe(NNSi$_2$) reveal its C_s symmetry in solution. In addition, the ^{1}H resonances attributed to the bound aryl ring are upfield-shifted (5.10 (H_{ortho}), 6.49 (H_{meta}), and 4.72 (H_{para}) ppm (Figure 3.8).

The solid-state structure (Figure 3.9) shows two independent molecules in the asymmetric unit. The short Fe–N distances (1.6607(5) and 1.6657(5) Å) are consistent with other trigonal Fe(NR) linkages and imply an Fe≡NNR triple bond.[8] The two unique

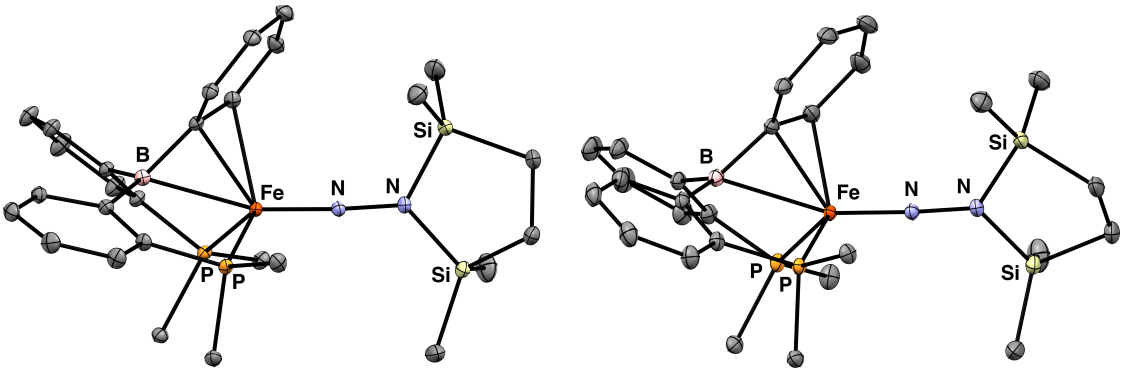

Figure 3.9 Displacement ellipsoid (50%) structure of both molecules of (DPB)Fe(NNSi$_2$) in the asymmetric unit. P^{i}Pr$_2$ groups are truncated and H atoms, the counteraction, and solvent molecules are omitted for clarity. Selected distances and angles for molecule A (left): Fe–N = 1.6605(5) Å; N–N = 1.3282(6) Å; Fe–B = 2.3768(6) Å; Fe-C$_{ipso}$ = 2.1492(5) Å; Fe-C$_{ortho}$ = 2.3403(6) Å; Fe–P = 2.2312(2) Å, 2.2660(2) Å; P–Fe–P = 109.52(1)°; Σ(∠CBC) = 355°. Selected distances and angles for molecule B (right): Fe–N = 1.6658(5) Å; N–N = 1.3242(7) Å; Fe–B = 2.4288(8) Å; Fe-C$_{ipso}$ = 2.1440(6) Å; Fe-C$_{ortho}$ = 2.2266(6) Å; Fe–P = 2.2287(2) Å, 2.2632(2) Å; P–Fe–P = 105.88(1)°; Σ(∠CBC) = 357°.

molecules display essential indistinguishable Fe–N, Fe–P, and Fe–C$_{ipso}$ distances, however the Fe–B and Fe–C$_{ortho}$ distances differ by +0.05 and -0.11 Å, respectively. Thus, the main geometrical distortion that relates the two molecules is a pivot about C$_{ipso}$; these metrics suggest that the η^3-BCC interaction is quite flexible as was also observed for [(DPB)Fe]$_2$(μ-1,2-N$_2$). In addition, the bound arenes display alternating bond lengths that vary between ca. 1.36 and 1.44 Å which is consistent with substantial back-donation to the arene ring.

Density functional theory calculations support the formulation of (DPB)FeNNSi$_2$ as a typical pseudotetrahedral d^6 Fe imide[15] that is similar to (TPB)FeNNSi$_2$ except that one phosphine donor in the latter has been replaced by the η^3-BCC interaction in the former (HOMO-9 and HOMO-10; Figure 3.10). Although the presence of an Fe–B bond is not

required for the stability of pseudotetrahedral d^6 Fe imides,[13] DFT calculations on (DPB)FeNNSi$_2$, (TPB)FeNNSi$_2$,[8] and related Fe imides[16] show some degree of Fe–B σ bonding (HOMO-2; Figure 3.10).

The reactions of E–H bonds with (DPB)Fe(NNSi$_2$) were next examined. Gratifyingly, in contrast to (TPB)Fe(NNSi$_2$) (*vide supra*), the RT addition of 1.1 equiv PhSiH$_3$ to (DPB)Fe(NNSi$_2$) readily generates a new, orange species identified as the trisilylhydrazido(-) product (DPB–H)Fe(N(Si)NSi$_2$) resulting from hydrosilylation of the Fe≡N bond with delivery of SiH$_2$Ph to N$_\alpha$ and H to B (Scheme 3.10). To my knowledge,

Scheme 3.10 Si–H bond addition to (DPB)Fe(NNSi$_2$)

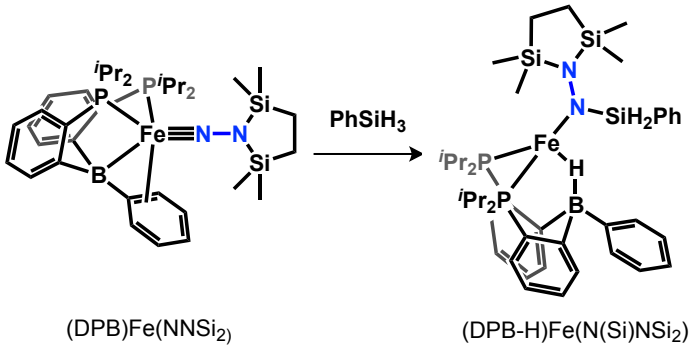

this is the first and only Fe hydrazido(-) complex to be derived from N$_2$, thereby adding to the body of previously-reported mononuclear Fe hydrazido(-) model complexes.[22] Having established this elementary step, I sought to combine the formation of (DPB)Fe(NNSi$_2$) with its subsequent hydrosilylation into a single procedure. Accordingly, (DPB–H)Fe(N(Si)NSi$_2$) may be generated in one pot from (DPB)FeBr or [(DPB)Fe]$_2$(μ-1,2-N$_2$) (Scheme 3.11).

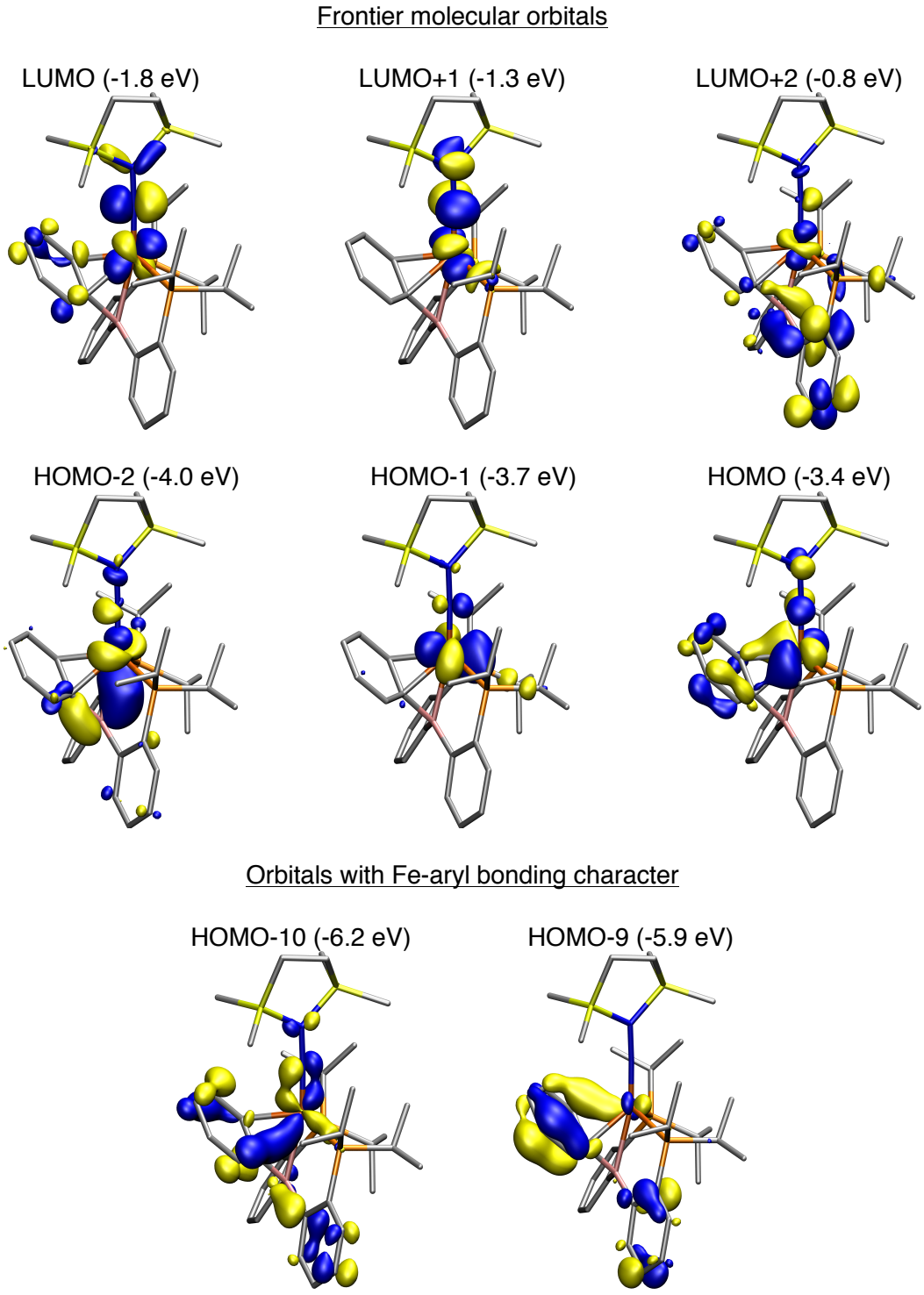

Figure 3.10 Frontier MOs of (DPB)Fe($NNSi_2$). Geometry optimized at the M06L/6-31g(d) level. Initial atomic coordinates were taken from one of the two unique molecules in the XRD structure. MOs shown with 0.05 isosurfaces.

Scheme 3.11 One-pot formation of an Fe hydrazido(-) complex

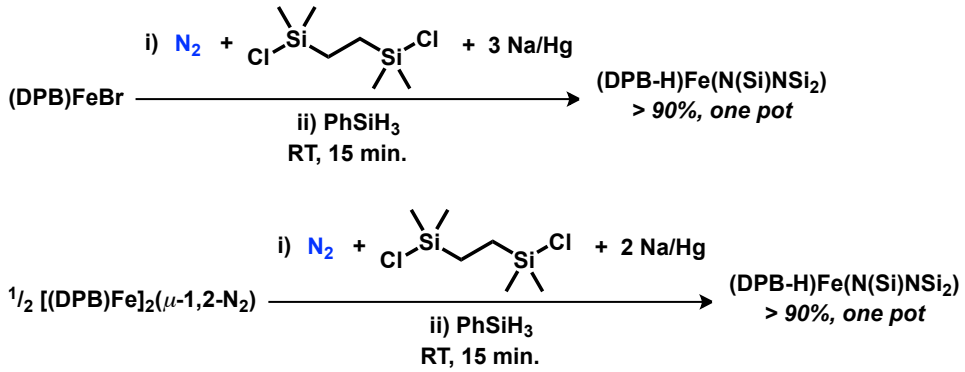

For (DPB–H)Fe(N(Si)NSi_2), an intense IR signal corresponding to the Si–H stretch is observed at 2090 cm^{-1} and a broad, intense IR stretch corresponding to the Fe–H–B functional group is observed at ca. 2000 cm^{-1}. The solution magnetic moment (μ_{eff} = 5.0μ_B, C_6D_6, RT) indicates an S = 2 spin state. Single crystals of (DPB–H)Fe(N(Si)NSi_2) were invariably small and twinned, however a suitable dataset was collected at the Stanford Linear Accelerator Center (see experimental section for details). The N–N bond is elongated from 1.326 Å (avg.) in (DPB)Fe($NNSi_2$) to 1.492(4) Å in (DPB–H)Fe(N(Si)NSi_2) (Figure 3.11). Although both distances are consistent with N–N single bonds, the comparatively short bond in (DPB)Fe($NNSi_2$) is due to the sp hybridization of Nα and some degree of N–N multiple bond character. The very long N–N bond in (DPB–H)Fe(N(Si)NSi_2) (longer than that of free N_2H_4) is likely due to a high degree of steric pressure exerted by its bulky Si and Fe substituents. The sum of the CBC angles is 334°, reflecting the tetrahedral geometry of the borohydride ligand.

Addition of H_2 to a C_6D_6 solution of (DPB)Fe($NNSi_2$) at RT results in formation of a pale brown solution and a new paramagnetic species (Scheme 3.12). The IR spectrum of

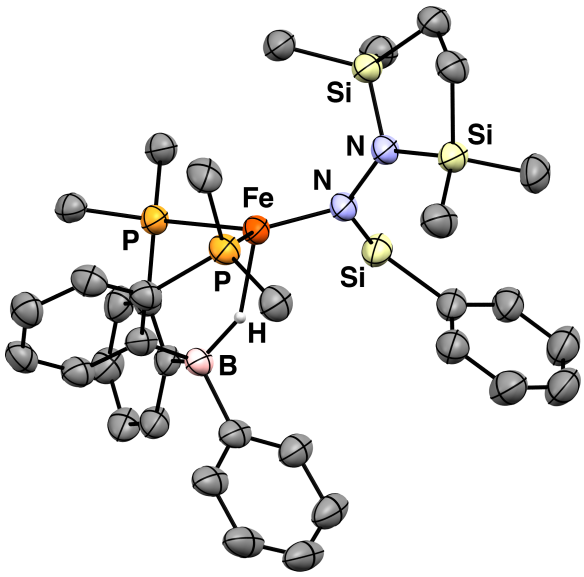

Figure 3.11 Displacement ellipsoid (50%) structure of (DPB-H)Fe(N(Si)NSi$_2$). P^{i}Pr$_2$ groups are truncated and H atoms are omitted for clarity. Selected distances and angles: Fe–N = 1.918(4) Å; N–N = 1.492(4) Å; Fe–B = 2.859(5) Å; Fe–P = 2.424(3) Å, 2.514(3) Å; ∠(P–Fe–P) = 111.54(6)°; Σ∠(C–B–C) = 334°.

Scheme 3.12 H_2 addition to (DPB)Fe(NNSi$_2$)

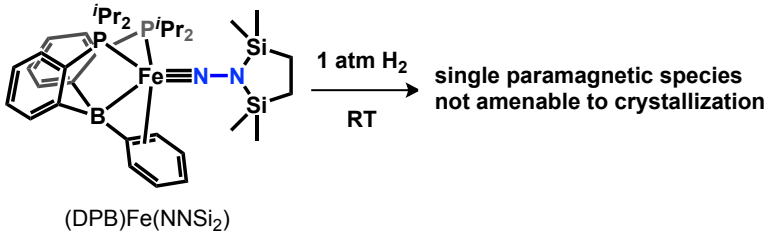

this reaction mixture shows a new feature at 3370 cm^{-1} and a very broad, intense feature at ~2170 cm^{-1} (Figure 3.12); using D_2 instead of H_2 results in the disappearance of these signals and the appearance of new signals at 2482 and ~1600 cm^{-1}. Thus, these may be assigned to stretches from N–H and B–H–Fe functional groups, respectively. Unfortunately, attempts at crystallizing this compound failed. Since it is paramagnetic, its

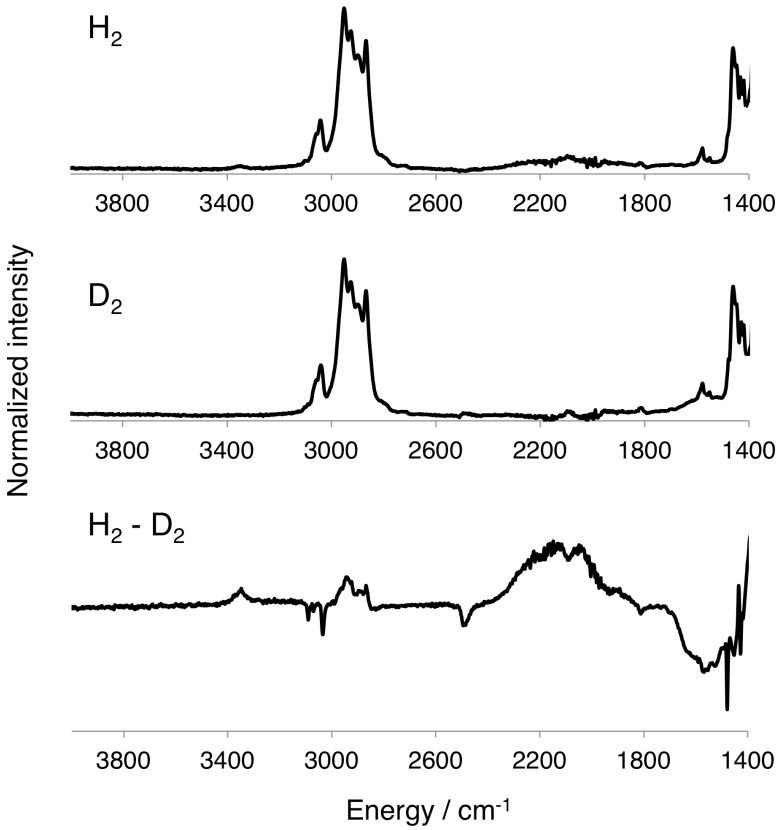

Figure 3.12 Thin film IR spectra resulting from addition of H_2 (top) or D_2 (middle) to (DPB)Fe($NNSi_2$). Subtraction spectrum (bottom).

unambiguous structural assignment is heavily reliant on XRD analysis. As such, I elected to attempt similar chemistry using Bourissou's phenyl-substituted DPB ligand (^{Ph}DPB: bis(2-(1-diphenylphosphinophenyl))phenylborane)[23] with the hope that the metallation, reduction, and N_2 functionalization chemistry would be preserved in this system and that the product of H_2 addition to an N_2-derived Fe aminoimide would be crystalline.

Before addressing N_2 functionalization chemistry with the ^{Ph}DPB, I will describe the synthesis of the relevant precursors. The metallation of ^{Ph}DPB with $FeBr_2$ to form (^{Ph}DPB)FeBr is analogous to the procedure for metallating DPB (Scheme 3.13). The properties of (^{Ph}DPB)FeBr are very similar to that of (DPB)FeBr. (^{Ph}DPB)FeBr is brown,

Scheme 3.13 Preparation of (^{Ph}DPB)FeBr

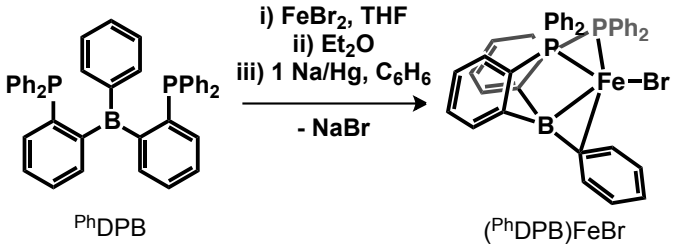

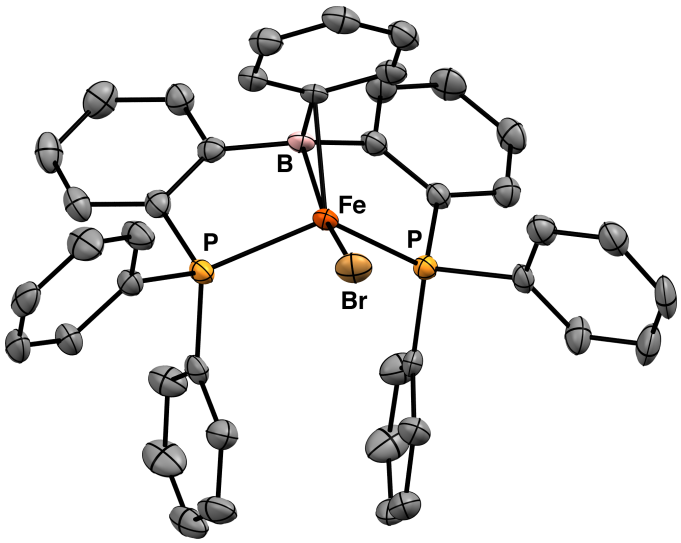

Figure 3.13 Displacement ellipsoid (50%) structure of (^{Ph}DPB)FeBr. H atoms are omitted for clarity. Selected distances and angles: Fe–B = 2.330(4) Å; Fe-C_{ipso} = 2.193(3) Å; Fe–P = 2.346(1) Å, 2.350(1) Å; ∠(P–Fe–P) = 110.33(4)°; Σ∠(CBC) = 354°.

shows a low-energy transition at 1003 nm (ε = 600 in toluene), adopts an $S = {}^3/_2$ spin state (μ_{eff} = 3.6 μ_B, C_6D_6, RT), and is C_s-symmetric in solution as indicated by its paramagnetically-shifted NMR spectrum. The solid-state structure (Figure 3.13) shows Fe–B and Fe–C_{ipso} bond lengths of 2.330(4) and 2.193(3) Å, respectively, and is otherwise unremarkable.

Reduction of (^{Ph}DPB)FeBr with 1 equiv Na/Hg does not trigger N_2 binding but instead generates the brown, diamagnetic complex (^{Ph}DPB)Fe that contains an η^7-BPh interaction (Scheme 3.14). The XRD structure of (^{Ph}DPB)Fe shows tight Fe–(η^7-BPh)

Scheme 3.14 Preparation of (^{Ph}DPB)Fe

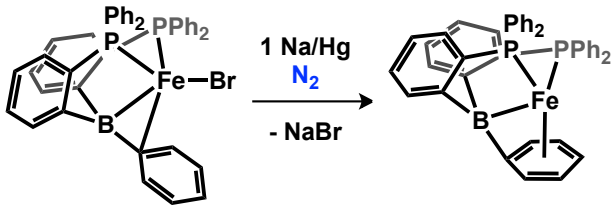

(^{Ph}DPB)FeBr (^{Ph}DPB)Fe

distances (Figure 3.14). The bound C_{ipso} atom is significantly pyramidalized as indicated by the sum of the two BCC and one CCC angles (342°). Further showing the significant geometrical distortion of the bound arene is the acute $BC_{ipso}C_{para}$ angle of 127.71(8)°. The η^7-BPh binding mode is maintained in solution based on the significantly upfield-shifted aryl resonances in the ^{1}H NMR spectrum (3.63 (H_{ortho}), 3.24 (H_{meta}), and 6.25 (H_{para}) ppm) and the ^{13}C NMR spectrum (106.77 (C_{ispo}), 99.41 (C_{ortho}), 86.36 (C_{meta}), and 78.73 (C_{para}) ppm) (assignments were made on the basis of ^{1}H-^{1}H COSY, HMQC, and HMBC spectra; see Figure 3.15 for the ^{1}H spectrum and Figure 3.16 for the ^{13}C spectrum). Given the unusual nature of the BPh binding mode in (^{Ph}DPB)Fe, some discussion of its bonding is warranted. On one hand, (^{Ph}DPB)Fe can be viewed as a diphosphine Fe^0 complex with some degree of Fe–B backbonding. In this bonding scenario, the BPh group serves as an L_3Z ligand (Figure 3.17). On the other hand, if the BPh group is considered to be formally reduced by two electrons, then three L_2X_2 and one $L_2X_2Z_2$ resonance structures

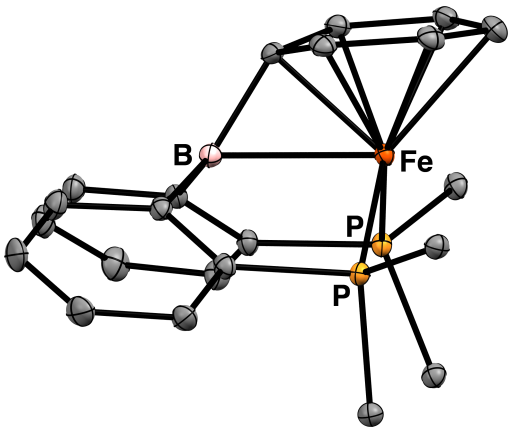

Figure 3.14 Displacement ellipsoid (50%) structure of (^{Ph}DPB)Fe. PPh_2 groups are truncated and H atoms and solvent molecules are omitted for clarity. Selected bond distances and angles: Fe–B = 2.2668(13) Å; Fe–C_{ipso} = 1.9667(11) Å; Fe–C_{ortho} = 2.0838(12) Å, 2.0962(12) Å; Fe–C_{meta} = 2.1676(11) Å, 2.1705(12) Å; Fe–C_{para} = 2.1934(11) Å; Fe–P = 2.1827(5) Å, 2.1840(6) Å; ∠(P–Fe–P) = 101.76(1)°; Σ∠(C–B–C) = 359°; B–C_{ipso}–C_{para} = 127.71(8)°.

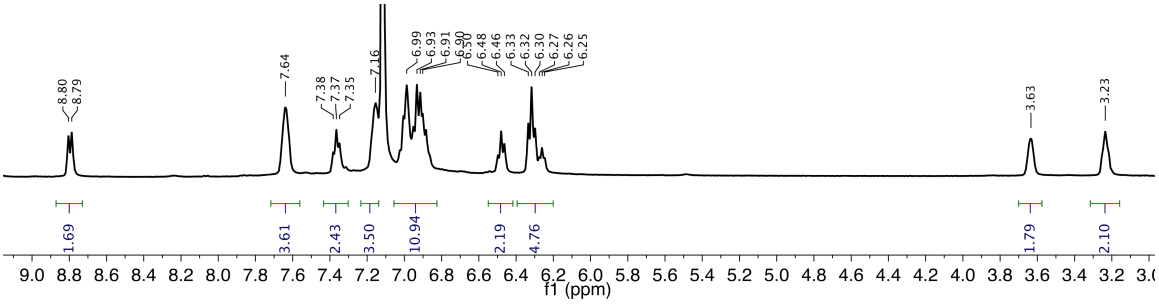

Figure 3.15 ^{1}H NMR spectrum of (^{Ph}DPB)Fe in C_6D_6.

are reasonable. Given that the C_{ipso}–C_{ortho} distances are significantly elongated in comparison to the other C–C distances and that the B–C_{ipso} distance for the bound C_{ipso} atom is shorter than for the two unbound C_{ipso} atoms (1.5625(16) Å vs. 1.5999(17) and 1.6070(17) Å; data not shown in Figure 3.17), there is likely significant contribution from the L_2X_2 resonance forms.

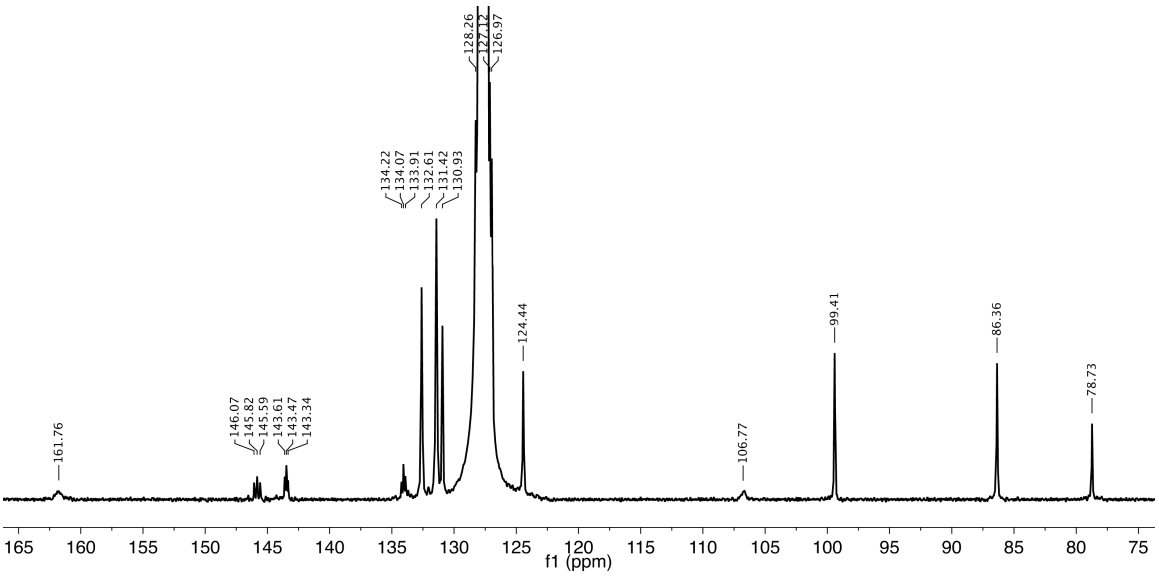

Figure 3.16 ^{13}C NMR spectrum of (^{Ph}DPB)Fe in C_6D_6.

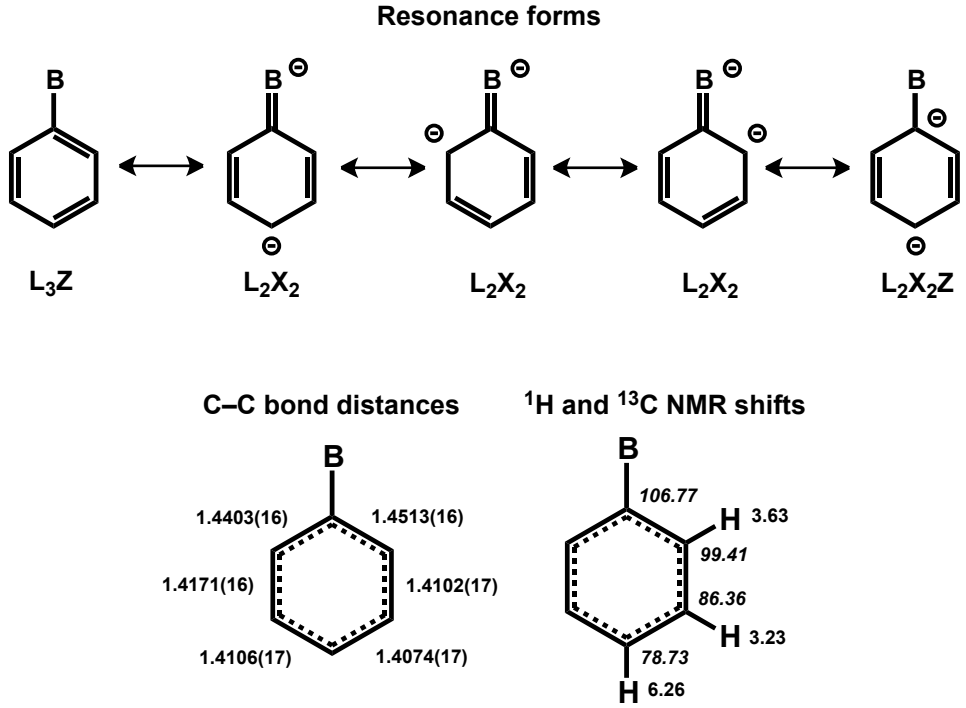

Figure 3.17 Possible resonance forms of the BPh ligand in (^{Ph}DPB)Fe with the corresponding CBC designation, C–C bond distances (Å) from the XRD structure, and ^{1}H and ^{13}C (ital.) NMR chemical shifts.

Although (^{Ph}DPB)Fe does not bind N_2 under ambient conditions, an Fe aminoimide can nevertheless be generated using the (^{Ph}DPB)Fe similarly to (DPB)Fe and (TPB)Fe (Scheme 3.15). The solid-state structure of (^{Ph}DPB)Fe(NNSi$_2$) (Figure 3.18) is very similar to that of(DPB)Fe(NNSi$_2$) and therefore will not be discussed. Solutions of (^{Ph}DPB)Fe(NNSi$_2$) are green and crystalline solids are dichroic green-brown. Interestingly, the ^{1}H NMR spectrum

Scheme 3.15 Preparation of (^{Ph}DPB)Fe(NNSi$_2$)

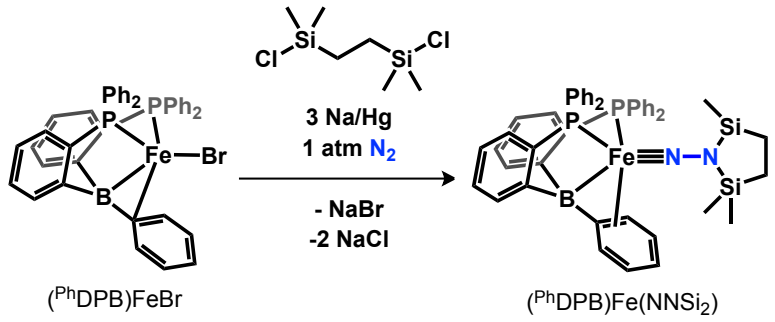

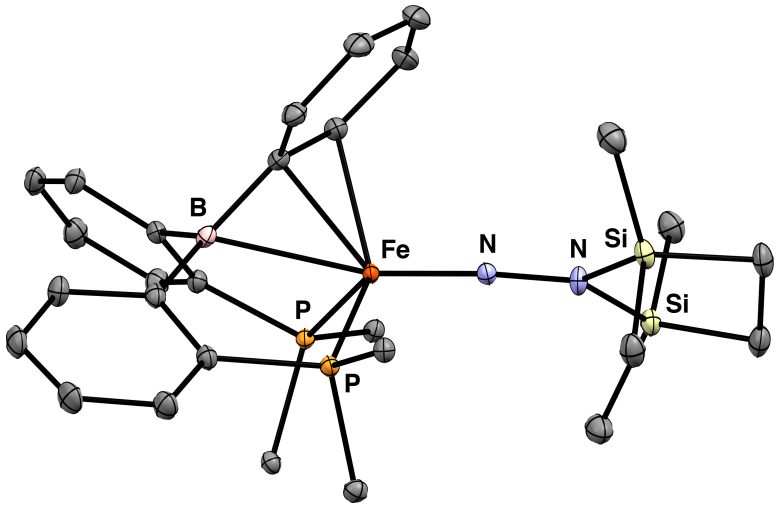

Figure 3.18 Displacement ellipsoid (50%) structure of (^{Ph}DPB)Fe(NNSi$_2$). PPh$_2$ groups are truncated and H atoms are omitted for clarity. Selected bond distances and angles: Fe–N = 1.6610(7) Å; N–N = 1.3193(10) Å; Fe–B = 2.4242(10) Å; Fe-C$_{ipso}$ = 2.1542(9) Å; Fe-C$_{ortho}$ = 2.2041(9) Å; Fe–P = 2.2026(3) Å, 2.2264(3) Å; ∠(P–Fe–P) = 103.66(1)°; Σ∠(C–B–C) = 357°.

of (^{Ph}DPB)Fe(NNSi$_2$) does not display upfield-shift resonances corresponding to the bound arene; the reasons for this difference with (DPB)Fe(NNSi$_2$) are unclear, though it may be attributed to less Fe–arene backdonation in the former due to a less electron-releasing Fe center.

With (^{Ph}DPB)Fe(NNSi$_2$) in hand, the reactivity of this Fe aminoimide with H_2 can be tested. After heating a C_6H_6 solution of (^{Ph}DPB)Fe(NNSi$_2$) under 1 atm H_2 at 50 ˚C for 2 hr., the solution turns from deep green to pale brown (Scheme 3.16). The nearly colorless

Scheme 3.16 H_2 addition to (^{Ph}DPB)Fe(NNSi$_2$)

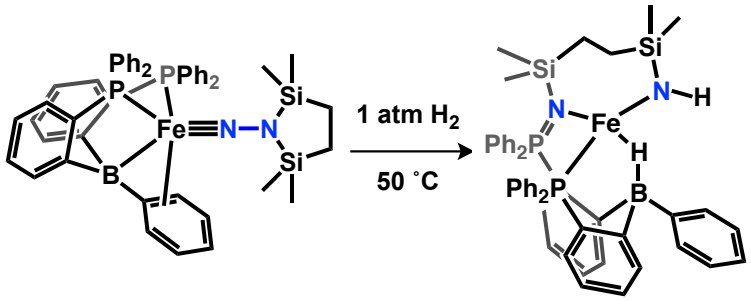

(^{Ph}DPB)Fe(NNSi$_2$) (^{Ph}DPB*–H)Fe(N$_2$Si$_2$H)

solids that are isolated from this reaction have a qualitatively similar paramagnetic ^{1}H NMR spectrum to those from the analogous reaction using (DPB)Fe(NNSi$_2$). The RT moment is 4.8 μ_B, indicating that the product adopts an $S = 2$ spin state. In addition, its IR spectrum has similar signals corresponding to N–H and B–H–Fe stretches (3343 and ~2100 cm^{-1}, respectively) that shift if D_2 is used instead of H_2 (2476 (2441 calc.) and ~1550 cm^{-1}, respectively) (Figure 3.19). Thus, the reaction of (^{Ph}DPB)Fe(NNSi$_2$) appears to proceed in the same manner as the reaction with (DPB)Fe(NNSi$_2$).

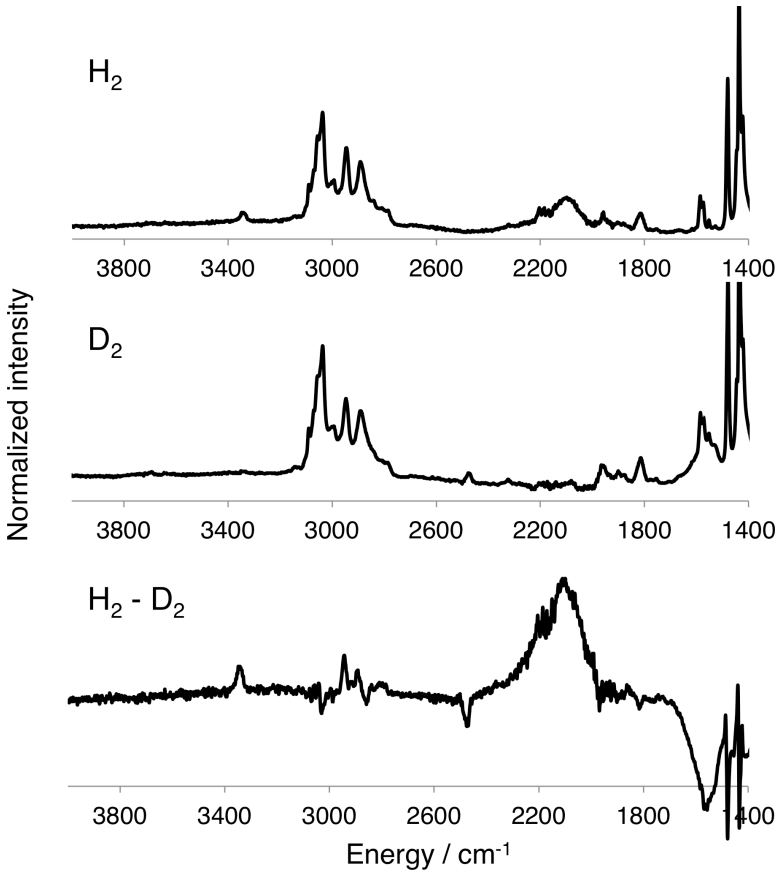

Figure 3.19 Thin film IR spectra resulting from addition of H_2 (top) or D_2 (middle) to (^{Ph}DPB)Fe($NNSi_2$). Subtraction spectrum (bottom).

The connectivity of the product was established by XRD analysis (Figure 3.20). In addition to the formation of new N–H and Fe–H–B bonds, the structure of (^{Ph}DPB*–H)Fe(N_2Si_2H) reflects cleavage of the N–N bond, rearrangement of the azadisilacyclopentane ring, and formal oxidation of one of the phosphines. Although no mechanistic information has been obtained, this overall transformation is sufficiently complex that it is worthwhile to put forth a tentative mechanism (Scheme 3.17). The hydrogenation of (^{Ph}DPB)Fe($NNSi_2$) to form A is analogous to the formation of (DPB–H)Fe($N(Si)NSi_2$) from (DPB)Fe($NNSi_2$). The hydrazine rearrangement step to

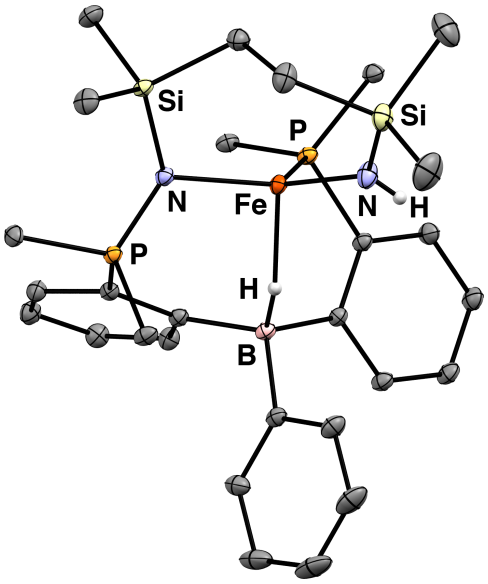

Figure 3.20 Displacement ellipsoid (50%) structure of (^{Ph}DPB*–H)Fe(N_2Si_2H). PPh_2 groups are truncated and H atoms and solvent molecules are omitted for clarity. Selected bond distances and angles: Fe–N(H)Si = 1.8996(7) Å; Fe–N(P)Si = 2.0194(6) Å; Fe–B = 2.8335(8) Å; Fe–P = 2.4248(2) Å; Σ∠(C–B–C) = 336°.

Scheme 3.17 Proposed mechanism of H_2 addition to (^{Ph}DPB)Fe($NNSi_2$)

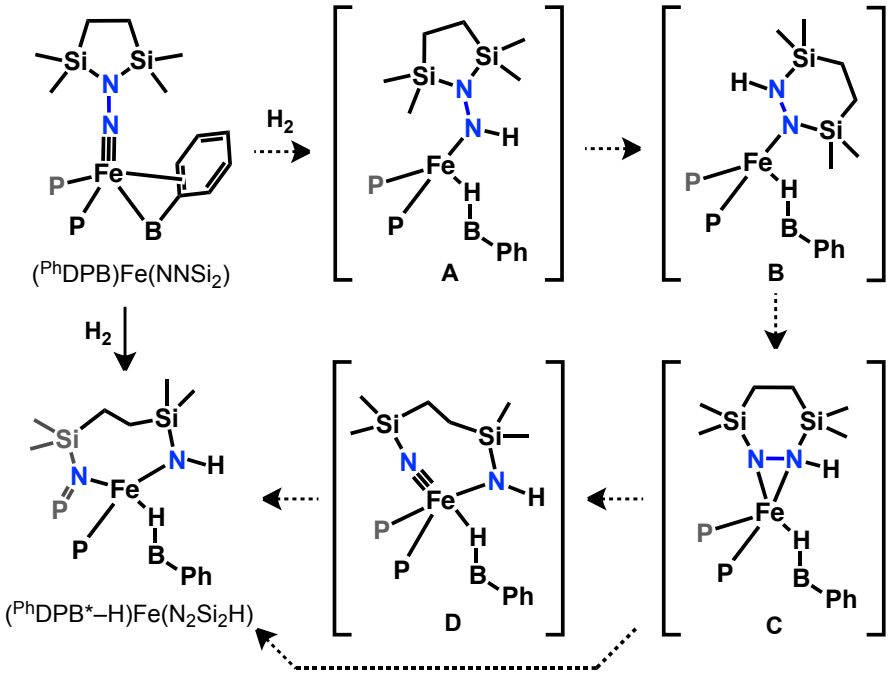

form B has precedent for closely-related disilylhydrazines.[24] Intermediate B may be sufficiently unencumbered to allow for η^2-NN binding to give C which could lead to direct N–N cleavage and group transfer to a phosphine. Alternatively, the N–N bond in C may be cleaved to form an Fe(IV) imide[25] D which then undergoes group transfer to give (DPB–H)Fe(N(Si)NSi_2). The transformation of (^{Ph}DPB)Fe($NNSi_2$) to (DPB–H)Fe(N(Si)NSi_2) is only the second example of N_2 functionalization with H_2 at a well-defined Fe complex.[12]

3.4 Summary

In this chapter, I have reported the generation of Fe aminoimides from N_2 that undergo subsequent addition of non-polar E–H bonds. The significant flexibility of the Fe–BPh interactions facilitate both the initial formation of the Fe aminoimide as well as the E–H activation step. Whereas previous functionalization reactions of terminal Fe–N_2 fragments allow for derivatization of Nβ, this report demonstrates that E–H addition to an unsaturated Fe–N bond is a viable strategy for Nα functionalization.

3.5 Experimental section

*General Considerations***.** All manipulations were carried out using standard Schlenk or glovebox techniques under an atmosphere of N_2. Solvents were degassed and dried by sparging with N_2 gas and passage through an activated alumina column. Deuterated solvents were purchased from Cambridge Isotopes Laboratories, Inc. and were degassed and stored over activated 3 Å molecular sieves prior to use. Reagents were purchased from commercial vendors and used without further purification unless otherwise noted.

(TPB)FeNNSi$_2$,[12] DPB,[8] and ^{Ph}DPB[26] were synthesized according to literature procedures. Elemental analyses were performed by Midwest Microlab (Indianapolis, IN) or Robertson Microlit Laboratories (Ledgewood, NJ).

Spectroscopic measurements. ^{1}H, ^{13}C, ^{31}P, and ^{11}B NMR spectra were collected at room temperature on a Varian 400 MHz spectrometer. ^{1}H and ^{13}C spectra were referenced to residual solvent resonances. ^{31}P spectra were referenced to external 85% phosphoric acid (δ = 0 ppm). ^{11}B spectra were referenced to BF_3•Et_2O (0 ppm). UV-vis measurements were performed with a Cary 50 instrument with Cary WinUV software. IR spectra were obtained as thin films formed by evaporation or as a solution using a cell with KBr windows using a Bruker Alpha Platinum ATR spectrometer with OPUS software.

X-ray Crystallography. Unless otherwise noted, X-ray diffraction studies were carried out at the Caltech Division of Chemistry and Chemical Engineering X-ray Crystallography Facility on a Bruker three-circle SMART diffractometer with a SMART 1K CCD detector or APEX CCD detector. Data were collected at 100K using Mo Kα radiation (λ = 0.71073 Å). Structures were solved by direct or Patterson methods using SHELXS and refined against F^2 on all data by full-matrix least squares with SHELXL-97.[27] Data for complex (DPB–H)Fe(N(Si)NSi$_2$) were collected with synchrotron radiation at the Stanford Synchrotron Radiation Laboratory (SSRL) beam line 12-2 at 17 keV using a single phi axis and recorded on a Dectris Pilatus 6M. The images were processed using XDS[28] and further workup of the data was analogous to the other datasets. All non-hydrogen atoms were refined anisotropically. All hydrogen atoms were placed at geometrically calculated positions and refined using a riding model. The isotropic

displacement parameters of all hydrogen atoms were fixed at 1.2 (1.5 for methyl groups) times the Ueq of the atoms to which they are bonded.

Computational Details. All calculations were performed using the Gaussian09 suite.[29] The geometry optimizations were done without any symmetry restraints using the B3LYP hybrid functional. The 6-311+g(d) basis set was used for all atoms. Minimized structures were verified with frequency calculations. The starting coordinates for the metal and ligand were taken from the crystal structures.

(DPB)FeBr: A solution of DPB (1.318 g, 2.778 mmol) and $FeBr_2$ (0.599 g, 2.778 mmol) in THF (50 mL) was stirred at RT until all of the solids dissolved. The solvent was removed in vacuo and Et_2O (100 mL) was added. The suspension was stirred vigorously to give a bright yellow precipitate. The solvent was removed in vacuo and benzene (100 mL) was added with a freshly-prepared 1% Na/Hg amalgam (Na: 63.9 mg, 2.778 mmol). The reaction was stirred vigorously for 18 hr to give a dark brown mixture. The mixture was decanted from the Hg and solvent was removed in vacuo. Et_2O (20 mL) was added and subsequently removed in vacuo. The dark solids were then dissolved by adding pentane (200 mL) and Et_2O (50 mL) and filtered through a pad of Celite. To the brown solids were added pentane (5 mL) and HMDSO (5 mL). The washings were removed and the solids were dried in vacuo. Lyophilization from benzene (10 mL) furnished brown microcrystals (1.423 g, 2.332 mmol, 84%). Single crystals suitable for X-ray diffraction may be obtained by concentration of an Et_2O solution. ^{1}H NMR (300 MHz, C_6D_6) δ 184.72, 78.42, 39.48, 33.44, 27.94, 25.39, 8.58, 0.91, -1.71, -5.56, -9.89, -11.76, -58.05. UV/vis (toluene, nm (M^{-1} cm^{-1})): 461 (1400, sh), 581 (550), 715 (250), 992 (590). μ_{eff}

(C_6D_6, 298 K) = 3.8 μ_B. Elemental analysis for $C_{30}H_{41}BBrFeP_2$: calc. C 59.05, H 6.77; found C 58.97, H 6.98.

[(DPB)Fe]$_2$(μ-1,2-N$_2$): A solution of DPB (0.942 g, 1.98 mmol) and $FeBr_2$ (0.428 g, 1.98 mmol) in THF (40 mL) was stirred at RT until all of the solids dissolved. The solvent was removed in vacuo and Et_2O (80 mL) was added. The suspension was stirred vigorously to give a bright yellow precipitate. The solvent was removed in vacuo and benzene (80 mL) was added with a freshly-prepared 1% Na/Hg amalgam (Na: 95.9 mg, 4.17 mmol). The reaction was stirred vigorously for 18 hr to give a dark red-brown mixture. The mixture was decanted from the Hg and filtered through Celite. The solvent was removed in vacuo to give a brown residue. Addition of pentane (5 mL) induced precipitation of dark crystals. The solvent was decanted and the solids were washed with cold Et_2O (3 x 5 mL) and dried in vacuo (0.762 g, 0.700 mmol, 71%). Single crystals suitable for X-ray diffraction may be obtained by concentration of an Et_2O solution. Alternative synthesis of [(DPB)Fe]N_2: a 2 mL THF solution of (DPB)FeBr (53.1 mg, 0.0870 mmol) was stirred over a freshly-prepared 1% Na/Hg (Na: 2.2 mg, 0.095 mmol) for 18 hr. The mixture was decanted from the Hg, concentrated in vacuo, and extracted with 5 mL benzene. The dark benzene solution was filtered through Celite, lyophilized, and recrystallized by concentration of an n-pentane solution to give crystals of **7** (31 mg, 0.028 mmol, 66%). ^{1}H NMR (400 MHz, C_6D_6) δ 171.85, 133.26, 43.95, 34.57, 28.15, 26.17, 7.42, 0.33, -1.50, -2.29, -6.28, -9.12, -76.00. UV/vis (toluene, nm (M^{-1} cm^{-1})): 405 (15000), 501 (8300, sh), 990 (8300). μ_{eff} (C_6D_6, 298 K) = 4.6 μ_B. Elemental analysis for $C_{60}H_{82}B_2Fe_2N_2P_4$: calc. C 66.20, H 7.59, N 2.57; found C 65.85 H 7.86 N 2.23.

(DPB–H)Fe(benzo[*h*]quinolin-10-yl): A solution of $[(DPB)Fe]_2(\mu\text{-}1,2\text{-}N_2)$ (19.1 mg, 0.0176 mmol) and benzo[*h*]quinoline (6.3 mg, 0.035 mmol) in 0.7 mL C_6D_6 was heated at 70 ˚C until all $[(DPB)Fe]_2(\mu\text{-}1,2\text{-}N_2)$ was consumed (~3 hr.). Solvent was removed in vacuo and the resulting solids were washed with cold pentane (3 x 1 mL) and dissolved in minimal Et_2O. Evaporation of the saturated Et_2O solution into HMDSO gave single crystals of the title compound which were lyophilized from C_6H_6 to give magenta solids (14.0 mg, 0.0197 mmol, 56%). ^{1}H NMR (500 MHz, C_6D_6) δ 9.02-8.86 (m, 1H), 7.56 (d, J = 8.7 Hz, 1H), 7.47 (d, J = 7.9 Hz, 2H), 7.46 (s, 1H), 7.45-7.41 (m, 4H), 7.39 (d, J = 6.6 Hz, 2H), 7.33-7.28 (m, 4H), 7.25-7.19 (m, 4H), 7.12 (s, 1H), 6.70 (d, J = 5.3 Hz, 1H), 6.41 (dd, J = 7.8, 5.4 Hz, 1H), 1.78-1.50 (m, 4H), 0.87 (d, J = 7.0 Hz, 6H), 0.73 (d, J = 6.3 Hz, 6H), 0.18 (s, 6H), 0.11 (d, J = 6.4 Hz, 6H), -22.80 (s, 1H). ^{11}B NMR (160 MHz, C_6D_6) δ -7.29. ^{13}C NMR (126 MHz, C_6D_6) δ 160.71, 153.81, 153.63, 147.23, 146.58, 144.03, 135.36, 132.95, 129.87, 129.67, 128.44, 126.20, 125.03, 124.62, 124.41, 122.23, 119.20, 116.80, 26.57, 23.35, 20.97, 18.75, 18.49, 18.36. ^{31}P NMR (202 MHz, C_6D_6) δ 41.26. Elemental analysis for $C_{43}H_{50}BFeNP_2$: calc. C 72.80, H 7.10, N 1.97; found C 72.51 H 6.84 N 1.84.

(DPB–H)Fe(2-(pyridin-2-yl)phenyl): A solution of $[(DPB)Fe]_2(\mu\text{-}1,2\text{-}N_2)$ (26.6 mg, 0.0244 mmol) and 2-phenylpyridine (7.6 mg, 0.049 mmol) in 0.7 mL C_6D_6 was heated at 70 ˚C until all $[(DPB)Fe]_2(\mu\text{-}1,2\text{-}N_2)$ was consumed (~3 hr.). Solvent was removed in vacuo and the resulting solids were washed with pentane (3 x 1 mL) and dissolved in minimal Et_2O. Evaporation of the saturated Et_2O solution into HMDSO gave single crystals

of the title compound which were lyophilized from C_6H_6 to give a burgundy powder (22.8 mg, 0.0333 mmol, 68%). ^{1}H NMR (500 MHz, C_6D_6) δ 8.67-8.60 (m, 1H), 7.51-7.46 (m, 1H), 7.43 (br s, 2H), 7.39 (d, J = 7.6 Hz, 2H), 7.32 (d, J = 7.4 Hz, 4H), 7.24-7.14 (m, 4H), 7.12-7.06 (m, 2H), 7.05-6.97 (m, 2H), 6.77-6.68 (m, 1H), 6.12 (d, J = 5.5 Hz, 1H), 5.98-5.91 (m, 1H), 1.94 (s, 2H), 1.76 (s, 2H), 0.99 (s, 6H), 0.79 (s, 6H), 0.50 (br s, 12H), -21.13 br (s, 1H). ^{11}B NMR (160 MHz, C_6D_6) δ -8.49. ^{13}C NMR (126 MHz, C_6D_6) δ 190.50, 170.79, 155.96, 154.25, 148.22, 147.82, 143.18, 135.23, 131.57, 128.35, 125.28, 125.11, 124.55, 122.56, 119.18, 118.17, 115.81, 26.61, 24.34, 24.29, 20.93, 19.07, 18.17. ^{31}P NMR (202 MHz, C_6D_6) δ 51.81. Elemental analysis for $C_{41}H_{50}BFeNP_2$: calc. C 71.84, H 7.35, N 2.04; found C 71.64 H 7.36 N 1.90.

(DPB–H)Fe(8-amidoquinline) (mixture of two isomers): A solution of $[(DPB)Fe]_2(\mu$-1,2-$N_2)$ (17.4 mg, 0.0160 mmol) and 8-aminoquinoline (4.6 mg, 0.032 mmol) in 0.7 mL C_6D_6 was allowed to stand at RT until all $[(DPB)Fe]_2(\mu$-1,2-$N_2)$ was consumed (~1 hr.). Solvent was removed in vacuo and the resulting solids were washed with cold pentane (3 x 1 mL) and dissolved in minimal Et_2O. Evaporation of the saturated Et_2O solution into HMDSO furnished crystals of the title compound which were lyophilized from C_6H_6 to give a red powder (18.0 mg, 0.0267 mmol, 83%). ^{1}H NMR (300 MHz, C_6D_6) δ 141.88, 103.99, 85.33, 83.94, 77.91, 72.22, 68.70, 58.27, 57.69, 51.90, 24.40, 22.51, 19.91, 17.52, 17.18, 15.04, 14.47, 12.77, 11.31, 2.17, 0.74, -1.81, -3.85, -7.08, -9.09, -9.45, -12.79, -15.24, -20.90, -25.02, -33.79, -81.35, -83.00, -84.84, -103.43. Solution magnetic moment (Evans method, RT, C_6D_6): 5.2 μ_B. Elemental analysis for $C_{39}H_{49}BFeN_2P_2$: calc. C 69.45, H 7.32, N 4.15;

found C 68.55 H 7.09 N 3.94. IR (thin film from C_6D_6, cm^{-1}): 3373 (N–H), 2130 (br, s, B–H–Fe for isomer A), 2000 (B–H–Fe for isomer B).

[(DPB)Fe(N_2)][K(benzo-15-crown-5)$_2$]: A solution of [(DPB)Fe]$_2$(μ-1,2-N_2) (25.3 mg, 0.0233 mmol) and K/Hg amalgam (1 g, 1% K by weight) in THF (1 mL) was stirred at RT for 4 hr. The dark red solution was decanted and filtered through glass fiber filter paper onto solid benzo-15-crown-5 (26.2 mg, 0.0978 mmol). Solvent was removed in vacuo and the resulting solids were washed with Et_2O (3 x 1 mL) and C_6H_6 (3 x 1 mL) to give dark solids (47.8 mg, 0.0422 mmol, 90%). Single crystals were grown by layering a THF solution with Et_2O and pentane. ^{1}H NMR (300 MHz, THF-d_8) δ 14.50, 12.05, 6.86 (crown), 6.73 (crown), 3.85 (crown), 3.72 (crown), 2.80, 1.01, -2.72, -4.78. IR (thin film from THF, cm^{-1}): 1935 (N–N).

(DPB)FeNNSi$_2$: A mixture of (DPB)FeBr (0.233 g, 0.381 mmol), 1,2-bis(chlorodimethylsilyl)ethane (0.0905 g, 0.420 mmol), and freshly-prepared 1% Na/Hg (Na: 0.0272 g, 1.18 mmol) was rapidly stirred in 5 mL THF under 1 atm N_2. The solution turned deep green within 15 min. and was decanted from the Hg. Solvent was removed in vacuo, benzene (3 mL) was added to the solids, and the solution was filtered through Celite. Solvent was removed in vacuo to give green solids which were dissolved in 5 mL pentane. Upon stand for 10 min., dark green crystals formed. The remaining solution was again filtered and allowed to evaporate into HMDSO thereby furnishing more dark green crystals. The combined crystals were washed with pentane (3 x 0.5 mL) and lyophilized from benzene to give the title compound (0.202 mg, 0.287 mmol, 75.5%). ^{1}H NMR (400

MHz, C_6D_6) δ 8.56 (d, *J* = 7.4 Hz, 2H), 7.52 (td, *J* = 7.3, 1.2 Hz, 2H), 7.44 (d, *J* = 7.6 Hz, 2H), 6.97 (td, *J* = 7.3, 1.2 Hz, 2H), 6.49 (t, *J* = 7.2 Hz, 1H), 5.11 (d, *J* = 6.5 Hz, 2H), 4.75 (t, *J* = 6.9 Hz, 2H), 2.31 (m, 2H), 1.54 (m, 2H), 1.19 - 1.06 (m, 6H), 1.06 - 0.94 (m, 6H), 0.81 (s, 4H), 0.73 - 0.55 (m, 12H), 0.27 (s, 12H). ^{13}C NMR (101 MHz, C_6D_6) δ 176.07, 140.35, 140.21, 137.17, 133.00, 130.09, 126.34, 124.92, 122.67, 113.68, 29.82, 21.14, 19.25, 18.54, 18.46, 15.15, 10.28, -5.53. ^{31}P NMR (162 MHz, C_6D_6) δ 29.43. ^{11}B NMR (128 MHz, C_6D_6) δ -28.16. UV/vis (toluene, nm (M^{-1} cm^{-1})): 651 (1100), 988 (1600). Elemental analysis for $C_{36}H_{57}BFeN_2P_2Si_2$: calc. C 61.54, H 8.18, N 3.99; found C 61.82, H 7.93, N 3.35.

(DPB-H)FeNSiNSi$_2$: A solution of (DPB)Fe(NNSi$_2$) (82.5 mg, 0.117 mmol) and $PhSiH_3$ (14.0 mg, 0.129 mmol) was allowed to stand in 2 mL benzene until the solution turned from green to deep orange (1 hr.). The benzene was lyophilized and the solids were extracted into TMS (5 mL) and filtered through Celite. Small orange crystals of the product formed upon concentration of the solution into HMDSO (41.0 mg, 0.0506 mmol, 43.2%). The reaction is quantitative by NMR, though the isolated yield of solids suffers due to the high solubility of the product. ^{1}H NMR (400 MHz, C_6D_6) δ 113.98, 52.22, 32.54, 25.37, 24.56, 18.16, 17.55, 12.78, 11.51, -1.09, -9.62, -10.32, -18.45, -25.52, -29.85, -33.94. IR (thin film from C_6D_6, cm^{-1}): 2090 (s, Si–H), 2000 (s and br, B–H–Fe). μ_{eff} (C_6D_6, 298 K) = 5.0 μ_B. Elemental analysis for $C_{42}H_{65}BFeN_2P_2Si_3$: calc. C 62.21, H 8.08, N 3.45; found C 61.92 H 7.81 N 1.95.

Synthesis of (DPB-H)FeNSiNSi$_2$ from (DPB)FeBr: A 2 mL THF solution of (DPB)FeBr (48.8 mg, 0.0800 mmol), 1,2-bis-(chlorodimethylsilyl)ethane (19.0 mg, 0.0881 mmol) and 1% Na/Hg (5.7 mg Na, 0.25 mmol) was vigorously stirred for 5 min. to give a green solution which was then added to neat $PhSiH_3$ (9.5 mg, 0.088 mmol). The solution deep orange within 10 min. The volatiles were removed in vacuo and the solids were dissolved in pentane and filtered through a plug of Celite. The volatiles were removed in vacuo to give an orange foam (57.7 mg) that was identified as (DPB-H)FeNSiNSi$_2$ (>95% purity by ^{1}H NMR).

Synthesis of (DPB-H)FeNSiNSi$_2$ from [(DPB)Fe]$_2$(μ-1,2-N$_2$): A 2 mL THF solution of [(DPB)Fe]$_2$(μ-1,2-N$_2$) (20.8 mg, 0.0191 mmol), 1,2-bis-(chlorodimethylsilyl)ethane (8.6 mg, 0.040 mmol) and 1% Na/Hg (1.8 mg Na, 0.078 mmol) was vigorously stirred for 5 min. to give a green solution which was then added to neat $PhSiH_3$ (4.3 mg, 0.040 mmol). The solution turned deep orange within 10 min. The volatiles were removed in vacuo and the solids were dissolved in pentane and filtered through a plug of Celite. The volatiles were removed in vacuo to give an orange foam (25.1 mg) that was identified as (DPB-H)FeNSiNSi$_2$ (>95% purity by ^{1}H NMR).

(^{Ph}DPB)FeBr: A solution of ^{Ph}DPB (1.398 g, 2.290 mmol) and $FeBr_2$ (0.494 g, 2.29 mmol) in THF (60 mL) was stirred at RT until all of the solids dissolved. The solvent was removed in vacuo and Et_2O (100 mL) was added. The suspension was stirred vigorously to give a bright yellow precipitate in a yellow solution. The solvent was removed in vacuo and benzene (60 mL) was added with a freshly-prepared 1% Na/Hg amalgam (Na: 52.7

mg, 2.29 mmol). The reaction was stirred vigorously for 18 hr to give a dark brown mixture. The mixture was decanted from the Hg, filtered through Celite, and dried in vacuo. The solids were washed with Et_2O (3 x 20 mL). The dark, microcrystalline solids were dried in vacuo. Lyophilization from benzene (10 mL) furnished brown microcrystals (1.095 g, 1.467 mmol, 64%). Single crystals suitable for X-ray diffraction may be obtained by diffusion of n-pentane into a concentrated benzene solution. ^{1}H NMR (400 MHz, C_6D_6) δ 82.99, 32.99, 31.22, 22.92, 10.53, 9.41, 5.50, 3.24, 1.83, -0.53, -4.50, -10.18, -72.92. UV/vis (toluene, nm (M^{-1} cm^{-1})): 474 (1600, sh), 581 (530), 717 (260), 1003 (600). μ_{eff} (C_6D_6, 298 K) = 3.6 μ_B. Elemental analysis for $C_{42}H_{33}BBrFeP_2$: calc. C 67.60, H 4.46; found C 67.59 H 4.49.

(^{Ph}DPB)Fe: A 3 mL THF solution of (^{Ph}DPB)FeBr (77.9 mg, 0.1044 mmol) was stirred over freshly-prepared 1% Na/Hg amalgam (Na: 2.5 mg, 0.11 mmol) for 10 hr. The red-brown solution was decanted from the Hg and solvent was removed in vacuo. The solids were extracted into benzene (5 mL) and filtered through Celite. The solvent was removed in vacuo. The solids were washed with Et_2O (2 x 2 mL) and dissolved in benzene (2 mL). Layering the solution with pentane furnished brown single crystals of the title compound (78.0 mg, 0.0948 mmol, 90.8% for (^{Ph}DPB)Fe•$2C_6H_6$). XRD studies revealed that the compound crystallizes with two molecules of C_6H_6. The compound exhibits a degree of paramagnetic speciation in C_6D_6 under N_2 or Ar but is fully diamagnetic in THF-d_8; as such, ^{1}H NMR data are reported in both solvents. ^{1}H NMR (400 MHz, C_6D_6) δ 8.80 (d, J = 7.2 Hz, 2H), 7.64 (s, 4H), 7.37 (t, J = 6.8 Hz, 2H), 7.16 (s, 4H), 7.06 - 6.83 (m, 12H), 6.48 (t, J = 7.0 Hz, 4H), 6.29 (t, J = 6.2 Hz, 1H), 3.63 (br s, 2H), 3.23 (br s, 2H). ^{1}H NMR (400

MHz, THF-d_8) δ 8.58 (d, J = 7.5 Hz, 2H), 7.56 (m, 4H), 7.41 (t, J = 7.5 Hz, 2H), 7.25 (d, J = 7.0 Hz, 6H), 7.07 (m, 6H), 6.97 - 6.82 (m, 2H), 6.73 (t, J = 7.4 Hz, 2H), 6.57 (m, 4H), 3.32 - 3.17 (br s, 2H), 3.07 (br s, 2H). ^{13}C NMR (101 MHz, C_6D_6) δ 161.76, 146.25-145.37 (m), 143.47 (t, J = 13.8 Hz), 134.07 (t, J = 15.8 Hz), 132.61, 131.42, 130.93, 128.26, 127.12, 126.97, 124.44, 106.77, 99.41, 86.36, 78.73. ^{11}B NMR (128 MHz, C_6D_6) δ 36.44. ^{31}P NMR (162 MHz, C_6D_6) δ 77.51. Elemental analysis for $C_{42}H_{33}BFeP_2$•0.5C_6H_6: calc. C 76.62, H 5.14, N 0; found C 76.55, H 5.60, N <0.02.

(^{Ph}DPB)FeNNSi$_2$: A mixture of (^{Ph}DPB)FeBr (0.195 g, 0.262 mmol), 1,2-bis(chlorodimethylsilyl)ethane (0.0621 g, 0.288 mmol), and freshly-prepared 1% Na/Hg (Na: 0.0187 g, 0.813 mmol) was rapidly stirred in 5 mL THF under 1 atm N_2. The solution turned deep green within 90 min. and was decanted from the Hg. Solvent was removed in vacuo, benzene (5 mL) was added to the solids, and the solution was filtered through Celite after standing at RT for 2 hr. Solvent was removed in vacuo to give green solids which were washed with pentane (3 x 1 mL) and redissolved in a minimal amount of benzene. The solution was again filtered and layer with pentane to provide dichroic green/brown crystals. The crystals were washed with pentane (3 x 0.5 mL) to give the title compound (0.188 g, 0.2242 mmol, 85.6%). ^{1}H NMR (400 MHz, C_6D_6) δ 8.08 (m, 4H), 7.95 (m, 2H), 7.36 - 6.90 (m, 15H), 6.75 (m, 8H), 6.53 (m, 4H), 0.34 (s, 4H), -0.22 (s, 12H). ^{13}C NMR (101 MHz, C_6D_6) δ 159.64 , 143.47 - 142.65 (m), 139.85 (t, J = 15.3 Hz), 139.28 - 138.72 (m), 134.58 , 132.15 , 130.32 , 130.10 , 128.57 , 126.33 , 125.81 , 115.89 , 97.93 , 7.93 , -1.82 . ^{31}P NMR (162 MHz, C_6D_6) δ 88.02. ^{11}B NMR (128 MHz, C_6D_6) δ 32.67. UV/vis

(toluene, nm (M^{-1} cm^{-1})): 653 (850). Elemental analysis for $C_{48}H_{49}BFeN_2P_2Si_2$: calc. C 68.74, H 5.89, N 3.34; found C 68.48, H 5.67, N 3.07.

(^{Ph}DPB-H)*FeNHSiNSi: A solution of (^{Ph}DPB)Fe($NNSi_2$) (45.0 mg, 0.0537 mmol) in benzene (5 mL) was stirred under 1 atm H_2 at 50 ˚C for three hours. The solution changed from dark green to light brown. Solvent was removed in vacuo to give a tan solid. The solids were washed with pentane (2 x 5 mL) and dissolved in minimal Et_2O (~10 mL). The solution was allowed to evaporate into HMDSO to give white solids (28.7 mg, 0.0341 mmol, 63.6%). Single crystals suitable for XRD were grown by vapor diffusion of n-pentane into a concentrated THF solution. ^{1}H NMR (400 MHz, C_6D_6) δ 188.54, 26.16, 25.70, 20.47, 16.37, 14.59, 12.01, 5.79, 4.77, 3.85, 3.23, 2.25, 1.97, 1.21, 0.84, 0.25, -0.04, -1.89, -7.20, -9.74. IR (thin film from C_6D_6, cm^{-1}): 3343 (w, N–H), ~2100 (s and br, B–H–Fe). μ_{eff} (C_6D_6, 298 K) = 4.8 μ_B. Satisfactory combustion analysis data were not obtained for (^{Ph}DPB-H)*FeNHSiNSi, though I am confident in my assignment of the product based on NMR and IR spectra of bulk samples as well as XRD analysis of single crystalline samples.

(^{Ph}DPB-D)*FeNDSiNSi: The D-labeled compound was generated in a procedure that is identical to that for the H-labeled compound using D_2 instead of H_2. ^{1}H NMR data are the same between the two species. IR (thin film from C_6D_6, cm^{-1}): 2476 (w, N–D), ~1550 (s and br, B–D–Fe).

Attempted reaction of (TPB)Fe(NNSi$_2$) with H$_2$: To a J. Young tube was added a C_6D_6 solution of (TPB)Fe(NNSi$_2$). The green solution as subjected to three freeze-pump-thaw cycles and 1 atm H_2 was added. No reaction occurred at RT after 15 min. by ^{1}H NMR analysis. After heating the solution to 50 ˚C for 2 hr., the ^{1}H NMR spectrum showed a mixture of (TPB)Fe(NNSi$_2$), the previously-characterized (TPB)Fe(N$_2$) complex, and other unidentified diamagnetic and paramagnetic species.

Attempted reaction of (TPB)Fe(NNSi$_2$) with PhSiH$_3$: To a J. Young tube was added a C_6D_6 solution of (TPB)Fe(NNSi$_2$) (9.5 mg, 0.0116 mmol) with $PhSiH_3$ (1.4 mg, 0.013 mmol). No reaction occurred at RT after 15 min. by ^{1}H NMR analysis. After heating the solution to 50 ˚C for 6 hr., the ^{1}H NMR spectrum showed mostly (TPB)Fe(NNSi$_2$) and small amounts of unidentified diamagnetic and paramagnetic species.

This chapter was reproduced in part with permission from

Suess, D. L. M.; Peters, J. C. *J. Am. Chem. Soc.* **2013**, *135*, 4938–4941.

(1) (a) Seefeldt, L. C.; Hoffman, B. M.; Dean, D. R. *Annu. Rev. Biochem.,* **2009,** *78*, 701; (b) Crossland, J. L.; Tyler, D. R. *Coord. Chem. Rev.,* **2010,** *254*, 1883; (c) Hazari, N. *Chem. Soc. Rev.,* **2010,** *39*, 4044; (d) Chatt, J.; Dilworth, J. R.; Richards, R. L. *Chem. Rev.,* **1978,** *78*, 589.
(2) Hoffman, B. M.; Dean, D. R.; Seefeldt, L. C. *Acc. Chem. Res.,* **2009,** *42*, 609.
(3) (a) Chatt, J.; Heath, G. A.; Richards, R. L. *J. Chem. Soc., Chem. Commun.,* **1972**, 1010; (b) Hidai, M.; Mizobe, Y. *Chem. Rev.,* **1995,** *95*, 1115; (c) Arashiba, K.; Miyake, Y.; Nishibayashi, Y. *Nature Chem.,* **2010,** *3*, 120; (d) Yuki, M.; Tanaka, H.; Sasaki, K.; Miyake, Y.; Yoshizawa, K.; Nishibayashi, Y. *Nat. Commun.,* **2012,** *3*, 1254; (e) Yandulov, D. V.; Schrock, R. R. *J. Am. Chem. Soc.,* **2002,** *124*, 6252; (f) Yandulov, D. V.; Schrock, R. R. *Science,* **2003,** *301*, 76.
(4) Hendrich, M. P.; Gunderson, W.; Behan, R. K.; Green, M. T.; Mehn, M. P.; Betley, T. A.; Lu, C. C.; Peters, J. C. *Proc. Natl. Acad. Sci. U.S.A.,* **2006,** *103*, 17107.
(5) Betley, T. A.; Peters, J. C. *J. Am. Chem. Soc.,* **2004,** *126*, 6252.
(6) Betley, T. A.; Peters, J. C. *J. Am. Chem. Soc.,* **2003,** *125*, 10782.
(7) Lee, Y.; Mankad, N. P.; Peters, J. C. *Nat. Chem.,* **2010,** *2*, 558.
(8) Moret, M.-E.; Peters, J. C. *J. Am. Chem. Soc.,* **2011,** *133*, 18118.
(9) Hoffman, B. M.; Lukoyanov, D.; Dean, D. R.; Seefeldt, L. C. *Acc. Chem. Res.,* **2013,** *46*, 587.
(10) (a) Brown, S. D.; Peters, J. C. *J. Am. Chem. Soc.,* **2004,** *126*, 4538; (b) Bart, S. C.; Lobkovsky, E.; Bill, E.; Chirik, P. J. *J. Am. Chem. Soc.,* **2006,** *128*, 5302.
(11) (a) Fryzuk, M. D.; Love, J. B.; Rettig, S. J.; Young, V. G. *Science,* **1997,** *275*, 1445; (b) Fryzuk, M. D.; MacKay, B. A.; Patrick, B. O. *J. Am. Chem. Soc.,* **2003,** *125*, 3234; (c) Pool, J. A.; Lobkovsky, E.; Chirik, P. J. *Nature,* **2004,** *427*, 527; (d) Pool, J. A.; Bernskoetter, W. H.; Chirik, P. J. *J. Am. Chem. Soc.,* **2004,** *126*, 14326; (e) Hirotsu, M.; Fontaine, P. P.; Epshteyn, A.; Sita, L. R. *J. Am. Chem. Soc.,* **2007,** *129*, 9284; (f) Hirotsu, M.; Fontaine, P. P.; Zavalij, P. Y.; Sita, L. R. *J. Am. Chem. Soc.,* **2007,** *129*, 12690; (g) Pun, D.; Bradley, C. A.; Lobkovsky, E.; Keresztes, I.; Chirik, P. J. *J. Am. Chem. Soc.,* **2008,** *130*, 14046; (h) Semproni, S. P.; Lobkovsky, E.; Chirik, P. J. *J. Am. Chem. Soc.,* **2011,** *133*, 10406.
(12) Rodriguez, M. M.; Bill, E.; Brennessel, W. W.; Holland, P. L. *Science,* **2011,** *334*, 780.
(13) Brown, S. D.; Peters, J. C. *J. Am. Chem. Soc.,* **2005,** *127*, 1913.
(14) Harman, W. H.; Peters, J. C. *J. Am. Chem. Soc.,* **2012,** *134*, 5080.
(15) Saouma, C. T.; Peters, J. C. *Coord. Chem. Rev.,* **2011,** *255*, 920.
(16) Moret, M.-E.; Peters, J. C. *Angew. Chem. Int. Ed.,* **2011,** *50*, 2063.
(17) Fong, H.; Lee, Y.; Peters, J. C. unpublished results.
(18) Klein, H.-F.; Camadanli, S.; Beck, R.; Leukel, D.; Flörke, U. *Angew. Chem. Int. Ed.,* **2005,** *44*, 975.
(19) (a) Baker, M. V.; Field, L. D. *J. Am. Chem. Soc.,* **1986,** *108*, 7433; (b) Field, L. D.; Guest, R. W.; Turner, P. *Inorg. Chem.,* **2010,** *49*, 9086.
(20) (a) Jones, W. D.; Foster, G. P.; Putinas, J. M. *J. Am. Chem. Soc.,* **1987,** *109*, 5047; (b) Norinder, J.; Matsumoto, A.; Yoshikai, N.; Nakamura, E. *J. Am. Chem. Soc.,* **2008,** *130*, 5858; (c) Yoshikai, N.; Matsumoto, A.; Norinder, J.; Nakamura, E. *Angew. Chem. Int. Ed.,* **2009,** *48*, 2925.

(21) (a) Schaad, D. R.; Landis, C. R. *J. Am. Chem. Soc.,* **1990,** *112*, 1628; (b) Fox, D. J.; Bergman, R. G. *J. Am. Chem. Soc.,* **2003,** *125*, 8984.
(22) (a) Smith, J. M.; Lachicotte, R. J.; Holland, P. L. *J. Am. Chem. Soc.,* **2003,** *125*, 15752; (b) Crossland, J. L.; Balesdent, C. G.; Tyler, D. R. *Dalton Trans.,* **2009**, 4420; (c) Saouma, C. T.; Kinney, R. A.; Hoffman, B. M.; Peters, J. C. *Angew. Chem. Int. Ed.,* **2011,** *50*, 3446.
(23) Sircoglou, M.; Bontemps, S.; Mercy, M.; Saffon, N.; Takahashi, M.; Bouhadir, G.; Maron, L.; Bourissou, D. *Angew. Chem. Int. Ed.,* **2007,** *46*, 8583.
(24) Pitt, C. G.; Skillern, K. R. *Inorg. and Nucl. Chem. Lett.,* **1966,** *2*, 237.
(25) Thomas, C. M.; Mankad, N. P.; Peters, J. C. *J. Am. Chem. Soc.,* **2006,** *128*, 4956.
(26) Bontemps, S.; Gornitzka, H.; Bouhadir, G.; Miqueu, K.; Bourissou, D. *Angew. Chem. Int. Ed.,* **2006,** *45*, 1611.
(27) Sheldrick, G. M., *SHELXTL 2000*. Universität Göttingen: Göttingen, Germany, 2000.
(28) Kabsch, W. *J. Appl. Cryst.,* **1993,** *1993*, 795.
(29) M. J. Frisch, G. W. T., H. B. Schlegel, G. E. Scuseria, M. A. Robb, J. R. Cheeseman, G. Scalmani, V. Barone, B. Mennucci, G. A. Petersson, H. Nakatsuji, M. Caricato, X. Li, H. P. Hratchian, A. F. Izmaylov, J. Bloino, G. Zheng, J. L. Sonnenberg, M. Hada, M. Ehara, K. Toyota, R. Fukuda, J. Hasegawa, M. Ishida, T. Nakajima, Y. Honda, O. Kitao, H. Nakai, T. Vreven, J. A. Montgomery, Jr., J. E. Peralta, F. Ogliaro, M. Bearpark, J. J. Heyd, E. Brothers, K. N. Kudin, V. N. Staroverov, R. Kobayashi, J. Normand, K. Raghavachari, A. Rendell, J. C. Burant, S. S. Iyengar, J. Tomasi, M. Cossi, N. Rega, J. M. Millam, M. Klene, J. E. Knox, J. B. Cross, V. Bakken, C. Adamo, J. Jaramillo, R. Gomperts, R. E. Stratmann, O. Yazyev, A. J. Austin, R. Cammi, C. Pomelli, J. W. Ochterski, R. L. Martin, K. Morokuma, V. G. Zakrzewski, G. A. Voth, P. Salvador, J. J. Dannenberg, S. Dapprich, A. D. Daniels, Ö. Farkas, J. B. Foresman, J. V. Ortiz, J. Cioslowski, and D. J. Fox *Guassian09 Revision B.01*, Gaussian, Inc.: Wallingford, CT, 2009.

Chapter 4 An Fe Dicarbyne that Releases Olefin upon Hydrogenation

4.1 Background

Hydrogenation of CO to form C_{2+}-containing products has been a longstanding focus in organometallic chemistry.[1] Whereas heterogeneous Fischer-Tropsch reactions generate a distribution of C_n-containing products, homogeneous processes have the potential to offer greater selectivity. For this reason, there has been substantial interest in studying homogeneous metal complexes that promote C–C coupling of CO-derived ligands. To this end, Lippard has described the disilylation of $Na[(dmpe)_2M(CO)_2]$ complexes (M = V, Nb, or Ta; dmpe = bis(1,2-dimethylphosphino)ethane) to form C–C-coupled η^2-alkyne complexes[2] which can undergo subsequent hydrogenation to release an olefin (for M = V or Ta).[2c, 3] Although dicarbyne intermediates have been proposed in these reactions,[4] no such intermediate has yet been detected. In this chapter, I describe the preparation of the first Fe dicarbyne complex as well as its hydrogenation to release a CO-derived olefin. Structural and spectroscopic characterization of several intermediates including the Fe dicarbyne permits a comparative analysis of the bonding in these highly covalent complexes.

The CO reduction chemistry described herein utilizes the (DPB)Fe platform which was shown in Chapter 3 to facilitate a high degree of N_2 functionalization (Scheme 4.1). In these complexes, the polyhaptic BPh ligand can function as a donor, an acceptor, or both. This feature provides access to complexes with a variety of electronic structures,

Scheme 4.1 N_2 and CO reduction reaction types facilitated by (DPB)Fe

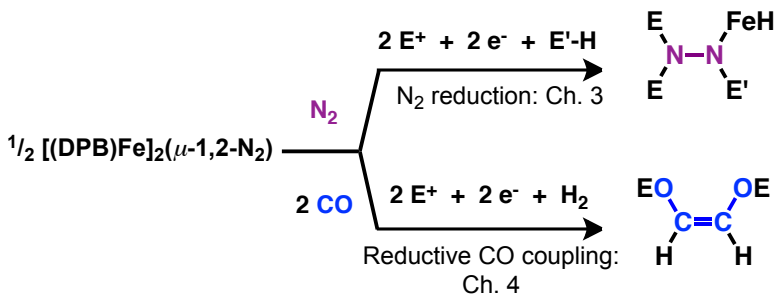

including reduced species that react with electrophiles at the β-atom of the diatomic ligand (Nβ in N_2). In addition, the B center can participate in E–H bond addition reactions (E = H or SiR_3) wherein the H atom is delivered to the B center and the E fragment is delivered to Nα. Given these results as well as the connection between N_2 and CO reduction (established both for coordination complexes and for nitrogenases[5]), I sought to employ the (DPB)Fe platform for CO functionalization.

4.2 Synthesis and properties of (DPB)Fe carbonyl complexes

For the purposes of CO coupling, I targeted (DPB)Fe complexes with >1 CO ligand. Whereas the neutral (TPB)Fe fragment binds one CO ligand at 1 atm CO,[6] the neutral (DPB)Fe platform should be more apt to bind >1 CO ligand owing to the labile η^3-BCC interaction. Indeed, addition of 1 atm CO to $[(DPB)Fe]_2(\mu\text{-}1,2\text{-}N_2)$ results in initial formation of red-orange $(DPB)Fe(CO)_2$ followed by pale yellow $(DPB)Fe(CO)_3$ (Scheme 4.2). Addition of 4 equiv CO (two per Fe center) to $[(DPB)Fe]_2(\mu\text{-}1,2\text{-}N_2)$ results in slow formation of $(DPB)Fe(CO)_2$ with mostly $[(DPB)Fe]_2(\mu\text{-}1,2\text{-}N_2)$ remaining after several hours at RT. This experiment suggests that addition of the first two equiv of CO for each

Scheme 4.2 Synthesis and reactions of (DPB)Fe carbonyl complexes

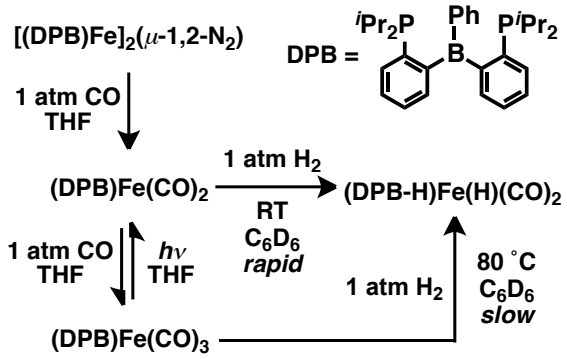

Fe in $[(DPB)Fe]_2(\mu\text{-}1,2\text{-}N_2)$ is faster than addition of the third equiv of CO to $(DPB)Fe(CO)_2$. In addition, no "(DPB)Fe(CO)" complex is observed, suggesting that such a species is not thermodynamically stable with respect to disproportionation to $[(DPB)Fe]_2(\mu\text{-}1,2\text{-}N_2)$ and $(DPB)Fe(CO)_2$. Prolonged photolysis of solutions of $(DPB)Fe(CO)_3$ results in loss of CO and regeneration of $(DPB)Fe(CO)_2$. This conversion is accompanied by binding of a phenylene linker in $(DPB)Fe(CO)_2$ (Figure 4.1) to give a

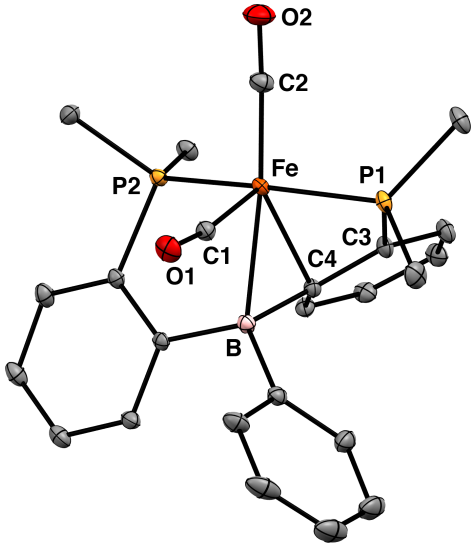

Figure 4.1 Displacement ellipsoid (50%) representation of $(DPB)Fe(CO)_2$. P^iPr_2 groups are truncated and H atoms are omitted for clarity. See Table 4.1 for selected distances and angles.

Table 4.1. Selected distances (Å) and angles (°) for neutral, monoanionic, and dianionic (DPB)Fe(CO)$_2$ complexes.

	(DPB)Fe(CO)$_2$	[(DPB)Fe(CO)$_2$] [K(benzo-15-c-5)$_2$]	[(DPB)Fe(CO)$_2$] [K(benzo-15-c-5)$_2$]$_2$
Fe-B	2.3080(15)	2.4192(15)	2.4099(9)
Fe-P1	2.1927(4)	2.2143(5)	2.1608(3)
Fe-P2	2.2322(4)	2.2100(5)	2.1539(3)
∠(P1-Fe-	159.21(2)	142.71(2)	120.60(1)
Fe-C1	1.7392(14)	1.7613(15)	1.7225(9)
Fe-C2	1.7509(15)	1.7505(14)	1.7311(9)
C1-O1	1.1707(18)	1.1675(17)	1.1930(12)
C2-O2	1.1647(19)	1.1773(16)	1.1956(11)
C1-B1	2.2983(20)	3.0171(21)	2.8602(13)
Fe-C3	2.4733(14)	3.3806(14)	3.2716(8)
Fe-C4	2.2897(13)	3.3307(14)	3.2571(8)
Σ(∠(C-B-C))	342°	330°	330°

geometrical motif that has been observed in the isoelectronic complex (TPB)Fe(CO).[6] The asymmetry in the solid-state structure of (DPB)Fe(CO)$_2$ is maintained in solution as evidenced by the presence of two sharp peaks in its ^{31}P NMR spectrum at 90.6 and 54.6 ppm ($^2J_{PP}$ = 65.3 Hz) and eight unique isopropyl CH$_3$ peaks in the ^{1}H NMR spectrum.

Given previous work with Fe and Ni complexes of this ligand class (as discussed in previous chapters),[7] it was anticipated that the η^3-BCC interaction in (DPB)Fe(CO)$_2$ could be labile and facilitate an E–H bond activation process. Accordingly, colorless (DPB–H)Fe(H)(CO)$_2$ is formed quantitatively over the course of minutes upon exposure of (DPB)Fe(CO)$_2$ to 1 atm H$_2$ at RT. Its ^{1}H NMR spectrum (Figure 4.2) shows the

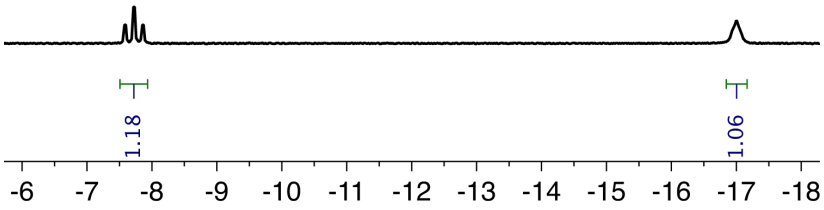

Figure 4.2 Hydride signals in the ^{1}H NMR spectrum of (DPB–H)Fe(H)(CO)$_2$ recorded at 400 MHz.

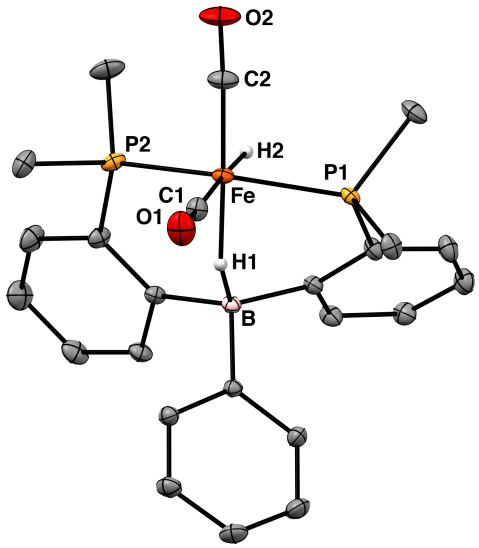

Figure 4.3 Displacement ellipsoid (50%) representation of (DPB–H)Fe(H)(CO)$_2$. P^{i}Pr$_2$ groups are truncated and H atoms are omitted for clarity. The P^{i}Pr$_2$ fragment for P1 is disordered over two positions; only the major component is shown. Selected distances and angles: Fe–B = 2.7426(6) Å; Fe–P1 = 2.249(2) Å; Fe–P2 = 2.2146(2) Å; Fe–C1 = 1.7970(5) Å; Fe–C2 = 1.7466(6) Å; ∠(P1–Fe–P2) = 150.71(5)°; Σ∠(C–B–C) = 340°.

presence of a terminal Fe–*H* signal at -7.73 ppm (1H, dt, $^{2}J_{HP}$ = 54.4 Hz, $^{2}J_{HH}$ = 7.6 Hz) and a bridging Fe–*H*–B signal at -17.0 ppm (1H, br); XRD analysis (Figure 4.3) establishes its *cis*-dihydride stereochemistry. A broad, intense resonance at ~2050 cm^{-1} is present in the IR spectrum that corresponds to a Fe–H–B stretch. Complex

$(DPB)Fe(CO)_3$ reacts with H_2 much more slowly compared with $(DPB)Fe(CO)_2$; complete conversion of $(DPB)Fe(CO)_3$ to $(DPB–H)Fe(H)(CO)_2$ is not realized after one week at 80 °C under 1 atm H_2. The greater reactivity of $(DPB)Fe(CO)_2$ with H_2 further underscores the substantial hemilability of η^3-BCC interactions in complexes of this ligand class.

Complex $(DPB)Fe(CO)_2$ exhibits two quasireversible waves in its cyclic voltammagram at -1.94 and -2.70 V vs. Fc/Fc^+ (Figure 4.4), prompting me to pursue one-

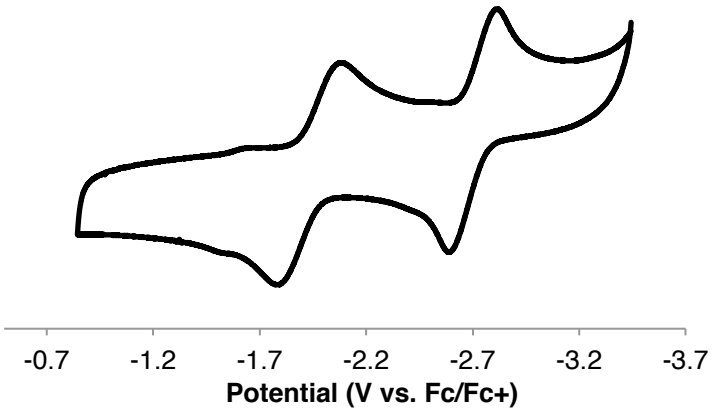

Figure 4.4 Cyclic voltammagram of $(DPB)Fe(CO)_2$ recorded in THF with 0.3 M Bu_4NPF_6 electrolyte at 100 mV s^{-1}.

and two-electron chemical reductions.[8] Stirring $(DPB)Fe(CO)_2$ over excess K until the red-orange solution turns inky yellow delivers 1.0 equiv K, thereby forming $(DPB)Fe(CO)_2(K(THF)_x)$ (Scheme 4.3); allowing this reaction to proceed for several hours results in formation of the red-brown two-electron reduced product, $(DPB)Fe(CO)_2(K(THF)_x)_2$. These species were crystallized with $[K(benzo\text{-}15\text{-}crown\text{-}5)_2]$ countercations. Structural characterization by XRD analysis (Figure 4.5) shows that both

Scheme 4.3 One- and two-electron reduction of $(DPB)Fe(CO)_2$

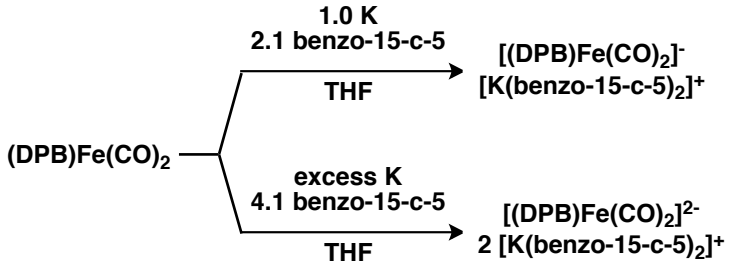

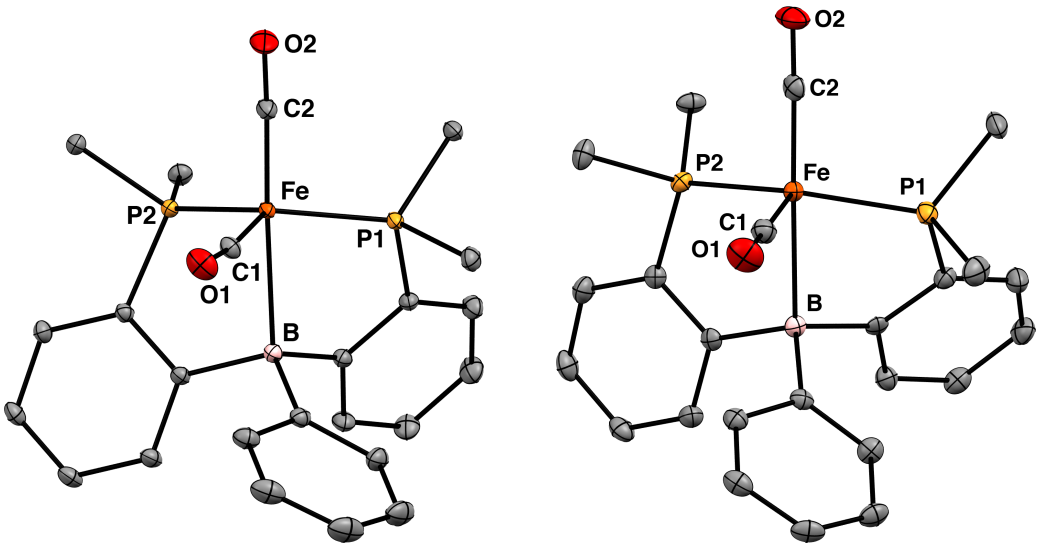

Figure 4.5 Displacement ellipsoid (50%) representations of (left) $[(DPB)Fe(CO)_2][K(benzo\text{-}15\text{-}c\text{-}5)_2]$ and (right) $[(DPB)Fe(CO)_2][K(benzo\text{-}15\text{-}c\text{-}5)_2]_2$. P^iPr_2 groups are truncated and H atoms, solvent molecules, and countercations are omitted for clarity. See Table 4.1 for selected distances and angles.

$[(DPB)Fe(CO)_2][K(benzo\text{-}15\text{-}c\text{-}5)_2]$ and $[(DPB)Fe(CO)_2][K(benzo\text{-}15\text{-}c\text{-}5)_2]_2$ lack the phenylene interaction that is present in $(DPB)Fe(CO)_2$.

Monoanion $[(DPB)Fe(CO)_2][K(benzo\text{-}15\text{-}c\text{-}5)_2]$ adopts a geometry between trigonal bipyramidal (TBP) and square pyramidal ($\tau = 0.44$)[9] with a wide $\angle(P\text{–}Fe\text{–}P) = 142.71(2)^\circ$ whereas dianion $[(DPB)Fe(CO)_2][K(benzo\text{-}15\text{-}c\text{-}5)_2]_2$ is TBP ($\tau = 0.93$) with a contracted

∠(P–Fe–P) = 120.60(1)°. The wide ∠(P–Fe–P) in [(DPB)Fe(CO)$_2$][K(benzo-15-c-5)$_2$] suggests that the unpaired electron resides in an orbital in the P–Fe–P plane; DFT calculations on [(DPB)Fe(CO)$_2$][K(benzo-15-c-5)$_2$] confirm the SOMO to be of $d_{x^2-y^2}$ character (where the Fe–B vector defines the z-axis). The rhombic X-band EPR signal of [(DPB)Fe(CO)$_2$][K(benzo-15-c-5)$_2$] is also consistent with this assignment. The Fe–B distances in [(DPB)Fe(CO)$_2$][K(benzo-15-c-5)$_2$] and [(DPB)Fe(CO)$_2$][K(benzo-15-c-5)$_2$]$_2$ are nearly equivalent at 2.4192(15) and 2.4099(9) Å, respectively, while the average Fe–P and Fe–C(O) distances contract upon reduction from [(DPB)Fe(CO)$_2$][K(benzo-15-c-5)$_2$] to [(DPB)Fe(CO)$_2$][K(benzo-15-c-5)$_2$]$_2$ (Table 4.1). A marked decrease in ν_{CO} upon reduction of (DPB)Fe(CO)$_2$ to [(DPB)Fe(CO)$_2$][K(benzo-15-c-5)$_2$] and [(DPB)Fe(CO)$_2$][K(benzo-15-c-5)$_2$] to [(DPB)Fe(CO)$_2$][K(benzo-15-c-5)$_2$]$_2$ is also observed (Figure 4.6). Taken together, these data suggest that the extra electron density in [(DPB)Fe(CO)$_2$][K(benzo-15-c-5)$_2$]$_2$ is absorbed largely by increased Fe–C(O) and Fe–P π backbonding rather than increased Fe–B σ bonding.

Complexes (DPB)Fe(CO)$_3$ and [(DPB)Fe(CO)$_2$][K(benzo-15-c-5)$_2$]$_2$ as well as the first reported Fe–borane complex, (κ^4-B(mim$^{t\text{Bu}}$)$_3$)Fe(CO)$_2$ (mim$^{t\text{Bu}}$ = 2-mercapto-1-*tert*-butylimidazolyl),[10] are all diamagnetic Fe-polycarbonyl complexes, and therefore constitute a unique set for comparison of their Fe–B bonding (Chart 4.1). Compared with [(DPB)Fe(CO)$_2$][K(benzo-15-c-5)$_2$]$_2$, (DPB)Fe(CO)$_3$ has a longer Fe–B distance (Figure 4.7) and a less pyramidalized B center. These data indicate stronger Fe–B bonding[11] in [(DPB)Fe(CO)$_2$][K(benzo-15-c-5)$_2$]$_2$ compared with (DPB)Fe(CO)$_3$, which may be rationalized by the dianionic charge and more electron-releasing Fe center in the former.

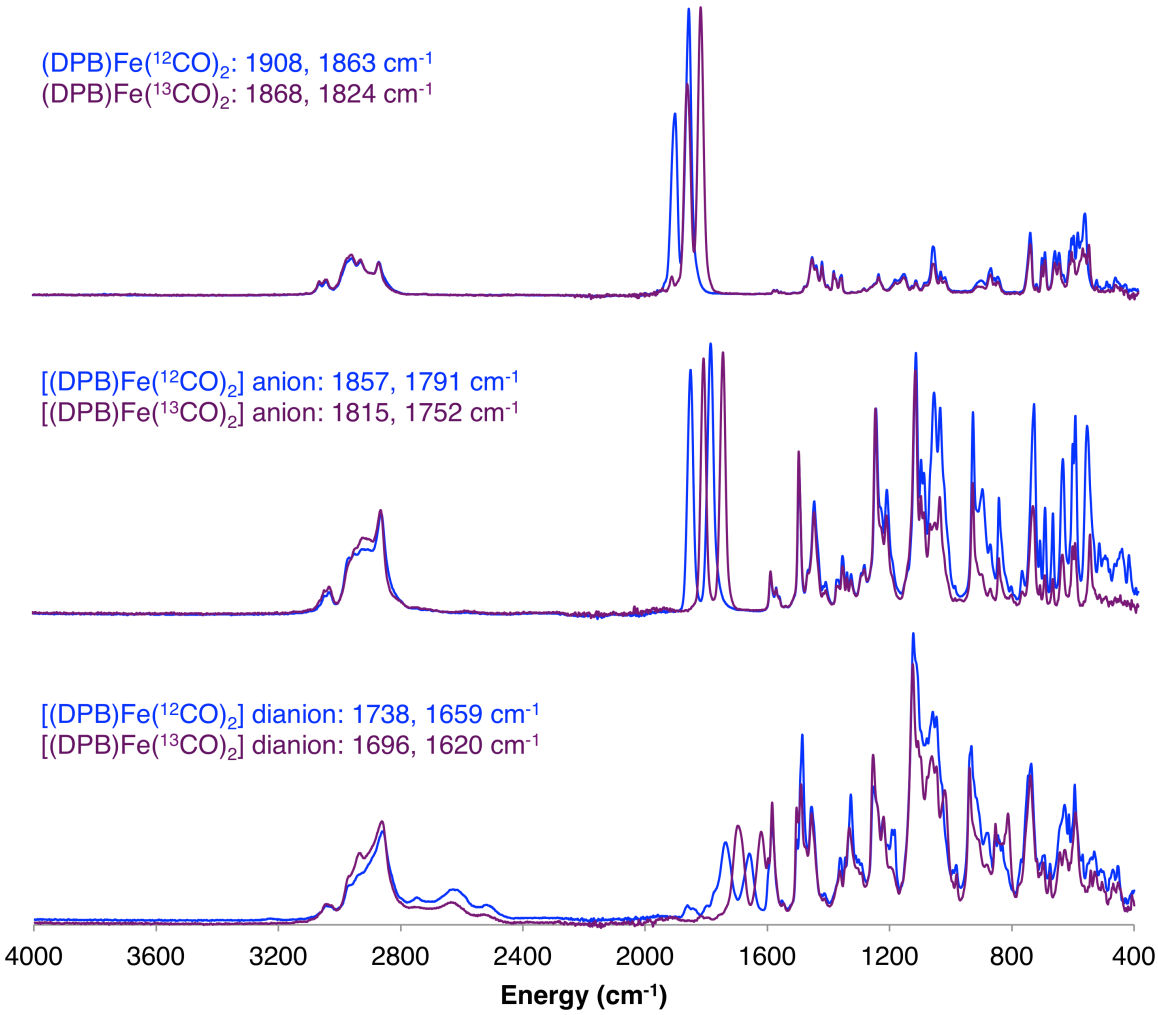

Figure 4.6 IR spectra of $(DPB)Fe(CO)_2$ (top), $[(DPB)Fe(CO)_2][K(benzo\text{-}15\text{-}c\text{-}5)_2]$ (middle), and $[(DPB)Fe(CO)_2][K(benzo\text{-}15\text{-}c\text{-}5)_2]_2$ (bottom) recorded as thin films by evaporation of C_6D_6 (top) or THF (middle and bottom) solutions.

Both $(DPB)Fe(CO)_3$ and $(\kappa^4\text{-}B(mim^{tBu})_3)Fe(CO)_2$ are nominally isoelectronic ML_5Z complexes[12] and their Fe centers could therefore be considered divalent (assuming strong Fe–B bonding) or zerovalent (assuming weak Fe–B bonding).[11a, 13] The most striking contrast between $(DPB)Fe(CO)_3$ and $(\kappa^4\text{-}B(mim^{tBu})_3)Fe(CO)_2$ is that the Fe–B distance in $(\kappa^4\text{-}B(mim^{tBu})_3)Fe(CO)_2$ is 2.108(6) Å—ca. 0.4 Å shorter than that in $(DPB)Fe(CO)_3$. In

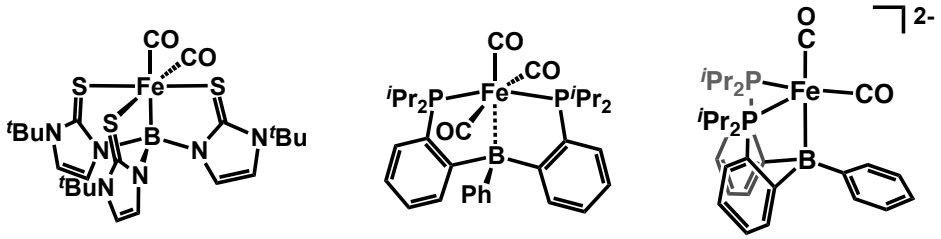

Chart 4.1 Comparison of key structural features of selected Fe-B complexes.

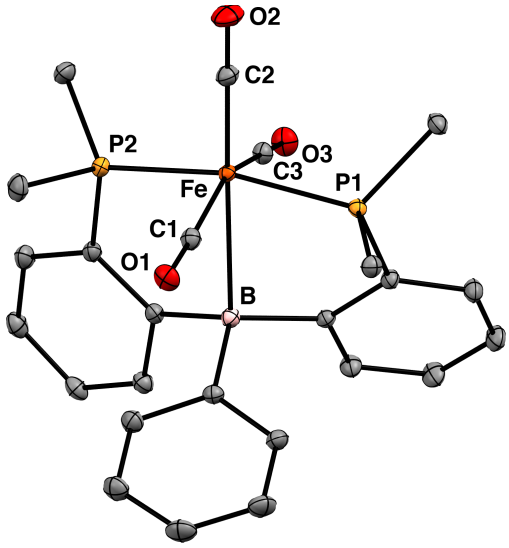

Figure 4.7 Displacement ellipsoid (50%) representation of (DPB)Fe(CO)$_3$. P^{i}Pr$_2$ groups are truncated and H atoms are omitted for clarity. Selected distances and angles: Fe–B = 2.5263(6) Å; Fe–P1 = 2.2349(2) Å; Fe–P2 = 2.2302(2) Å; Fe–C1 = 1.7738(6) Å; Fe–C2 = 1.7844(5) Å; Fe–C3 = 1.7972(6) Å; ∠(P1–Fe–P2) = 164.82(1)˚; ∠(C1–Fe–C3) = 153.38(2)˚; Σ∠(C–B–C) = 342˚.

addition, the B center in (κ^4-B(mim$^{t\text{Bu}}$)$_3$)Fe(CO)$_2$ is fully pyramidalized (Σ∠(N–B–N) = 327˚). I attribute these differences primarily to the greater Lewis acidity of the B center of (κ^4-B(mim$^{t\text{Bu}}$)$_3$)Fe(CO)$_2$ (though the electron richness of the Fe centers may also be a contributing factor). The B atom in (DPB)Fe(CO)$_3$ has three C substituents and can

conjugate into the π system of the phenyl group; in contrast, the B atom in (κ^4-B(mim$^{t\text{Bu}}$)$_3$)Fe(CO)$_2$ has three electronegative N substituents that contribute little π electron density to B owing to their orthogonal orientation with respect to B. As such, the Lewis acidity of the B atom in (κ^4-B(mim$^{t\text{Bu}}$)$_3$)Fe(CO)$_2$ is expected to be much greater than that of the B atom in (DPB)Fe(CO)$_3$. Accordingly, while the Fe center in (κ^4-B(mim$^{t\text{Bu}}$)$_3$)Fe(CO)$_2$ may be formulated as divalent, the Fe center in (DPB)Fe(CO)$_3$ is more appropriately considered zerovalent, akin to Fe(CO)$_5$.

4.3 Synthesis and hydrogenation of an Fe dicarbyne

The low C–O stretching frequencies of [(DPB)Fe(CO)$_2$][K(benzo-15-c-5)$_2$]$_2$ suggest that the O atoms could have nucleophilic character. In situ reduction of (DPB)Fe(CO)$_2$ with excess K and addition to a -78 °C solution of 2.2 equiv TMSOTf results in silylation of both O atoms to give the dicarbyne (DPB)Fe(COSiMe$_3$)$_2$ (Scheme 4.4). Since few Fe

Scheme 4.4 Preparation of (DPB)Fe(COSiMe$_3$)$_2$

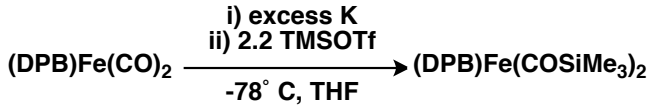

carbynes have been reported[14] and (DPB)Fe(COSiMe$_3$)$_2$ is the first example of an Fe dicarbyne, its molecular and electronic structures are of particular interest. Although (DPB)Fe(COSiMe$_3$)$_2$ reconverts to (DPB)Fe(CO)$_2$ in solution over several days, the rate of this decomposition is sufficiently slow to allow for solid- and solution-state characterization.

Single crystals of (DPB)Fe($COSiMe_3$)$_2$ contain two molecules in the asymmetric unit and were studied by XRD analysis (Figure 4.8). The very short Fe–C distances of 1.639

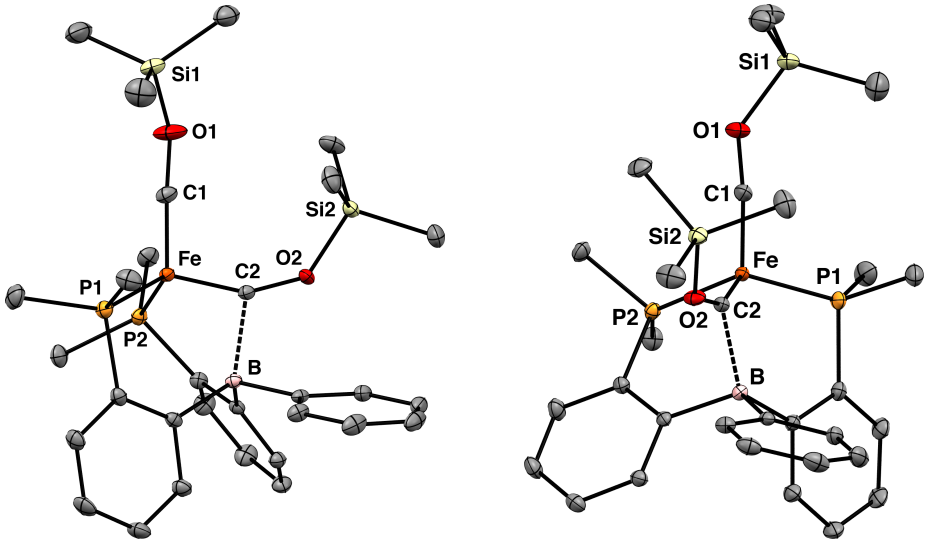

Figure 4.8 Displacement ellipsoid (50%) representations of one of the two crystallographically-independent molecules of (DPB)Fe($COSiMe_3$)$_2$ from different perspectives. P^{i}Pr$_2$ groups are truncated and H atoms are omitted for clarity. Selected distances and angles are given in Table 4.2.

Å (Fe–C1 avg.) and 1.676 Å (Fe–C2 avg.) are similar to the Fe–($COSiMe_3$) distance of 1.671(2) Å reported for (SiP_3)Fe($COSiMe_3$)[14b] and indicate Fe–C multiple-bond character for both carbyne ligands. The C2 carbyne ligand is distinguished by a long yet non-negligible B–C2 interaction (1.86 Å (avg.)) and a contracted ∠(Fe–C2–O2) of 151° (avg.), compared with 171° (avg.) for ∠(Fe–C1–O1). In solution, the two carbyne ligands in ^{13}C-labeled samples are further differentiated by their ^{13}C NMR resonances at 230.2 ppm (d, $^2J_{CC}$ = 3.2 Hz) and 261.9 ppm (dt, $^2J_{CP}$ = 9.0 Hz, $^2J_{CC}$ = 3.2 Hz), assigned to C1 and C2, respectively, on the basis of DFT calculations. For reference, the chemical shift corresponding to the carbyne ligand in (SiP_3)Fe($^{13}COSiMe_3$) is 250.3 ppm (q, $^2J_{CP}$).[15] The

Table 4.2 Selected bond lengths (Å) and angles (°) of (DPB)Fe($COSiMe_3$)$_2$ and of its optimized geometry (Gaussian09, M06L/6-311+g(d)).

	Mol. 1	Mol. 2	Calc.
Fe-C1	1.6430(12)	1.6357(11)	1.642
Fe-C2	1.6759(10)	1.6764(11)	1.682
Fe-B	2.5931(12)	2.5635(12)	2.557
Fe-P1	2.2238(4)	2.2135(4)	2.219
Fe-P2	2.2428(4)	2.2370(4)	2.238
C1-O1	1.2847(14)	1.2829(14)	1.284
C2-O2	1.3046(13)	1.3110(13)	1.297
Fe-C1-O1	173.93(10)	168.17(11)	170°
Fe-C2-O2	151.31(8)	151.48(8)	151°
C1-O1-Si1	138.16(8)	143.28(10)	133°
C2-O2-Si2	132.58(7)	129.31(8)	127°
B-C2	1.8619(16)	1.8485(15)	1.823
B-C_{aryl} avg.	1.65	1.65	1.64
Σ∠(C-B-C)	328°	328°	330°

B atom is pyramidalized in both the solution and solid states as indicated by the low Σ∠(C–B–C) = 328° (avg.) and upfield-shifted ^{11}B NMR signal (-6.4 ppm). In addition, the isomer shift in the Mössbauer spectrum of (DPB)Fe($COSiMe_3$)$_2$ (Figure 4.9) is substantially more negative than that of (DPB)Fe(CO)$_2$ ($\Delta\delta$ = -0.287 mm s^{-1}) which suggests a greater degree of covalent bonding in (DPB)Fe($COSiMe_3$)$_2$. Taken together, these XRD, NMR, and Mössbauer data indicate that extensive Fe–C multiple bonding and additional C2–B bonding must be considered when assessing the valence bonding in (DPB)Fe($COSiMe_3$)$_2$.

In order to account for these features, I propose several possible resonance structures for (DPB)Fe($COSiMe_3$)$_2$ (Figure 4.10). Lewis structures **A**, **B**, and **C** have two dicarbyne

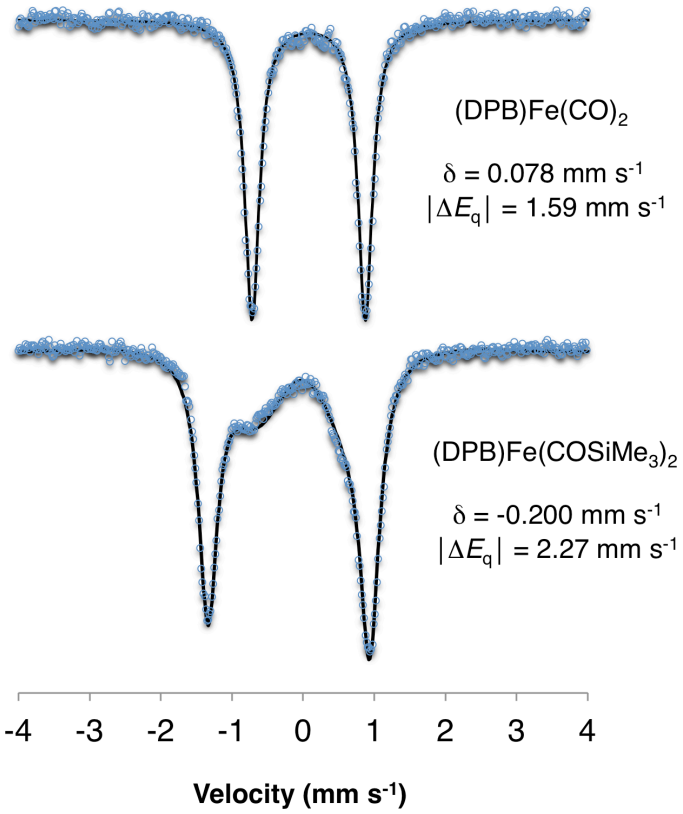

Figure 4.9 Mössbauer spectra of $(DPB)Fe(CO)_2$ and $(DPB)Fe(COSiMe_3)_2$ recorded at 5 K. The spectrum of $(DPB)Fe(COSiMe_3)_2$ contains multiple minor impurities arising from contamination with $(DPB)Fe(CO)_2$ as well as additional impurities resulting form exposure to air during sample handling.

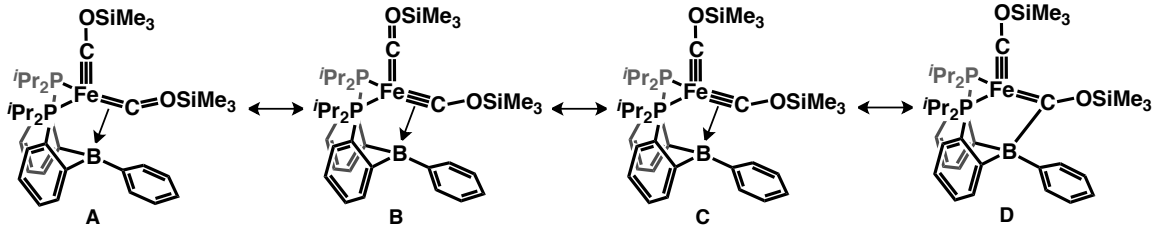

Figure 4.10 Possible resonance structures of $(DPB)Fe(COSiMe_3)_2$.

ligands (by the IUPAC definition),[16] one of which exhibits dative bonding to the pendant borane. Structures **A** and **B** emphasize that a d-block metal does not have enough orbitals

to form three independent π bonds[17] (as in structure **C**), although DFT calculations show the presence of four orbitals with significant Fe–C π bonding character (vide infra). Structure **C** may be a valid resonance contributor if either three-center hyperbonding[18] or mixing with Fe 4p orbitals is invoked,[11b] and it therefore should not be discarded without an in-depth theoretical study that is beyond the scope of this work. (A crude MO diagram for a hypothetical linear dicarbyne complex (Figure 4.11) shows a limiting case in which

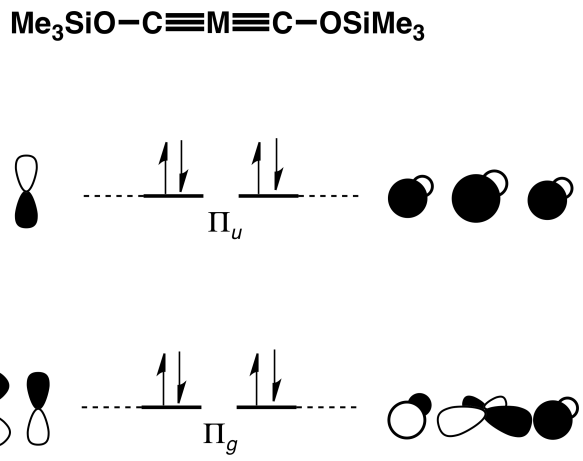

Figure 4.11 HOMOs of a hypothetical linear dicarbyne complex of $D_{\infty h}$ symmetry.

metal $4p_x$ and $4p_y$ orbital participation can increase the overall number of independent M–C π bonds from two to four.) Thus, for the purposes of this chapter, I do not distinguish between resonance structures **A**, **B**, and **C** because they differ only in the linear independence of the atomic orbitals that constitute the Fe–C π bonding orbitals.

The most important difference between the depiction of the bonding in resonance form **D** and that in resonance forms **A**, **B**, and **C** is that the boron atom in **D** has a normal covalent bond[19] to one of the carbynes, thereby rendering that fragment a zwitterionic

Fischer-type carbene with a formal negative charge on the boron atom. A boratocarbene ligand as depicted in **D** would be expected to display four nearly equivalent B–C bonds since each carbon substituent would have sp^2 hybridization; however, the B–C2 distance is ~0.2 Å (avg.) longer than the other B–C_{sp2} distances (1.65 Å (avg.)). In addition, the average Fe–C distance of all structurally-characterized O-substituted Fischer-type Fe carbenes is 1.90 Å,[20] which is >0.2 Å (avg.) longer than the Fe–C2 distance observed in (DPB)Fe($COSiMe_3$)$_2$. Given these structural metrics, resonance contributors **A**, **B**, and **C** should be weighted more heavily than **D**.

In order to gain further insight into the bonding in (DPB)Fe($COSiMe_3$)$_2$, DFT calculations were performed on (DPB)Fe($COSiMe_3$)$_2$ and a hypothetical, simplified model, (PMe_3)$_2$Fe($COSiH_3$)$_2$. The five highest filled MOs of (PMe_3)$_2$Fe($COSiH_3$)$_2$ (Figure 4.12) include one essentially non-bonding orbital with some degree of Fe–P backbonding (HOMO) as well as four highly covalent orbitals with significant Fe–C π bonding (HOMO-1 through HOMO-4). The diagram in Figure 4.12b shows how the MOs in Figure 4.12a may be crudely decomposed into atomic orbitals, though it should be emphasized that additional mixing with 4s and 4p orbitals is likely. Given these considerations, (PMe_3)$_2$Fe($COSiH_3$)$_2$ may be regarded as isoelectronic to known compounds of the form (PR_3)$_2$Fe(NO)$_2$.[21]

The filled MOs of (DPB)Fe($COSiMe_3$)$_2$ with significant Fe 3d character are shown in Figure 4.13. Although these MOs are more complex than those of (PMe_3)$_2$Fe($COSiH_3$)$_2$ owing to the lower overall symmetry of (DPB)Fe($COSiMe_3$)$_2$ as well as mixing with aryl π orbitals, the shapes and ordering of the orbitals for the two molecules correlate with good fidelity. For example, the Fe–C π bonding in the HOMO-2 of (PMe_3)$_2$Fe($COSiH_3$)$_2$

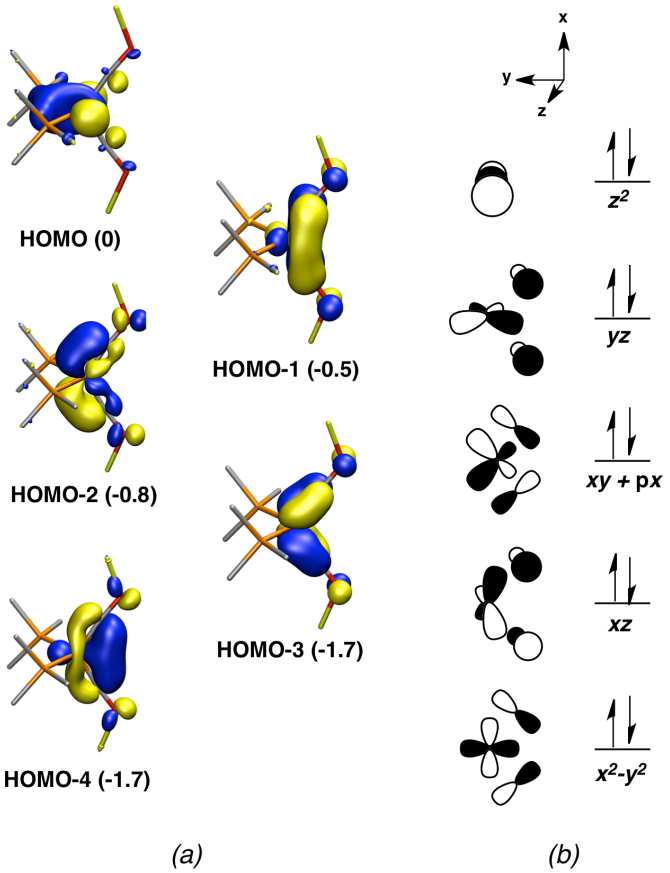

Figure 4.12 (a) Calculated MOs of $(PMe_3)_2Fe(COSiH_3)_2$ that have substantial Fe 3d character (Gaussian09, M06L/6-311+g(d), C_{2v} symmetry). (b) Scheme showing Fe and C atomic orbital contributions to the MOs.

is also the dominant feature of the HOMO-2 of $(DPB)Fe(COSiMe_3)_2$ with some additional mixing with B in the latter. Mixing of B pz into an Fe–C π bonding orbital is also observed for the HOMO-10 of $(DPB)Fe(COSiMe_3)_2$. Thus, these calculations suggest that the electronic structures of $(DPB)Fe(COSiMe_3)_2$ and $(PMe_3)_2Fe(COSiH_3)_2$ are largely analogous and that $(DPB)Fe(COSiMe_3)_2$ may be considered a perturbation of $(PMe_3)_2Fe(COSiH_3)_2$.

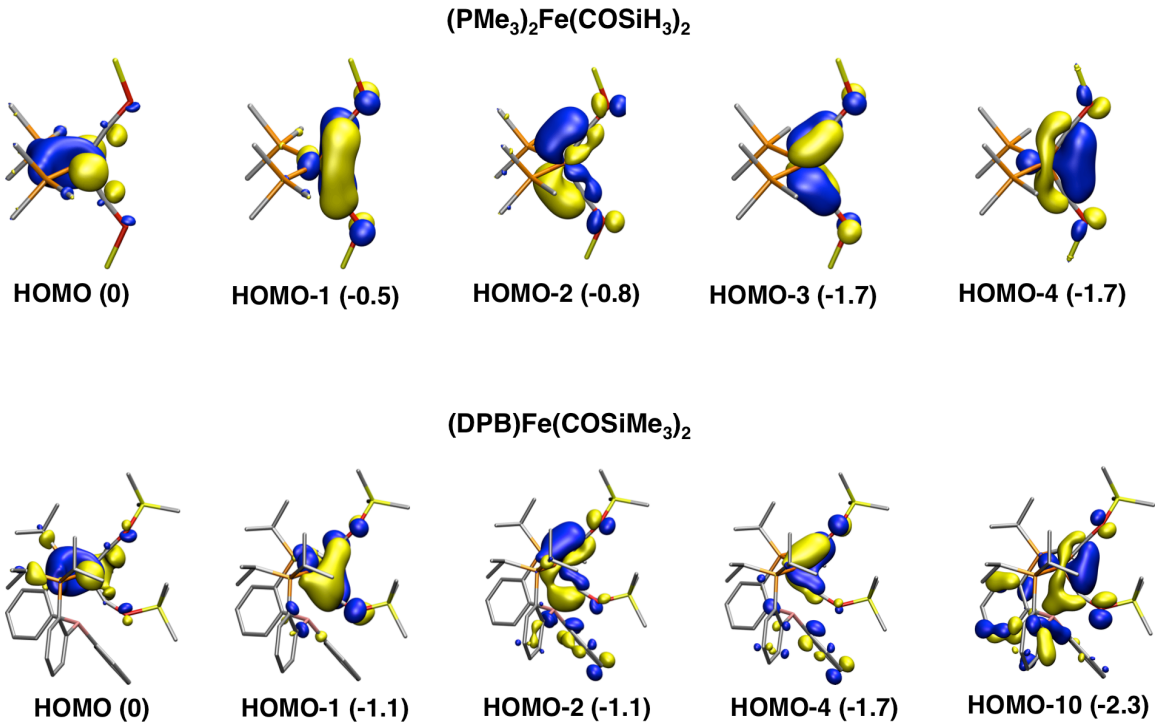

Figure 4.13 Calculated MOs with substantial Fe 3d character in $(PMe_3)_2Fe(COSiH_3)_2$ (top, reproduced from Figure 4.12) and $(DPB)Fe(COSiMe_3)_2$ (bottom). Calculations performed using Gaussian09 with the M06L functional and 6-311+g(d) basis set.

In order to calibrate the strength of the B–C2 interaction in $(DPB)Fe(COSiMe_3)_2$, I sought to calculate the minimum geometry of a related compound that would be expected to have a negligible B–L bond. The optimized geometry of $(DPB)Fe(NO)_2$ (Figure 4.14) has a long B–N2 distance of nearly 3 Å and a nearly planar B center, both of which suggest a negligible interaction. The B–N2 interaction in $(DPB)Fe(NO)_2$ is weaker than the B–C2 interaction in $(DPB)Fe(COSiMe_3)_2$ because the Fe–N π bonding orbitals in $(DPB)Fe(NO)_2$ are lower in energy that the Fe–C π bonding orbitals in $(DPB)Fe(COSiMe_3)_2$ and therefore do not match as well with the empty B p_z orbital.

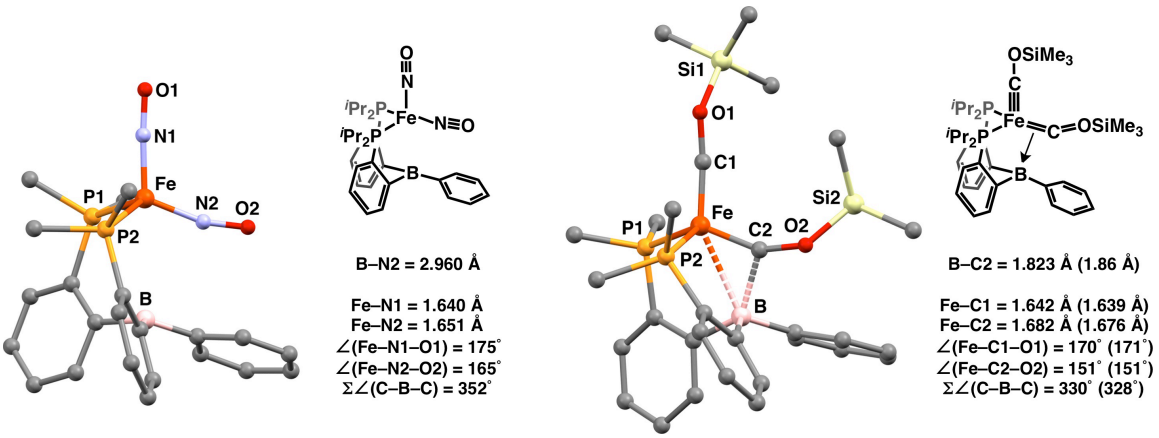

Figure 4.14 Optimized structures of (DPB)Fe(NO)$_2$ (left) and (DPB)Fe(COSiMe$_3$)$_2$ (right). Calculations performed using Gaussian09 using the M06L functional and the 6-311+g(d) basis set. All starting coordinates were generated by modifying the solid-state structure of (DPB)Fe(COSiMe$_3$)$_2$.

These comparisons further support the description of the B–C2 bond in (DPB)Fe(COSiMe$_3$)$_2$ as a weak but important interaction.

The stability of the dicarbyne form of (DPB)Fe(COSiMe$_3$)$_2$ with respect to C–C coupling is in marked contrast to the related dmpe-ligated V, Nb, and Ta dicarbonyls which yield C–C-coupled η^2-alkyne complexes upon reductive disilylation (vide supra).[2] Nevertheless, facile C–C coupling is achieved upon RT addition of 1 atm H$_2$ to solutions of (DPB)Fe(COSiMe$_3$)$_2$ which results in liberation of the olefin *Z*-1,2-bis(trimethylsiloxy)ethylene ("*Z*-BTSE") in 43% yield (avg. of three runs; Scheme 4.5).

Scheme 4.5 Hydrogenation of (DPB)Fe(COSiMe$_3$)$_2$

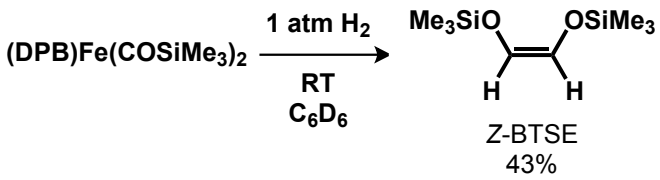

The hydrogenation of (DPB)Fe($COSiMe_3$)$_2$ is highly stereoselective, forming *Z*-BTSE without any detected *E*-BTSE. Performing the hydrogenation with ^{13}C-labeled (DPB)Fe($COSiMe_3$)$_2$ gives exclusively ^{13}C-labeled *Z*-BTSE, establishing that (DPB)Fe($COSiMe_3$)$_2$ is the source of the C–C coupled product. No other ^{13}C-labeled products have been observed, and I have not yet been able to fully characterize the resulting paramagnetic Fe-containing species.

A few Fe systems have been reported to promote reductive CO coupling,[22] though the release of an olefin by a hydrogenative CO reductive coupling pathway has not been previously reported for Fe. The hydrogenation of the aforementioned CO-derived [(dmpe)$_2$M(η^2-alkyne)]X complexes proceeds either at elevated H_2 pressures (~8 atm H_2 for the V system)[2c] or with the aid of a hydrogenation catalyst (1 atm H_2 and 5% Pd/C for the Ta system).[3] By comparison, hydrogenation of (DPB)Fe($COSiMe_3$)$_2$ occurs within minutes at 1 atm H_2.

A number of fascinating questions remain about the details of C–C coupling in the present system. Why do the carbyne ligands in (DPB)Fe($COSiMe_3$)$_2$ not spontaneously couple to give an alkyne complex? What (if any) role does the borane play in the stability of the dicarbyne form of (DPB)Fe($COSiMe_3$)$_2$ or in its hydrogenation? Does C–C coupling proceed after one or more hydrogenation steps or is C–C coupling promoted simply by initial H_2 binding? Future experimental and theoretical studies should be directed toward addressing these questions.

4.4 Summary

In this chapter, I described the conversion of an Fe dicarbonyl to an Fe dicarbyne that undergoes hydrogenative release of an *E*-olefin. The complex (DPB)Fe($COSiMe_3$)$_2$ is the first Fe dicarbyne and the first dicarbyne of any metal that has been isolated as an intermediate in a reductive CO coupling pathway. Like the Fe aminoimide intermediate in (DPB)Fe-mediated N_2 reduction, this dicarbyne features extensive Fe–L multiple bonding. This commonality highlights the potential role for highly covalent intermediates[23] in synthetic and biological Fe-mediated nitrogen and carbon fixation.

4.5 Experimental

*General Considerations***.** All manipulations were carried out using standard Schlenk or glovebox techniques under an atmosphere of dinitrogen. Solvents were degassed and dried by sparging with N_2 gas and passage through an activated alumina column. Deuterated solvents were purchased from Cambridge Isotopes Laboratories, Inc. and were degassed and stored over activated 3 Å molecular sieves prior to use. Reagents were purchased from commercial vendors and used without further purification unless otherwise noted. [(DPB)Fe]$_2$(μ-1,2-N_2) was synthesized according to a literature procedure.[7b] Elemental analyses were performed by Midwest Microlab (Indianapolis, IN) and Robertson Microlit Laboratories (Ledgewood, NJ).

Spectroscopic measurements. ^{1}H, ^{13}C, ^{31}P, and ^{11}B NMR spectra were collected at room temperature on a Varian 400 MHz spectrometer. ^{1}H and ^{13}C spectra were referenced to residual solvent resonances. ^{31}P spectra were referenced to external 85% phosphoric acid (δ = 0 ppm). ^{11}B spectra were referenced to BF_3•Et_2O (0 ppm). UV-vis measurements

were performed with a Cary 50 instrument with Cary WinUV software. IR measurements were obtained as thin films formed by evaporation using a Bruker Alpha Platinum ATR spectrometer with OPUS software.

X-ray Crystallography. X-ray diffraction studies were carried out at the Caltech Division of Chemistry and Chemical Engineering X-ray Crystallography Facility on a Bruker three-circle SMART diffractometer with a SMART 1K CCD detector. Data were collected at 100K using Mo Kα radiation (λ = 0.71073 Å). Structures were solved by direct or Patterson methods using SHELXS and refined against F^2 on all data by full-matrix least squares with SHELXL-97.[24] All non-hydrogen atoms were refined anisotropically. All hydrogen atoms were placed at geometrically calculated positions and refined using a riding model. The isotropic displacement parameters of all hydrogen atoms were fixed at 1.2 (1.5 for methyl groups) times the Ueq of the atoms to which they are bonded.

Computational Details. All calculations were performed using the Gaussian09 suite.[25] The geometry optimizations were done without any symmetry restraints using the B3LYP hybrid functional. The 6-311+g(d) basis set was used for all atoms. Minimized structures were verified with frequency calculations. The starting coordinates for the metal and ligand were taken from the crystal structures.

(DPB)Fe(CO)$_2$: A red-brown solution of [(DPB)Fe]$_2$(μ-1,2-N$_2$) (524.2 mg, 0.482 mmol) in THF (20 mL) was subjected to three freeze-pump-thaw cycles and subsequently exposed to 1 atm CO. The solution was vigorously stirred until the color changed to red-orange (about 15 min.). Consumption of [(DPB)Fe]$_2$(μ-1,2-N$_2$) was monitored by ^{1}H

NMR spectroscopy of aliquots. Extended reaction times result in overcarbonylation to give (DPB)Fe(CO)$_3$, so the reaction should be monitored diligently. After complete consumption of (DPB)Fe(CO)$_2$, vacuum was applied to the solution giving a dark red residue. Residual THF was removed by addition of Et_2O (5 mL) and drying *in vacuo*. The resulting red solids were washed with cold Et_2O (5 x 2 mL) to give (DPB)Fe(CO)$_2$ (420.0 mg, 0.717 mmol, 74%). An additional batch of (DPB)Fe(CO)$_2$ may be obtained by concentration of the Et2O washings into HMSDO (51.9 mg, 0.0886 mmol, 9%). Single crystals suitable for X-ray diffraction may be obtained by concentration of a saturated Et_2O solution. ^{1}H NMR (400 MHz, C_6D_6) δ 8.63 (d, J = 7.7 Hz, 1H), 7.42 (d, J = 7.4 Hz, 1H), 7.32 (t, J = 7.4 Hz, 2H), 7.26 (t, J = 6.7 Hz, 1H), 7.16-7.00 (m, 6H), 6.89 (t, J = 7.2 Hz, 1H), 6.42 (d, J = 7.3 Hz, 1H), 2.44 (dh, J = 14.6, 7.3 Hz, 2H), 1.50-1.40 (m, 4H), 1.28 (dd, J = 14.9, 6.9 Hz, 3H), 1.27-1.19 (m, 4H), 1.10 (dd, J = 15.3, 6.9 Hz, 3H), 0.95 (dd, J = 19.5, 7.6 Hz, 3H), 0.88 (dd, J = 11.6, 7.2 Hz, 3H), 0.65 (dd, J = 13.4, 7.2 Hz, 3H), 0.36 (dd, J = 16.4, 7.5 Hz, 3H). ^{13}C NMR (101 MHz, C_6D_6) δ 220.92 (dd, J = 23.3, 17.6 Hz), 214.42-213.63 (m), 165.11, 151.59, 146.18, 146.05, 141.60, 141.22, 136.75, 136.59, 135.71, 131.04, 129.64, 129.03, 126.37, 126.29, 125.22, 116.95, 98.52, 98.36, 30.05 (d, J = 18.1 Hz), 28.60 (dd, J = 28.4, 12.7 Hz), 26.74 (d, J = 16.3 Hz), 22.14, 22.10, 20.82, 19.34, 18.70, 18.17, 18.13, 17.79. ^{31}P NMR (162 MHz, C_6D_6) δ 90.64 (d, J = 65.3 Hz), 54.62 (d, J = 65.3 Hz). ^{11}B NMR (128 MHz, C_6D_6) δ 11.47. UV/vis (toluene, nm {M^{-1} cm^{-1}}): 482 {sh, 2000}. Elemental analysis for $C_{32}H_{41}BFeO_2P_2$: calc. C 65.65, H 7.05, N 0; found C 65.48, H 7.14, N <0.02. IR of (DPB)Fe(^{12}CO)$_2$ (cm^{-1}): 1908, 1863. IR of (DPB)Fe(^{13}CO)$_2$ (cm^{-1}): 1868, 1824.

(DPB)Fe(CO)$_3$: A J. Young NMR tube was charged with (DPB)Fe(CO)$_2$ (22.0 mg, 0.0375 mmol) and 0.7 mL C_6D_6 under N_2. After three freeze-pump-thaw cycles, 1 atm CO was added and the NMR tube was rotated at RT for 1 hr. The solution changed from red-orange to very pale yellow and NMR and IR spectroscopies showed quantitative conversion to (DPB)Fe(CO)$_2$. Solutions and colorless powders of (DPB)Fe(CO)$_3$ slowly reconvert to (DPB)Fe(CO)$_2$ under 1 atm N_2 or vacuum. As such, (DPB)Fe(CO)$_3$ is best studied in solution under 1 atm CO. Single crystals suitable for X-ray diffraction may be obtained by concentration of an Et_2O solution (with a small contamination of red-orange crystals of (DPB)Fe(CO)$_2$). ^{1}H NMR (400 MHz, C_6D_6) δ 8.03 (d, J = 7.7 Hz, 2H), 7.26-6.91 (m, 9H), 6.88-6.76 (m, 2H), 2.73 (m, 2H), 2.38 (m, 2H), 1.25 (m, 12H), 1.06 (m, 12H). ^{13}C NMR (101 MHz, C_6D_6) δ 217.61 (t, J = 26.2 Hz), 215.83 (t, J = 30.8 Hz), 213.58 (t, J = 10.7 Hz), 166.72, 157.76, 141.94-139.56 (m), 135.84, 132.62 (t, J = 8.6 Hz), 129.32, 128.76, 126.60, 125.65, 123.73, 31.40 (t, J = 11.5 Hz), 26.70-25.98 (m), 20.41, 20.14, 18.88, 16.93. ^{31}P NMR (162 MHz, C_6D_6) δ 87.51. ^{11}B NMR (128 MHz, C_6D_6) δ 20.25. Elemental analysis data were not obtained due to the instability of (DPB)Fe(CO)$_3$ with respect to CO loss when not stored under 1 atm CO. IR of (DPB)Fe(^{12}CO)$_3$ (cm^{-1}): 2002 (w), 1932 (vs).

(DPB-H)Fe(H)(CO)$_2$: A J. Young NMR tube was charged with (DPB)Fe(CO)$_2$ (24.3 mg, 0.0415 mmol) and 0.7 mL C_6D_6 under N_2. After three freeze-pump-thaw cycles, 1 atm H_2 was added and the NMR tube was rotated at RT for 1 hr. The solution changed from red-orange to very pale green and NMR and IR spectroscopies showed quantitative conversion to (DPB-H)Fe(H)(CO)$_2$. Solvent was removed in vacuo and the resulting

colorless solids were extracted into n-pentane. Recrystallization by evaporation of this solution into HMDSO afforded large, polychroic (magenta, teal, green) single crystals suitable for X-ray diffraction (23.0 mg, 0.0391 mmol, 94%). ^{1}H NMR (400 MHz, C_6D_6) δ 7.76 (d, J = 6.9 Hz, 2H), 7.12 (m, 9H), 7.00 (m, 3H), 2.40 (m, 2H), 2.13 (m, 2H), 1.04 (m, 18H), 0.88 (m, 6H), -7.73 (td, J = 54.4, 7.6 Hz, 1H), -17.00 (br m, 1H). ^{13}C NMR (101 MHz, C_6D_6) δ 217.38, 214.80, 162.85, 155.47, 139.49 (t, J = 25.8 Hz), 134.14, 132.83 (t, J = 7.3 Hz), 128.60, 128.45, 126.79, 125.42, 124.59, 30.55 (t, J = 8.3 Hz), 28.15 (t, J = 16.2 Hz), 18.94, 18.61, 18.40, 18.35. ^{31}P NMR (162 MHz, C_6D_6) δ 92.97. ^{11}B NMR (128 MHz, C_6D_6) δ 11.80. UV/vis (toluene, nm {M^{-1} cm^{-1}}): 332 {sh, 900}. Elemental analysis for $C_{32}H_{43}BFeO_2P_2$: calc. C 65.33, H 7.37, N 0; found C 65.03, H 7.26, N <0.02. IR of (DPB–H)Fe(H)($^{13}CO)_2$ (cm^{-1}): 2080 (br, Fe–H–B), 1815 (s, C–O asym.), 1752 (s, C–O sym.).

[(DPB)Fe(CO)$_2$][K(benzo-15-c-5)$_2$]: A red-orange solution of (DPB)Fe(CO)$_2$ (28.6 mg, 0.0488 mmol) in THF (3 mL) was stirred over excess K until the solution turned inky yellow (<5 min.). The solution was decanted from the K onto benzo-15-crown-5 (28.8 mg, 0.107 mmol). Solvent was removed in vacuo to provide a brown residue that was washed with Et_2O (3 x 1 mL) and C_6H_6 (3 x 1 mL). Diffusion of n-pentane into a THF solution afforded single crystals of the title compound (53.1 mg, 0.0457 mmol, 94%). ^{1}H NMR (300 MHz, THF) δ 8.73, 8.58, 8.17, 5.70, 5.54, 3.16, 2.75, -0.04 (v br). Solution magnetic moment by Evans method (THF, RT): 1.7 μ_B. Elemental analysis for $C_{60}H_{81}BFeKO_{12}P_2$: calc. C 62.02, H 7.03, N 0; found C 61.71, H 7.15, N <0.02. IR of

[(DPB)Fe(^{12}CO)$_2$][K(benzo-15-c-5)$_2$] (cm^{-1}): 1857, 1791. IR of [(DPB)Fe(^{12}CO)$_2$][K(benzo-15-c-5)$_2$]: 1815, 1752.

[(DPB)Fe(CO)$_2$][K(benzo-15-c-5)$_2$]$_2$: Due to its extremely high air and moisture sensitivity, ((DPB)Fe(CO)$_2$)(K(THF)$_x$)$_2$ is best generated in situ (by stirring a THF solution of (DPB)Fe(CO)$_2$ over excess K for 6 hr.) and used immediately. A cation-encapsulated species was generating for NMR, IR, and XRD characterization according to the following procedure. A red-orange solution of (DPB)Fe(CO)$_2$ (12.9 mg, 0.0219 mmol) in THF-d_8 (0.7 mL) was stirred over K for 6 hr. The solution initially changed to inky yellow and subsequently to dark red-brown. This solution was added to benzo-15-crown-5 (24.7 mg, 0.0921 mmol) and transferred to a J. Young tube for NMR characterization. Vapor diffusion of Et$_2$O into this THF solution afforded dark solids from which a single crystal was selected for XRD analysis. ^{1}H NMR (300 MHz, THF-d_8) δ 7.14-6.99 (m, 4H), 6.80 (m, 18H), 6.60 (m, 4H), 6.50 (t, J = 7.2 Hz, 2H), 6.36 (t, J = 5.8 Hz, 1H), 3.91 (br s, 16H), 3.72 (br s, 16H), 3.63 (br s, 32H), 2.28 (br s, 2H), 2.03 (br s, 2H), 1.22 (br s, 6H), 1.06 (br s, 6H), 0.90 (br s, 6H), 0.77 (br s, 6H). ^{11}B NMR (160 MHz, THF-d_8) δ 14.05. ^{13}C NMR (126 MHz, THF-d_8) δ 244.70 (t, J = 10.5 Hz), 244.06 (t, J = 17.5 Hz), 183.05, 159.77, 154.09, 141.12, 137.41, 130.28, 128.90 (t, J = 23.8 Hz), 126.37 (d, J = 47.1 Hz), 124.41, 122.43, 118.90 (d, J = 44.0 Hz), 75.29, 74.70, 73.80, 73.32, 37.83 (d, J = 20.7 Hz), 35.30-34.12 (m), 30.83, 26.79-25.95 (m), 25.95-25.03 (m), 24.03. ^{31}P NMR (121 MHz, THF-d_8) δ 102.43 (dd in ^{13}C-labeled sample; s in ^{12}C-labeled sample). IR of [(DPB)Fe(^{12}CO)$_2$][K(benzo-15-c-5)$_2$]$_2$ (cm^{-1}): 1738, 1659. IR of [(DPB)Fe(^{13}CO)$_2$][K(benzo-15-c-5)$_2$]$_2$ (cm^{-1}): 1696, 1620.

(DPB)Fe(COSiMe$_3$)$_2$: A red-orange solution of (DPB)Fe(CO)$_2$ (20.8 mg, 0.0354 mmol) in THF (2 mL) was stirred over K for 6 hr. The solution initially changed to inky yellow and subsequently to dark red-brown. The solution was cooled to -78 ˚C and then added dropwise to a precooled (-78 ˚C) 0.4 M toluene solution of TMSOTf (0.185 mL, 0.0743 mmol). The cold solution immediately turned to a lighter brown. After stirring for 15 min. at -78 ˚C, the solution was brought to RT and solvent was removed in vacuo. Residual THF and toluene was removed by addition of pentane (2 mL) followed by drying in vacuo. The resulting solids were dissolved in n-pentane (2 mL) and filtered through Celite to afford a brown solution. Removal of the solvent in vacuo afforded brown solids (18.0 mg) with compositions that are typically 85-90% (DPB)Fe(COSiMe$_3$)$_2$ and 10-15% (DPB)Fe(CO)$_2$ as judged by ^{1}H and ^{31}P NMR spectroscopy. In solution, (DPB)Fe(COSiMe$_3$)$_2$ converts to (DPB)Fe(CO)$_2$ over several days; as such, samples of (DPB)Fe(COSiMe$_3$)$_2$ are best prepared immediately before use. Brown single crystals of (DPB)Fe(COSiMe$_3$)$_2$ (contaminated by single crystals of (DPB)Fe(CO)$_2$) may be obtained by evaporation of a concentrated SiMe$_4$ solution into HMDSO. ^{1}H NMR (400 MHz, C$_6$D$_6$) δ 7.90 (d, J = 7.8 Hz, 2H), 7.51 (d, J = 6.9 Hz, 2H), 7.46-7.35 (m, 2H), 7.19 (t, J = 7.4 Hz, 2H), 7.08 (m, 3H), 6.96 (t, J = 7.3 Hz, 2H), 2.55-2.41 (m, 2H), 2.16 (dq, J = 13.8, 6.9 Hz, 2H), 1.27 (m, 12H), 1.02 (dd, J = 13.2, 7.2 Hz, 6H), 0.79 (dd, J = 13.2, 6.9 Hz, 6H), 0.12 (s, 9H), -0.08 (s, 9H). ^{13}C NMR (101 MHz, C$_6$D$_6$) δ 261.93 (td, J = 9.0, 3.1 Hz), 230.22 (d, J = 3.1 Hz). ^{31}P NMR (162 MHz, C$_6$D$_6$) δ 87.53 (for ^{13}C-labeled sample: d, J = 9.0 Hz). ^{11}B NMR (128 MHz, C$_6$D$_6$) δ 6.42. Elemental analysis data were not obtained due to the thermal instability of (DPB)Fe(COSiMe$_3$)$_2$.

Hydrogenation of (DPB)Fe(COSiMe$_3$)$_2$: Three samples of freshly-prepared (DPB)Fe(COSiMe$_3$)$_2$ (~7 mg each) were mixed with ferrocene (~2 mg each), dissolved in C_6D_6 (~0.7 mL each), and added to separate J. Young tubes. A ^{1}H NMR spectrum was recorded for each sample to determine the relative amounts of (DPB)Fe(COSiMe$_3$)$_2$ (as judged by two the aryl resonances at 7.90 and 7.51 ppm) and Fc. The samples were subjected to three freeze-pump-thaw cycles and exposed to 1 atm H_2. The brown solutions turned yellow over a period of 15 min. at which time another ^{1}H NMR spectrum was recorded. Yields of *Z*-1,2-bis(trimethylsiloxy)ethylene were determined by integrating the olefinic resonance (a singlet in natural-abundance ^{12}C samples and a complicated multiplet in ^{13}C-enriched samples) against Fc. The identity of *Z*-1,2-bis(trimethylsiloxy)ethylene was established by comparison with an independently-prepared, authentic sample.[26] The three runs gave yields of 45, 42, and 41%, for an average of 43%.

(1) West, N. M.; Miller, A. J. M.; Labinger, J. A.; Bercaw, J. E. *Coord. Chem. Rev.,* **2011,** *255*, 881.
(2) (a) Bianconi, P. A.; Williams, I. D.; Engeler, M. P.; Lippard, S. J. *J. Am. Chem. Soc.,* **1986,** *108*, 311; (b) Bianconi, P. A.; Vrtis, R. N.; Rao, C. P.; Williams, I. D.; Engeler, M. P.; Lippard, S. J. *Organometallics,* **1987,** *6*, 1968; (c) Protasiewicz, J. D.; Lippard, S. J. *J. Am. Chem. Soc.,* **1991,** *22*, 6564; (d) Carnahan, E. M.; Protasiewicz, J. D.; Lippard, S. J. *Acc. Chem. Res.,* **1993,** *26*, 90.
(3) Vrtis, R. N.; Bott, S. G.; Rardin, R. L.; Lippard, S. J. *Organometallics,* **1991,** *10*, 1364.
(4) (a) Protasiewicz, J. D.; Masschelein, A.; Lippard, S. J. *J. Am. Chem. Soc.,* **1993,** *115*, 808; (b) Protasiewicz, J. D.; Bronk, B. S.; Masschelein, A.; Lippard, S. J. *Organometallics,* **1994,** *13*, 1300.
(5) (a) Lee, C. C.; Hu, Y.; Ribbe, M. W. *Science,* **2010,** *329*, 642; (b) Yang, Z. Y.; Dean, D. R.; Seefeldt, L. C. *J. Biol. Chem.,* **2011,** *286*, 19417; (c) Hu, Y.; Lee, C. C.; Ribbe, M. W. *Science,* **2011,** *333*, 753.
(6) Moret, M.-E.; Peters, J. C. *Angew. Chem. Int. Ed.,* **2011,** *50*, 2063.
(7) (a) Harman, W. H.; Peters, J. C. *J. Am. Chem. Soc.,* **2012,** *134*, 5080; (b) Suess, D. L. M.; Peters, J. C. *J. Am. Chem. Soc.,* **2013,** *135*, 4938.
(8) Tondreau, A. M.; Milsmann, C.; Lobkovsky, E.; Chirik, P. J. *Inorg. Chem.,* **2011,** *50*, 9888.
(9) Addison, A. W.; Rao, T. N.; Reedijk, J.; van Rijn, J.; Verschoor, G. C. *J. Chem. Soc., Dalton Trans.,* **1984**, 1349.
(10) Figueroa, J. S.; Melnick, J. G.; Parkin, G. *Inorg. Chem.,* **2006,** *45*, 7056.
(11) (a) Sircoglou, M.; Bontemps, S.; Mercy, M.; Saffon, N.; Takahashi, M.; Bouhadir, G.; Maron, L.; Bourissou, D. *Angew. Chem. Int. Ed.,* **2007,** *46*, 8583; (b) Moret, M.-E.; Zhang, L.; Peters, J. C. *J. Am. Chem. Soc.,* **2013**, 130304112449007.
(12) Green, M. L. H. *J. Organomet. Chem.,* **1995,** *500*, 127.
(13) (a) Hill, A. F. *Organometallics,* **2006,** *25*, 4741; (b) Parkin, G. *Organometallics,* **2006,** *25*, 4744; (c) Suess, D. L. M.; Tsay, C.; Peters, J. C. *J. Am. Chem. Soc.,* **2012,** *134*, 14158; (d) Anderson, J. S.; Moret, M.-E.; Peters, J. C. *J. Am. Chem. Soc.,* **2013,** *135*, 534.
(14) (a) Fischer, E. O.; Schneider, J.; Neugebauer, D. *Angew. Chem. Int. Ed.,* **1984,** *23*, 820; (b) Lee, Y.; Peters, J. C. *J. Am. Chem. Soc.,* **2011,** *133*, 4438.
(15) Caution should be exercised when interpreting these 13C shifts since transition metal carbyne and carbene ligands can assume a wide range of chemical shift values.
(16) IUPAC definition of a carbyne: "The neutral species HC••• and its derivatives formed by substitution in which a univalent carbon atom is covalently bonded to one group and also bears three nonbonding electrons. (This term carries no implication about spin-pairing)." Source: IUPAC. Compendium of Chemical Terminology, 2nd ed. (the "Gold Book"). Compiled by A. D. McNaught and A. Wilkinson. Blackwell Scientific Publications, Oxford (1997). XML on-line corrected version: http://goldbook.iupac.org (2006-) created by M. Nic, J. Jirat, B. Kosata; updates compiled by A. Jenkins. ISBN 0-9678550-9-8. doi:10.1351/goldbook
(17) (a) Wilker, C. N.; Hoffmann, R.; Eisenstein, O. *Nouv. J. Chim.,* **1983,** *7*, 585; (b) Brower, D. C.; Templeton, J. L.; Mingos, D. *J. Am. Chem. Soc.,* **1987,** *109*, 5203; (c) Filippou, A. C.; Hofmann, P.; Kiprof, P.; Schmid, H. R.; Wagner, C. *J. Organomet. Chem,* **1993,** *459*, 233.
(18) Landis, C. R.; Weinhold, F. *J. Comput. Chem.,* **2006,** *28*, 198.

(19) Haaland, A. *Angew. Chem. Int. Ed.,* **1989,** *28*, 992.
(20) Data from a Cambridge Structural Database search up to the Nov. 2012 update.
(21) Harrison, W.; Trotter, J. *J. Chem. Soc., A,* **1971**, 1542.
(22) (a) Bennett, M. J.; Graham, W.; Smith, R. A.; Stewart, R. P. *J. Am. Chem. Soc.,* **1973,** *95*, 1684; (b) Wong, A.; Atwood, J. D. *J. Organomet. Chem.,* **1980,** *199*, C9; (c) Okazaki, M.; Ohtani, T.; Inomata, S.; Tagaki, N.; Ogino, H. *J. Am. Chem. Soc.,* **1998,** *120*, 9135; (d) Sazama, G. T.; Betley, T. A. *Organometallics,* **2011,** *30*, 4315.
(23) (a) Betley, T. A.; Peters, J. C. *J. Am. Chem. Soc.,* **2004,** *126*, 6252; (b) Hendrich, M. P.; Gunderson, W.; Behan, R. K.; Green, M. T.; Mehn, M. P.; Betley, T. A.; Lu, C. C.; Peters, J. C. *Proc. Natl. Acad. Sci. U.S.A.,* **2006,** *103*, 17107.
(24) Sheldrick, G. M., *SHELXTL 2000*. Universität Göttingen: Göttingen, Germany, 2000.
(25) M. J. Frisch, G. W. T., H. B. Schlegel, G. E. Scuseria, M. A. Robb, J. R. Cheeseman, G. Scalmani, V. Barone, B. Mennucci, G. A. Petersson, H. Nakatsuji, M. Caricato, X. Li, H. P. Hratchian, A. F. Izmaylov, J. Bloino, G. Zheng, J. L. Sonnenberg, M. Hada, M. Ehara, K. Toyota, R. Fukuda, J. Hasegawa, M. Ishida, T. Nakajima, Y. Honda, O. Kitao, H. Nakai, T. Vreven, J. A. Montgomery, Jr., J. E. Peralta, F. Ogliaro, M. Bearpark, J. J. Heyd, E. Brothers, K. N. Kudin, V. N. Staroverov, R. Kobayashi, J. Normand, K. Raghavachari, A. Rendell, J. C. Burant, S. S. Iyengar, J. Tomasi, M. Cossi, N. Rega, J. M. Millam, M. Klene, J. E. Knox, J. B. Cross, V. Bakken, C. Adamo, J. Jaramillo, R. Gomperts, R. E. Stratmann, O. Yazyev, A. J. Austin, R. Cammi, C. Pomelli, J. W. Ochterski, R. L. Martin, K. Morokuma, V. G. Zakrzewski, G. A. Voth, P. Salvador, J. J. Dannenberg, S. Dapprich, A. D. Daniels, Ö. Farkas, J. B. Foresman, J. V. Ortiz, J. Cioslowski, and D. J. Fox *Guassian09 Revision B.01*, Gaussian, Inc.: Wallingford, CT, 2009.
(26) Scharf, H. D.; Mattay, J. *Tet. Lett.,* **1976,** *17*, 3509.

Chapter 5 Late Metal Diphosphinosulfinyl S(O)P_2 Pincer-Type Complexes

5.1 Background

The development of pincer-type ligands has led to new insights and discoveries in late transition metal chemistry in recent years. Studies on pincer-type complexes have, for example, demonstrated unusually facile elementary bond activation steps that have been exploited to mediate useful catalytic transformations and to probe the mechanisms of such transformations.[1] The propensity of certain pincer-type ligands to display redox non-innocence,[2] to store hydride equivalents,[3] and to display hemilability[4] has contributed to the richness of their chemistry. Furthermore, small variations in the electronic and steric features of a given family of pincer ligands often have translated to large differences in the properties of their respective transition metal complexes. In addition to the diverse reaction chemistry they mediate, pincer-type systems have recently been used to stabilize highly unusual bonding motifs,[5] as illustrated by a terminal iridium nitrido complex[6] and a terminal platinum oxo complex.[7]

In this article, we introduce the preparation and properties of complexes that feature a pincer-type ligand with electron-accepting properties at a central sulfinyl donor. Phosphine-containing pincer-type ligands featuring a strong central σ-acceptor such as a borane[8] have been reported, but little work has been described on such ligands featuring a strong central π-acceptor.[9] We therefore reasoned that sulfinyl-containing pincer-type ligands would complement the rich and growing body of diphosphine pincer-type complexes in the literature.

Toward this goal, we chose to pursue a PS(O)P pincer-type ligand containing two phosphines that flank a central diarylsulfoxide. Sulfoxide ligands can serve as good σ-donors and π-acceptors when bound to the metal *via* sulfur.[10] In addition, sulfoxides—unlike carbon monoxide—may be easily incorporated into a chelate and be made chiral.[11] I opted to perform my studies using bis(2-(diphenylphosphino)phenyl)sulfoxide ("SOP_2"), a variant of an ethylene-linked ligand reported in 1994 by Leung and Mok (Chart 5.1).[12] The phenylene linkers in the SOP_2 ligand were incorporated in order to

Chart 5.1 PS(O)P pincer-type ligands

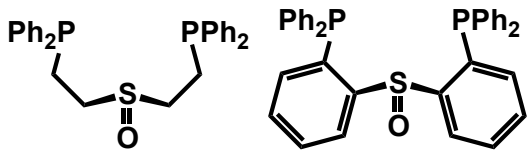

endow greater rigidity and π-accepting capabilities to the sulfinyl donor. In this chapter, I describe the preparation of SOP_2 and a host of its group 9 and 10 complexes. This study aims to assess the electronic effects of incorporating a sulfinyl donor into a pincer-type ligand to help guide future studies with this ligand type.

5.2 Results

SOP_2 may be synthesized in two steps from commercially available materials on a multi-gram scale. Reaction of 2.2 equiv 2-(diphenylphosphino)phenylmagnesium bromide (generated *in situ* from the corresponding aryl bromide) with dimethylsulfate using TMSCl as an electrophilic promoter (Scheme 5.1) results in the formation of SOP_2

Scheme 5.1 Preparation of SOP_2

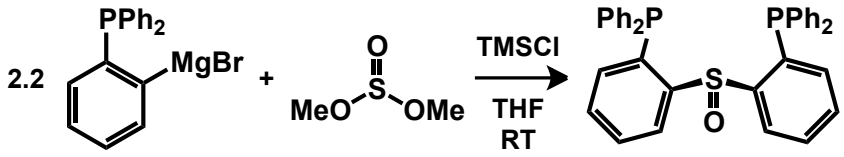

in 60% yield. The ligand is isolated as a colorless solid by precipitation from THF solution and may be crystallized by slow evaporation. Its key spectroscopic features are as expected (^{31}P NMR (CD_2Cl_2): -18.3 ppm, $\nu_{(S\text{-}O)}$: 1,055 cm^{-1}). The solid-state structure (Figure 5.1) was determined by XRD analysis and shows an S–O distance of 1.496(1) Å.

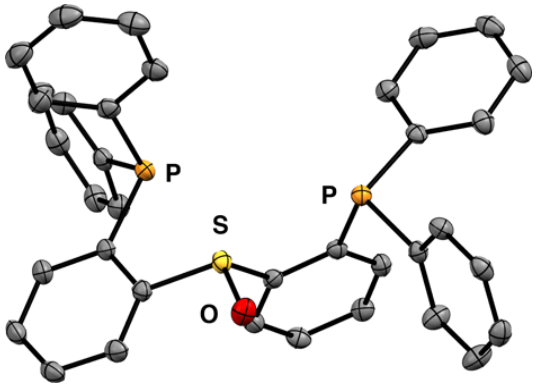

Figure 5.1 Displacement ellipsoid representation (50%) of SOP_2. H atoms are omitted for clarity. Selected distance: S–O = 1.496(1) Å.

Complexes of Rh(I) may be accessed from $(SOP_2)RhCl$, a convenient starting material generated by metallation of SOP_2 with 0.5 equiv $[(COD)RhCl]_2$ and loss of COD (Scheme 5.2). Bright yellow $(SOP_2)RhCl$ exhibits a single ^{31}P NMR signal at 48.8 ppm, downfield from that of free SOP_2; coordination to Rh is further demonstrated by the

Scheme 5.2 Preparation of $(SOP_2)Rh$ complexes

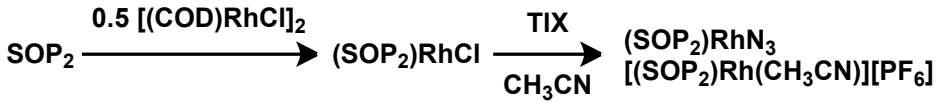

prominent $^1J_{RhP}$ = 148 Hz. The solid-state structure (Figure 5.2) reveals a short Rh–S distance of 2.1340(8) Å which is substantially shorter than the Rh–P distances (2.25 Å avg.) and is the shortest Rh–S distance for any crystallographically characterized sulfoxide complex of rhodium.[13] Also noteworthy is that its coordination geometry is distorted between square planar and *cis*-divacant octahedral: the chloride ligand is *trans* to the sulfoxide donor in a nearly linear arrangement (Cl–Rh–S = 172.81(3)˚) and the P–Rh–P angle is contracted to 146.54(3)˚. Rh(I) complexes that feature π-accepting tridentate ligands and *cis*-divacant octahedral geometries have been shown to exhibit

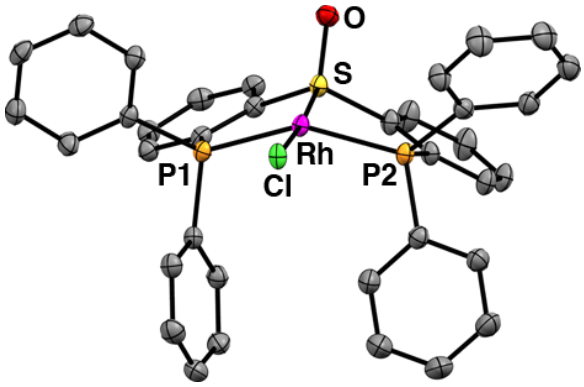

Figure 5.2 Displacement ellipsoid representation (50%) of $(SOP_2)RhCl$. H atoms and solvent molecules are omitted for clarity. Selected distances and angles: Rh–S = 2.1340(8) Å; Rh–P1 = 2.2438(9) Å; Rh–P2 = 2.2643(9); Rh–Cl = 2.3713(8); S–O = 1.484(2) Å; P1–Rh–P2 = 146.54(3)˚.

unusual properties and reactivity.[14] Reaction of $(SOP_2)RhCl$ with TlN_3 provides yellow $(SOP_2)RhN_3$ and halide abstraction of $(SOP_2)RhCl$ with $TlPF_6$ in CH_3CN gives yellow

[$(SOP_2)Rh(NCCH_3)$][PF_6]; the P–Rh–P angles in these complexes widen to 160.51(1)° and 166.44(1)°, respectively (Figure 5.3).

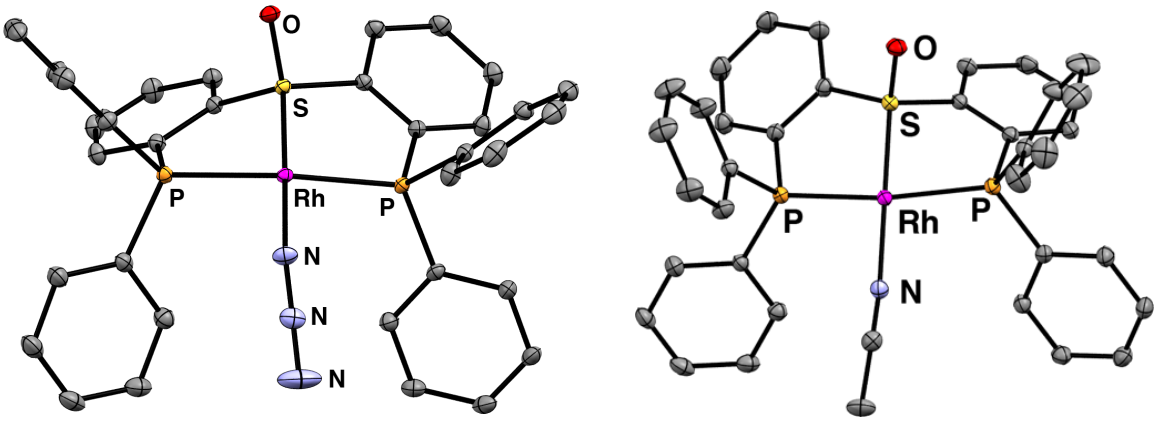

Figure 5.3 Displacement ellipsoid representation (50%) of $(SOP_2)RhN_3$ (left) and [$(SOP_2)Rh(CH_3CN)$][PF_6] (right). H atoms, solvent molecules, and counteranions are omitted for clarity. Selected distances and angles for $(SOP_2)RhN_3$: Rh–S = 2.1394(3) Å; Rh–P = 2.2689(4), 2.2958(4) Å; Rh–N = 2.0639(12); S–O = 1.4802(10) Å; P1–Rh–P2 = 160.51(1)°. Selected distances and angles for [$(SOP_2)Rh(NCCH_3)$][PF_6]: Rh–S = 2.1581(4) Å; Rh–P1 = 2.2736(4), 2.2961(4) Å; Rh–N = 2.0453(14) Å; S–O = 1.4782(11) Å; P1–Rh–P2 = 166.44(1)°.

The corresponding $(SOP_2)IrCl$ complex may be accessed in three steps from $[(COE)_2IrCl]_2$ (Scheme 5.3). Heating a THF solution of SOP_2 and 0.5 equiv $[(COE)_2IrCl]_2$ results in formation of the yellow-orange 18-electron complex (*fac*-SOP_2)Ir(COE)Cl. In addition to the usual aryl resonances, the ^{1}H NMR spectrum of (*fac*-SOP_2)Ir(COE)Cl contains one set of broad resonances attributable to the bound COE ligand. The olefinic nuclei are shifted upfield to a broad peak at 4.43 ppm compared with the sharp multiplet at 5.6 ppm observed for free COE. The RT ^{31}P NMR spectrum contains one exceptionally broad resonance centered at ca. 35 ppm. The X-ray structure of (*fac*-SOP_2)Ir(COE)Cl

Scheme 5.3 Preparation of $(SOP_2)Ir$ complexes

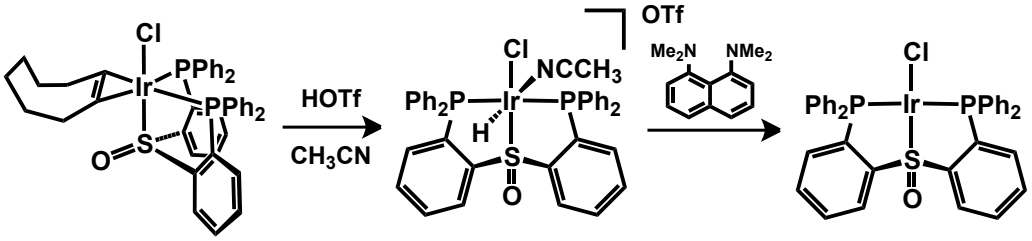

(Figure 5.4) reveals an approximately trigonal bipyramidal (TBP) geometry and a contracted P–Ir–P angle of 111.08(4)°. The olefinic COE carbons are pyramidalized as expected.

Protonation of (*fac*-SOP_2)Ir(COE)Cl by HOTf in CH_3CN results in oxidative addition of H^+, expulsion of cyclooctene, and coordination of CH_3CN to give colorless [(*mer*-SOP_2)Ir(CH_3CN)(Cl)(H)][OTf], the stereochemistry of which was established by X-ray diffraction (Figure 5.5). Although the hydride in [(*mer*-SOP_2)Ir(CH_3CN)(Cl)(H)][OTf] could not be located in the difference map, its ^{1}H NMR resonance is readily observed as a triplet at –19.1 ppm with $^2J_{PH}$ = 13.8 Hz. A doublet is observed in the ^{31}P NMR spectrum at 30.4 ppm, and the ^{19}F spectrum displays a singlet at -77 ppm corresponding to unbound triflate. Subsequent deprotonation of [(*mer*-SOP_2)Ir(CH_3CN)(Cl)(H)][OTf] by proton sponge generates yellow (*mer*-SOP_2)IrCl which displays a downfield-shifted ^{31}P NMR resonance at 47.6 ppm and no hydride resonance in its ^{1}H NMR spectrum. This complex has a square planar geometry about Ir ($\Sigma\angle$(L–Ir–L) = 359.9°; Figure 5.6). Analogously to $(SOP_2)RhCl$, the Ir–S distance is more than 0.1 Å shorter than the average Ir–P distance and shorter than any previously structurally characterized sulfoxide complex of iridium.

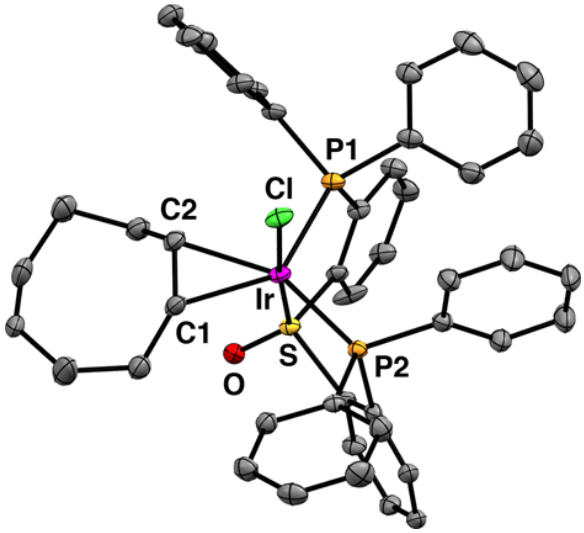

Figure 5.4 Displacement ellipsoid representation (50%) of (*fac*-SOP-$_2$)Ir(COE)Cl. H atoms and solvent molecules are omitted for clarity. Selected distances and angles: Ir–C1 = 2.206(5) Å; Ir–C2 = 2.181(4) Å; Ir–S = 2.170(1) Å; Ir–P1 = 2.323(1) Å; Ir–P2 = 2.3147(8); Ir–Cl = 2.417(1); S–O = 1.474(3) Å; P1–Ir–P2 = 111.08(4)˚.

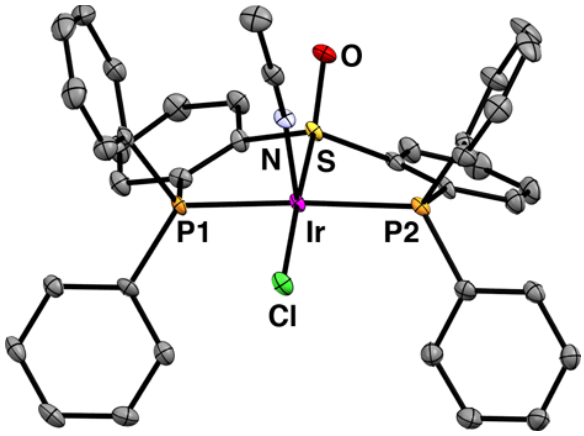

Figure 5.5 Displacement ellipsoid representation (50%) of [(*mer*-SOP$_2$)Ir(CH$_3$CN)(Cl)(H)][OTf]. H atoms, solvent molecules, and counteranion are omitted for clarity. Selected distances and angles: Ir–N = 2.1322(26) Å; Ir–S = 2.1911(7) Å; Ir–P1 = 2.3061(9) Å; Ir–P2 = 2.3104(9); Ir–Cl = 2.3877(7); S–O = 1.475(2) Å; P1–Ir–P2 = 166.56(4)˚.

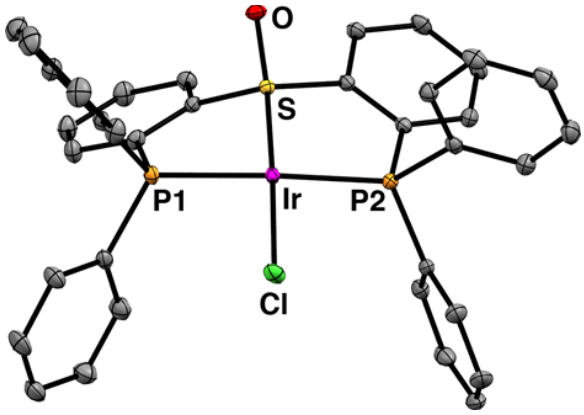

Figure 5.6 Displacement ellipsoid representation (50%) of (SOP_2)IrCl. H atoms and solvent molecules are omitted for clarity. Selected distances and angles: Ir–S = 2.1341(5) Å; Ir–P1 = 2.2599(5) Å; Ir–P2 = 2.2791(5); Ir–Cl = 2.3551(5); S–O = 1.486(1) Å; P1–Ir–P2 = 164.78(2)°.

With two *trans*-disposed triaryl phosphines, a chloride, and a sulfoxide coordinated in a square planar geometry about Ir, the topology of (SOP_2)IrCl is very similar to that of Vaska's complex, which is well known in the context of classic oxygen binding studies.[15] As such, the two complexes are expected to have similar frontier molecular orbitals. DFT calculations on Vaska's complex show that the orbital of d(xz) parentage (where the x-axis is defined by the Ir–Cl vector) has the anticipated Ir–Cl π* and Ir–CO π interactions (Figure 5.7). Nearly identical results are seen in an orbital analysis of (SOP_2)IrCl, with Ir–Cl π* and Ir–SO π contributions; this suggests that the sulfoxide donor in SOP_2 is a competent π-acceptor. To test if SOP_2 behaves chemically as an ancillary, chelating surrogate of one CO donor and two PPh_3 donors, a CD_2Cl_2 solution of (SOP_2)IrCl was exposed to 1 atm O_2 (Scheme 5.4). This resulted in rapid bleaching of the solution to very pale yellow and a new ^{31}P NMR signal at 24.5 ppm. The solid-state structure of (*fac*-SOP_2)Ir(η^2-O_2)(Cl) (Figure 5.8) shows an η^2-peroxide ligand bound to the (SOP_2)IrCl

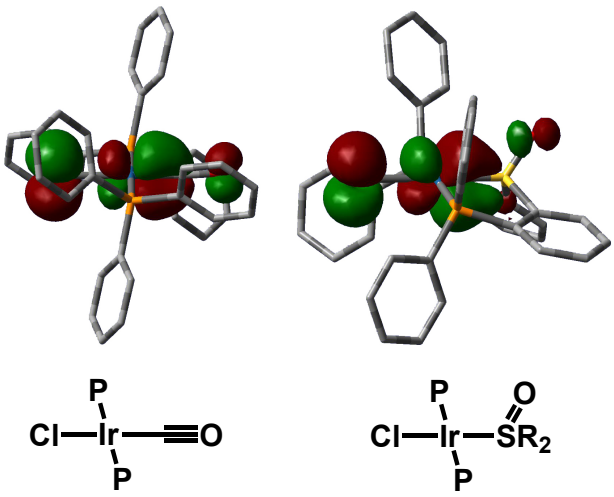

Figure 5.7 Calculated HOMO-1 orbitals of Vaska's complex (left) and $(SOP_2)IrCl$ (right).

Scheme 5.4 O_2 binding by $(SOP_2)IrCl$

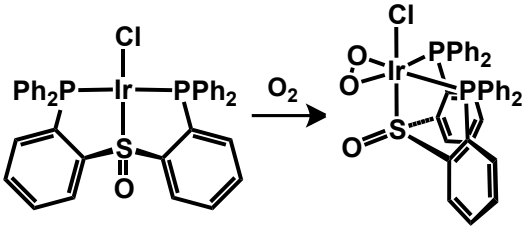

fragment in an approximately TBP geometry ($\tau = 0.66$ if the O_2 fragment is treated as one ligand), with the chloride and sulfoxide donors located in axial positions. The geometry and metrics are reminiscent of the dioxygen adduct of Vaska's complex $(PPh_3)_2Ir(CO)Cl(O_2)$, except that the phosphines occupy equatorial rather than axial positions in (*fac*-SOP_2)Ir(η^2-O_2)(Cl). More saliently, the O–O bond length is 1.464(3) Å in (*fac*-SOP_2)Ir(η^2-O_2)(Cl)—identical to that in $(PPh_3)_2Ir(CO)Cl(O_2)$ (1.465(4) Å)[16]—and their respective $\nu_{(O\text{-}O)}$ IR stretching frequencies are very similar (847 and 855 cm^{-1} for

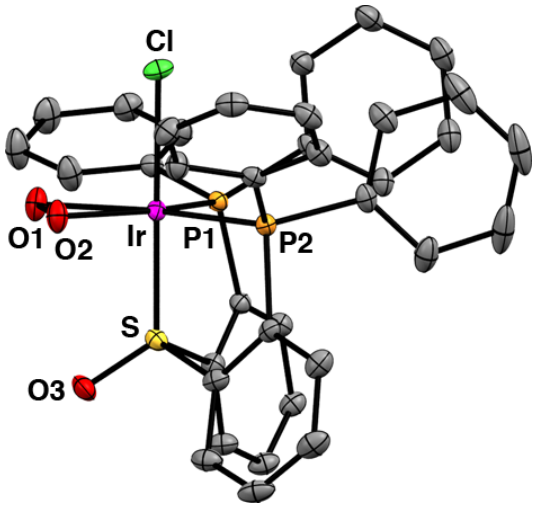

Figure 5.8 Displacement ellipsoid representation (50%) of (*fac*-SOP_2)Ir(η^2-O_2)(Cl). H atoms are omitted for clarity. Selected distances and angles: Ir–O1 = 2.041(2) Å; Ir–O2 = 2.051(2) Å; Ir–S = 2.1901(5) Å; Ir–P1 = 2.2821(7) Å; Ir–P2 = 2.2918(6); Ir–Cl = 2.3867(6); O1–O2 = 1.464(3); S–O3 = 1.465(2) Å; P1–Ir–P2 = 99.38(2)˚.

(*fac*-SOP_2)Ir(η^2-O_2)(Cl) and $(PPh_3)_2$Ir(CO)Cl(O_2), respectively).[17] Taken together, these computational and experimental results lend credence to the analogy between the diarylsulfoxide moiety in SOP_2 and a CO ligand, with each ligand serving as π-acceptors using S–O σ* and C–O π* orbitals, respectively.

Entry into nickel starting materials of SOP_2 may be accessed using common nickel sources (Scheme 5.5). Ligation of $(PPh_3)_2Ni(CO)_2$ by SOP_2 results in liberation of PPh_3 and formation of (SOP_2)Ni(CO). Its solid-state structure (Figure 5.9) reveals a distorted tetrahedral geometry about Ni with L–Ni–L angles ranging from 92.47(5)˚ (S–Ni–P2) to

Scheme 5.5 Preparation of (SOP_2)Ni complexes

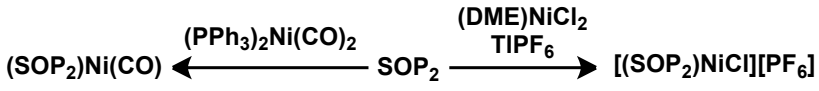

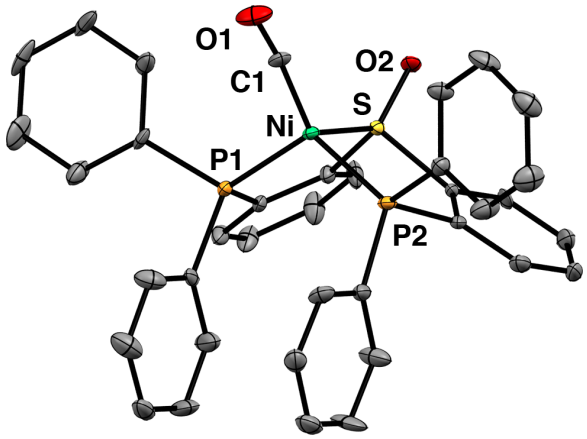

Figure 5.9 Displacement ellipsoid representation (50%) of $(SOP_2)Ni(CO)$. H atoms and solvent molecules are omitted for clarity. Selected distances and angles: Ni–C1 = 1.760(6) Å; C1–O1 = 1.145(6) Å; Ni–S = 2.129(1) Å; Ni–P1 = 2.162(1) Å; Ni–P2 = 2.171(1) Å; S–O2 = 1.490(3) Å, P1–Ni–P2 = 116.06(3)˚.

126.90(16)˚ (S–Ni–C) and a C–O length of 1.145(6). The IR spectrum exhibits a strong C–O stretch at 1,957 cm^{-1}, higher than that observed in $(PPh_3)_3Ni(CO)$ and (triphos)Ni(CO) (Table 5.1; triphos = $(Ph_2PCH_2)_3CH$)).

Table 5.1 Comparison of $(SOP_2)M(CO)$ C–O stretching frequencies with those of related phosphine complexes

Compound	$\nu_{(CO)}$ (cm^{-1})	ref.
$(SOP_2)Ni(CO)$	1957	this work
$(PPh_3)_3Ni(CO)$	1928	18
(triphos)Ni(CO)	1901	18
$(SOP_2)Pd(CO)$	1985	this work
$(PPh_3)_3Pd(CO)$	1955	19
(triphos)Pd(CO)	1919	20
$(SOP_2)Pt(CO)$	1945	this work
$(PPh_3)_3Pt(CO)$	1903	21

The cationic complex $[(SOP_2)NiCl][PF_6]$ may be generated by stirring a mixture of $(DME)NiCl_2$, SOP_2, and $TlPF_6$ in THF. The resulting square planar complex is orange-red in THF, red-purple in CH_2Cl_2, and deep purple in CH_3CN; $[(SOP_2)NiCl][PF_6]$ remains diamagnetic in each of these solvents and thus maintains its square planar geometry in solution as well as the solid state (Figure 5.10). This bathochromic shift indicates a

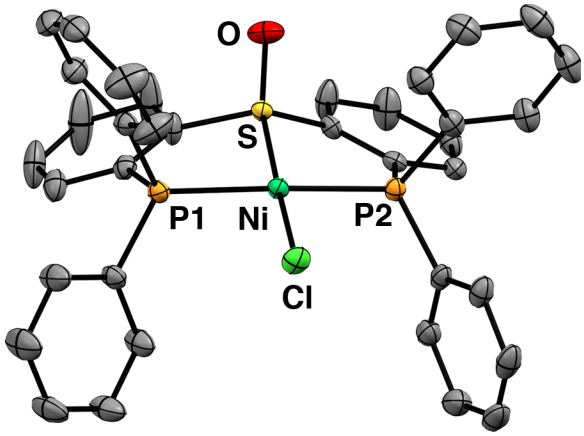

Figure 5.10 Displacement ellipsoid representation (50%) of $[(SOP_2)NiCl][PF_6]$. H atoms, solvent molecules, and counteranion are omitted for clarity. Selected distances and angles: Ni–S = 2.0985(6) Å; Ni–P1 = 2.1865(7) Å; Ni–P2 = 2.1916(7) Å; Ni–Cl = 2.1376(6) Å; S–O = 1.466(2) Å; P1–Ni–P2 = 171.62(3)˚.

substantial change in the dipole between the ground and excited states and it is therefore presumed to be a charge-transfer transition. The cyclic voltammagram of $[(SOP_2)NiCl][PF_6]$ with 0.1 M Bu_4NPF_6 electrolyte in CH_3CN shows two quasi-reversible waves at -0.54 and -0.95 V versus Fc/Fc^+ (Figure 5.11). The relatively anodic potentials of these processes speak to the electrophilicity of $[(SOP_2)NiCl][PF_6]$ and the electron withdrawing properties of SOP_2.

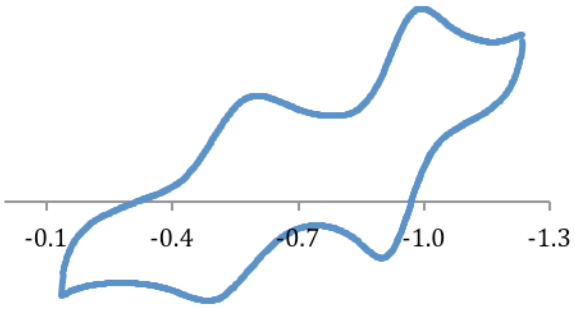

Figure 5.11 Cyclic voltammagram of $[(SOP_2)NiCl][PF_6]$ in CH_3CN with 0.1 M Bu_4NPF_6 electrolyte at 0.01 V/sec referenced to Fc/Fc^+.

In order to probe the electronic features imparted by SOP_2 on palladium and platinum, the monocarbonyl complexes were targeted in analogy to $(SOP_2)Ni(CO)$ (Scheme 5.6). Starting materials of the form $(SOP_2)M(PPh_3)$ (M = Pd and Pt) are

Scheme 5.6 Preparation $(SOP_2)Pd$ and $(SOP_2)Pt$ complexes

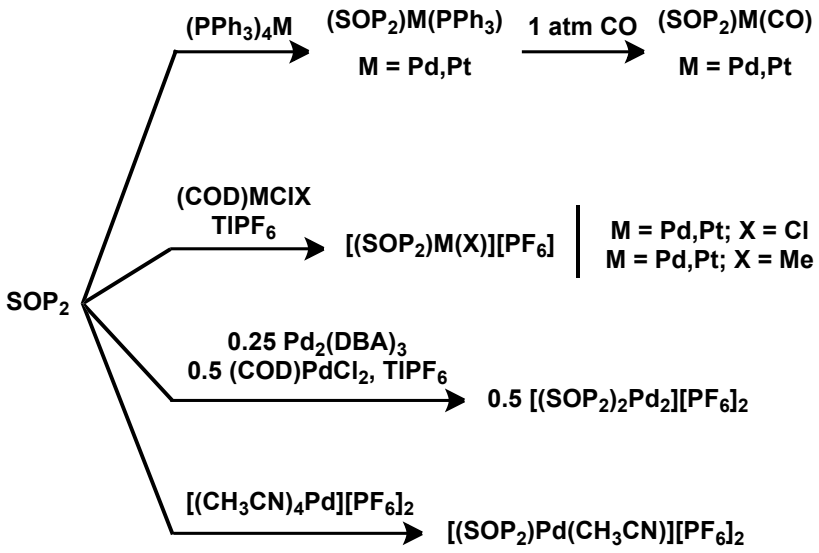

obtained by metallation of SOP_2 with $(PPh_3)_4Pd$ or $(PPh_3)_4Pt$. Both pseudotetrahedral, inky orange-red complexes were crystallographically characterized (Figure 5.12). The ^{31}P

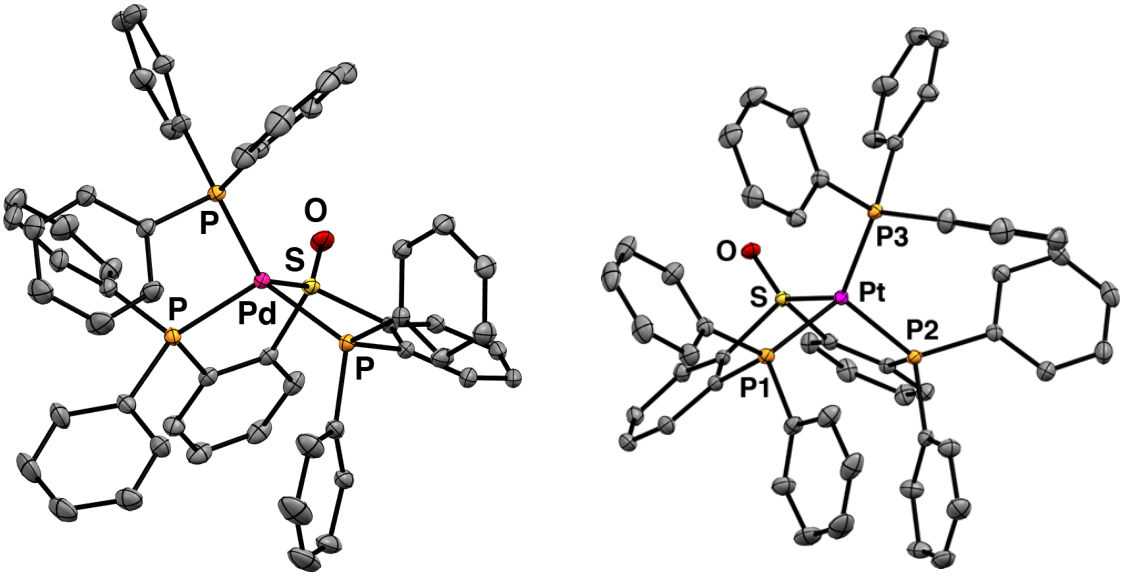

Figure 5.12 Displacement ellipsoid representation (50%) of $(SOP_2)Pd(PPh_3)$ (left) and $(SOP_2)Pt(PPh_3)$ (right). H atoms and solvent molecules are omitted for clarity. Selected distances and angles for $(SOP_2)Pd(PPh_3)$: Pt–S = 2.3131(3) Å; Pt–P1 = 2.2762(4) Å; Pt–P2 = 2.2709(4); Pt–P3 = 2.2809(4) Å; S–O = 1.494(1) Å; P1–Pt–P2 = 112.17(2)˚. Selected distances and angles for $(SOP_2)Pt(PPh_3)$: Pt–S = 2.3131(3) Å; Pt–P1 = 2.2762(4) Å; Pt–P2 = 2.2709(4); Pt–P3 = 2.2809(4) Å; S–O = 1.494(1) Å; P1–Pt–P2 = 112.17(2)˚.

NMR spectrum of $(SOP_2)Pt(PPh_3)$ displays a complicated set of features due to the presence of three inequivalent ^{31}P nuclei, ^{31}P–^{31}P coupling, and ^{31}P–^{195}Pt coupling. However, simulation of the ^{31}P NMR spectrum allows for all relevant chemical shifts and coupling constants to be determined (Figure 5.13); importantly, these derived values can be used to suitably predict the complicated ^{195}Pt NMR spectrum (Figure 5.14). Exposure

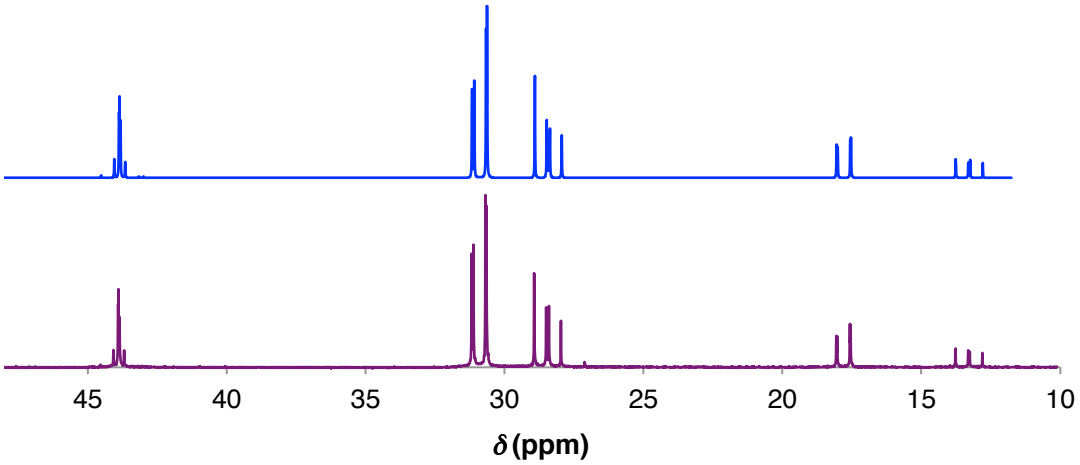

Figure 5.13 Simulated (top) and experimental (bottom) ^{31}P NMR spectra of $(SOP_2)Pt(PPh_3)$ (162 MHz, CD_2Cl_2). Values derived from simulation: P_A = 30.90 ppm, P_B = 30.88 ppm, P_C = 28.50, $J_{PA\text{-}PB}$ = 0 Hz, $J_{PA\text{-}PC}$ = 82.5 Hz, $J_{PB\text{-}PC}$ = 75.6 Hz, $J_{PA\text{-}Pt}$ = 4244 Hz, $J_{PB\text{-}Pt}$ = 4238 Hz, $J_{PC\text{-}Pt}$ = 4917 Hz.

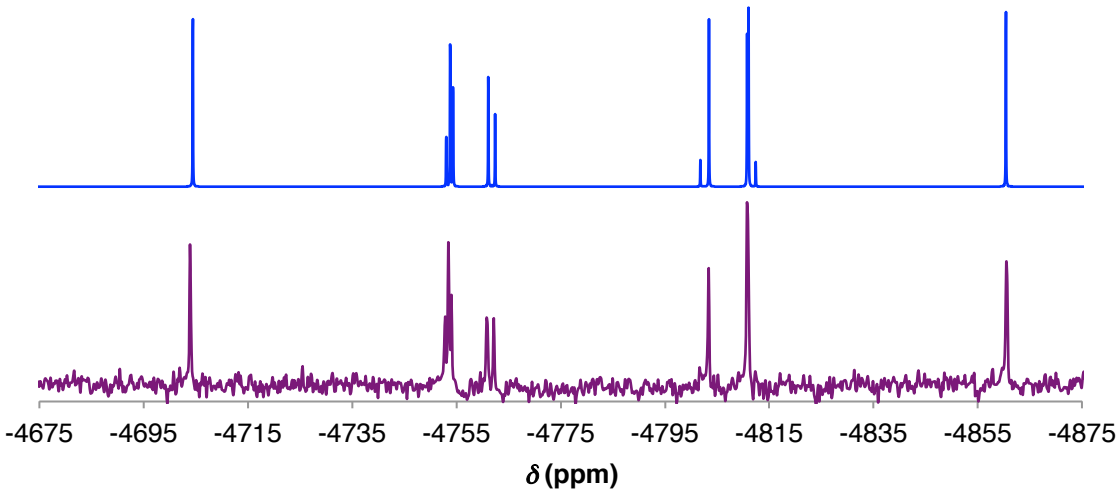

Figure 5.14 Simulated (top) and experimental (bottom) ^{195}Pt NMR spectra of $(SOP_2)Pt(PPh_3)$ (86 MHz, CD_2Cl_2). Values used as input for simulation: $J_{PA\text{-}Pt}$ = 4244 Hz, $J_{PB\text{-}Pt}$ = 4238 Hz, $J_{PC\text{-}Pt}$ = 4917 Hz.

of either $(SOP_2)Pd(PPh_3)$ or $(SOP_2)Pt(PPh_3)$ to 1 atm CO in CD_2Cl_2 results in clean formation of new products by NMR that are formulated as $(SOP_2)M(CO)$ (M = Pd and Pt) on the basis of new strong bands in their IR spectra: $\nu_{(C\text{-}O)}$ = 1,985 and 1,945,

respectively. As for $(SOP_2)Ni(CO)$, the C–O stretching frequencies are significantly higher than those in related compounds (Table 5.1).

A variety of X-type ligands may occupy the site *trans* to the sulfoxide donor of SOP_2 in divalent complexes of Pd and Pt. For example, chlorides of the form $[(SOP_2)MCl][PF_6]$ (M = Pd and Pt) may be obtained in analogy to $[(SOP_2)NiCl][PF_6]$ by reaction of SOP_2 with $(COD)MCl_2$ and $TlPF_6$ in CH_3CN. Both $[(SOP_2)PdCl][PF_6]$ and $[(SOP_2)PtCl][PF_6]$ are colorless and square planar and $[(SOP_2)PtCl][PF_6]$ displays characteristic Pt satellites in its ^{31}P NMR spectrum ($^1J_{PtP}$ = 2,496 Hz). Colorless cationic methyl complexes $[(SOP_2)PdMe][PF_6]$ and $[(SOP_2)PtMe][PF_6]$ ($^1J_{PtP}$ = 2,840 Hz) are obtained under identical conditions by metallation of SOP_2 with $(COD)M(CH_3)Cl$ and $TlPF_6$. The structures of $[(SOP_2)PdCl][PF_6]$ and $[(SOP_2)PdMe][PF_6]$ are similar (Figure 5.15) except

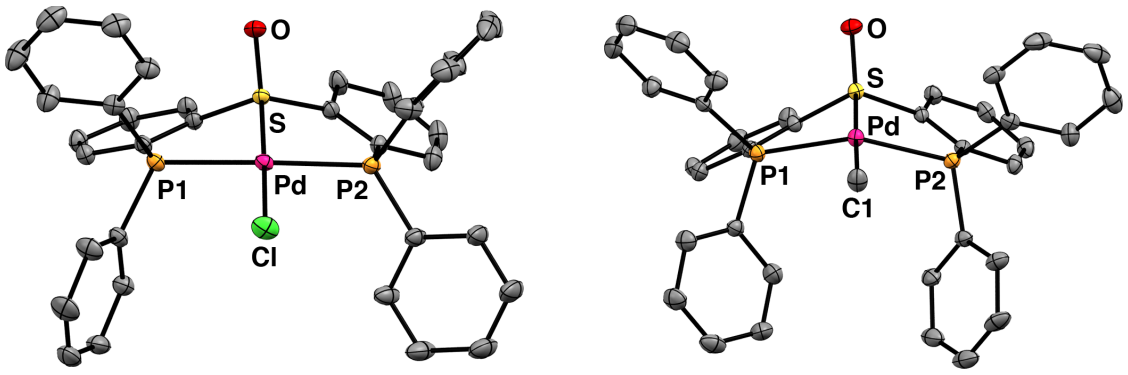

Figure 5.15 Displacement ellipsoid representation (50%) of $[(SOP_2)PdX][PF_6]$ (X = Cl, left; X = Me, right). H atoms, solvent molecules, and counteranions are omitted for clarity. Selected distances and angles for $[(SOP_2)PdCl][PF_6]$: Pd–S = 2.2111(3) Å; Pd–P1 = 2.3097(3) Å; Pd–P2 = 2.3029(4) Å; Pd–Cl = 2.2934(4) Å; S–O = 1.469(1) Å; P1–Pd–P2 = 167.79(1)°. Selected distances and angles for $[(SOP_2)PdMe][PF_6]$ (avg. of two molecules in the asymmetric unit): Pd–S = 2.31 Å; Pd–P = 2.28 Å; Pd–C1 = 2.08 Å; S–O = 1.48 Å; P1–Pd–P2 = 153°.

that the Pd–S distance is greater (2.31 Å (avg.) vs. 2.2111(3) Å) and the P–Pd–P angle is lower (155˚ (avg.) vs. 167.79(1)˚) in $[(SOP_2)PdMe][PF_6]$**,** likely owing to its strongly *trans* influencing methyl ligand. Interestingly, these effects are not observed in the analogous Pt complexes (Figure 5.16).

Initial attempts to generate $[(SOP_2)PdMe][PF_6]$ from $[(SOP_2)PdCl][PF_6]$ using CH_3MgCl or CH_3Li at -78 ˚C led to a mixture of products including a red, dicationic

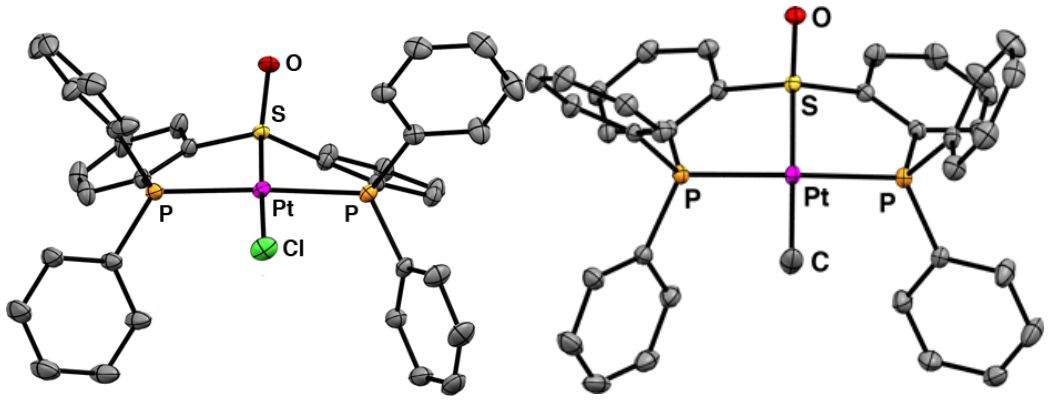

Figure 5.16 Displacement ellipsoid representation (50%) of $[(SOP_2)PtX][PF_6]$ (X = Cl, left; X = Me, right). H atoms, solvent molecules, and counteranions are omitted for clarity. Selected distances and angles for $[(SOP_2)PtCl][PF_6]$: Pt–S = 2.1930(4) Å; Pt–P = 2.2966(4), 2.3044(4) Å; Pt–Cl = 2.3008(4) Å; S–O = 1.4668(13) Å; P–Pt–P = 168.45(1)˚. Selected distances and angles for $[(SOP_2)PtMe][PF_6]$: Pt–S = 2.2678(8) Å; Pt–P = 2.2707(9), 2.2761(9) Å; Pt–C = 2.093(3) Å; S–O = 1.472(2) Å; P–Pt–P = 167.04(3)˚.

Pd(I)-Pd(I) species $[(SOP_2)Pd]_2[PF_6]_2$ that can be independently synthesized from two equiv SOP_2, one equiv $(COD)PdCl_2$, 0.5 equiv $(DBA)_3Pd_2$, and two equiv $TlPF_6$ (Scheme 5.6). Indeed, I have typically observed net reduction—rather than substitution—of $[(SOP_2)PdCl][PF_6]$ upon exposure to strong nucleophiles such as ^-OR, $^-NR_2$, and HNR_2 to form $[(SOP_2)Pd]_2[PF_6]_2$ in varying amounts. The solid-state structure of

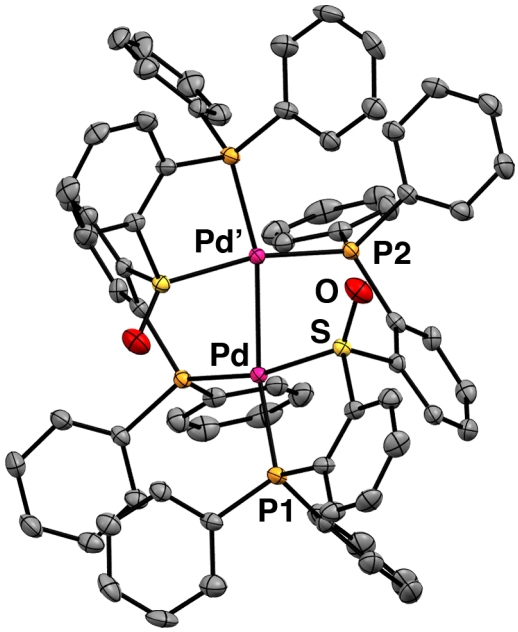

Figure 5.17 Displacement ellipsoid representation (50%) of $[(SOP_2)_2Pd]_2[PF_6]_2$. H atoms, solvent molecules, and counteranions are omitted for clarity. Selected distances and angles: Pd–Pd' = 2.5793(4) Å; Pd–S = 2.289(1) Å; Pd–P1 = 2.336(1) Å; Pd'–P2 = 2.321(1) Å; S–O = 1.466(3) Å.

$[(SOP_2)Pd]_2[PF_6]_2$ (Figure 5.17) reveals two SOP_2 ligands bound to two Pd(I) centers, each in a κ^2-Pd-κ^1-Pd' fashion where Pd and Pd' are related by a crystallographic two-fold proper rotation axis. The Pd–Pd' distance is 2.5793(4) Å and the intraligand P2–Pd–Pd'–S dihedral angle is 63.9°.

Given the great interest in highly electrophilic group 10 complexes in catalysis,[11,22] I sought to prepare Pd(II) synthons featuring SOP_2 and a potentially more labile ligand *trans* to the sulfoxide donor. Accordingly, I found that SOP_2 readily ligates $[(CH_3CN)_4Pd][PF_6]_2$ to form bright yellow $[(SOP_2)Pd(NCCH_3)][PF_6]_2$. The latter species is a potent Lewis acid and polymerizes THF. In the solid state (Figure 5.18),

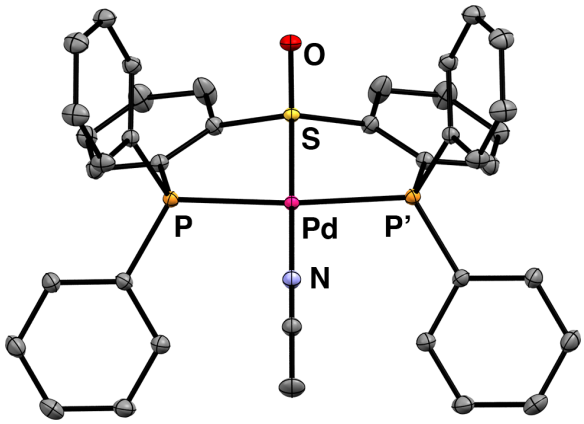

Figure 5.18 Displacement ellipsoid representation (50%) of $[(SOP_2)Pd(NCCH_3)][PF_6]_2$. H atoms, solvent molecules, and counteranions are omitted for clarity. Selected distances and angles: Pd–S = 2.2315(4) Å; Pd–P = 2.3123(3) Å; Pd–N = 2.033(1) Å; S–O = 1.466(1) Å; P–Pd–P' = 169.51(1)˚.

$[(SOP_2)Pd(NCCH_3)][PF_6]_2$ lies on a mirror plane and has Pd–SOP_2 and S–O distances (Pd–S = 2.2315(4) Å, Pd–P = 2.3123(3) Å, and S–O = 1.466(1) Å) similar to those in $[(SOP_2)PdCl][PF_6]$. Cyclic voltammetry of $[(SOP_2)Pd(NCCH_3)][PF_6]_2$ using 0.1 M Bu_4NPF_6 electrolyte in CH_3CN (Figure 5.19) reveals two irreversible one-electron reduction events at -0.51 and -0.88 V vs. Fc/Fc^+. These values are markedly anodic of the single irreversible reduction reported by Dubois for the dicationic CO_2 reduction

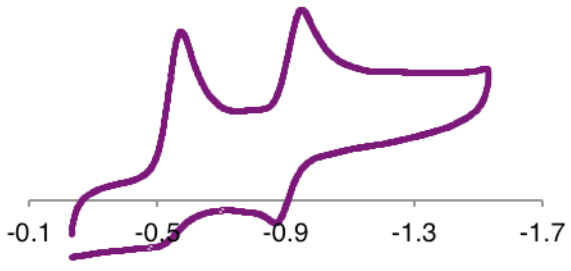

Figure 5.19 Cyclic voltammagram of $[(SOP_2)Pd(NCCH_3)][PF_6]_2$ in CH_3CN with 0.1 M Bu_4NPF_6 electrolyte at 0.01 V/sec referenced to Fc/Fc^+.

electrocatalyst $[PhP(CH_2CH_2PPh_2)_2Pd(NCCH_3)][BF_4]_2$, which is observed at -1.35 V vs. Fc/Fc^+;[23] similarly to $[(SOP_2)NiCl][PF_6]$, one or both of the reduction events observed in $[(SOP_2)Pd(NCCH_3)][PF_6]_2$ may involve substantial ligand participation.

5.3 Discussion

The late-metal chemistry of SOP_2 demonstrates that the ligand behaves as a κ^3-PS(O)P donor. Unlike DMSO and other non-chelating sulfoxides, SOP_2 has not yet been observed to bind through the oxygen atom probably owing to the formation of two five-member rings upon S-chelation; the ambidentate coordination of labile sulfoxides is important since it may contribute to reduced catalytic activity.[24] The SOP_2 ligand is sufficiently flexible to support both *mer* and *fac* coordination modes, M–S distances ranging from 2.0985(6) Å in $[(SOP_2)NiCl][PF_6]$ to 2.31 Å avg. in $[(SOP_2)PdMe][PF_6]$, and P–M–P angles ranging from nearly linear in $[(SOP_2)NiCl][PF_6]$ (171.62(3)°) to nearly orthogonal in (*fac*-SOP_2)Ir(η^2-O_2)(Cl) (99.38(2)°). This flexibility accommodates a variety of classic metal coordination geometries (pseudotetrahedral, square planar, trigonal bipyramidal, and octahedral) as well as geometries that lie on the continuum between square planar and *cis*-divacant octahedral.

The data presented here demonstrate that the diarylsulfoxide donor in SOP_2 renders the metal center relatively electron deficient, and in so doing mimics a CO ligand in the company of two phosphine donors. The values of $\nu_{C\text{-}O}$ in the zero-valent group 10 complexes $(SOP_2)Ni(CO)$, $(SOP_2)Pd(CO)$, and $(SOP_2)Pt(CO)$ are significantly higher (ca. 30-40 cm^{-1}) than the frequencies observed for their closest trisphosphine analogs. This trend could arise from the poorer π-donating or stronger π-accepting properties of the

diarylsulfoxide donor compared with those of a phosphine. The diarylsulfoxide-CO analogy is more obvious in (*mer*-SOP_2)IrCl, in which the sulfinyl serves as a π-acceptor much like the CO ligand in Vaska's complex. In addition, the unusually anodic reduction potentials of [(SOP_2)NiCl][PF_6] and [(SOP_2)Pd($NCCH_3$)][PF_6]$_2$ speak to the high electrophilicity that SOP_2 engenders on divalent group 10 metals. The electronic origins of these results may arise from some combination of two rationales: the sulfoxide donor is a competent σ-donor and a strong π-acceptor, or the sulfoxide is rendered a weak σ-donor by its oxygen atom but is persistent in ligation because of the chelate effect. In order to investigate the plausibility of these two hypotheses, I analyzed the relationship between the M–S and S–O bond lengths in the d^8 complexes of Rh, Ir, Pd, and Pt.[25] Two clear and opposing trends emerge when M–S vs. S–O distances are plotted separately for group 9 and group 10 complexes. For Rh and Ir (Chart 5.2), shorter M–S distances correspond to longer S–O distances, consistent with strong M–(SO) π backbonding. On the other hand, the d^8 Pd and Pt complexes show the opposite trend with the S–O distances decreasing with decreasing M–S distance (Chart 5.3). The latter correlation may be explained by the electrostatic argument: more electrophilic metal centers bind the sulfur atom more tightly which in turn binds the oxygen atom more tightly. Indeed, the longest S–O bond of all SOP_2-containing molecules is observed in the free ligand. These arguments have been offered in related contexts elsewhere.[10] The relatively high C–O stretching frequencies of (SOP_2)Ni(CO), (SOP_2)Pd(CO), and (SOP_2)Pt(CO) may be explained by relatively stronger M–S(O) backbonding and/or a relatively weaker ligand field. Thus, although the sulfoxide in SOP_2 has an electron-withdrawing effect compared

Chart 5.2 Relationship between Rh/Ir–S and and S–O distances for d^8 complexes $(SOP_2)RhCl$, $(SOP_2)RhN_3$, $[(SOP_2)Rh(NCCH_3)][PF_6]$, (*fac*-$SOP_2$)Ir(COE)Cl, (*mer*-$SOP_2$)IrCl, and (*fac*-$SOP_2$)Ir($\eta^2$-$O_2$)(Cl). The ESDs are ≤ 0.0029 Å for all S–O distances and ≤ 0.0009 Å for all M–S distances.

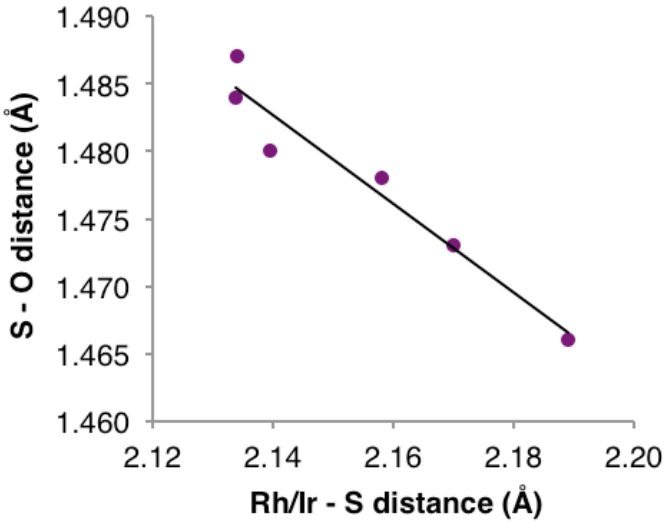

Chart 5.3 Relationship between Pd/Pt–S and and S–O distances for d^8 complexes $[(SOP_2)PdCl][PF_6]$, $[(SOP_2)PtCl][PF_6]$, $[(SOP_2)PdMe][PF_6]$, $[(SOP_2)PtMe][PF_6]$, and $[(SOP_2)Pd(NCCH_3)][PF_6]_2$. The ESDs are ≤ 0.0029 Å for all S–O distances and ≤ 0.0008 Å for all M–S distances.

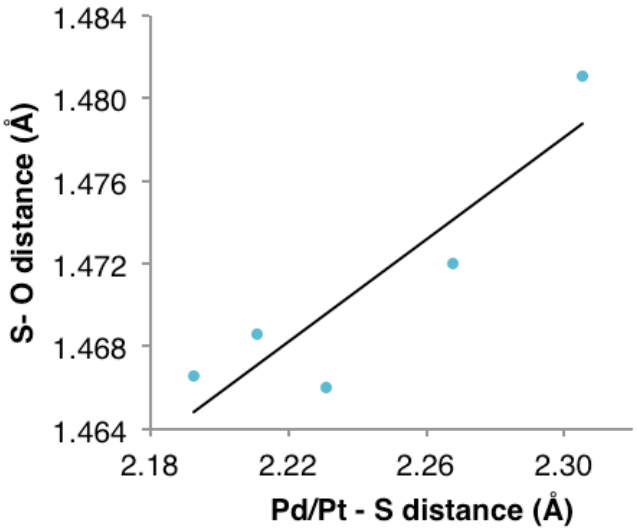

with a phosphine donor in all complexes described here, the origins of this effect is most simply explained by π-backbonding for Rh and Ir and weak σ-donation for all of the metals canvassed.

5.4 Summary

The pincer-type diphosphinosulfinyl ligand SOP_2 may be easily prepared in multi-gram quantities and binds late metals in a κ^3-PS(O)P fashion. The centrally positioned sulfoxide has not thus far displayed ambidentate binding and confers electrophilic properties to the metal by virtue of weak σ-donation and—for at least the Rh and Ir complexes discussed—relatively strong π-acceptance. The π-accepting capabilities of SOP_2 may allow for stabilization of low-valent complexes bearing π-donating ligands, and the ligand's geometric flexibility and ability to form highly electrophilic complexes may prove useful for bond activation processes and catalysis. Efforts in these areas are ongoing in our laboratory.

5.5 Experimental

General Considerations. All manipulations were carried out using standard Schlenk or glove box techniques under a dinitrogen atmosphere. Dry, degassed solvents were purged with Ar and passed through an activated alumina column from S. G. Waters (Nashau, NH, USA) prior to use. All other reagents were purchased from commercial vendors and used as received without further purification unless otherwise noted. Deuterated solvents were purchased from Cambridge Isotope Laboratories, Inc. NMR experiments were

performed on Varian 300, 400, and 500 MHz spectrometers. ^{1}H NMR spectra were referenced to residual solvent. ^{31}P NMR spectra were referenced to H_3PO_4. ^{195}Pt NMR spectra were referenced to K_2PtCl_4. IR spectra were acquired on a Bio-Rad FTS 300 instrument. Combustion analysis was performed by Midwest Microlab LLC in Indianapolis, IN, USA.

SOP_2: A hot 100 mL three neck flask was charged with a magnetic stir bar, Mg turnings (3.65 g, 150.0 mmol), and 2-(diphenylphosphino)bromobenzene[26] (9.89 g, 29.0 mmol) and dried in vacuo. THF (30 mL) was added to the cooled solid and the solution was heated with vigorous stirring to 90 ˚C. After the solution turned deep orange-brown, it was stirred at 90 ˚C for an additional 1 hr. before cooling to room temperature. The Grignard solution was cannula transferred to a preformed stirring solution of dimethylsulfate (1.10 mL, 11.6 mmol) in 100 mL THF. Neat TMSCl (2.21 g, 17.4 mmol) was added via syringe and the solution was stirred for 20 min. Water (300 mL) was added followed by CH_2Cl_2 (300 mL). The organic layer was collected and the aqueous layer was extracted with CH_2Cl_2 (3 x 100 mL). Solvent was removed from the organics by rotary evaporation and the residue was dissolved in THF (100 mL). Layering the solution with hexanes (300 mL) and allowing to stand overnight yielded colorless crystals (5.20 g, 9.11 mmol, 62.8%). Single crystals suitable for x-ray diffraction were grown by vapor diffusion of n-pentane into a THF solution. ^{1}H NMR (400 MHz, CD_2Cl_2) δ 7.73 (d, J = 8.0 Hz, 2H), 7.46 (t, J = 7.6 Hz, 2H), 7.38 - 7.31 (m, 8H), 7.27 (d, J = 6.9 Hz, 6H), 7.22 (t, J = 7.5 Hz, 4H), 7.19 - 7.09 (m, 6H). ^{13}C NMR (101 MHz, CD_2Cl_2) δ 152.19 - 150.49 (m), 137.90 - 137.18 (m), 136.94 (t, J = 5.3 Hz), 135.89 (t, J = 5.7 Hz), 135.40,

133.89 (t, J = 9.8 Hz), 131.29, 130.78, 129.17, 129.04, 128.91 (t, J = 3.5 Hz), 128.70 (t, J = 3.6 Hz), 127.02 (t, J = 4.5 Hz). ^{31}P NMR (162 MHz, CD_2Cl_2) δ -18.28. IR (CCl_4 solution): 1,055 cm^{-1} (S-O). Elemental analysis for $C_{36}H_{28}OP_2S$: calc. C 75.77 H 4.95, found C 75.55 H 4.82.

$(SOP_2)RhCl$: A vial was charged with SOP_2 (103 mg, 0.181 mmol), $[(cod)RhCl]_2$ (44.6 mg, 0.0905 mmol), a magnetic stirbar, and THF (5 mL). The orange solution was refluxed for 30 min and cooled to room temperature. Solvent was removed in vacuo and benzene (10 mL) was added to the orange residue. The solution was heated to 80 ˚C and filtered while hot. The resulting clear yellow-orange solution was layered with pentane (20 mL) and allowed to stand at room temperature overnight to give a yellow microcrystalline solid (116 mg, 0.163 mmol, 90.6%). Crystals suitable for x-ray diffraction were grown by vapor diffusion of n-pentane into a THF solution. ^{1}H NMR (400 MHz, CD_2Cl_2) δ 8.38 (d, J = 7.9 Hz, 2H), 7.78 (q, J = 6.3 Hz, 4H), 7.69 (dd, J = 8.1, 3.7 Hz, 2H), 7.67 - 7.57 (m, 6H), 7.46 (m, J = 13.5, 7.0 Hz, 8H), 7.36 (t, J = 7.6 Hz, 4H). ^{13}C NMR (101 MHz, CD_2Cl_2) δ 157.43 - 156.13 (m), 135.03 (t, J = 19.5 Hz), 133.85 (dd, J = 13.4, 6.6 Hz), 133.44 (t, J = 7.7 Hz), 132.84, 132.66 - 131.70 (m), 131.57, 130.51, 130.28, 128.82 (t, J = 5.1 Hz), 128.19 (t, J = 5.2 Hz), 125.37 (t, J = 7.0 Hz). ^{31}P NMR (162 MHz, CD_2Cl_2) δ 47.33 (d, J = 148.4 Hz). Elemental analysis for $C_{36}H_{28}ClOP_2RhS$: calc. C 60.99 H 3.98, found C 61.08 H 4.14.

$(SOP_2)RhN_3$: A Schlenk tube was charged with $(SOP_2)RhCl$ (45.2 mg, 0.0638 mmol), TlN_3 (18.9 mg, 0.0766 mmol), CH_3CN (3 mL), and a magnetic stirbar. The suspension

was heated with rapid stirring at 90 ˚C for five days. After cooling to room temperature, the orange solution was filtered and the solvent was removed in vacuo. Benzene (10 mL) was added to the orange residue and the solution was heated to 80 ˚C. The orange solution was filtered while hot and the filtrate was lyophilized to give a fluffy orange powder (44.0 mg, 0.0615 mmol, 96.45). Single crystals suitable for x-ray diffraction were grown by cooling a concentrated THF to -35 ˚C. ^{1}H NMR (400 MHz, CD_3CN) δ 8.45 (d, J = 7.9 Hz, 2H), 7.89 (q, J = 6.2 Hz, 4H), 7.84 - 7.74 (m, 8H), 7.74 - 7.66 (m, 4H), 7.51 (m, 4H), 7.38 (dd, J = 9.3, 6.0 Hz, 2H), 7.27 (t, J = 7.6 Hz, 4H). ^{13}C NMR (101 MHz, CD_3CN) δ 137.13 (d, J = 15.8 Hz), 134.69, 134.24, 133.92, 133.52 (d, J = 19.7 Hz), 131.94, 130.84, 130.45, 129.39, 129.06, 128.69, 128.40, 125.86 - 125.49 (m). ^{31}P NMR (162 MHz, CD_3CN) δ 50.05 (d, J = 158.5 Hz). Elemental analysis for $C_{36}H_{28}N_3OP_2RhS$: calc. C 60.43 H 3.94, found C 59.60 H 4.29.

[(SOP_2)Rh(CH_3CN)][PF_6]: A Schlenk tube was charged with (SOP_2)RhCl (82.3 mg, 0.116 mmol), $TlPF_6$ (48.6 mg, 0.139 mmol), CH_3CN (5 mL), and a magnetic stirbar. The vessel was heated to 80 ˚C for 1 hr and then cooled to room temperature. The suspension was filtered and the resulting bright yellow solution was layered with toluene to give bright yellow crystals (70.4 mg, 0.0819 mmol, 70.6%). A single crystal for x-ray diffraction was selected from these crystals. ^{1}H NMR (400 MHz, CD_2Cl_2) δ 8.38 (d, J = 8.1 Hz, 2H), 7.78 (m, 8H), 7.69 - 7.50 (m, 8H), 7.45 (d, J = 6.4 Hz, 8H), 7.32 - 7.12 (m, 2H), 2.10 (d, J = 200.0 Hz, 3H). ^{13}C NMR (101 MHz, CD_2Cl_2) δ 155.34 - 154.56 (m), 134.74, 134.16 (dd, J = 15.7, 7.8 Hz), 133.31, 133.06 (t, J = 6.8 Hz), 132.21, 131.76, 131.20 - 130.36 (m), 129.85 (t, J = 5.6 Hz), 129.55 (t, J = 5.2 Hz), 129.34, 128.60 (d, J =

14.2 Hz), 126.50 (t, J = 7.3 Hz), 125.61, 3.08. ^{31}P NMR (162 MHz, CD_2Cl_2) δ 51.74 (d, J = 140.6 Hz). Elemental analysis for $C_{38}H_{31}F_6NOP_3RhS \bullet C_7H_8$: calc. C 56.79 H 4.13, found C 57.07 H 4.34.

(SOP_2)IrCl(COE): A vial was charged with SOP_2 (105 mg, 0.183 mmol), $[(COE)_2IrCl]_2$ (82.2 mg, 0.0917 mmol), THF (4 mL), and a magnetic stirbar. The solution was refluxed for 30 min, cooled to room temperature, and filtered. The solvent was removed in vacuo and the orange residue was triturated with pentane (3 x 10 mL). The solid was dissolved in benzene (10 mL) at 80 ˚C, filtered while hot, cooled, and lyophilized to give a yellow solid (136 mg, 0.150 mmol, 81.8%). ^{1}H NMR (400 MHz, CD_2Cl_2) δ 8.35 (d, J = 7.8 Hz, 2H), 7.70 (ddt, J = 7.5, 5.5, 3.4 Hz, 4H), 7.64 (t, J = 7.7 Hz, 2H), 7.60 (q, J = 3.5 Hz, 2H), 7.53 (t, J = 7.2 Hz, 2H), 7.47 - 7.40 (m, 4H), 7.37 (s, 2H), 7.29 (t, J = 7.3 Hz, 2H), 7.21 (q, J = 6.0 Hz, 4H), 7.11 (t, J = 7.6 Hz, 4H), 3.84 (br, 2H), 1.81 (br, 4H), 1.49 (br, 4H), 1.33 (br, 4H). ^{13}C NMR (101 MHz, CD_2Cl_2) δ 158.57, 134.31 (d, J = 25.8 Hz), 132.80 (q, J = 6.6, 6.0 Hz), 132.00, 131.44, 129.81, 129.56, 128.29 (d, J = 5.2 Hz), 128.01 (t, J = 4.9 Hz), 125.19 (t, J = 7.1 Hz), 31.47, 26.29 (d, J = 6.3 Hz). ^{31}P NMR (162 MHz, CD_2Cl_2) δ 29.69 (br, s). Elemental analysis for $C_{44}H_{42}ClIrOP_2S$: calc. C 58.17 H 4.66, found C 58.25 H 4.77.

(SOP_2)IrCl(H)(OTf): A vial was charged with (SOP_2)IrCl(COE) (116.6 mg, 0.128 mmol), CH_3CN (3 mL), and a magnetic stirbar. A solution of HOTf (18.3 mg, 0.122 mmol) in CH_3CN (2 mL) was added dropwise at room temperature resulting in an immediate lightening of the solution. After stirring for 5 min, the volatiles were removed

in vacuo to give a pale yellow residue. THF (2 mL) was added and a white microcrystalline solid formed from the supersaturated solution. The solution was decanted and the solids were washed with Et_2O (3 x 2 mL) and pentane (2 mL) and dried to give a white solid (78.3 mg, 0.0826 mmol, 64.3%). Single crystals suitable for x-ray diffraction of the CH_3CN adduct (with an outer-sphere triflate counteranion) were grown by vapor diffusion of Et_2O into a CH_3CH solution. ^{1}H NMR (400 MHz, CD_2Cl_2) δ 8.73 (d, J = 8.3 Hz, 2H), 8.01 (t, J = 7.8 Hz, 2H), 7.82 (t, J = 7.5 Hz, 2H), 7.76 (q, J = 6.8 Hz, 4H), 7.67 (dd, J = 15.6, 7.1 Hz, 4H), 7.57 (dt, J = 19.0, 7.2 Hz, 10H), 7.47 (t, J = 6.5 Hz, 4H), -19.13 (t, J = 13.4 Hz, 1H). ^{13}C NMR (101 MHz, CD_2Cl_2) δ 153.78 (t, J = 12.7 Hz), 134.91 (t, J = 3.8 Hz), 134.60 (t, J = 6.4 Hz), 134.20 (d, J = 5.0 Hz), 132.82, 132.25 (t, J = 6.2 Hz), 131.97, 129.23 (dt, J = 15.2, 5.7 Hz), 127.61-126.31 (m), 124.29 (t, J = 32.8 Hz). ^{31}P NMR (162 MHz, CD_2Cl_2) δ 28.85 (d, J = 11.2 Hz). ^{19}F NMR (376 MHz, CD_2Cl_2) δ -78.82. Elemental analysis for $C_{37}H_{29}ClF_3IrO_4P_2S_2$: calc. C 46.56 H 3.38, found C 46.86 H 3.08.

(SOP_2)IrCl: A Schlenk tube was charged with (SOP_2)IrCl(H)(OTf) (25.5 mg, 0.0269 mmol), proton sponge (1,8-bis(dimethylamino)naphthalene, 5.5 mg, 0.0256 mmol), THF (2 mL), and a magnetic stirbar. The mixture was heated at 80 ˚C for 30 min. and cooled to room temperature. The solvent was removed in vacuo and the resulting residue was extracted into hot benzene (3 mL) and filtered. A yellow solid (20.1 mg, 0.0252 mmol, 93.6%) was obtained by precipitation with pentane (5 mL) followed by drying in vacuo. Single crystals suitable for X-ray diffraction were grown by vapor diffusion into a THF solution. ^{1}H NMR (400 MHz, CD_2Cl_2) δ 8.42 (d, J = 7.7 Hz, 2H), 7.78 (dtd, J = 8.6, 5.7,

2.2 Hz, 4H), 7.62 (m, 10H), 7.45 (m, 8H), 7.40 - 7.31 (m, 4H). ^{13}C NMR (101 MHz, CD_2Cl_2) δ 157.68 (t, J = 15.8 Hz), 135.33, 133.84 - 133.20 (m), 132.33 (t, J = 3.4 Hz), 131.70 - 131.11 (m), 130.52 (d, J = 15.5 Hz), 128.79 (t, J = 5.3 Hz), 128.34 - 127.85 (m), 124.89 (t, J = 6.2 Hz). ^{31}P NMR (162 MHz, CD_2Cl_2) δ 47.60. Elemental analysis for $C_{36}H_{28}ClIrOP_2S$: calc. C 54.16 H 3.54, found C 55.01 H 3.84.

(SOP_2)Ir(O_2)Cl: A J. Young tube containing a yellow solution of (SOP_2)IrCl in CD_2Cl_2 was degassed by three freeze-pump-thaw cycles. Dioxygen was introduced to the tube which resulted in an immediate quenching of the color. NMR indicates complete conversion of (SOP_2)IrCl to (SOP_2)Ir(O_2)Cl. ^{1}H NMR (400 MHz, CD_2Cl_2) δ 8.40 (d, J = 7.9 Hz, 2H), 7.80 (m, 4H), 7.70 (t, J = 7.5 Hz, 2H), 7.53 (q, J = 7.1, 6.2 Hz, 4H), 7.40 (d, J = 6.4 Hz, 4H), 7.35 (s, 2H), 7.24 (m, 2H), 6.96 - 6.87 (m, 8H). ^{13}C NMR (101 MHz, CD_2Cl_2) δ 156.17 - 155.73 (m), 134.73 - 134.40 (m), 133.56, 133.20 (d, J = 11.3 Hz), 132.49 (dd, J = 11.3, 6.4 Hz), 131.44, 130.69, 128.64 (dt, J = 17.4, 5.9 Hz), 128.25, 126.07 - 125.64 (m). ^{31}P NMR (162 MHz, CD_2Cl_2) δ 20.52. IR: $\nu_{(O\text{-}O)}$ = 847 cm^{-1}. The O_2 ligand is slowly labile under vacuum; as such, combustion analysis data were not obtained. Single crystals for X-ray diffraction were grown by allowing a dilute sample of (SOP_2)Ir(O_2)Cl in CH_3CN under 1 atm air to stand for several days.

(SOP_2)Ni(CO): A vial was charged with SOP_2 (243 mg, 0.426 mmol), (PPh_3)$_2$Ni(CO)$_2$ (272 mg, 0.426 mmol), THF (5 mL), and a magnetic stirbar. The mixture was refluxed for 30 min. Solvent was removed in vacuo. The resulting orange residue was triturated with pentane (5 mL) to give a yellow solid. Volatiles were again removed and the solids

were washed with Et_2O (3 x 3 mL) and recrystallized by dissolving in a minimum volume of THF (ca. 3 mL) and layering with pentane (ca. 15 mL). The title compound was thus isolated as a yellow-orange solid (238 mg, 0.362 mmol, 85.0%). ^{1}H NMR (400 MHz, CD_2Cl_2) δ 8.39 (d, J = 8.2 Hz, 2H), 7.70 (d, J = 5.8 Hz, 4H), 7.61 (t, J = 7.2 Hz, 2H), 7.44 - 7.30 (m, 10H), 7.11 (t, J = 7.6 Hz, 2H), 6.86 (t, J = 7.7 Hz, 4H), 6.69 (q, J = 7.4, 6.2 Hz, 4H). ^{13}C NMR (101 MHz, CD_2Cl_2) δ 201.08 (t, J = 8.0 Hz), 157.05 (t, J = 21.8 Hz), 137.93 (t, J = 19.6 Hz), 135.02 (t, J = 14.7 Hz), 133.91 - 132.05 (m), 131.92 - 130.76 (m), 129.62, 128.21 (td, J = 11.0, 5.7 Hz), 124.55 (t, J = 6.9 Hz). ^{31}P NMR (162 MHz, CD_2Cl_2) δ 41.25 (s). Elemental analysis for $C_{37}H_{28}NiO_2P_2S$: calc. C 67.61 H 4.29, found C 67.35 H 4.58.

[(SOP_2)NiCl][PF_6]: A vial was charged with SOP_2 (28.7 mg, 0.0503 mmol), (DME)$NiCl_2$ (11.1 mg, 0.0503 mmol), $TlPF_6$ (18.5 mg, 0.0529 mmol), THF (3 mL), and a magnetic stirbar. The suspension was refluxed for 2 hr and the solvent was removed in vacuo. Addition of CH_3CN (2 mL) resulted in formation of a deep purple solution which was filtered and dried in vacuo. The brown residue was triturated with benzene (5 mL) to give an orange-yellow solid (21.2 mg, 0.0262 mmol, 52.1%). ^{1}H NMR (400 MHz, CD_3CN) δ 8.38 (d, J = 8.1 Hz, 1H), 8.03 (d, J = 6.0 Hz, 2H), 7.88 (d, J = 7.2 Hz, 2H), 7.70 (dd, J = 29.2, 7.5 Hz, 4H), 7.59 - 7.32 (m, 4H), 7.19 (d, J = 7.5 Hz, 2H). ^{13}C NMR (101 MHz, CD_3CN) δ 137.06, 135.62, 135.30, 133.11, 132.54, 129.68, 128.68, 127.79. ^{31}P NMR (162 MHz, CD_3CN) δ 49.87 (br). Elemental analysis for $C_{36}H_{28}ClF_6NiOP_3S$: calc. C 53.40 H 3.49, found C 52.57 H 4.00.

(SOP_2)Pd(PPh_3): A vial was charged with SOP_2 (52.3 mg, 0.0917 mmol), $(PPh_3)_4Pd$ (106 mg, 0.0917 mmol), and THF (5 mL). A deep red-orange solution was formed immediately. Layering the solution with pentane (15 mL) provided red-orange blocks of the title compound (76.1 mg, 0.0810 mmol, 88.4%). Single crystals suitable for x-ray diffraction were obtained by vapor diffusion of Et_2O into a saturated THF solution. ^{1}H NMR (400 MHz, CD_2Cl_2) δ 8.44 (d, J = 8.0 Hz, 2H), 7.56 (t, J = 7.5 Hz, 2H), 7.43 - 7.34 (m, 8H), 7.26 (t, J = 7.4 Hz, 2H), 7.18 (q, J = 8.8, 7.6 Hz, 5H), 7.13 - 7.02 (m, 10H), 7.00 - 6.90 (m, 4H), 6.90 - 6.80 (m, 10H). ^{13}C NMR (101 MHz, CD_2Cl_2) δ 157.19 (dd, J = 19.7, 4.1 Hz), 139.91 - 138.54 (m), 135.95, 134.27 - 132.94 (m), 131.98 (dt, J = 17.9, 8.5 Hz), 130.39, 129.70, 128.91, 128.11, 127.71 (td, J = 9.1, 8.3, 4.4 Hz), 125.17, 124.66 (t, J = 6.3 Hz). ^{31}P NMR (162 MHz, CD_2Cl_2) δ 30.43 (t, J = 42.3 Hz, 1P), 21.09 (d, J = 42.3 Hz, 2P). Elemental analysis for $C_{54}H_{43}OP_3PdS$: calc. C 69.05 H 4.61, found C 69.01 H 4.82.

(SOP_2)Pt(PPh_3): A vial was charged with SOP_2 (46.8 mg, 0.0820 mmol), $(PPh_3)_4Pt$ (102 mg, 0.0820 mmol), and benzene (5 mL). The solution was agitated until all solids were dissolved and allowed to stand for 2 hr. Layering the deep red solution with pentane (15 mL) provided red crystals of the title compound (59.0 mg, 0.0574 mmol, 70.0%). Single crystals suitable for x-ray diffraction were obtained by vapor diffusion of Et_2O into a saturated CH_2Cl_2 solution. ^{1}H NMR (400 MHz, CD_2Cl_2) δ 8.70 (d, J = 8.2 Hz, 2H), 7.53 (ddd, J = 8.1, 5.5, 2.7 Hz, 2H), 7.45 (ddd, J = 10.1, 7.3, 2.1 Hz, 6H), 7.39 (d, J = 2.6 Hz, 2H), 7.24 (m, 4H), 7.19 - 7.11 (m, 4H), 7.07 (t, J = 7.5 Hz, 6H), 7.00 (d, J = 7.6 Hz, 2H), 6.99 - 6.81 (m, 15H). ^{13}C NMR (101 MHz, CD_2Cl_2) δ 159.89 (t, J = 18.7 Hz), 139.90,

139.55, 138.37, 136.92 (d, J = 10.9 Hz), 133.79 - 133.08 (m), 131.33 (q, J = 8.3 Hz), 130.68, 129.84, 128.49, 128.20 (d, J = 17.3 Hz), 127.79, 127.65 - 127.21 (m), 124.18 (t, J = 7.3 Hz). The ^{31}P and ^{195}Pt NMR spectra display complicated ^{31}P-^{31}P and ^{31}P-^{195}Pt coupling. As such, their simulations are described in a separate section and their signal positions are listed here. ^{31}P NMR (162 MHz, CD_2Cl_2) δ 44.55, 44.08, 43.90, 43.86, 43.70, 43.04, 31.19, 31.12, 30.69, 30.66, 30.59, 28.94, 28.51, 28.41, 27.98, 18.06, 18.03, 17.57, 17.55, 13.77, 13.32, 13.26, 12.80. ^{195}Pt NMR (86 MHz, CD_2Cl_2) δ -4703.92, -4752.83, -4753.47, -4754.03, -4760.85, -4762.16, -4803.37, -4810.79, -4860.51. Elemental analysis for $C_{54}H_{43}OP_3PtS$: calc. C 63.09 H 4.22, found C 63.43 H 4.46.

(SOP_2)Pd(CO): To a J. Young NMR tube was added (SOP_2)Pd(PPh_3) and CD_2Cl_2 (0.7 mL). The inky yellow-orange solution was degassed by three freeze-pump-thaw cycles and 1 atm CO was introduced. The solution became more yellow. NMR indicated quantitative conversion to a new species. The NMR solution was transferred a solution IR cell in order to record the C-O stretch. ^{1}H NMR (300 MHz, CD_2Cl_2) δ 8.36 (d, J = 8.2 Hz, 2H), 7.59 (t, J = 7.3 Hz, 2H), 7.39 - 7.19 (m, 14H), 7.15 (t, J = 7.3 Hz, 2H), 6.94 (t, J = 7.6 Hz, 4H), 6.69 (dt, J = 7.9, 4.8 Hz, 2H). ^{31}P NMR (121 MHz, CD_2Cl_2) δ 21.38. IR: ν(C–O) = 1985 cm^{-1}.

(SOP_2)Pt(CO): To a J. Young NMR tube was added (SOP_2)Pt(PPh_3) and CD_2Cl_2 (0.7 mL). The red-orange solution was degassed by three freeze-pump-thaw cycles and 1 atm CO was introduced. The solution became more yellow. NMR indicated quantitative conversion to a new species. The NMR solution was transferred a solution IR cell in

order to record the C-O stretch. ^{1}H NMR (300 MHz, CD_2Cl_2) δ 8.18 (s, 2H), 7.74 - 7.62 (m, 6H), 7.57 (d, J = 7.0 Hz, 2H), 7.54 - 7.39 (m, 10H), 7.10 (q, J = 7.0, 6.2 Hz, 4H), 6.90 (t, J = 7.6 Hz, 2H), 6.75 (s, 2H). ^{31}P NMR (121 MHz, CD_2Cl_2) δ 27.82 (br). IR: ν(C–O) = 1945 cm^{-1}.

[(SOP_2)PdCl][PF_6]: To a Schlenk tube were added SOP_2 (56.1 mg, 0.0983 mmol), (cod)$PdCl_2$ (28.1 mg, 0.0983 mmol), $TlPF_6$ (41.2 mg, 0.118 mmol), CH_3CN (3 mL), and a magnetic stirbar. The suspension was heated to 80 ˚C for 1 hr, cooled, and filtered. Benzene (10 mL) was layered onto the yellow solution which precipitated a yellow microcrystalline solid. The solids were washed with benzene (3 x 2 mL) and pentane (3 x 2 mL) and dried to give a pale yellow solid (68.3 mg, 0.0797 mmol, 81.0%). Single crystals suitable for x-ray diffraction were grown by diffusion of Et_2O into a CH_3CN solution. ^{1}H NMR (400 MHz, CD_2Cl_2) δ 8.66 (d, J = 8.2 Hz, 2H), 8.16 (t, J = 7.8 Hz, 2H), 8.00 (t, J = 7.4 Hz, 2H), 7.75 (dd, J = 8.0, 4.1 Hz, 2H), 7.68 (q, J = 6.6, 5.7 Hz, 8H), 7.64 - 7.47 (m, 12H). ^{13}C NMR (101 MHz, CD_2Cl_2) δ 149.41 (t, J = 15.3 Hz), 136.91, 135.89, 134.15 (t, J = 6.8 Hz), 133.52 (t, J = 7.3 Hz), 133.28, 131.83 (t, J = 22.9 Hz), 129.96 (t, J = 5.9 Hz), 129.80 - 129.21 (m), 128.98 (t, J = 6.3 Hz), 125.72 - 124.28 (m). ^{31}P NMR (162 MHz, CD_2Cl_2) δ 49.44 (s), -144.47 (septet, J = 709.7 Hz). ^{19}F NMR (376 MHz, CD_2Cl_2) δ -73.25 (d, J = 710.3 Hz). Elemental analysis for $C_{36}H_{28}F_6OP_3PdS \bullet C_6H_6$: calc. C 53.92 H 3.66, found C 53.72 H 3.75.

[(SOP_2)PtCl][PF_6]: To a Schlenk tube were added SOP_2 (48.8 mg, 0.0855 mmol), (cod)$PtCl_2$ (32.0 mg, 0.0855 mmol), $TlPF_6$ (35.8 mg, 0.103 mmol), CH_3CN (3 mL), and a

magnetic stirbar. The suspension was heated to 80 ˚C for 1 hr., cooled, and filtered. Benzene (10 mL) was layered onto the colorless solution which precipitated a white microcrystalline solid. The solids were washed with benzene (3 x 2 mL) and pentane (3 x 2 mL) and dried to give a colorless solid (68.0 mg, 0.0719 mmol, 84.0%). Single crystals suitable for x-ray diffraction were grown by diffusion of Et_2O into a CH_3CN solution. ^1H NMR (400 MHz, CD_2Cl_2) δ 8.68 (d, J = 7.8 Hz, 2H), 8.12 (t, J = 8.0 Hz, 2H), 7.98 (t, J = 7.5 Hz, 2H), 7.81 (d, J = 6.4 Hz, 2H), 7.74 (t, J = 7.1 Hz, 4H), 7.68 (t, J = 6.8 Hz, 2H), 7.63 (d, J = 8.1 Hz, 4H), 7.58 - 7.46 (m, 10H). ^{13}C NMR (101 MHz, CD_2Cl_2) δ 150.07 (t, J = 13.0 Hz), 136.81, 135.72, 135.41, 134.06 (t, J = 6.8 Hz), 133.70 (t, J = 7.1 Hz), 133.37 (d, J = 8.4 Hz), 132.15, 131.87, 131.62, 130.01 (t, J = 6.0 Hz), 129.46 (t, J = 6.0 Hz), 128.54 - 128.15 (m), 124.82, 124.52, 124.21, 123.89. ^{31}P NMR (162 MHz, CD_2Cl_2) δ 45.95 (m, J_{PPt} = 2494 Hz), -144.47 (septet, J = 709.7 Hz). ^{19}F NMR (376 MHz, CD_2Cl_2) δ -73.25 (d, J = 710.3 Hz). Elemental analysis for $C_{36}H_{28}F_6OP_3PtS \bullet C_6H_6$: calc. C 49.25 H 3.35, found C 48.78 H 3.40.

[(SOP_2)PdMe][PF_6]: A Schlenk tube was charged with SOP_2 (54.9 mg, 0.0962 mmol), (cod)Pd(Me)Cl (25.5 mg, 0.0962 mmol), $TlPF_6$ (40.3 mg, 0.115 mmol), CH_3CN (3 mL), and a magnetic stirbar. The suspension was heated to 80 ˚C for 1 hr., cooled, and filtered. Solvent was removed in vacuo and the residue was dissolved in THF (3 mL). Layering the solution with Et_2O (15 mL) precipitated an off-white solid which was washed with Et_2O (3 x 3 mL) and pentane (3 x 3 mL) and dried to give the title compound (61.1 mg 0.0730, 75.9%). Single crystals suitable for x-ray diffraction were grown by diffusion of Et_2O into a CH_3CN solution. ^1H NMR (400 MHz, CD_2Cl_2) δ 8.67 (d, J = 8.2 Hz, 2H),

8.06 (t, J = 7.7 Hz, 2H), 7.91 (t, J = 7.6 Hz, 2H), 7.66 (m, 14H), 7.55 (t, J = 7.7 Hz, 4H), 7.37 (q, J = 6.6 Hz, 4H), 1.03 (t, J = 6.0 Hz, 3H). ^{13}C NMR (101 MHz, CD_2Cl_2) δ 149.10 - 148.61 (m), 135.83 (d, J = 3.3 Hz), 135.32, 134.94, 133.66 (t, J = 7.8 Hz), 133.24 (t, J = 6.7 Hz), 132.82, 132.43, 129.96 (t, J = 5.7 Hz), 129.62 (t, J = 5.7 Hz), 128.54 (t, J = 5.2 Hz), 128.27, 126.73, 126.58 - 126.13 (m), 126.03, 125.77, 5.10. ^{31}P NMR (162 MHz, CD_2Cl_2) δ 43.94, -144.47 (septet, J = 709.7 Hz). ^{19}F NMR (376 MHz, CD_2Cl_2) δ -73.25 (d, J = 710.3 Hz). Elemental analysis for $C_{37}H_{31}F_6OP_3PdS$: calc. C 53.09 H 3.73, found C 52.74 H 4.28.

[(SOP_2)PtMe][PF_6]: A Schlenk tube was charged with SOP_2 (51.0 mg, 0.0894 mmol), (cod)Pt(Me)Cl (31.6 mg, 0.0894 mmol), $TlPF_6$ (37.5 mg, 0.107 mmol), CH_3CN (3 mL), and a magnetic stirbar. The suspension was heated to 80 ˚C for 1 hr., cooled, and filtered. Solvent was removed in vacuo and the residue was dissolved in THF (3 mL). Layering the solution with Et_2O (15 mL) precipitated a white solid which was washed with Et_2O (3 x 3 mL) and pentane (3 x 3 mL) and dried to give the title compound (73.8 mg, 0.0797 mmol, 89.2%). Single crystals suitable for x-ray diffraction were grown by diffusion of Et_2O into a CH_3CN solution. ^{1}H NMR (400 MHz, CD_2Cl_2) δ 8.68 (d, J = 8.2 Hz, 2H), 8.03 (t, J = 7.8 Hz, 2H), 7.89 (t, J = 7.4 Hz, 2H), 7.68 (ddd, J = 27.9, 20.7, 6.3 Hz, 14H), 7.53 (t, J = 7.7 Hz, 4H), 7.37 (dd, J = 12.4, 4.5 Hz, 4H), 1.05 (m, J_{HPt} = 32.8 Hz , J_{HP} = 7.0 Hz, 3H). ^{13}C NMR (101 MHz, CD_2Cl_2) δ 150.10 (t, J = 12.9 Hz), 135.96, 135.02 (d, J = 14.5 Hz), 133.85 (t, J = 8.1 Hz), 133.38 (t, J = 6.6 Hz), 133.09, 132.75, 129.95 (t, J = 5.9 Hz), 129.50 (t, J = 6.0 Hz), 128.33 (t, J = 5.3 Hz), 125.96 (t, J = 29.2 Hz), 124.68 (t, J = 31.8 Hz), -2.93 to -10.13 (m, J_{CPt} = 582 Hz , J_{CP} = 6.4 Hz). ^{31}P NMR (162 MHz,

CD_2Cl_2) δ 46.0 (m, J_{PPt} = 2837 Hz), -144.48 (septet, J = 710 Hz). ^{19}F NMR (376 MHz, CD_2Cl_2) δ -73.25 (d, J = 710.3 Hz). Elemental analysis for $C_{72}H_{56}F_{12}O_2P_6Pd_2S_2$: calc. C 48.01 H 3.38, found C 47.84 H 3.65.

$[(SOP_2)Pd]_2[PF_6]_2$: A Schlenk tube was charged with SOP_2 (68.2 mg, 0.120 mmol), (cod)$PdCl_2$ (17.1 mg, 0.0598 mmol), $(PPh_3)_4Pd$ (69.1 mg, 0.0598 mmol), $TlPF_6$ (41.8 mg, 0.120 mmol), CH_3CN (3 mL), and a magnetic stirbar. The suspension was heated to 80 ˚C for 12 hr., cooled, and filtered. Solvent was removed in vacuo and the deep red residue was dissolved in THF (2 mL). Upon standing, an orange precipitate formed. The solids were washed with cold THF (2 x 2 mL), Et_2O (2 x 2 mL), and pentane (2 x 2 mL). Drying the solid gave the title compound (45.5 mg, 0.0554 mmol, 46.3%). Single crystals suitable for x-ray diffraction were grown by cooling a hot saturated THF solution. ^1H NMR (400 MHz, CD_2Cl_2) δ 8.39 (br d, J = 7.6 Hz, 2H), 8.07 (t, J = 7.8 Hz, 2H), 7.91 (t, J = 7.5 Hz, 2H), 7.60 (ddd, J = 13.7, 8.8, 5.2 Hz, 6H), 7.52 - 7.37 (m, 6H), 7.28 (d, J = 6.1 Hz, 8H), 7.22 (q, J = 7.1, 5.5 Hz, 4H), 7.08 (t, J = 7.8 Hz, 4H), 7.02 (d, J = 6.8 Hz, 2H), 6.90 (dp, J = 15.4, 5.7, 4.7 Hz, 14H), 6.75 - 6.57 (br, 4H), 6.43 (br, J = 11.1 Hz, 2H). ^{13}C NMR (101 MHz, CD_2Cl_2) δ 146.43 (d, J = 17.2 Hz), 135.90, 134.93 (d, J = 14.5 Hz), 134.56 - 134.12 (m), 133.67, 133.15 (dd, J = 21.6, 14.5 Hz), 132.27 (t, J = 14.1 Hz), 131.45, 129.43 (d, J = 12.7 Hz), 128.93, 128.47 (d, J = 11.0 Hz), 128.07, 126.02 (d, J = 14.0 Hz), 125.71, 125.43 (d, J = 14.9 Hz). ^{31}P NMR (162 MHz, CD_2Cl_2) δ 34.12 (br), 29.66 (br), -144.48 (septet, J = 710 Hz). ^{19}F NMR (376 MHz, CD_2Cl_2) δ -73.25 (d, J = 710.3 Hz). Elemental analysis for $C_{37}H_{31}F_6OP_3PtS$: calc. C 52.60 H 3.43, found C 52.51 H 3.62.

[(SOP_2)Pd($NCCH_3$)][PF_6]: A vial was charged with SOP_2 (92.0 mg, 0.161 mmol), $[Pd(NCCH_3)_4][PF_6]_2$ (90.3 mg, 0.161 mmol), and CH_3CN (5 mL). The solution immediately turned bright yellow. The solvent was reduced to 2 mL in vacuo and Et_2O (10 mL) was added to produce bright yellow crystals which were dried in vacuo (162 mg, 0.148 mmol, 91.9%). The compound is sensitive to nucleophilic solvents including alcohols and THF and slowly decomposes in the solid state at room temperature to give some palladium black. ^{1}H NMR (400 MHz, CD_2Cl_2) δ 8.61 (d, J = 8.1 Hz, 1H), 8.19 (t, J = 7.8 Hz, 1H), 8.08 (t, J = 7.4 Hz, 1H), 7.90 (dt, J = 8.5, 4.6 Hz, 1H), 7.72 (qd, J = 7.2, 5.8, 2.6 Hz, 6H), 7.62 (dt, J = 5.3, 3.3 Hz, 4H). ^{13}C NMR (101 MHz, CD_2Cl_2) δ 148.96 (t, J = 15.1 Hz), 137.68, 136.50, 135.54, 134.14, 133.64 (dt, J = 31.8, 7.4 Hz), 130.41 (dd, J = 19.2, 8.5 Hz), 129.96, 129.33, 128.09, 123.24 (d, J = 7.6 Hz), 122.97 (d, J = 7.0 Hz), 122.72, 119.00 (d, J = 19.5 Hz), 118.57 (d, J = 12.0 Hz). ^{31}P NMR (162 MHz, CD_2Cl_2) δ 53.97 (s), -144.48 (septet, J = 710 Hz). ^{19}F NMR (376 MHz, CD_2Cl_2) δ -73.25 (d, J = 710.3 Hz). Spectroscopically pure samples submitted for combustion analysis were routinely low on C which may reflect their thermal sensitivity.

This chapter was reproduced in part with permission from

Suess, D. L. M.; Peters, J. C. *Organometallics* **2012**, *31*, 5213–5222.

(1) (a) Choi, J.; MacArthur, A. H. R.; Brookhart, M.; Goldman, A. S. *Chem. Rev.,* **2011,** *111*, 1761; (b) Julian, L. D.; Hartwig, J. F. *J. Am. Chem. Soc.,* **2010,** *132*, 13813; (c) van der Boom, M. E.; Milstein, D. *Chem. Rev.,* **2003,** *103*, 1759; (d) Denney, M. C.; Smythe, N. A.; Cetto, K. L.; Kemp, R. A.; Goldberg, K. I. *J. Am. Chem. Soc.,* **2006,** *128*, 2508; (e) Fafard, C. M.; Adhikari, D.; Foxman, B. M.; Mindiola, D. J.; Ozerov, O. V. *J. Am. Chem. Soc.,* **2007,** *129*, 10318; (f) Whited, M. T.; Grubbs, R. H. *J. Am. Chem. Soc.,* **2008,** *130*, 5874; (g) Gunanathan, C.; Ben-David, Y.; Milstein, D. *Science,* **2007,** *317*, 790.
(2) Bart, S. C.; Chłopek, K.; Bill, E.; Bouwkamp, M. W.; Lobkovsky, E.; Neese, F.; Wieghardt, K.; Chirik, P. J. *J. Am. Chem. Soc.,* **2006,** *128*, 13901.
(3) Zhang, J.; Leitus, G.; Ben-David, Y.; Milstein, D. *J. Am. Chem. Soc.,* **2005,** *127*, 10840.
(4) (a) Poverenov, E.; Gandelman, M.; Shimon, L. J. W.; Rozenberg, H.; Ben-David, Y.; Milstein, D. *Chem. Eur. J.,* **2004,** *10*, 4673; (b) Fulmer, G. R.; Kaminsky, W.; Kemp, R. A.; Goldberg, K. I. *Organometallics,* **2011,** *30*, 1627.
(5) (a) Bernskoetter, W. H.; Schauer, C. K.; Goldberg, K. I.; Brookhart, M. *Science,* **2009,** *326*, 553; (b) Hebden, T. J.; St John, A. J.; Gusev, D. G.; Kaminsky, W.; Goldberg, K. I.; Heinekey, D. M. *Angew. Chem. Int. Ed.,* **2010,** *50*, 1873; (c) Hojilla Atienza, C. C.; Bowman, A. C.; Lobkovsky, E.; Chirik, P. J. *J. Am. Chem. Soc.,* **2010,** *132*, 16343; (d) Walstrom, A.; Pink, M.; Yang, X.; Tomaszewski, J.; Baik, M.-H.; Caulton, K. G. *J. Am. Chem. Soc.,* **2005,** *127*, 5330; (e) Watson, L. A.; Ozerov, O. V.; Pink, M.; Caulton, K. G. *J. Am. Chem. Soc.,* **2003,** *125*, 8426.
(6) Schöffel, J.; Rogachev, A. Y.; DeBeer George, S.; Burger, P. *Angew. Chem. Int. Ed.,* **2009,** *48*, 4734.
(7) Poverenov, E.; Efremenko, I.; Frenkel, A. I.; Ben-David, Y.; Shimon, L. J. W.; Leitus, G.; Konstantinovski, L.; Martin, J. M. L.; Milstein, D. *Nature,* **2008,** *455*, 1093.
(8) (a) Crossley, I. R.; Hill, A. F.; Willis, A. C. *Organometallics,* **2005,** *24*, 1062; (b) Bontemps, S.; Sircoglou, M.; Bouhadir, G.; Puschmann, H.; Howard, J. A. K.; Dyer, P. W.; Miqueu, K.; Bourissou, D. *Chem. Eur. J.,* **2008,** *14*, 731.
(9) Derrah, E. J.; Ladeira, S.; Bouhadir, G.; Miqueu, K.; Bourissou, D. *Chem. Commun. (Camb.),* **2011,** *47*, 8611.
(10) Calligaris, M.; Carugo, O. *Coord. Chem. Rev.,* **1996,** *153*, 83.
(11) (a) Chen, M. S.; White, M. C. *J. Am. Chem. Soc.,* **2004,** *126*, 1346; (b) Mariz, R.; Luan, X.; Gatti, M.; Linden, A.; Dorta, R. *J. Am. Chem. Soc.,* **2008,** *130*, 2172.
(12) Siah, S.-Y.; Leung, P.-H.; Mok, K. F. *Polyhedron,* **1994,** *13*, 3253.
(13) Searches were performed on the Cambridge Structural Database with all updates up to and including May 2011.
(14) Maire, P.; Sreekanth, A.; Büttner, T.; Harmer, J.; Gromov, I.; Rüegger, H.; Breher, F.; Schweiger, A.; Grützmacher, H. *Angew. Chem. Int. Ed.,* **2006,** *45*, 3265.
(15) Vaska, L. *Science,* **1963,** *140*, 809.
(16) Lebel, H.; Ladjel, C.; Bélanger-Gariépy, F.; Schaper, F. *J. Organomet. Chem,* **2008,** *693*, 2645.
(17) Read, C. A.; Roper, W. R. *J. Chem. Soc., Dalton Trans.,* **1973**, 1370.
(18) Hou, H.; Rheingold, A. L.; Kubiak, C. P. *Organometallics,* **2005,** *24*, 231.
(19) Kudo, K.; Hidai, M.; Uchida, Y. *J. Organomet. Chem,* **1971,** *33*, 393.
(20) Grevin, J.; Kalck, P.; Daran, J.; Vaissermann, J.; Bianchini, C. *Inorg. Chem.,* **1993,** *32*, 4965.
(21) Booth, G.; Chatt, J.; Chini, P. *Chem. Commun.,* **1965**, 639.

(22) (a) Driver, T. G.; Williams, T. J.; Labinger, J. A.; Bercaw, J. E. *Organometallics,* **2007,** *26*, 294; (b) Thomas, J. C.; Peters, J. C. *J. Am. Chem. Soc.,* **2003,** *125*, 8870; (c) Rendina, L. M.; Puddephatt, R. J. *Chem. Rev.,* **1997,** *97*, 1735; (d) Shilov, A. E.; Shul'pin, G. B. *Chem. Rev.,* **1997,** *97*, 2879.
(23) DuBois, D. L.; Miedaner, A. *J. Am. Chem. Soc.,* **1987,** *109*, 113.
(24) Fernández, I.; Khiar, N. *Chem. Rev.,* **2003,** *103*, 3651.
(25) SOP_2 d^8 complexes of Rh, Ir, Pd, and Pt were selected because each metal is similar in size (Ni is significantly smaller) and because they have the same formal d electron count.
(26) Whited, M. T.; Rivard, E.; Peters, J. C. *Chem. Commun.,* **2006**, 1613.

Chapter 6 Ligand Design for the Site-Selective Installation of Pd and Pt Centers to Generate Homo- and Heteropolymetallic Motifs

6.1 Background

Natural and synthetic polymetallic reaction sites mediate a wide range of small molecule transformations that have not been realized in monometallic analogs.[1] For example, synthetic bimetallic complexes that contain d^8-d^8 interactions display unusual photochemical reactivity[2] and have interesting electronic structures[3] owing to the metal-metal orbital interaction. Studies of these systems—and of polymetallic complexes more generally—are enhanced by the synthetic ability to rationally generate specific homo- and heteropolymetallics of interest.[4] This chapter describes my work toward the synthesis and site-selective metallation of polynucleating ligands that feature a common nitrogen-rich pincer-type framework. I herein establish the utility of this family of ligands for the site-selective installation of palladium and platinum centers which can result in bi- and trimetallic systems featuring d^8-d^8 interactions in the solid-state and in solution.

The four ligands described in this chapter feature two or three tridentate binding sites. Common to each ligand is a monoanionic, bis(quinolinyl)amide (BQA) pincer-type binding site. Decoration of the pincer scaffold with one or two neutral binding sites affords access to the polymetallic complexes of interest herein. I chose to target Pd and Pt species due to the Peters group's prior experience with the chemistry of group 10 BQA complexes,[5] and due to their comparatively low lability by comparison to first row late metals.

6.2 Results and discussion

The ligand synthesis of the dinucleating $L1^{R}H$ series is accomplished in three steps from 8-bromo-2-methylquinoline (Scheme 6.1). Oxidation of **1** with SeO_2 provides

Scheme 6.1 Synthesis of $L1^{R}H$ ligands

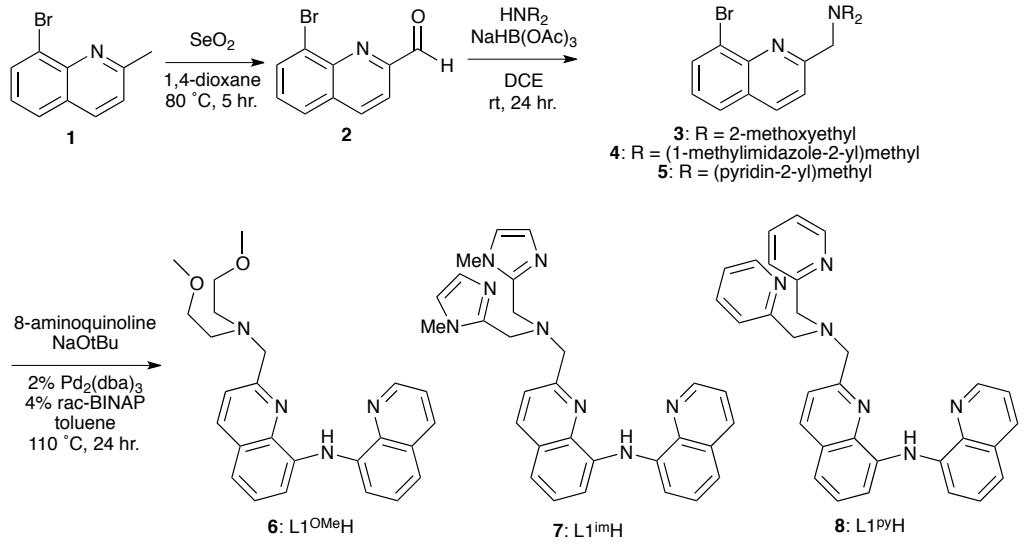

access to aldehyde **2**. Reductive amination of **2** with $NaHB(OAc)_3$ and the appropriate secondary amine installs the neutral tridentate binding sites in amine intermediates **3**, **4**, and **5**. The BQA binding pocket is generated by Pd-mediated C-N cross-coupling of **3**, **4**, and **5** with 8-aminoquinoline to give yellow ligands $L1^{OMe}H$, $L1^{im}H$, and $L1^{py}H$, respectively. The latter transformation proceeds to remarkably high conversion (>90%) given the potential for these ligands to poison the palladium cross-coupling catalyst.

A nonadentate, trinucleating ligand ($L2^{py}H$) is prepared in an analogous synthesis from **5** and 8-amino-2-methylquinoline (Scheme 6.2). Phthalimide protection of **10** to give **11** which allows for facile SeO_2 oxidation of the 2-methyl group to provide aldehyde **12**. Reductive amination with 2,2'-dipicolylamine and $NaHB(OAc)_3$ followed by

Scheme 6.2 Synthesis of L2^{py}H

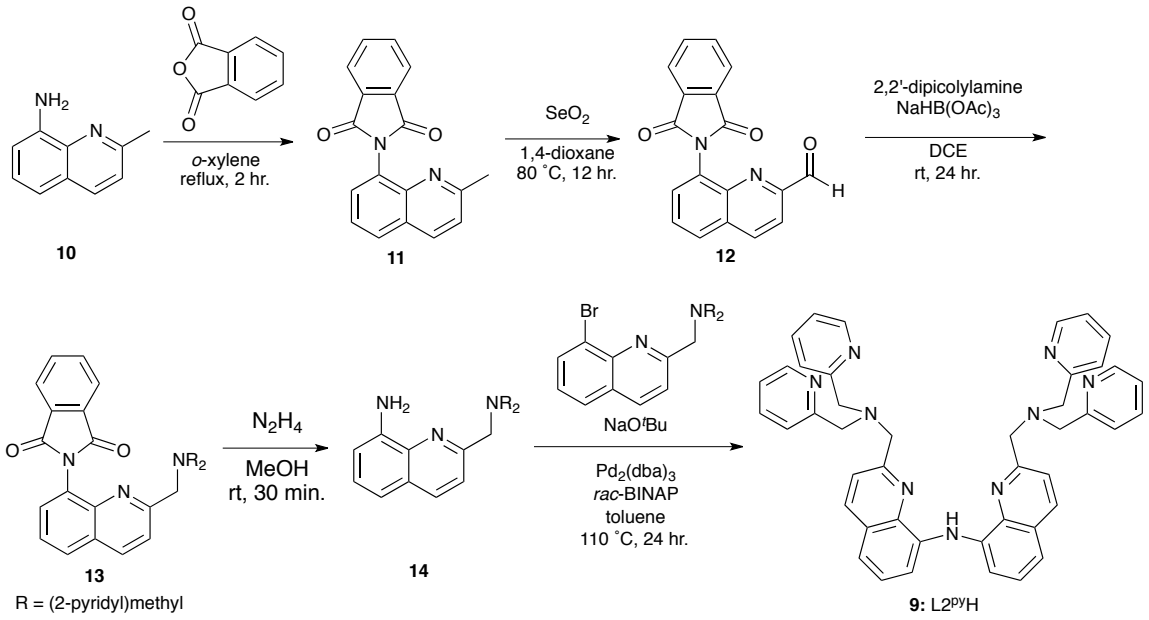

phthalimide deprotection gives amine **14**. Cross-coupling with **5** provides the inky yellow ligand L2^{py}H.

The installation of palladium into the anionic binding site of L1^{OMe}H is readily achieved by reaction with (COD)Pd(Me)Cl and catalytic Et_3N to form red, neutral L1^{OMe}PdCl with concomitant loss of methane. Alternatively, L1^{OMe}PdCl may be generated using (COD)$PdCl_2$ and stoichiometric Et_3N; however, the use of (COD)Pd(Me)Cl obviates the need to purify L1^{OMe}PdCl from Et_3N•HCl. ^{1}H NMR spectroscopy of L1^{OMe}PdCl shows the disappearance of the bis(quinolinyl)amine resonance. The solid-state structure of L1^{OMe}PdCl (determined by X-ray crystallography, Figure 6.1) confirms the installation of palladium into the bis(quinolinyl)amido site; the neutral bis(2-methoxyethyl)amine binding site remains open.

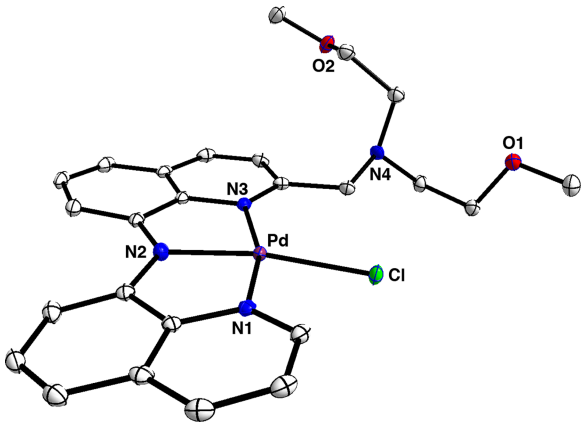

Figure 6.1 Displacement ellipsoid (40%) representation of L1^{OMe}PdCl. H atoms are omitted for clarity. Selected distances and angles: Pd–N1 = 2.0212(17) Å; Pd–N2 = 1.9645(17) Å; Pd–N3 = 2.0846(17) Å; Pd–Cl1 = 2.3492(5) Å.

Reaction between L1^{im}H, (COD)PdCl$_2$, and Et$_3$N affords the red salt [L1^{im}Pd]Cl, the solid-state structure of which demonstrates that one imidazole occupies the coordination site trans to the amide, thereby forming an eight-member ring (Figure 6.2). Variable-

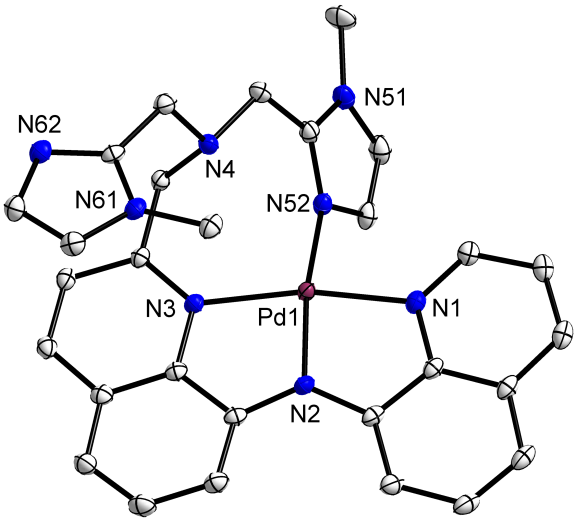

Figure 6.2 Displacement ellipsoid (40%) representation of [L1^{im}Pd]Cl. H atoms, counteranion, and solvent molecules are omitted for clarity. Selected distances and angles: Pd–N1 = 2.010(7) Å; Pd–N2 = 1.965(7) Å; Pd–N3 = 2.051(7) Å; Pd–N52 = 2.069(7) Å.

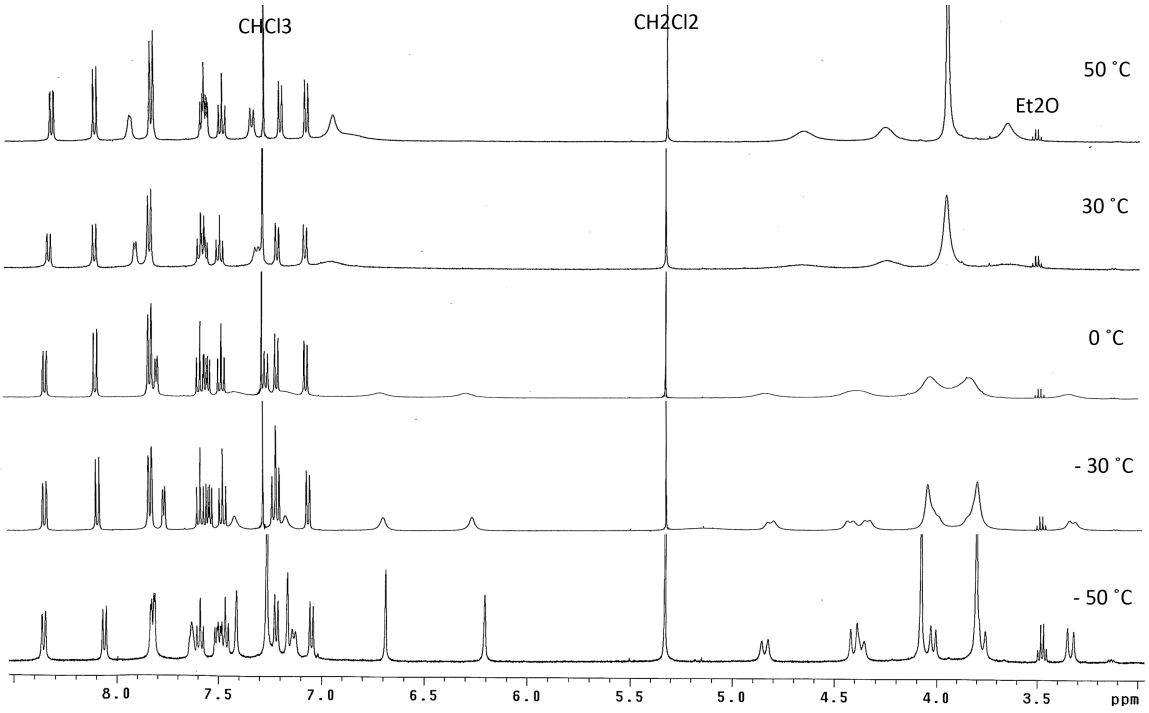

Figure 6.3 ^{1}H VT-NMR spectrum of [L1^{im}Pd]Cl (500 MHz in $CDCl_3$).

temperature ^{1}H NMR spectroscopy reveals that the solution-state structure in $CDCl_3$ is consistent with the solid-state structure (Figure 6.3). At low temperature (ca. -50 ˚C), the two imidazole rings are inequivalent and each methylene proton is coupled to its diastereotopic partner; coalescence is observed near room temperature and the averaged signals can be seen at higher temperature (ca. 50 ˚C).

For L1^{py}H, the kinetically preferred site for metal uptake is the neutral bis((pyridin-2-yl)methyl)amine pocket; reaction of L1^{py}H with one equiv (COD)Pd(Me)Cl and one equiv $TlPF_6$ thus provides yellow [L1^{py}(H)PdMe][PF_6] with precipitation of TlCl. ^{1}H NMR spectroscopy of [L1^{py}(H)PdMe][PF_6] reveals that the bis(quinolinyl)amine N*H* proton is still present and that the methylene protons between the pyridine rings and the tertiary amine are diastereotopic. Both observations are consistent with selective

metallation of the bis((pyridin-2-yl)methyl)amine binding pocket. The solid-state structure confirms this assignment (Figure 6.4).

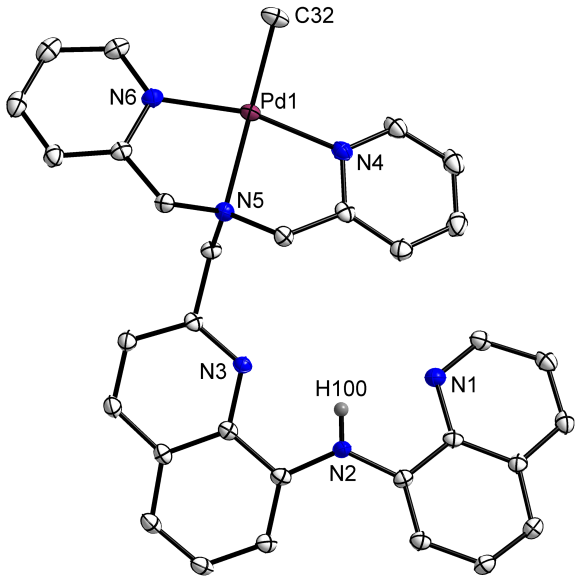

Figure 6.4 Displacement ellipsoid (40%) representation of $[L1^{py}(H)PdMe][PF_6]$. H atoms, counteranion, and solvent molecules are omitted for clarity. Selected distances and angles: Pd–N4 = 2.027(2) Å; Pd–N5 = 2.132(2) Å; Pd–N6 = 2.023(2) Å; Pd–C32 = 2.022(2) Å.

I was gratified to find that the BQA site of $[L1^{py}(H)PdMe][PF_6]$ is readily metallated with an additional equivalent of (COD)Pd(Me)Cl and catalytic Et_3N to give purple-red $[L1^{py}(PdCl)PdMe][PF_6]$. The solid-state structure of $[L1^{py}(PdCl)PdMe][PF_6]$ (Figure 6.5) reveals a Pd-Pd d^8-d^8 interaction with an average Pd-Pd distance of 3.1909(7) Å, which is less than the sum of the van der Waals radii (3.26 Å).[6] This favorable zero bond order interaction has been explained by mixing of $4d_{z^2}$ and $5p_z$ orbitals between the interacting metals.[7] Among the DFT-calculated occupied orbitals are two orbitals that have Pd-Pd σ and σ* character (Figure 6.6). The ^{1}H NMR spectrum of $[L1^{py}(PdCl)PdMe][PF_6]$ in $CDCl_3$ is consistent with a C_s symmetric structure at room temperature; however, cooling

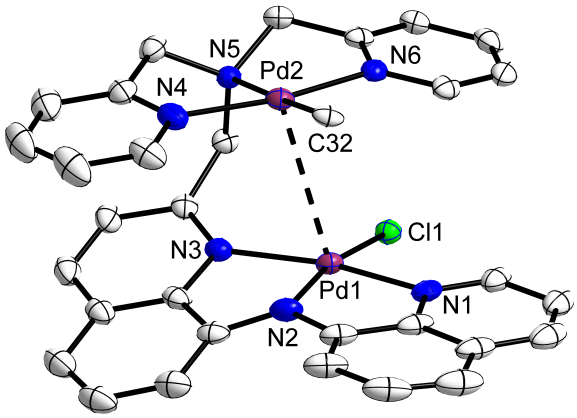

Figure 6.5 Displacement ellipsoid (40%) representation of [L1^{py}(PdCl)PdMe][PF_6]. H atoms, counteranion, and solvent molecules are omitted for clarity. Selected distances and angles: Pd1–Pd2 = 3.1909(7) Å; Pd1–N1 = 2.016(4) Å; Pd1–N2 = 1.968(4) Å; Pd1–N3 = 2.054(4) Å; Pd1–Cl1 = 2.3329(11) Å; Pd2–N4 = 2.032(4) Å; Pd2–N5 = 2.129(4) Å; Pd2–N6 = 2.023(4) Å; Pd2–C32 = 2.083(4) Å.

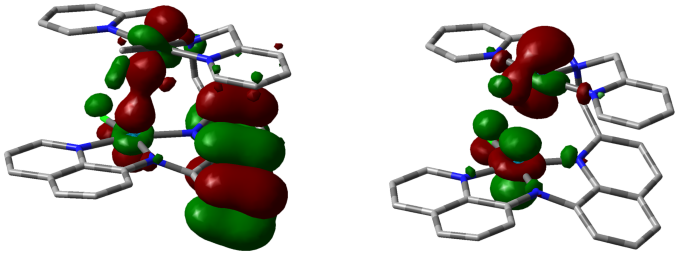

Figure 6.6 HOMO-10 (left) and HOMO-1 (right) of [L1^{py}(PdCl)PdMe][PF_6] shown with 0.04 e^{-1} $Å^{-3}$ isosurfaces. Calculations performed with Gaussian03 using the B3LYP functional and a basis set of LANL2DZ for Pd and Cl and 6-31+g(d) for all other atoms.

the solution results in decoalescence of the signals at ca. -40 ˚C and a spectrum that requires a C_1 symmetric structure at -58 ˚C (Figure 6.7). Thus, the ^{1}H NMR behavior of [L1^{py}(PdCl)PdMe][PF_6] appears to be consistent with its solid-state structure. I examined the possibility of a $\sigma^*(dz^2) \rightarrow \sigma(pz)$ transition resulting from a d^8-d^8 interaction in solution by comparing the electronic absorption spectrum of [L1^{py}(PdCl)PdMe][PF_6] with

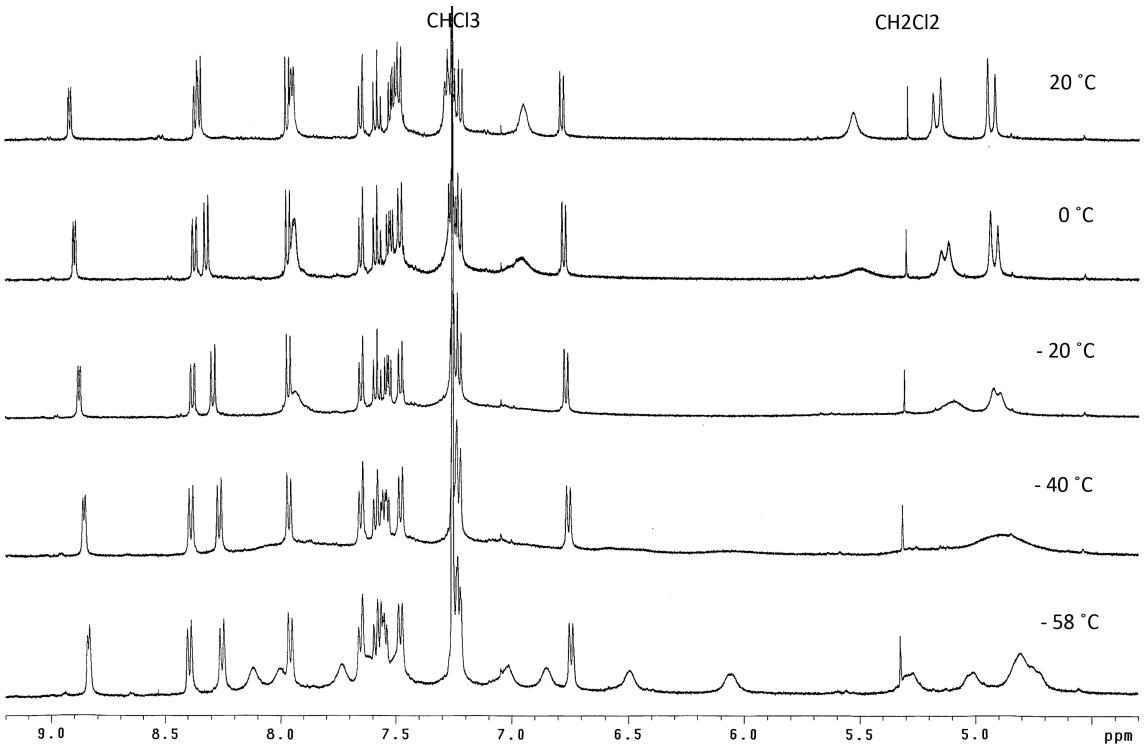

Figure 6.7 ^{1}H VT-NMR of [L1^{py}(PdCl)PdMe][PF_6] recorded at 500 MHz in $CDCl_3$.

those of its independently prepared monometallic fragments, [(*N*-methyl-bis(pyridin-2-ylmethyl)amine)PdMe][PF_6] ("[(MDPA)PdMe][PF_6]"; see Experimental section for the synthetic procedure) and (BQA)PdCl.[5a] Unfortunately, no such interaction could be rigorously identified (Figure 6.8), possibly due to overlap with intense ligand- centered π-π* transitions as suggested elsewhere.[8]

Given that the bimetallic metallation of [L1^{py}(PdCl)PdMe][PF_6] proceeds in a step-wise and selective manner, I sought to extend this synthetic strategy to the generation of heterobimetallics. As an illustration, the platinum-containing analog of [L1^{py}(H)PdMe][PF_6] can be generated by reaction of [L1^{py}(PdCl)PdMe][PF_6] with 1

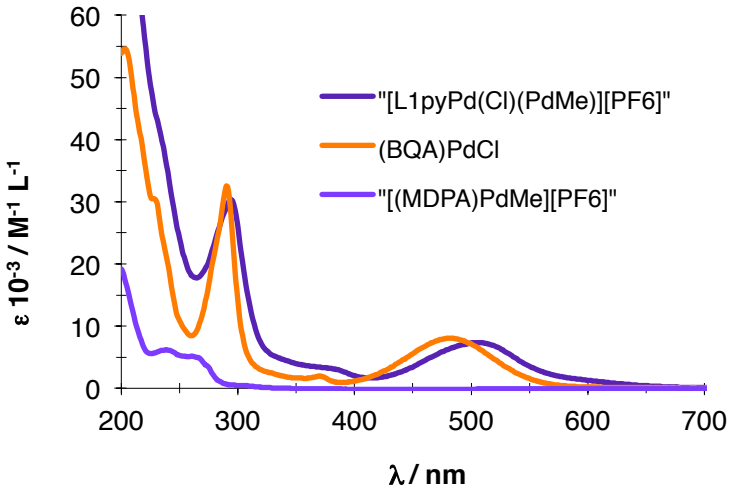

Figure 6.8 UV/vis spectra of [L1^{py}(PdCl)PdMe][PF_6], (BQA)PdCl, and [(MDPA)PdMe][PF_6] recorded in $CDCl_3$ at RT.

equiv (COD)Pt(Me)Cl and 1 equiv $TlPF_6$ to give [L1^{py}(H)PtMe][PF_6], the solid- and solution-state structure of which is analogous to that of [L1^{py}(H)PdMe][PF_6] based on ^{1}H NMR spectroscopic studies. Further metallation with (COD)Pd(Me)Cl and catalytic Et_3N provides red heterobimetallic [L1^{py}(PdCl)PtMe][PF_6], which also contains a d^8-d^8 interaction in the solid- (Figure 6.9) and solution-states. The Pd-Pt distance of 3.1668(3) Å is shorter than the sum of the van der Waals radii, 3.35 Å.[6] DFT calculations support the presence of a d^8-d^8 interaction (Figure 6.10). The ^{195}Pt NMR chemical shift of [L1^{py}(PdCl)PtMe][PF_6] is downfield of that of [L1^{py}(H)PtMe][PF_6], (-3,038 and -3,059 ppm vs. K_2PtCl_6, respectively) which is consistent with donation of electron density to the palladium atom in the solution phase. As for the related [L1^{py}(PdCl)PdMe][PF_6] complex, the UV/vis spectra of [L1^{py}(PdCl)PtMe][PF_6], [(MDPA)PtMe][PF_6], and (BQA)PtCl do not provide additional evidence for a d^8-d^8 interaction in solution (Figure 6.11). The stepwise metallation of L1^{py}H demonstrates that this framework offers the potential for

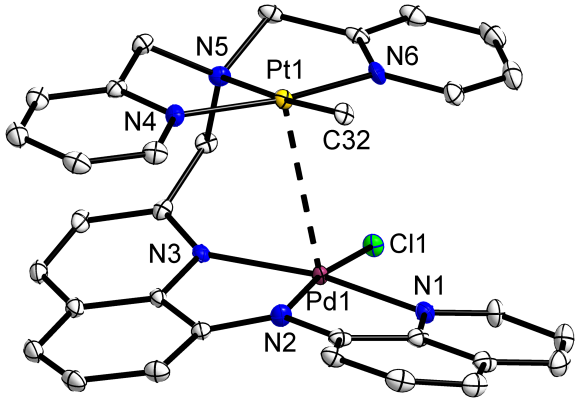

Figure 6.9 Displacement ellipsoid (40%) representation of [L1^{py}(PdCl)PtMe][PF_6]. H atoms, counteranion, and solvent molecules are omitted for clarity. Selected distances and angles: Pd1–Pt1 = 3.1668(3) Å; Pd1–N1 = 2.012(3) Å; Pd1–N2 = 1.956(3) Å; Pd1–N3 = 2.055(3) Å; Pd1–Cl1 = 2.3392(8) Å; Pt1–N4 = 2.009(3) Å; Pt1–N5 = 2.133(3) Å; Pt1–N6 = 1.999(3) Å; Pt1–C32 = 2.071(3) Å.

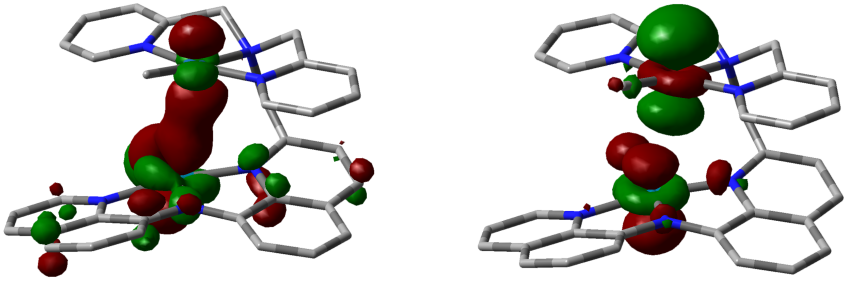

Figure 6.10 HOMO-10 (left) and HOMO-1 (right) of [L1^{py}(PdCl)PtMe][PF_6] shown with 0.04 e^{-1} $Å^{-3}$ isosurfaces. Calculations performed with Gaussian03 using the B3LYP functional and a basis set of LANL2DZ for Pt, Pd and Cl and 6-31+g(d) for all other atoms.

the generation of a range of homo- and heterobimetallics and the study of weak metal-metal interactions between metals in different ligand fields.

The procedure for installing palladium into ligand L1^{py}H may be applied to the related trinucleating ligand L2^{py}H. The room temperature addition of 3 equiv [$(CH_3CN)_4$Pd][BF_4]$_2$ to L2^{py}H results in the immediate metallation at the two neutral

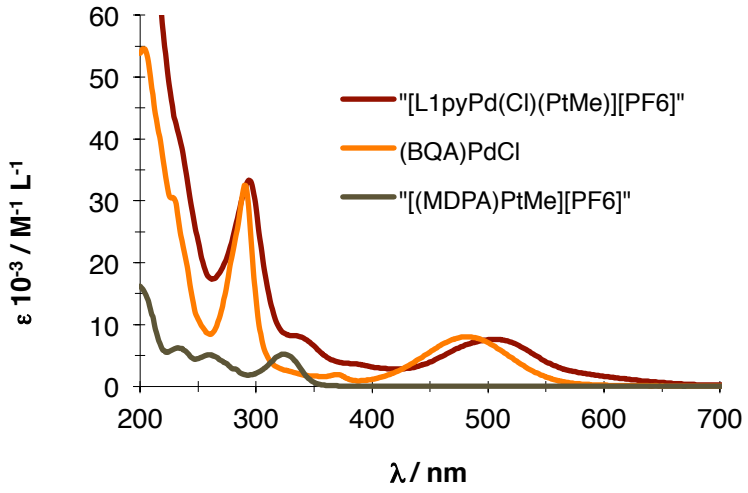

Figure 6.11 UV/vis spectra of $[L1^{py}(PdCl)PtMe][PF_6]$, (BQA)PdCl, and $[(MDPA)PtMe][PF_6]$ recorded in $CDCl_3$ at RT.

bis((pyridin-2-yl)methyl)amine sites as determined by ^{1}H NMR spectroscopy. The final palladation of the bis(quinolinyl)amine fragment occurs upon the addition of Et_3N and the application of heat. Purple $[L2^{py}(PdBr)_3][BF_4]_2$ is formed when the putative intermediate $[L2^{py}(Pd(CH_3CN))_3][BF_4]_5$ is treated with 3 equiv TBABr. The solid-state structure of $[L2^{py}(PdBr)_3][BF_4]_2$ reveals three unique palladium atoms (Figure 6.12); the Pd1-Pd2 distance (3.2447(10) Å) is shorter than the sum of the van der Waals radii whereas the Pd2-Pd3 distance (3.4411(10) Å) is longer. These bond lengths are consistent with the limiting formulation of two square pyramidal palladium centers and one that is square planar. Similarly to $[L1^{py}(PdCl)PdMe][PF_6]$ and $[L1^{py}(PdCl)PtMe][PF_6]$, $[L2^{py}(PdBr)_3][BF_4]_2$ is fluxional in solution as demonstrated by the broad resonances in its ^{1}H NMR spectrum.

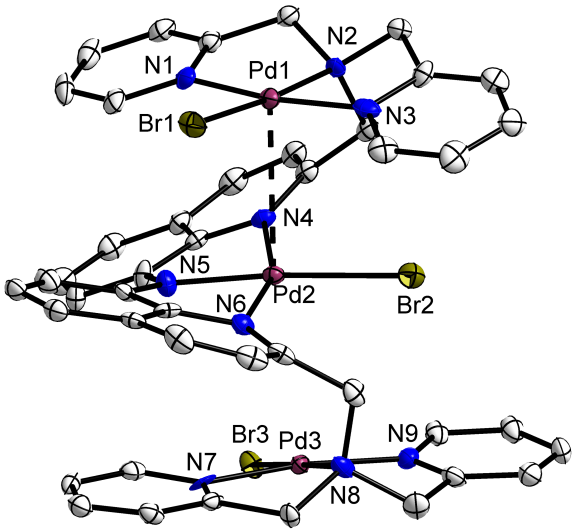

Figure 6.12 Displacement ellipsoid (40%) representation of $[L2^{py}(PdBr)_3][BF_3]_2$. H atoms, counteranions, and solvent molecules are omitted for clarity. Selected distances and angles: Pd1–Pd2 = 3.2447(10) Å; Pd2–Pd3 = 3.4411(10) Å; Pd1–N1 = 2.019(9) Å; Pd1–N2 = 2.047(7) Å; Pd1–N3 = 2.013(9) Å; Pd1–Br1 = 2.4115(12) Å; Pd2–N4 = 2.084(7) Å; Pd2–N5 = 1.955(8) Å; Pd2–N6 = 2.107(8) Å; Pd2–Br2 = 2.4861(13) Å; Pd3–N7 = 2.021(8) Å; Pd3–N8 = 2.044(8) Å; Pd3–N9 = 2.032(8) Å; Pd3–Br3 = 2.4297(11) Å.

6.3 Summary

The complexation chemistry presented here demonstrates that selective metallation of a polynucleating ligand demands careful tuning of the binding pockets. For example, the BQA site in $L1^{im}H$ is metallated with 1 equiv of a Pd(II) source whereas metallation of $L1^{py}H$ occurs most readily at the neutral bis((pyridin-2-yl)methyl)amine site. The modular synthesis of these ligands, in which a multitude of pendant binding pockets can be prepared, allows for such tuning.

6.4 Experimental

General Considerations. All manipulations were carried out using standard Schlenk or glove box techniques under a dinitrogen atmosphere. Dry, degassed solvents were purged with Ar and passed through an activated alumina column from S. G. Waters (Nashau, NH, USA) prior to use. All other reagents were purchased from commercial vendors and used as received without further purification unless otherwise noted. Deuterated solvents were purchased from Cambridge Isotope Laboratories, Inc. NMR experiments were performed on Varian 500 MHz spectrometers. ^{1}H NMR spectra were referenced to residual solvent. ^{195}Pt NMR spectra were referenced to K_2PtCl_4. UV/vis spectra were acquired on a Cary 50 instrument. IR spectra were acquired on a Bio-Rad FTS 300 instrument. ESI-MS data were acquired by Ms. Li Li on a Bruker Daltonics APEXIV 4.7 Tesla Fourier Transform Ion Cyclotron Resonance Mass Spectrometer in the MIT Dept. of Chemistry Instrumentation Facility. Combustion analaysis was performed by Midwest Microlab LLC in Indianapolis, IN, USA. Computational work was done using the Gaussian03 Revision B.01 software package.[9]

8-bromoquinoline-2-carbaldehyde (2): A 200 ml Schlenk tube charged with SeO_2 (10.2 g, 91.8 mmol) and a magnetic stir bar was purged with N_2 for 5 min. 1,4-dioxane (180 ml) was added and the mixture was heated to 80 ˚C before adding 8-bromo-2-methylquinoline[10] (20.2 g, 90.9 mmol) under a stream of N_2. The dark mixture was maintained at 80 ˚C for 12 hr., cooled to room temperature, and filtered through alumina eluting with CH_2Cl_2. Solvent was removed on a rotary evaporator to give a tan solid which was washed with cold acetone (3 x 20 ml). The remaining solid (11.2 g, 52%) was

used without further purification. The brown acetone filtrate was condensed and again washed with cold acetone (3 x 10 ml) to give additional product (7.75 g, 36%, total of 88%). ^{1}H NMR ($CDCl_3$, 500 MHz, 20 °C): *d* (ppm) 10.31 (s, 1H), 8.34 (dd, *J* = 8.4 Hz, *J* = 0.5 Hz, 1H), 8.17 (dd, *J* = 7.5 Hz, *J* = 1.3 Hz, 1H), 8.10 (d, *J* = 8.4 Hz, 1H), 7.89 (dd, *J* = 8.2 Hz, *J* = 1.3 Hz, 1H), 7.55 (dd, *J* = 8.1 Hz, *J* = 7.5 Hz, 1H). ^{13}C NMR ($CDCl_3$, 125 MHz, 20 °C): *d* (ppm) 193.4, 153.1, 145.0, 138.2, 134.3, 131.4, 129.6, 127.8, 126.1, 118.1. IR (CCl_4 solution): 1,711 cm^{-1}. ESI-MS: calc. for $C_{10}H_7BrNO$ $(M+H)^+$ 235.9706, found 235.9711. Elemental analysis for $C_{10}H_6BrNO$: calc. C 50.88 H 2.56, found C 50.72 H 2.71.

***N*-(8-bromoquinolin-2-methyl)-*N*,*N*-bis(2-methoxyethyl)amine (3)**: A 250 ml flask was charged with a magnetic stir bar, 100 ml 1,2-dichloroethane, **2** (2.18 g, 9.24 mmol), bis(2-methoxyethyl)amine (1.29 g, 9.69 mmol), and one drop of formic acid. The solution was allowed to stir for 30 min. before $NaHB(OAc)_3$ (2.35 g, 11.1 mmol) was added in one portion. The mixture was stirred at room temperature for 24 hr. and quenched with sat. aqueous $NaHCO_3$ (50 ml). The aqueous and organic phases were separated and the aqueous layer was extracted with CH_2Cl_2 (3 x 50 ml). The combined organics were dried over Na_2SO_4 and condensed on a rotary evaporator to give a dark yellow oil. Purification by flash chromatography (silica gel, 2:2:96 to 4:2:94 CH_3OH:Et_3N:CH_2Cl_2 gradient) gave the product as a viscous, pale yellow oil (2.08 g, 64%). ^{1}H NMR ($CDCl_3$, 500 MHz, 20 °C) *d* (ppm) 8.11 (d, *J* = 8.4 Hz, 1H), 8.02 (dd, *J* = 7.4 Hz, *J* = 1.3 Hz, 1H), 7.77 (dd, *J* = 8.2 Hz, *J* = 1.3 Hz, 1H), 7.76 (d, *J* = 8.4 Hz, 1H), 4.36 (dd, *J* = 7.8 Hz, *J* = 7.8 Hz, 1H), 4.16 (s, 2H), 3.55 (t, *J* = 6.0 Hz, 4H), 3.32 (s, 6H),

2.91 (t, *J* = 6.0 Hz, 4H). ^{13}C NMR ($CDCl_3$, 125 MHz, 20 ˚C): *d* (ppm) 144.6, 136.6, 132.9, 128.6, 127.5, 126.3, 124.6, 121.9, 71.1, 61.5, 58.8, 54.3. ESI-MS: calc. for $C_{16}H_{22}BrN_2O_2Br$ $(M+H)^+$ 353.0865, found 353.0867. Elemental Analysis for $C_{16}H_{21}BrN_2O_2$: calc. C 54.40 H 5.99, found C 54.52 H 5.77.

***N*-(8-bromoquinolin-2-methyl)-*N*,*N*-bis((1-methyl-1*H*-imidazole-2-yl)methyl)amine (4)**: A 250 ml flask was charged with a magnetic stir bar, 100 ml 1,2-dichloroethane, **2** (771 mg, 3.27 mmol), bis((1-methyl-1*H*-imidazole-2-yl)methyl)amine[11] (664 mg, 3.23 mmol), and one drop of formic acid. The solution was allowed to stir for 30 min. before $NaHB(OAc)_3$ (762 mg, 3.59 mmol) was added in one portion. The mixture was stirred at room temperature for 24 hr. and quenched with sat. aqueous $NaHCO_3$ (50 ml). The aqueous and organic phases were separated and the aqueous layer was extracted with CH_2Cl_2 (3 x 50 ml). The combined organics were dried over Na_2SO_4 and condensed on a rotary evaporator to give a dark yellow oil. Purification by flash chromatography (silica gel, 2:2:96 to 4:2:94 CH_3OH:Et_3N:CH_2Cl_2 gradient) gave the product as a viscous, pale yellow oil which was triterated with pentane to afford a light tan solid (870 mg, 63%). ^{1}H NMR ($CDCl_3$, 500 MHz, 20 ˚C) *d* (ppm) 8.04 (d, *J* = 8.4 Hz, 1H), 8.03 (dd, *J* = 7.5 Hz, *J* = 1.3 Hz, 1H), 7.75 (dd, *J* = 8.2 Hz, *J* = 1.3 Hz, 1H), 7.36 (dd, *J* = 7.5 Hz, *J* = 8.2 Hz, 1H), 7.31 (d, *J* = 8.4 Hz, 1H), 6.91 (d, *J* = 1.2 Hz, 2H), 6.76 (d, *J* = 1.2 Hz, 2H), 4.02 (s, 2H), 3.92 (s, 4H), 3.42 (s, 6H). ^{13}C NMR ($CDCl_3$, 125 MHz, 20 ˚C): *d* (ppm) 160.2, 145.0, 133.4, 126.7, 133.0, 128.3, 127.5, 127.1, 127.6, 124.5, 122.6, 121.5, 59.9, 50.1, 32.6. ESI-MS: calc. for $C_{20}H_{22}BrN_6$ $(M+H)^+$ 427.1069, found 427.1052. Elemental analysis for $C_{20}H_{21}BrN_6$: calc C 56.48 H 4.98, found C 55.71 H 4.84.

***N*-(8-bromoquinolin-2-methyl)-*N*,*N*-bis(pyridin-2-ylmethyl)amine (5):** A 250 ml flask was charged with a magnetic stir bar, 100 ml 1,2-dichloroethane, **2** (3.87 g, 16.4 mmol), and 2,2'-dipicolylamine (3.11 g, 15.6 mmol). The solution was allowed to stir for 30 min. before $NaHB(OAc)_3$ (3.97 g, 18.7 mmol) was added in one portion. The mixture was stirred at room temperature for 24 hr. and quenched with sat. aqueous $NaHCO_3$ (50 ml). The aqueous and organic phases were separated and the aqueous layer was extracted with CH_2Cl_2 (3 x 50 ml). The combined organics were dried over Na_2SO_4 and condensed on a rotary evaporator to give a dark yellow oil. Purification by flash chromatography (silica gel, 2:2:96 to 4:2:94 CH_3OH:Et_3N:CH_2Cl_2 gradient) gave the product as a viscous, pale yellow oil (4.0 g, 61%). ^{1}H NMR ($CDCl_3$, 500 MHz, 20 ˚C): *d* (ppm) 8.54 (m, 2H), 8.10 (d, *J* = 8.4 Hz, 1H), 8.02 (dd, *J* = 7.4 Hz, *J* = 1.3 Hz, 1H), 7.65-7.76 (m, 6H), 7.35 (dd, *J* = 7.5 Hz, *J* = 1.5 Hz, 1H), 7.14 (ddd, *J* = 7.3 Hz, *J* = 4.9 Hz, *J* = 1.3 Hz, 2H), 4.10 (s, 2H), 3.97 (s, 4H). ^{13}C NMR ($CDCl_3$, 125 MHz, 20 ˚C): *d* (ppm) 161.4, 159.2, 149.1, 144.7, 136.9, 136.8, 133.1, 128.6, 127.5, 126.6, 124.8, 123.5, 122.7, 122.5, 60.3, 60.2. ESI-MS: calc. for $C_{22}H_{20}BrN_4$ $(M+H)^+$ 421.0851, found 421.0850. Elemental analysis for $C_{22}H_{19}BrN_4$: calc. C 63.02 H 4.57, found C 62.74 H 4.67.

2-((bis(2-methoxylethyl)amino)methyl)-*N*-(quinolin-8-yl)quinolin-8-amine (6, $L1^{OMe}H$): A 100 ml Schlenk tube charged with a magnetic stir bar, $Pd_2(dba)_3$ (79.8 mg, 0.0871 mmol), and *rac*-BINAP (108.6 mg, 0.174 mmol) was evacuated and back-filled with N_2 three times. Toluene (10 ml) was added and the solution was allowed to stir for 5 min. before **3** (1.54 g, 4.76 mmol), 8-aminoquinoline (755 mg, 5.24 mmol), NaO^tBu (549

mg, 5.71 mmol), and an additional 40 ml toluene were added. The solution was stirred at 110 ˚C for 20 hr., cooled to room temperature, filtered through Celite, and condensed on a rotary evaporator. The resulting brown oil was purified by flash chromatography (silica gel, 4:2:94 CH_3OH:Et_3N:CH_2Cl_2) to give 1.60 g (88%) of the title compound as a viscous yellow oil. ^{1}H NMR ($CDCl_3$, 500 MHz, 20 ˚C) *d* (ppm) 10.69 (s, 1H), 8.95 (dd, *J* = 4.2 Hz, *J* = 1.7 Hz 1H), 8.16 (dd, *J* = 8.3 Hz, *J* = 1.7 Hz, 1H), 8.12 (d, *J* = 8.4 Hz, 1H), 7.90 (m, 2H), 7.67 (d, *J* = 8.4 Hz, 1H), 7.53 (dd, *J* = 7.9 Hz, *J* = 7.9 Hz, 1H), 7.49 (dd, *J* = 8.01 Hz, *J* = 8.01 Hz, 1H), 7.48 (dd, *J* = 8.51, *J* = 4.15, 1H), 7.35-7.30 (m, 2H), 4.23 (s, 2H), 3.61 (t, *J* = 5.9 Hz, 4H), 3.35 (s, 6H), 3.01 (t, *J* = 5.9 Hz, 4H). ^{13}C NMR ($CDCl_3$, 500 MHz, 20 ˚C) *d* (ppm) 158.25, 147.97, 140.25, 139.14, 139.10, 138.65, 136.47, 136.20, 129.11, 127.94, 127.30, 126.64, 121.88, 121.71, 117.76, 117.72, 110.02, 71.51, 61.37, 58.91, 54.41. ESI-MS: calc. for $C_{25}H_{29}N_4O_2$ $(M+H)^+$ 417.2285, found 417.2265. Elemental analysis for $C_{25}H_{28}N_4O_2$: calc. C 72.09 H 6.78, found C 71.27 H 6.78.

2-((bis((1-methyl-1*H*-imidazole-2-yl)methyl)amino)methyl)-*N*-(quinolin-8-yl)quinolin-8-amine (7, L1^{im}H): A 100 ml Schlenk tube charged with a magnetic stir bar, $Pd_2(dba)_3$ (23.8 mg, 0.026 mmol), and *rac*-BINAP (32.3 mg, 0.052 mmol) was evacuated and back-filled with N_2 three times. Toluene (10 ml) was added and the solution was allowed to stir for 5 min. before **4** (552 mg, 1.30 mmol), 8-aminoquinoline (189 mg, 1.31 mmol), NaO^{t}Bu (150 mg, 1.56 mmol), and an additional 20 ml toluene were added. The solution was stirred at 110 ˚C for 20 hr., cooled to room temperature, filtered through Celite, and condensed on a rotary evaporator. The resulting brown oil was purified by flash chromatography (silica gel, 4:2:94 CH_3OH:Et_3N:CH_2Cl_2) to give

597 mg (94%) of the title compound as a yellow solid. ^{1}H NMR ($CDCl_3$, 500 MHz, 20 ˚C): *d* (ppm) 10.65 (s, 1H), 8.74 (dd, *J* = 4.2 Hz, *J* = 1.8 Hz, 1H), 8.14 (dd, *J* = 8.3 Hz, *J* = 0.7 Hz, 1H), 8.06 (d, 8.4 Hz, 1H), 7.87 (m, 2H), 7.52 (dd, *J* = 7.9 Hz, 7.9 Hz, 1H), 7.50 (dd, *J* = 7.9 Hz, *J* = 7.9 Hz, 1H), 7.44 (8.2 Hz, 4.2 Hz, 1H), 7.28-7.24 (m, 3H), 6.94 (d, *J* = 1.3 Hz, 2H), 6.74 (d, *J* = 1.3 Hz, 2H), 4.09 (s, 2H), 4.06 (s, 4H), 3.35 (s, 6H). ^{13}C NMR ($CDCl_3$, 500 MHz, 20 ˚C) *d* (ppm) 156.8, 147.8, 145.4, 139.9, 138.9, 138.7, 138.5, 136.6, 136.1, 128.9, 127.7, 127.2, 127.1, 126.9, 122.4, 121.7, 121.4, 117.9, 117.5, 110.1, 109.8, 60.0, 50.2, 32.5. ESI-MS: calc. for $C_{29}H_{29}N_8$ $(M+H)^+$ 489.2515 found 489.2505. Elemental analysis for $C_{29}H_{28}N_8$: calc. C 71.29 H 5.78, found C 70.85 H 5.92.

2-((bis((pyridin-2-yl)methyl)amino)methyl)-*N*-(quinolin-8-yl)quinolin-8-amine (8, L1^{py}H): A 100 ml Schlenk tube charged with a magnetic stir bar, $Pd_2(dba)_3$ (99 mg, 0.11 mmol), and *rac*-BINAP (135 mg, 0.22 mmol) was evacuated and back-filled with N_2 three times. Toluene (10 ml) was added and the solution was allowed to stir for 5 min. before **5** (2.27 g, 5.42 mmol), 8-aminoquinoline (790 mg, 5.48 mmol), NaO^{t}Bu (573 mg, 5.97 mmol), and an additional 40 ml toluene were added. The solution was stirred at 110 ˚C for 20 hr., cooled to room temperature, filtered through Celite, and condensed on a rotary evaporator. The resulting brown oil was purified by flash chromatography (silica gel, 4:2:94 CH_3OH:Et_3N:CH_2Cl_2) to give 2.38 g (91%) of the title compound as a viscous yellow oil. ^{1}H NMR (CD_3OD, 500 MHz, 20 ˚C): *d* (ppm) 8.58 (dd, *J* = 4.1 Hz, *J* = 1.6 Hz, 1H), 8.21 (m, 2H), 7.99 (dd, *J* = 8.3 Hz, *J* = 1.6 Hz, 1H), 7.86 (d, *J* = 8.5 Hz, 1H), 7.65 (d, *J* = 7.8 Hz, 2H), 7.62 (dd, *J* = 7.7 Hz, *J* = 1.0 Hz, 1H), 7.59 (dd, *J* = 7.7 Hz, *J* = 1.0 Hz, 1H), 7.36 (ddd, *J* = 7.7 Hz, *J* = 7.7 Hz, *J* = 1.8 Hz, 2H), 7.32 (d, *J* = 8.3 Hz, 1H),

7.21-7.30 (m, 3H), 7.12 (dd, J = 8.2 Hz, J = 0.9 Hz, 1H), 7.05 (dd, J = 8.2 Hz, J = 0.9 Hz, 1H), 6.97 (ddd, J = 7.5 Hz, J = 5.0 Hz, J = 1.0 Hz, 2H), 3.83 (s, 2H), 3.77 (s, 4H). ^{13}C NMR (CD_3OD, 125 MHz, 20 ˚C): *d* (ppm) 160.2, 157.9, 149.1, 148.3, 140.8, 130.0, 139.6, 139.3, 138.4, 137.7, 137.3, 130.2, 129.1, 128.3, 127.8, 124.8, 123.6, 122.7, 122.7, 118.8, 118.7, 111.0, 110.5, 61.3, 60.9. ESI-MS: calc. for $C_{31}H_{27}N_6$ $(M+H)^+$ 483.2297, found 483.2293. Elemental analysis for $C_{31}H_{26}N_6$: calc. C 77.16 H 5.43, found C 76.83 H 5.56.

2-(2-methylquinolin-8-yl)isoindoline-1,3-dione (11): A 250 ml flask equipped with a reflux condenser and charged with phthalic anhydride (5.53 g, 37.3 mmol) and 8-amino-2-methylquinoline (5.85 g, 37.0 mmol) was heated to reflux for 2 hr. The brown solution was cooled to room temperature. The off-white microcrystals thus generated were isolated by filtration, washed with cold toluene, and used without further purification (9.01 g, 85%). ^{1}H NMR ($CDCl_3$, 500 MHz, 20 ˚C): *d* (ppm) 8.09 (d, J = 8.4 Hz, 1H), 8.02 (m, 2H), 7.92 (dd, J = 7.3 Hz, J = 1.5 Hz, 1H), 7.83 (m, 2H), 7.71 (dd, J = 7.2 Hz, J = 1.4 Hz, 1H), 7.59 (dd, J = 7.7 Hz, J = 7.7 Hz, 1H), 7.31 (d, J = 8.4 Hz, 1H), 2.59 (s, 3H). ^{13}C NMR ($CDCl_3$, 125 MHz, 20 ˚C): *d* (ppm) 168.3, 160.1, 143.9, 136.3, 134.3, 132.7, 130.3, 129.5, 127.7, 125.4, 124.0, 123.1, 25.8. ESI-MS: calc. for $C_{18}H_{13}N_2O_2$ $(M+H)^+$ 289.0972, found 289.0982. Elemental analysis for $C_{18}H_{12}N_2O_2$: calc. C 74.99 H 4.20, found C 74.91 H 4.31.

8-(1,3-dioxoisoindolin-2-yl)quinoline-2-carbaldehyde (**12**): A 200 ml Schlenk tube charged with SeO_2 (3.47 g, 31.3 mmol) and a magnetic stir bar was purged with N_2 for 5

min. 1,4-dioxane (180 ml) was added and the mixture was heated to 80 ˚C before adding **11** (9.01 g, 31.3 mmol) under a stream of N_2. The dark mixture was maintained at 80 ˚C for 12 hr., cooled to room temperature, and filtered through alumina eluting with CH_2Cl_2. Solvent was removed on a rotary evaporator to give a tan solid (9.35 g, 99%). ^{1}H NMR ($CDCl_3$, 500 MHz, 20 ˚C): *d* (ppm) 9.96 (d, *J* = 0.8 Hz, 1H), 8.40 (dd, *J* = 8.5 Hz, *J* = 0.8 Hz, 1H), 8.03-8.08 (m, 4H), 7.82-7.88 (m, 4H). ^{13}C NMR ($CDCl_3$, 125 MHz, 20 ˚C): *d* (ppm) 193.8, 168.0, 153.8, 144.2, 138.0, 134.6, 132.5, 131.5, 131.2, 129.7, 129.0, 124.2, 124.0, 118.3. ESI-MS: calc. for $C_{18}H_{11}N_2O_3$ $(M+H)^+$ 303.0764, found 303.0770. Elemental analysis for $C_{18}H_{10}N_2O_3$: calc. C 71.52 H 3.33, found C 71.14 H 3.68.

2-(2-((bis(pyridin-2-ylmethyl)amino)methyl)quinolin-8-yl)isoindoline-1,3-dione (**13**): A 250 ml flask was charged with a magnetic stir bar, 100 ml 1,2-dichloroethane, **12** (4.43 g, 14.7 mmol), and 2,2'-dipicolylamine (2.89 g, 14.5 mmol). The solution was allowed to stir for 30 min. before $NaHB(OAc)_3$ (3.42 g, 16.1 mmol) was added in one portion. The mixture was stirred at room temperature for 24 hr. and quenched with sat. aqueous $NaHCO_3$ (50 ml). The aqueous and organic phases were separated and the aqueous layer was extracted with CH_2Cl_2 (3 x 100 ml). The combined organics were dried over Na_2SO_4 and condensed on a rotary evaporator to give a dark yellow oil. Purification by flash chromatography (silica gel, 2:2:96 to 6:2:92 CH_3OH:Et_3N:CH_2Cl_2 gradient) gave the product as a tan solid (5.41 g, 76%). The product may be recrystallized by slow evaporation from a CH_2Cl_2/hexanes solution to give yellow needles. ^{1}H NMR ($CDCl_3$, 500 MHz, 20 ˚C): *d* (ppm) 8.48 (m, 2H), 8.17 (d, *J* = 8.4 Hz, 1H), 7.99 (m, 2H), 7.93 (dd, *J* = 8.3 Hz, *J* = 1.5 Hz, 1H), 7.83 (m, 2H), 7.72 (dd, *J* = 7.2 Hz, *J* = 1.4 Hz, 1H), 7.66 (d,

J = 8.5 Hz, 1H), 7.63 (dd, *J* = 8.2 Hz, *J* = 7.2 Hz, 1H), 7.46-7.51 (m, 4H), 7.08 (m, 2H), 3.82 (two overlapping singlets, 6H). ^{13}C NMR ($CDCl_3$, 125 MHz, 20 °C): *d* (ppm) 168.2, 161.0, 159.4, 149.2, 143.8, 136.6, 136.4, 134.4, 132.7, 130.3, 129.8, 129.5, 128.5, 125.9, 124.0, 123.4, 122.2, 122.1, 60.4, 60.2. ESI-MS: calc. for $C_{30}H_{24}N_5O_2$ $(M+H)^+$ 486.1925, found 486.1916. Elemental analysis for $C_{30}H_{23}N_5O_2$: calc. C 74.21 H 4.77, found C 73.21 H 4.99.

2-((bis(pyridin-2-ylmethyl)amino)methyl)quinolin-8-amine (**14**): A 50 ml flask was charged with **13** (209 mg, 0.43 mmol) and 5 ml methanol. To this mixture was added 1 ml N_2H_4•H_2O in one portion. The resulting yellow solution was allowed to sit at room temperature for 30 min. Then 50 ml dichloromethane was added followed by 1 M NaOH until the pH reached >12. The phases were separated and the aqueous phase was washed with dichloromethane (3 x 30 ml). The aqueous phase was properly disposed. The combined organics were dried over Na_2SO_4 and condensed on a rotary evaporator to give pure product as a bright yellow oil (153 mg, 100%). ^{1}H NMR ($CDCl_3$, 500 MHz, 20 °C): *d* (ppm) 8.54 (m, 2H), 8.02 (d, *J* = 8.5 Hz, 1H), 7.60-7.68 (m, 5H), 7.28 (dd, *J* = 8.0 Hz, *J* = 7.4 Hz, 1H), 7.10-7.15 (m, 3H), 6.90 (dd, *J* = 7.4 Hz, *J* = 1.2 Hz, 1H), 5.01 (s (br), 2H), 4.00 (s, 2H), 3.93 (s, 4H). ^{13}C NMR ($CDCl_3$, 125 MHz, 20 °C): *d* (ppm) 159.7, 157.0, 149.3, 144.0, 137.7, 136.6, 136.5, 127.9, 127.1, 123.1, 122.2, 121.4, 115.9, 110.2, 60.7, 60.5. ESI-MS: calc. for $C_{22}H_{22}N_5$ $(M+H)^+$ 356.1870, found 356.1876. Since the product is somewhat hygroscopic and the phthalimide deprotection is quantitative by NMR spectroscopy, the product is typically stored as phthalimide-protected **22** and used in the cross-coupling step immediately after deprotection.

Bis(2-((bis(pyridin-2-ylmethyl)amino)methyl)quinolin-8-yl)amine (9, L2^{py}H): A 100 ml Schlenk tube charged with a magnetic stir bar, $Pd_2(dba)_3$ (7.9 mg, 0.009 mmol), and *rac*-BINAP (10.8 mg, 0.017 mmol) was evacuated and back-filled with N_2 three times. Toluene (2 ml) was added and the solution was allowed to stir for 5 min. before **14** (153 mg, 0.43 mmol), **5** (182 mg, 0.43 mmol), NaO^{t}Bu (50.1 mg, 0.52 mmol), and 3 ml toluene were added. The solution was stirred at 110 ˚C for 24 hr., cooled to room temperature, filtered through Celite, and condensed on a rotary evaporator. The resulting brown oil was purified by flash chromatography (silica gel, 4:2:94 CH_3OH:Et_3N:CH_2Cl_2) to give 287 g (96%) of **9** as a yellow solid. In spite of a slight (~1%) and persistent impurity revealed by ^{1}H NMR, samples of **9** were sufficiently pure for further reactions to generate analytically pure compounds (such as **16**). ^{1}H NMR ($CDCl_3$, 500 MHz, 20 ˚C): *d* (ppm) 10.61 (s, 1H), 8.48 (m, 4H), 8.08 (d, *J* = 8.4 Hz, 2H), 7.82 (dd, *J* = 7.7 Hz, *J* = 1.1 Hz, 2H), 7.74 (d, *J* = 8.4 Hz, 2H), 7.59 (d (br), *J* = 7.9 Hz, 4H), 7.51 (ddd, *J* = 7.6 Hz, *J* = 7.6 Hz, *J* = 1.8 Hz, 4H), 7.43 (dd, *J* = 8.0 Hz, *J* = 8.0 Hz, 2H), 7.25 (dd, *J* = 8.2 Hz, *J* = 0.9 Hz, 2H), 7.05 (ddd, *J* = 7.4 Hz, *J* = 4.9 Hz, *J* = 1.2 Hz, 4H), 4.04 (s, 4H), 3.90 (s, 8H). ^{13}C NMR ($CDCl_3$, 125 MHz, 20 ˚C): *d* (ppm) 159.5, 157.5, 149.1, 139.2, 138.7, 136.6, 136.4, 128.0, 126.7, 123.2, 122.0, 121.6, 117.5, 110.1, 60.9, 60.9. ESI-MS: calc. for $C_{44}H_{40}N_9$ $(M+H)^+$ 694.3401, found 694.3407.

L1^{OMe}PdCl: A 25 ml Schlenk tube was charged with L1^{OMe}H (515 mg, 1.24 mmol), (COD)Pd(Me)Cl (328 mg, 1.24 mmol), Et_3N (0.02 ml, 0.12 mmol), 5 ml THF, and a magnetic stirbar. The solution was heated overnight at 60 ˚C. Solvent was removed in vacuo. The solids were dissolved in a minimum volume of dichloromethane and

precipitated upon the addition of Et_2O. Additional washing with Et_2O provided the title compound (553 mg, 80%). Single crystals suitable for x-ray diffraction were grown by slow diffusion of Et_2O into a CH_3CN solution. ^1H NMR ($CDCl_3$, 500 MHz, 20 ˚C): *d* (ppm) 9.21 (dd, *J* = 5.2 Hz, *J* = 1.1 Hz, 1H), 8.24 (dd, *J* = 8.3 Hz, *J* = 1.4 Hz, 1H), 8.15 (d, *J* = 8.5 Hz, 1H), 7.98 (d, *J* = 8.5 Hz, 1H), 7.70-7.73 (m, 2H), 7.44-7.50 (m, 2H), 7.39 (dd, *J* = 7.9, 1H), 7.10 (d, *J* = 8.0 Hz, 1H), 7.04 (d, *J* = 7.9 Hz, 1H), 4.66 (s, 2H), 3.58 (t, *J* = 5.7 Hz, 4H), 3.29 (s, 6H), 2.97 (t, *J* = 5.7 Hz, 4H). ^{13}C NMR ($CDCl_3$, 125 MHz, 20 ˚C): *d* (ppm) 149.4, 149.2, 148.5, 148.2, 147.5, 139.0, 138.9, 131.0, 129.9, 129.2, 128.4, 122.0, 121.2, 115.3, 115.2, 112.9, 111.1, 71.1, 64.2, 58.8, 55.7. ESI-MS: calc. for $C_{25}H_{28}ClN_4O_2Pd$ $(M+H)^+$ 559.0939, found 559.0933. Elemental analysis for $C_{25}H_{27}ClN_4O_2Pd$: calc. C 53.87 H 4.88, found C 53.50 H 4.85.

[L1^{im}Pd][Cl]: A 25 ml Schlenk tube was charged with L1^{im}H (96.7 mg, 0.20 mmol), (COD)$PdCl_2$ (56.5 g, 0.20 mmol), Et_3N (0.030 ml, 0.22 mmol), 2 ml $CHCl_3$, and a magnetic stirbar. The solution was heated overnight at 60 ˚C. Solvent was removed in vacuo. Recrystallization by slow diffusion of Et_2O into a dichloromethane solution provided the title compound as red solid (76 mg, 61%). Single crystals suitable for x-ray diffraction were grown by slow diffusion of Et_2O into a $CHCl_3$ solution. ^1H NMR ($CDCl_3$, 500 MHz, -50 ˚C): *d* (ppm) 8.35 (d, *J* = 7.7 Hz, 1H), 8.05 (d, *J* = 7.5 Hz, 1H), 7.82 (dd, *J* = 7.9 Hz, *J* = 2.7 Hz, 2H), 7.63 (br, 1H), 7.58 (dd, *J* = 7.7 Hz, *J* = 7.7 Hz, 1H), 7.50 (dd, *J* = 7.9 Hz, *J* = 5.5 Hz, 1H), 7.46 (dd, *J* = 7.9 Hz, *J* = 7.9 Hz, 1H), 7.41 (s, 1H), 7.21 (d, *J* = 8.0 Hz, 1H), 7.16 (s, 1H), 7.13 (d (br), *J* = 8.0 Hz, 1H), 6.68 (s, 1H), 6.20 (s, 1H), 4.83 (d, *J* = 14.7 Hz, 1H), 4.35-4.41 (m, 2H), 4.07 (s, 3H), 4.01 (d, *J* = 12.8 Hz, 1H),

3.75-3.80 (m, 4H), 3.30 (d, *J* = 14.8 Hz, 1H). Despite several purifications, satisfactory carbon and hydrogen combustion analysis could not be obtained on otherwise spectroscopically-pure samples.

[L1^{py}HPdMe][PF$_6$]: A 20 ml scintillation vial was charged with (COD)Pd(Me)Cl (44 mg, 0.17 mmol), 2 ml acetonitrile, and a magnetic stirbar. Addition of $TlPF_6$ (58 mg, 0.17 mmol) afforded a white precipitate. Dropwise addition of a solution of L1^{py}H (80 mg, 0.17 mmol) in 1 ml CH_3CN produced a brilliant yellow solution. After stirring for 1 hr., solvent was removed in vacuo. The resulting solid was suspended in 5 ml CH_2Cl_2 and filtered. The yellow filtrate was treated with Et_2O which resulted in precipitation of a yellow solid which was washed with pentate and dried to provide analytically pure product. ^{1}H NMR ($CDCl_3$, 500 MHz, 20 ˚C): *d* (ppm) 10.56 (s, 1H), 9.02 (dd, *J* = 4.3 Hz, *J* = 1.7 Hz, 1H), 8.41 (d, *J* = 7.0 Hz, 1H), 8.04 (d, *J* = 8.4 Hz, 1H), 8.02 (d, *J* = 5.0 Hz, 2H), 7.93 (d, *J* = 7.6 Hz, 1H), 7.78 (dd, *J* = 8.2 Hz, *J* = 3.2 Hz, 2H), 7.62-7.70 (m, 4H), 7.53 (d, *J* = 8.2 Hz, 1H), 7.48 (dd, *J* = 7.9 Hz, *J* = 7.9 Hz, 1H), 7.35 (7.8 Hz, 2H), 7.22 (d, *J* = 8.2 Hz, 1H), 7.16 (br, 2H), 4.92 (d, *J* = 15.8 Hz, 2H), 4.78 (d, *J* = 15.8 Hz, 2H), 4.30 (s, 2H), 0.58 (s, 3H). ^{13}C NMR (CD_3CN, 125 MHz, 20 ˚C): *d* (ppm) 164.8, 151.4, 148.9, 148.5, 139.8, 139.1, 139.1, 138.3, 138.2, 137.9, 136.9, 136.6, 129.1, 128.0, 127.8, 127.4, 124.2, 124.0, 124.0, 122.2, 118.4, 110.3, 109.9, 64.2, 63.0, 3.6 ESI-MS: calc. for $C_{32}H_{29}N_6Pd$ $(M\text{-}PF_6)^+$ 603.1499, found 603.1476. Elemental analysis for $C_{32}H_{29}F_6N_6PPd$: calc. C 51.31 H 3.90, found C 51.05 H 3.85.

[L1^{py}Pd(Cl)(PdMe)][PF$_6$]: A 25 ml Schlenk tube was charged with [L1^{py}HPdMe][PF$_6$] (121 mg, 0.162 mmol), (COD)Pd(Me)Cl (85.6 mg, 0.324 mmol), Et_3N (2.2 ml, 0.016 mmol), 2 ml CH_3CN, and a magnetic stirbar. A deep red-purple solution formed upon heating at 80 ˚C overnight. Addition of 10 ml Et_2O precipitated a solid which was redissolved in 1 ml CH_3CN and again precipitated with Et_2O to give a red-purple solid (115 mg, 80%). Single crystals suitable for x-ray diffraction were grown by slow diffusion of Et_2O into a 3:1 CH_2Cl_2/DMSO solution. ^{1}H NMR (CD_3CN, 500 MHz, 20 ˚C): *d* (ppm) 8.73 (dd, *J* = 5.2 Hz, *J* = 1.4 Hz, 1H), 8.47 (dd, *J* = 8.4 Hz, *J* = 1.2 Hz, 1H), 7.95 (d, *J* = 8.2 Hz, 1H), 7.86 (d (br), *J* = 4.7 Hz, 2H), 7.73 (dd, *J* = 7.8 Hz, *J* = 0.8 Hz, 1H), 7.52-7.62 (m, 6H), 7.27 (d, *J* = 7.6 Hz, 1H), 7.25 (dd, *J* = 7.9 Hz, *J* = 7.9 Hz, 1H), 7.10 (br, 2H), 7.02 (br, 2H), 6.76 (d, *J* = 7.8 Hz, 1H), 5.12 (br, 2H), 4.90 (d, *J* = 15.7 Hz, 2H), 4.28 (d, *J* = 15.7 Hz, 2H), 0.32 (s, 3H). ^{13}C NMR (CD_3CN, 125 MHz, 20 ˚C): *d* (ppm) 164.5, 156.8, 149.9, 149.8, 149.6, 149.5, 149.1, 148.9, 141.3, 140.5, 139.2, 132.3, 131.0, 130.7, 130.4, 127.6, 124.7, 124.3, 123.0, 117.1, 115.3, 114.6, 112.3, 66.0, 65.3, 6.3. ESI-MS: calc. for $C_{32}H_{28}ClN_6Pd_2$ $(M\text{-}PF_6)^+$ 745.0147, found 745.0127. Elemental analysis for $C_{32}H_{28}ClF_6N_6PPd_2$: calc. C 43.19 H 3.17, found C 43.07 H 3.45.

[L1^{py}HPtMe][PF$_6$]: A 20 ml scintillation vial was charged with (COD)Pt(Me)Cl (74 mg, 0.21 mmol), 2 ml acetonitrile, and a magnetic stirbar. Addition of $TlPF_6$ (73 mg, 0.21 mmol) afforded a white precipitate. Dropwise addition of a solution of L1^{py}H (101 mg, 0.21 mmol) in 2 ml CH_3CN produced a yellow-orange solution. After stirring overnight, solvent was removed in vacuo. The resulting solid was suspended in 5 ml CH_2Cl_2 and filtered. The yellow-brown filtrate was treated with Et_2O which resulted in precipitation

of a yellow-brown solid which was washed with pentate and dried to provide analytically pure product. ^{1}H NMR (CD_3CN, 500 MHz, 20 ˚C): *d* (ppm) 10.75 (s, 1H), 9.09 (dd, *J* = 4.3 Hz, *J* = 1.7 Hz, 1H), 8.39 (dd, *J* = 8.2 Hz, *J* = 1.7 Hz, 1H), 8.30 (d, 5.8Hz, $^{3}J_{PtH}$ = 19.6 Hz, 2H), 8.05 (d, 8.4 Hz, 1H), 7.93 (d, 7.6 Hz, 1H), 7.84 (dd, *J* = 10.7 Hz, *J* = 7.8 Hz, 2H), 7.63-7.72 (m, 3H), 7.53 (m, 2H), 7.41 (d, *J* = 7.6 Hz, 2H), 7.15 (dd, *J* = 6.7 Hz, *J* = 6.7 Hz, 2H), 5.13 (d, *J* = 5.6 Hz, 2H), 4.91 (d, *J* = 5.6 Hz, 2H), 4.51 (s, 2H), 0.69 (s, $^{3}J_{PtH}$ = 37.5 Hz, 3H). ^{13}C NMR (CD_3CN, 125 MHz, 20 ˚C): *d* (ppm) 167.0, 151.6, 149.3, 149.2, 140.4, 139.4, 138.8, 138.7, 137.4, 137.3, 129.8, 128.9, 128.4, 128.2, 125.5, 125.1, 124.8, 122.9, 119.1, 111.0, 110.5, 66.1, 64.2, -11.6. ^{195}Pt NMR (CD_3CN, 107 MHz, 20 ˚C): *d* (ppm) -3,059. ESI-MS: calc. for $C_{32}H_{29}N_6Pt$ $(M\text{-}PF_6)^+$ 692.2101, found 692.2083. Elemental analysis for $C_{32}H_{29}F_6N_6PPt$: calc. C 45.88 H 3.49, found C 45.82 H 3.55.

[L1^{py}Pd(Cl)(PtMe)][PF_6]: A 25 ml Schlenk tube was charged with [L1^{py}HPtMe][PF_6] (55.9 mg, 0.067 mmol), (COD)Pd(Me)Cl (17.7 mg, 0.067 mmol), Et_3N (1 ml, 0.007 mmol), 1 ml CH_3CN, and a magnetic stirbar. A deep red-purple solution formed upon heating at 80 ˚C overnight. Addition of 10 ml Et_2O precipitated a red-purple solid (62 mg, 95%). Single crystals suitable for x-ray diffraction were grown by slow diffusion of Et_2O into a 3:1 CH_2Cl_2/DMSO solution. ^{1}H NMR (CD_3CN, 500 MHz, 20 ˚C): *d* (ppm) 8.72 (dd, *J* = 5.2 Hz, *J* = 1.5 Hz, 1H), 8.44 (dd, *J* = 8.5 Hz, *J* = 1.4 Hz, 1H), 8.06 (br, 2H), 7.94 (d, *J* = 8.4 Hz, 1H), 7.71 (dd, *J* = 7.9 Hz, *J* = 0.9 Hz, 1H), 7.53-7.60 (m, 6H), 7.24 (m, 2H), 7.07 (br, 2H), 6.98 (br, 2H), 6.73 (d, *J* = 7.9 Hz, 1H), 5.32 (br, 2H), 4.83 (d, *J* = 15.6 Hz, 2H), 4.43 (d, *J* = 15.6 Hz, 2H), 0.22 (s, $^{3}J_{PtH}$ = 34.8 Hz, 3H). ^{13}C NMR (CD_3CN, 125 MHz, 20 ˚C): *d* (ppm) 165.6, 155.5, 149.8, 149.4, 149.3, 149.1, 148.7, 141.0, 140.1,

138.4, 132.0, 130.8, 130.5, 130.2, 127.3, 124.8, 124.0, 122.8, 116.8, 115.0, 114.2, 112.1, 65.6, -10.9. ^{195}Pt NMR (CD_3CN, 107 MHz, 20 ˚C): *d* (ppm) -3,038. ESI-MS: calc. for $C_{32}H_{28}ClN_6PdPt$ $(M\text{-}PF_6)^+$ 833.0747, found 833.0742. Elemental analysis for $C_{32}H_{28}ClF_6N_6PPdPt$: calc. C 39.28 H 2.88, found C 38.99 H 3.08.

[L2^{py}(PdBr)$_3$][BF$_4$]$_2$: A sealable NMR tube (J. Young) was charged with a solution of $[(CH_3CN)_4Pd][BF_4]_2$ (63.0 mg, 0.141 mmol) in 0.5 ml CD_3CN, a solution of L2^{py}H (32.8 mg, 0.047 mmol) in 0.5 ml CD_3CN, and Et_3N (9.9 ml, 0.071 mmol). Upon heating to 50 ˚C for 8 hr., the solution turned deep red-purple. To this solution was added TBABr (45.7 mg, 0.142 mmol) under an inert atmosphere. The solution turned deep purple immediately. The purple product was purified by recrystallization from a CH_3CN solution layered with Et_2O and crushing and drying the crystals (65 mg, 97%). Crystals suitable for x-ray diffraction were grown by slow diffusion of Et_2O into a CH_3CN solution. The ^{1}H and ^{13}C NMR signals are broad owing to at least one fluxional process. Five sharper peaks of similar intensity in the ^{1}H NMR spectrum with *d* (ppm) = 8.23 (d, *J* = 8.3 Hz, 2H), 7.94 (d, *J* = 8.3 Hz, 2H), 7.60 (d, *J* = 7.8 Hz, 2H), 7.49 (dd, *J* = 7.8 Hz, *J* = 7.8 Hz, 2H), and 7.06 (*J* = 7.9 Hz, 2H) ppm are tentatively assigned as the quinoline peaks; the broad methylene resonances occur between *d* = 4.0 and 5.6 ppm (see Figure SI38). Elemental analysis for $C_{44}H_{38}B_2Br_3F_8N_9Pd_3$: calc. C 37.07 H 2.69, found C 37.05 H 3.02.

[(MDPA)PdMe][PF$_6$]: (MDPA = *N*-methyl-2,2'-dipicolylamine): A 20 ml scintillation vial was charged with (COD)Pd(Me)Cl (809 mg, 3.05 mmol), a magnetic stirbar, and 10

ml CH_3CN. Addition of $TlPF_6$ (1.07 g, 3.05 mmol) afforded a white precipitate. A solution of MDPA (651 mg, 3.05 mmol) in 5 ml CH_3CN was added dropwise and the mixture was allowed to stir for 15 min. The mixture was then filtered and the TlCl was properly disposed. The filtrate was concentrated *in vacuo*, redissolved in a minimum volume of CH_2Cl_2, and precipated with Et_2O to give a pale yellow solid (1.14 g, 78%). ^{1}H NMR (CD_3CN, 500 MHz, 20 ˚C): *d* (ppm) 8.40 (d (br), 2H), 8.04 (ddd, J = 9.4 Hz, J = 7.8 Hz, J = 1.6 Hz, 2H), 7.58 (d (br), 2H), 7.52 (m, 2H), 4.80 (d, J =15.5 Hz, 2H), 4.21 (d, J = 15.5 Hz, 2H), 2.58 (s, 3H), 0.80 (s, 3H). ^{13}C NMR (CD_3CN, 125 MHz, 20 ˚C): *d* (ppm) 165.5, 150.6, 141.0, 126.0, 125.4, 65.6, 45.2, 4.0. ESI-MS: calc. for $C_{14}H_{18}N_3Pd$ $(M\text{-}PF_6)^+$ 334.0541, found 334.0539. Elemental analysis for $C_{14}H_{18}F_6N_3PPd$: calc. C 35.05 H 3.78, found C 35.19 H 3.79.

[(MDPA)PtMe][PF_6] (MDPA = *N*-methyl-2,2'-dipicolylamine): A 20 ml scintillation vial was charged with (COD)Pt(Me)Cl (50.6 mg, 0.143 mmol), a magnetic stirbar, and 1 ml CH_3CN. Addition of $TlPF_6$ (49.9 mg, 0.143 mmol) afforded a white precipitate. A solution of MDPA (30.5 mg, 0.143 mmol) in 1 ml CH_3CN was added dropwise and the mixture was allowed to stir overnight. The mixture was then filtered and the TlCl was properly disposed. The filtrate was concentrated in vacuo, redissolved in a minimum volume of CH_2Cl_2, and precipated with Et_2O to give a pale yellow solid (62 mg, 76%). ^{1}H NMR (CD_3CN, 500 MHz, 20 ˚C): δ (ppm) 8.60 (d (br), J = 5.8 Hz, $^3J_{PtH}$ = 25.2 Hz, 2H), 8.10, (ddd, J = 7.8 Hz, J = 7.8 Hz, J = 1.5 Hz, 2H), 7.58 (d (br), 7.8 Hz, 2H), 7.47 (m, 2H), 4.74 (d, J = 15.4 Hz, 2H), 4.41 (d, J = 15.4 Hz, $^3J_{PtH}$ = 11.0 Hz, 2H), 2.73 (s, $^3J_{PtH}$ = 6.5 Hz, 3H), 0.83 (s, $^3J_{PtH}$ = 32.8 Hz, 3H). ^{13}C NMR (CD_3CN, 125 MHz, 20 ˚C): *d*

(ppm) 166.8, 150.2, 140.6, 126.4, 125.5, 66.8, 46.4. ESI-MS: calc. for $C_{14}H_{18}N_3Pt$ $(M-PF_6)^+$ 423.1139, found 423.1154. Elemental analysis for $C_{14}H_{18}F_6N_3PPt$: calc. C 29.59 H 3.19, found C 29.57 H 3.15.

This chapter was reproduced in part with permission from

Suess, D. L. M.; Peters, J. C. *Chem. Commun.* **2010**, *46*, 6554.

(1) van den Beuken, E. K.; Feringa, B. L. *Tetrahedron,* **1998,** *54*, 12985.
(2) (a) Roundhill, D. M.; Gray, H. B.; Che, C.-M. *Acc. Chem. Res.,* **1989,** *22*, 55; (b) Wan, K.-T.; Che, C.-M.; Cho, K.-C. *J. Chem. Soc., Dalton Trans.,* **1991**, 1077; (c) Baralt, E.; Lukehart, C. M. *Inorg. Chem.,* **1991,** *30*, 319; (d) Kalsbeck, W. A.; Gingell, D. M.; Malinsky, J. E.; Thorp, H. H. *Inorg. Chem.,* **1994,** *33*, 3313.
(3) (a) Stiegman, A. E.; Rice, S. F.; Gray, H. B.; Miskowski, V. M. *Inorg. Chem.,* **1987,** *26*, 1112; (b) Che, C.-M.; Yam, V. W.-W.; Wong, W. T.; Lai, T. F. *Inorg. Chem.,* **1989,** *28*, 2908; (c) Bailey, J. A.; Miskowski, V. M.; Gray, H. B. *Inorg. Chem.,* **1993,** *32*, 369; (d) Yip, H. K.; Lin, H. M.; Wang, Y.; Che, C.-M. *Inorg. Chem.,* **1993,** *32*, 3402; (e) Xia, B.-H.; Che, C.-M.; Phillips, D. L.; Leung, K.-H.; Cheung, K.-K. *Inorg. Chem.,* **2002,** *41*, 3866; (f) Pan, Q.-J.; Zhang, H.-X.; Zhou, X.; Fu, H.-G.; Yu, H.-T. *J. Phys. Chem. A,* **2007,** *111*, 287.
(4) Bercaw, J. E.; Day, M. W.; Golisz, S. R.; Hazari, N.; Henling, L. M.; Labinger, J. A.; Schofer, S. J.; Virgil, S. *Organometallics,* **2009,** *28*, 5017.
(5) (a) Peters, J. C.; Harkins, S. B.; Brown, S. D.; Day, M. W. *Inorg. Chem.,* **2001,** *40*, 5083; (b) Harkins, S. B.; Peters, J. C. *Organometallics,* **2002,** *21*, 1753; (c) Harkins, S. B.; Peters, J. C. *Inorg. Chem.,* **2006,** *45*, 4316.
(6) Bondi, A. *J. Phys. Chem.,* **1964,** *68*, 441.
(7) Mann, K. R.; Gordon, J. G.; Gray, H. B. *J. Am. Chem. Soc.,* **1975,** *97*, 3553.
(8) Bercaw, J. E.; Durrell, A. C.; Gray, H. B.; Green, J. C.; Hazari, N.; Labinger, J. A.; Winkler, J. R. *Inorg. Chem.,* **2010,** *49*, 1801.
(9) M. J. Frisch, G. W. T., H. B. Schlegel, G. E. Scuseria, M. A. Robb, J. R. Cheeseman, J. A. Montgomery, Jr., T. Vreven, K. N. Kudin, J. C. Burant, J. M. Millam, S. S. Iyengar, J. Tomasi, V. Barone, B. Mennucci, M. Cossi, G. Scalmani, N. Rega, G. A. Petersson, H. Nakatsuji, M. Hada, M. Ehara, K. Toyota, R. Fukuda, J. Hasegawa, M. Ishida, T. Nakajima, Y. Honda, O. Kitao, H. Nakai, M. Klene, X. Li, J. E. Knox, H. P. Hratchian, J. B. Cross, V. Bakken, C. Adamo, J. Jaramillo, R. Gomperts, R. E. Stratmann, O. Yazyev, A. J. Austin, R. Cammi, C. Pomelli, J. W. Ochterski, P. Y. Ayala, K. Morokuma, G. A. Voth, P. Salvador, J. J. Dannenberg, V. G. Zakrzewski, S. Dapprich, A. D. Daniels, M. C. Strain, O. Farkas, D. K. Malick, A. D. Rabuck, K. Raghavachari, J. B. Foresman, J. V. Ortiz, Q. Cui, A. G. Baboul, S. Clifford, J. Cioslowski, B. B. Stefanov, G. Liu, A. Liashenko, P. Piskorz, I. Komaromi, R. L. Martin, D. J. Fox, T. Keith, M. A. Al-Laham, C. Y. Peng, A. Nanayakkara, M. Challacombe, P. M. W. Gill, B. Johnson, W. Chen, M. W. Wong, C. Gonzalez, and J. A. Pople. *Gaussian 03, Revision B.01*, Gaussian Inc.: Wallingford, CT, 2004.
(10) Lin, N.; Yan, J.; Huang, Z.; Altier, C.; Li, M.; Carrasco, N.; Suyemoto, M.; Johnston, L.; Wang, S.; Wang, Q.; Fang, H.; Caton-Williams, J.; Wang, B. *Nucleic Acids Res.,* **2007,** *35*, 1222.
(11) Banerjee, S. R.; Levadala, M. K.; Lazarova, N.; Wei, L.; Valliant, J. F.; Stephenson, K. A.; Babich, J. W.; Maresca, K. P.; Zubieta, J. *Inorg. Chem.,* **2002,** *41*, 6417.

Appendix A X-ray Diffraction Tables

Table A.1 Crystal data and structure refinement for (TPB)CoBr.

Identification code	(TBP)CoBr	
Empirical formula	C36 H54 B Br Co P3	
Formula weight	729.35	
Temperature	100(2) K	
Wavelength	0.71073 Å	
Crystal system	Triclinic	
Space group	P-1	
Unit cell dimensions	a = 10.8175(6) Å	α = 91.488(3)°
	b = 11.5615(7) Å	β = 97.701(3)°
	c = 15.9277(9) Å	γ = 117.196(2)°
Volume	1747.20(17) $Å^3$	
Z	2	
Density (calculated)	1.386 Mg/m^3	
Absorption coefficient	1.797 mm^{-1}	
F(000)	764	
Crystal size	0.37 x 0.30 x 0.26 mm^3	
Theta range for data collection	2.14 to 44.17°	
Index ranges	-21<=h<=21, -22<=k<=22, -31<=l<=31	
Reflections collected	147389	
Independent reflections	27532 [R(int) = 0.0486]	
Completeness to theta = 44.17°	99.8 %	
Absorption correction	Semi-empirical from equivalents	
Max. and min. transmission	0.6523 and 0.5562	
Refinement method	Full-matrix least-squares on F^2	
Data / restraints / parameters	27532 / 0 / 391	
Goodness-of-fit on F^2	1.012	
Final R indices [I>2sigma(I)]	R1 = 0.0321, wR2 = 0.0718	
R indices (all data)	R1 = 0.0545, wR2 = 0.0796	
Largest diff. peak and hole	1.166 and -0.396 e $Å^{-3}$	

Table A.2 Crystal data and structure refinement for (TPB)Co(N_2).

Identification code	(TPB)Co(N_2)	
Empirical formula	C36 H54 B Co N2 P3	
Formula weight	677.46	
Temperature	100(2) K	
Wavelength	0.71073 Å	
Crystal system	Triclinic	
Space group	P-1	
Unit cell dimensions	a = 10.8940(3) Å	α = 91.2180(10)°
	b = 11.4465(3) Å	β = 95.1680(10)°
	c = 16.0319(5) Å	γ = 118.1020(10)°
Volume	1751.68(9) $Å^3$	
Z	2	
Density (calculated)	1.284 Mg/m^3	
Absorption coefficient	0.655 mm^{-1}	
F(000)	722	
Crystal size	0.42 x 0.42 x 0.14 mm^3	
Theta range for data collection	1.28 to 43.07°	
Index ranges	-20<=h<=20, -21<=k<=21, -30<=l<=29	
Reflections collected	54492	
Independent reflections	22993 [R(int) = 0.0324]	
Completeness to theta = 25.00°	99.6 %	
Absorption correction	Semi-empirical from equivalents	
Max. and min. transmission	0.9139 and 0.7706	
Refinement method	Full-matrix least-squares on F^2	
Data / restraints / parameters	22993 / 0 / 400	
Goodness-of-fit on F^2	1.049	
Final R indices [I>2sigma(I)]	R1 = 0.0475, wR2 = 0.1110	
R indices (all data)	R1 = 0.0754, wR2 = 0.1258	
Largest diff. peak and hole	1.818 and -0.548 e $Å^{-3}$	

Table A.3 Crystal data and structure refinement for [(TPB)Co(N_2)][(Na(12-crown-4)$_2$].

Identification code	[(TPB)Co(N_2)][(Na(12-crown-4)$_2$]	
Empirical formula	C52 H86 B Co N2 Na O8 P3	
Formula weight	1052.87	
Temperature	100(2) K	
Wavelength	0.71073 Å	
Crystal system	Monoclinic	
Space group	P2(1)/n	
Unit cell dimensions	a = 10.8142(5) Å	α = 90°
	b = 27.5046(13) Å	β = 91.141(2)°
	c = 22.3660(10) Å	γ = 90°
Volume	6651.2(5) Å^3	
Z	4	
Density (calculated)	1.051 Mg/m^3	
Absorption coefficient	0.380 mm^{-1}	
F(000)	2256	
Crystal size	0.30 x 0.24 x 0.20 mm^3	
Theta range for data collection	1.97 to 43.13°	
Index ranges	-20<=h<=20, -52<=k<=52, -43<=l<=43	
Reflections collected	451328	
Independent reflections	49547 [R(int) = 0.0632]	
Completeness to theta = 43.13°	99.9 %	
Refinement method	Full-matrix least-squares on F^2	
Data / restraints / parameters	49547 / 1385 / 1158	
Goodness-of-fit on F^2	1.098	
Final R indices [I>2sigma(I)]	R1 = 0.0617, wR2 = 0.1541	
R indices (all data)	R1 = 0.0986, wR2 = 0.1731	
Largest diff. peak and hole	1.709 and -1.053 e Å^{-3}	

Table A.4 Crystal data and structure refinement for [(TPB)Co][BAr^F_4].

Identification code	[(TPB)Co][BAr^F_4]	
Empirical formula	C68 H66 B2 Co F24 P3	
Formula weight	1512.67	
Temperature	100(2) K	
Wavelength	0.71073 Å	
Crystal system	Orthorhombic	
Space group	Pbca	
Unit cell dimensions	a = 26.3920(15) Å	α = 90°
	b = 19.7049(13) Å	β = 90°
	c = 26.4995(19) Å	γ = 90°
Volume	13781.1(16) $Å^3$	
Z	8	
Density (calculated)	1.458 Mg/m^3	
Absorption coefficient	0.424 mm^{-1}	
F(000)	6176	
Crystal size	0.25 x 0.22 x 0.22 mm^3	
Theta range for data collection	1.86 to 32.03°	
Index ranges	-39<=h<=39, -23<=k<=29, -39<=l<=39	
Reflections collected	377520	
Independent reflections	23962 [R(int) = 0.0539]	
Completeness to theta = 32.03°	99.9 %	
Refinement method	Full-matrix least-squares on F^2	
Data / restraints / parameters	23962 / 1174 / 1007	
Goodness-of-fit on F^2	1.052	
Final R indices [I>2sigma(I)]	R1 = 0.0459, wR2 = 0.1085	
R indices (all data)	R1 = 0.0720, wR2 = 0.1241	
Largest diff. peak and hole	1.268 and -1.343 e $Å^{-3}$	

Table A.5 Crystal data and structure refinement for (TPB)Co(H_2).

Identification code	(TPB)Co(H_2)	
Empirical formula	C36 H54 B Co P3	
Formula weight	649.44	
Temperature	100(2) K	
Wavelength	0.71073 Å	
Crystal system	Triclinic	
Space group	P-1	
Unit cell dimensions	a = 10.8535(5) Å	α = 91.474(2)°
	b = 11.2160(5) Å	β = 101.653(2)°
	c = 16.7367(8) Å	γ = 118.930(2)°
Volume	1728.21(14) $Å^3$	
Z	2	
Density (calculated)	1.248 Mg/m^3	
Absorption coefficient	0.659 mm^{-1}	
F(000)	694	
Crystal size	0.37 x 0.26 x 0.05 mm^3	
Theta range for data collection	2.10 to 39.16°	
Index ranges	-18<=h<=19, -19<=k<=19, -29<=l<=29	
Reflections collected	89604	
Independent reflections	19439 [R(int) = 0.0338]	
Completeness to theta = 25.00°	100.0 %	
Absorption correction	Semi-empirical from equivalents	
Max. and min. transmission	0.9678 and 0.7926	
Refinement method	Full-matrix least-squares on F^2	
Data / restraints / parameters	19439 / 0 / 382	
Goodness-of-fit on F^2	1.041	
Final R indices [I>2sigma(I)]	R1 = 0.0348, wR2 = 0.0876	
R indices (all data)	R1 = 0.0559, wR2 = 0.0964	
Largest diff. peak and hole	1.543 and -0.556 e $Å^{-3}$	

Table A.6 Crystal data and structure refinement for (DPB)FeBr.

Identification code	(DPB)FeBr	
Empirical formula	C30 H41 B Br Fe P2	
Formula weight	610.14	
Temperature	100(2) K	
Wavelength	0.71073 Å	
Crystal system	Monoclinic	
Space group	C2/c	
Unit cell dimensions	a = 18.921(3) Å	α = 90°
	b = 9.9768(12) Å	β = 104.872(8)°
	c = 31.705(4) Å	γ = 90°
Volume	5784.4(13) $Å^3$	
Z	8	
Density (calculated)	1.401 Mg/m^3	
Absorption coefficient	2.031 mm^{-1}	
F(000)	2536	
Crystal size	0.388 x 0.312 x 0.298 mm^3	
Theta range for data collection	2.23 to 44.08°	
Index ranges	-36<=h<=36, -19<=k<=19, -59<=l<=62	
Reflections collected	130537	
Independent reflections	22550 [R(int) = 0.0437]	
Completeness to theta = 44.08°	99.3 %	
Absorption correction	None	
Refinement method	Full-matrix least-squares on F^2	
Data / restraints / parameters	22550 / 0 / 344	
Goodness-of-fit on F^2	1.039	
Final R indices [I>2sigma(I)]	R1 = 0.0414, wR2 = 0.0929	
R indices (all data)	R1 = 0.0675, wR2 = 0.1012	
Largest diff. peak and hole	0.987 and -1.739 e $Å^{-3}$	

Table A.7 Crystal data and structure refinement for $[(DPB)Fe]_2(\mu\text{-}1,2\text{-}N_2)$.

Identification code	$[(DPB)Fe]_2(\mu\text{-}1,2\text{-}N_2)$	
Empirical formula	C60 H82 B2 Fe2 N2 P4	
Formula weight	1088.54	
Temperature	100(2) K	
Wavelength	0.71073 Å	
Crystal system	Monoclinic	
Space group	P2(1)/c	
Unit cell dimensions	a = 13.6080(5) Å	$\alpha = 90^\circ$
	b = 22.6752(7) Å	$\beta = 103.3660(10)^\circ$
	c = 18.8057(7) Å	$\gamma = 90^\circ$
Volume	5645.6(3) $Å^3$	
Z	4	
Density (calculated)	1.281 Mg/m^3	
Absorption coefficient	0.667 mm^{-1}	
F(000)	2312	
Crystal size	0.46 x 0.38 x 0.25 mm^3	
Theta range for data collection	1.43 to 46.11°	
Index ranges	-27<=h<=27, -45<=k<=45, -37<=l<=37	
Reflections collected	485205	
Independent reflections	48837 [R(int) = 0.0684]	
Completeness to theta = 25.00°	100.0 %	
Absorption correction	None	
Refinement method	Full-matrix least-squares on F^2	
Data / restraints / parameters	48837 / 0 / 687	
Goodness-of-fit on F^2	1.023	
Final R indices [I>2sigma(I)]	R1 = 0.0359, wR2 = 0.0795	
R indices (all data)	R1 = 0.0668, wR2 = 0.0916	
Largest diff. peak and hole	0.972 and -0.338 e $Å^{-3}$	

Table A.8 Crystal data and structure refinement for (DPB–H)Fe(benzo[*h*]quinolin-10-yl).

Identification code	(DPB–H)Fe(benzo[*h*]quinolin-10-yl)	
Empirical formula	C43 H50 B Fe N O P2	
Formula weight	725.44	
Temperature	100(2) K	
Wavelength	0.71073 Å	
Crystal system	Monoclinic	
Space group	P2(1)/n	
Unit cell dimensions	a = 11.1418(5) Å	α = 90°
	b = 12.7713(6) Å	β = 96.033(2)°
	c = 30.2507(13) Å	γ = 90°
Volume	4280.7(3) $Å^3$	
Z	4	
Density (calculated)	1.126 Mg/m^3	
Absorption coefficient	0.457 mm^{-1}	
F(000)	1536	
Crystal size	0.34 x 0.32 x 0.22 mm^3	
Theta range for data collection	1.89 to 45.34°	
Index ranges	-22<=h<=22, -25<=k<=25, -60<=l<=47	
Reflections collected	131767	
Independent reflections	35224 [R(int) = 0.0431]	
Completeness to theta = 25.00°	99.7 %	
Refinement method	Full-matrix least-squares on F^2	
Data / restraints / parameters	35224 / 0 / 482	
Goodness-of-fit on F^2	1.030	
Final R indices [I>2sigma(I)]	R1 = 0.0522, wR2 = 0.1435	
R indices (all data)	R1 = 0.0733, wR2 = 0.1565	
Largest diff. peak and hole	1.761 and -1.298 e $Å^{-3}$	

Table A.9 Crystal data and structure refinement for (DPB–H)Fe(2-(pyridin-2-yl)phenyl).

Identification code	(DPB–H)Fe(2-(pyridin-2-yl)phenyl)	
Empirical formula	C41 H50 B Fe N P2	
Formula weight	685.42	
Temperature	100(2) K	
Wavelength	0.71073 Å	
Crystal system	Monoclinic	
Space group	P2(1)/n	
Unit cell dimensions	a = 11.4679(6) Å	α = 90.0000(3)°
	b = 17.2177(8) Å	β = 96.494(3)°
	c = 18.2046(6) Å	γ = 90.0000(3)°
Volume	3571.5(3) $Å^3$	
Z	4	
Density (calculated)	1.275 Mg/m^3	
Absorption coefficient	0.542 mm^{-1}	
F(000)	1456	
Crystal size	0.33 x 0.30 x 0.28 mm^3	
Theta range for data collection	1.63 to 31.03°	
Index ranges	-16<=h<=16, -24<=k<=24, -26<=l<=26	
Reflections collected	100878	
Independent reflections	11375 [R(int) = 0.0370]	
Completeness to theta = 31.03°	99.7 %	
Max. and min. transmission	0.8631 and 0.8414	
Refinement method	Full-matrix least-squares on F^2	
Data / restraints / parameters	11375 / 0 / 427	
Goodness-of-fit on F^2	1.041	
Final R indices [I>2sigma(I)]	R1 = 0.0292, wR2 = 0.0756	
R indices (all data)	R1 = 0.0344, wR2 = 0.0791	
Largest diff. peak and hole	0.515 and -0.357 e $Å^{-3}$	

Table A.10 Crystal data and structure refinement for (DPB–H)Fe(8-amidoquinoline).

Identification code	(DPB–H)Fe(8-amidoquinoline)	
Empirical formula	C39 H48 B Fe N2 P2	
Formula weight	673.39	
Temperature	100(2) K	
Wavelength	0.71073 Å	
Crystal system	Monoclinic	
Space group	P2(1)/n	
Unit cell dimensions	a = 11.9514(10) Å	α = 90°
	b = 22.7818(15) Å	β = 102.923(5)°
	c = 13.2520(11) Å	γ = 90°
Volume	3516.8(5) $Å^3$	
Z	4	
Density (calculated)	1.272 Mg/m^3	
Absorption coefficient	0.550 mm^{-1}	
F(000)	1428	
Crystal size	0.27 x 0.27 x 0.24 mm^3	
Theta range for data collection	1.79 to 35.47°	
Index ranges	-18<=h<=19, -35<=k<=35, -21<=l<=21	
Reflections collected	115929	
Independent reflections	15227 [R(int) = 0.0794]	
Completeness to theta = 25.00°	100.0 %	
Refinement method	Full-matrix least-squares on F^2	
Data / restraints / parameters	15227 / 1119 / 555	
Goodness-of-fit on F^2	0.831	
Final R indices [I>2sigma(I)]	R1 = 0.0459, wR2 = 0.1245	
R indices (all data)	R1 = 0.1018, wR2 = 0.1469	
Largest diff. peak and hole	0.711 and -0.645 e $Å^{-3}$	

Table A.11 Crystal data and structure refinement for [(DPB)Fe(N_2)][K(benzo-15-crown-5)$_2$].

Identification code	[(DPB)Fe(N_2)][K(benzo-15-crown-5)$_2$]	
Empirical formula	C58 H81 B Fe K N2 O10 P2	
Formula weight	1133.95	
Temperature	100(2) K	
Wavelength	0.71073 Å	
Crystal system	Triclinic	
Space group	P-1	
Unit cell dimensions	a = 15.072(4) Å	α = 65.274(8)°
	b = 16.020(2) Å	β = 67.441(8)°
	c = 16.354(3) Å	γ = 76.842(10)°
Volume	3301.5(11) Å^3	
Z	2	
Density (calculated)	1.141 Mg/m^3	
Absorption coefficient	0.391 mm^{-1}	
F(000)	1206	
Crystal size	0.30 x 0.10 x 0.10 mm^3	
Theta range for data collection	1.69 to 30.19°	
Index ranges	-21<=h<=21, -22<=k<=21, -22<=l<=22	
Reflections collected	119765	
Independent reflections	18004 [R(int) = 0.0608]	
Completeness to theta = 30.19°	91.8 %	
Max. and min. transmission	0.9620 and 0.8918	
Refinement method	Full-matrix least-squares on F^2	
Data / restraints / parameters	18004 / 854 / 797	
Goodness-of-fit on F^2	1.046	
Final R indices [I>2sigma(I)]	R1 = 0.0486, wR2 = 0.1389	
R indices (all data)	R1 = 0.0850, wR2 = 0.1604	
Largest diff. peak and hole	1.167 and -0.828 e Å^{-3}	

Table A.12 Crystal data and structure refinement for (DPB)Fe($NNSi_2$).

Identification code	(DPB)Fe($NNSi_2$)	
Empirical formula	C36 H57 B Fe N2 P2 Si2	
Formula weight	702.62	
Temperature	100(2) K	
Wavelength	0.71073 Å	
Crystal system	Triclinic	
Space group	P-1	
Unit cell dimensions	a = 10.5707(8) Å	α = 118.196(3)°
	b = 19.9433(14) Å	β = 97.760(4)°
	c = 20.5612(15) Å	γ = 92.754(3)°
Volume	3754.1(5) $Å^3$	
Z	4	
Density (calculated)	1.243 Mg/m^3	
Absorption coefficient	0.578 mm^{-1}	
F(000)	1504	
Crystal size	0.38 x 0.38 x 0.31 mm^3	
Theta range for data collection	1.96 to 50.11°	
Index ranges	-22<=h<=22, -42<=k<=43, -43<=l<=44	
Reflections collected	501556	
Independent reflections	77845 [R(int) = 0.0593]	
Completeness to theta = 25.00°	99.8 %	
Absorption correction	Semi-empirical from equivalents	
Max. and min. transmission	0.8411 and 0.8102	
Refinement method	Full-matrix least-squares on F^2	
Data / restraints / parameters	77845 / 0 / 857	
Goodness-of-fit on F^2	1.003	
Final R indices [I>2sigma(I)]	R1 = 0.0378, wR2 = 0.0824	
R indices (all data)	R1 = 0.0690, wR2 = 0.0937	
Largest diff. peak and hole	0.858 and -0.431 e $Å^{-3}$	

Table A.13 Crystal data and structure refinement for (DPB–H)FeN(Si)NSi_2.

Identification code	(DPB–H)FeN(Si)NSi_2	
Empirical formula	C42 H65 B Fe N2 P2 Si3	
Formula weight	810.83	
Temperature	100(2) K	
Wavelength	0.073 Å	
Crystal system	Triclinic	
Space group	P-1	
Unit cell dimensions	a = 10.167(15) Å	α = 99.79(5)°
	b = 12.843(12) Å	β = 95.23(5)°
	c = 18.21(3) Å	γ = 101.42(5)°
Volume	2277(5) $Å^3$	
Z	2	
Density (calculated)	1.183 Mg/m^3	
Absorption coefficient	0.510 mm^{-1}	
F(000)	868	
Crystal size	0.05 x 0.04 x 0.04 mm^3	
Theta range for data collection	1.65 to 24.55°	
Index ranges	-11<=h<=11, -14<=k<=14, -20<=l<=21	
Reflections collected	11316	
Independent reflections	5912 [R(int) = 0.0330]	
Completeness to theta = 24.55°	77.8 %	
Refinement method	Full-matrix least-squares on F^2	
Data / restraints / parameters	5912 / 0 / 485	
Goodness-of-fit on F^2	1.068	
Final R indices [I>2sigma(I)]	R1 = 0.0543, wR2 = 0.1547	
R indices (all data)	R1 = 0.0648, wR2 = 0.1615	
Largest diff. peak and hole	0.778 and -0.295 e $Å^{-3}$	

Table A.14 Crystal data and structure refinement for (^{Ph}DPB)FeBr.

Identification code	(^{Ph}DPB)FeBr	
Empirical formula	C42 H33 B Br Fe P2	
Formula weight	726.2	
Temperature	100(2) K	
Wavelength	0.71073 Å	
Crystal system	Triclinic	
Space group	P-1	
Unit cell dimensions	a = 9.6143(6) Å	α = 87.525(3)°
	b = 9.7710(5) Å	β = 88.376(4)°
	c = 19.9222(14) Å	γ = 68.912(2)°
Volume	1744.39(19) Å^3	
Z	2	
Density (calculated)	1.421 Mg/m^3	
Absorption coefficient	1.699 mm^{-1}	
F(000)	762	
Crystal size	0.18 x 0.16 x 0.08 mm^3	
Theta range for data collection	2.05 to 27.11°	
Index ranges	-12<=h<=12, -12<=k<=12, -25<=l<=25	
Reflections collected	66744	
Independent reflections	7693 [R(int) = 0.0822]	
Completeness to theta = 25.00°	99.9 %	
Absorption correction	None	
Refinement method	Full-matrix least-squares on F^2	
Data / restraints / parameters	7693 / 434 / 444	
Goodness-of-fit on F^2	1.038	
Final R indices [I>2sigma(I)]	R1 = 0.0461, wR2 = 0.1122	
R indices (all data)	R1 = 0.0774, wR2 = 0.1196	
Largest diff. peak and hole	0.545 and -0.474 e Å^{-3}	

Table A.15 Crystal data and structure refinement for (^{Ph}DPB)Fe

Identification code	(^{Ph}DPB)Fe	
Empirical formula	C54 H45 B1 Fe1 P2	
Formula weight	822.5	
Temperature	100(2) K	
Wavelength	0.71073 Å	
Crystal system	Triclinic	
Space group	P-1	
Unit cell dimensions	a = 9.8333(19) Å	α = 78.661(7)°
	b = 11.167(3) Å	β = 76.780(5)°
	c = 19.774(3) Å	γ = 88.148(8)°
Volume	2072.3(7) Å^3	
Z	2	
Density (calculated)	1.318 Mg/m^3	
Absorption coefficient	0.479 mm^{-1}	
F(000)	860	
Crystal size	0.32 x 0.30 x 0.19 mm^3	
Theta range for data collection	1.08 to 41.29°	
Index ranges	-18<=h<=18, -20<=k<=20, -36<=l<=36	
Reflections collected	88753	
Independent reflections	25823 [R(int) = 0.0617]	
Completeness to theta = 25.00°	100.0 %	
Absorption correction	None	
Refinement method	Full-matrix least-squares on F^2	
Data / restraints / parameters	25823 / 0 / 543	
Goodness-of-fit on F^2	0.987	
Final R indices [I>2sigma(I)]	R1 = 0.0505, wR2 = 0.1162	
R indices (all data)	R1 = 0.0929, wR2 = 0.1311	
Largest diff. peak and hole	1.331 and -0.473 e Å^{-3}	

Table A.16 Crystal data and structure refinement for (^{Ph}DPB)Fe(NNSi$_2$).

Identification code	(^{Ph}DPB)Fe(NNSi$_2$)	
Empirical formula	C48 H49 B Fe N2 P2 Si2	
Formula weight	838.67	
Temperature	100(2) K	
Wavelength	0.71073 Å	
Crystal system	Monoclinic	
Space group	P2(1)/n	
Unit cell dimensions	a = 10.7196(6) Å	α = 90°
	b = 18.1906(11) Å	β = 92.637(2)°
	c = 21.7101(10) Å	γ = 90°
Volume	4228.9(4) Å^3	
Z	4	
Density (calculated)	1.317 Mg/m^3	
Absorption coefficient	0.526 mm^{-1}	
F(000)	1760	
Crystal size	0.37 x 0.16 x 0.08 mm^3	
Theta range for data collection	1.88 to 41.63°	
Index ranges	-19<=h<=19, -33<=k<=33, -39<=l<=40	
Reflections collected	196104	
Independent reflections	28150 [R(int) = 0.0667]	
Completeness to theta = 25.00°	100.0 %	
Absorption correction	Semi-empirical from equivalents	
Max. and min. transmission	1.0000 and 0.9285	
Refinement method	Full-matrix least-squares on F^2	
Data / restraints / parameters	28150 / 0 / 529	
Goodness-of-fit on F^2	1.012	
Final R indices [I>2sigma(I)]	R1 = 0.0407, wR2 = 0.0901	
R indices (all data)	R1 = 0.0750, wR2 = 0.1024	
Largest diff. peak and hole	0.789 and -0.378 e Å^{-3}	

Table A.17 Crystal data and structure refinement for (^{Ph}DPB*–H)FeN(H)NSi$_2$.

Identification code	(^{Ph}DPB*–H)FeN(H)NSi$_2$	
Empirical formula	C56 H67 B Fe N2 O2 P2 Si2	
Formula weight	984.90	
Temperature	100(2) K	
Wavelength	0.71073 Å	
Crystal system	Triclinic	
Space group	P-1	
Unit cell dimensions	a = 12.2122(7) Å	α = 88.967(3)°
	b = 13.2685(8) Å	β = 80.813(3)°
	c = 16.1433(12) Å	γ = 84.376(2)°
Volume	2569.8(3) Å^3	
Z	2	
Density (calculated)	1.273 Mg/m^3	
Absorption coefficient	0.446 mm^{-1}	
F(000)	1044	
Crystal size	0.3 x 0.22 x 0.2 mm^3	
Theta range for data collection	1.96 to 44.14°	
Index ranges	-23<=h<=23, -25<=k<=25, -31<=l<=31	
Reflections collected	310067	
Independent reflections	40098 [R(int) = 0.0425]	
Completeness to theta = 44.14°	99.0 %	
Absorption correction	None	
Refinement method	Full-matrix least-squares on F^2	
Data / restraints / parameters	40098 / 585 / 627	
Goodness-of-fit on F^2	1.040	
Final R indices [I>2sigma(I)]	R1 = 0.0371, wR2 = 0.1070	
R indices (all data)	R1 = 0.0607, wR2 = 0.1162	
Largest diff. peak and hole	1.304 and -0.835 e Å^{-3}	

Table A.18 Crystal data and structure refinement for $(DPB)Fe(CO)_2$.

Identification code	$(DPB)Fe(CO)_2$	
Empirical formula	C32 H41 B Fe O2 P2	
Formula weight	586.25	
Temperature	100(2) K	
Wavelength	0.71073 Å	
Crystal system	Monoclinic	
Space group	P2(1)/c	
Unit cell dimensions	a = 16.8731(10) Å	$\alpha = 90^\circ$
	b = 9.0298(5) Å	$\beta = 110.704(2)^\circ$
	c = 21.5015(12) Å	$\gamma = 90^\circ$
Volume	3064.4(3) $Å^3$	
Z	4	
Density (calculated)	1.271 Mg/m^3	
Absorption coefficient	0.623 mm^{-1}	
F(000)	1240	
Crystal size	0.40 x 0.30 x 0.30 mm^3	
Theta range for data collection	1.29 to 39.03°	
Index ranges	-29<=h<=29, -15<=k<=15, -37<=l<=37	
Reflections collected	187067	
Independent reflections	17354 [R(int) = 0.0933]	
Completeness to theta = 25.00°	100.0 %	
Absorption correction	Semi-empirical from equivalents	
Max. and min. transmission	0.8351 and 0.7886	
Refinement method	Full-matrix least-squares on F^2	
Data / restraints / parameters	17354 / 0 / 351	
Goodness-of-fit on F^2	1.075	
Final R indices [I>2sigma(I)]	R1 = 0.0528, wR2 = 0.1146	
R indices (all data)	R1 = 0.0927, wR2 = 0.1320	
Largest diff. peak and hole	1.514 and -0.498 e $Å^{-3}$	

Table A.19 Crystal data and structure refinement for (DPB–H)Fe(H)$(CO)_2$.

Identification code	(DPB–H)Fe(H)$(CO)_2$	
Empirical formula	C32 H43 B Fe O2 P2	
Formula weight	588.26	
Temperature	100(2) K	
Wavelength	0.71073 Å	
Crystal system	Triclinic	
Space group	P-1	
Unit cell dimensions	a = 9.5324(6) Å	α = 98.981(3)°
	b = 9.7170(7) Å	β = 99.435(3)°
	c = 17.8890(16) Å	γ = 105.950(2)°
Volume	1535.9(2) $Å^3$	
Z	2	
Density (calculated)	1.272 Mg/m^3	
Absorption coefficient	0.622 mm^{-1}	
F(000)	624	
Crystal size	0.34 x 0.28 x 0.28 mm^3	
Theta range for data collection	2.23 to 48.60°	
Index ranges	-20<=h<=19, -19<=k<=19, -37<=l<=37	
Reflections collected	196119	
Independent reflections	29527 [R(int) = 0.0410]	
Completeness to theta = 25.00°	100.0 %	
Absorption correction	Semi-empirical from equivalents	
Max. and min. transmission	0.8451 and 0.8164	
Refinement method	Full-matrix least-squares on F^2	
Data / restraints / parameters	29527 / 451 / 427	
Goodness-of-fit on F^2	1.015	
Final R indices [I>2sigma(I)]	R1 = 0.0333, wR2 = 0.0924	
R indices (all data)	R1 = 0.0515, wR2 = 0.0976	
Largest diff. peak and hole	1.050 and -0.482 e $Å^{-3}$	

Table A.20 Crystal data and structure refinement for [(DPB)Fe(CO)$_2$][K(benzo-15-crown-5)$_2$].

Identification code	[(DPB)Fe(CO)$_2$][K(benzo-15-crown-5)$_2$]	
Empirical formula	C60 H81 B Fe K O12 P2	
Formula weight	1161.95	
Temperature	100(2) K	
Wavelength	0.71073 Å	
Crystal system	Monoclinic	
Space group	P2(1)/c	
Unit cell dimensions	a = 16.736(3) Å	$\alpha = 90^\circ$
	b = 11.266(2) Å	$\beta = 92.526(10)^\circ$
	c = 31.692(9) Å	$\gamma = 90^\circ$
Volume	5969(2) Å^3	
Z	4	
Density (calculated)	1.293 Mg/m^3	
Absorption coefficient	0.435 mm^{-1}	
F(000)	2468	
Crystal size	0.35 x 0.12 x 0.04 mm^3	
Theta range for data collection	1.73 to 32.68°	
Index ranges	-25<=h<=24, -16<=k<=16, -46<=l<=46	
Reflections collected	196722	
Independent reflections	20375 [R(int) = 0.0930]	
Completeness to theta = 25.00°	100.0 %	
Absorption correction	Semi-empirical from equivalents	
Max. and min. transmission	0.9828 and 0.8625	
Refinement method	Full-matrix least-squares on F^2	
Data / restraints / parameters	20375 / 0 / 702	
Goodness-of-fit on F^2	0.919	
Final R indices [I>2sigma(I)]	R1 = 0.0375, wR2 = 0.0756	
R indices (all data)	R1 = 0.0807, wR2 = 0.0833	
Largest diff. peak and hole	0.438 and -0.534 e Å^{-3}	

Table A.21 Crystal data and structure refinement for $[(DPB)Fe(CO)_2][K(benzo\text{-}15\text{-}crown\text{-}5)_2]_2$.

Identification code	$[(DPB)Fe(CO)_2][K(benzo\text{-}15\text{-}crown\text{-}5)_2]_2$	
Empirical formula	C46 H64.50 B0.50 Fe0.50 K O11.50 P	
Formula weight	904.88	
Temperature	100(2) K	
Wavelength	0.71073 Å	
Crystal system	Triclinic	
Space group	P-1	
Unit cell dimensions	a = 14.3954(14) Å	α = 96.728(4)°
	b = 14.7510(12) Å	β = 96.954(2)°
	c = 24.5846(14) Å	γ = 115.227(2)°
Volume	4604.3(6) $Å^3$	
Z	4	
Density (calculated)	1.305 Mg/m^3	
Absorption coefficient	0.361 mm^{-1}	
F(000)	1928	
Crystal size	0.30 x 0.30 x 0.20 mm^3	
Theta range for data collection	1.66 to 42.89°	
Index ranges	-27<=h<=27, -28<=k<=27, -46<=l<=46	
Reflections collected	340219	
Independent reflections	64746 [R(int) = 0.0551]	
Completeness to theta = 25.00°	100.0 %	
Absorption correction	Semi-empirical from equivalents	
Max. and min. transmission	0.9314 and 0.8995	
Refinement method	Full-matrix least-squares on F^2	
Data / restraints / parameters	64746 / 0 / 1098	
Goodness-of-fit on F^2	1.021	
Final R indices [I>2sigma(I)]	R1 = 0.0472, wR2 = 0.1091	
R indices (all data)	R1 = 0.0857, wR2 = 0.1242	
Largest diff. peak and hole	1.257 and -1.146 e $Å^{-3}$	

Table A.22 Crystal data and structure refinement for $(DPB)Fe(CO)_3$.

Identification code	$(DPB)Fe(CO)_3$	
Empirical formula	C33 H41 B Fe O3 P2	
Formula weight	614.26	
Temperature	100(2) K	
Wavelength	0.71073 Å	
Crystal system	Monoclinic	
Space group	P2(1)/n	
Unit cell dimensions	a = 10.1059(5) Å	$\alpha = 90^\circ$
	b = 16.9341(7) Å	$\beta = 92.838(2)^\circ$
	c = 18.0259(9) Å	$\gamma = 90^\circ$
Volume	3081.1(3) $Å^3$	
Z	4	
Density (calculated)	1.324 Mg/m^3	
Absorption coefficient	0.626 mm^{-1}	
F(000)	1296	
Crystal size	0.39 x 0.32 x 0.23 mm^3	
Theta range for data collection	2.26 to 47.13°	
Index ranges	-20<=h<=20, -34<=k<=34, -37<=l<=25	
Reflections collected	423493	
Independent reflections	28099 [R(int) = 0.0543]	
Completeness to theta = 25.00°	99.9 %	
Absorption correction	None	
Refinement method	Full-matrix least-squares on F^2	
Data / restraints / parameters	28099 / 0 / 369	
Goodness-of-fit on F^2	1.043	
Final R indices [I>2sigma(I)]	R1 = 0.0302, wR2 = 0.0871	
R indices (all data)	R1 = 0.0499, wR2 = 0.0921	
Largest diff. peak and hole	1.574 and -0.440 e $Å^{-3}$	

Table A.23 Crystal data and structure refinement for (DPB)Fe($COSiMe_3$)$_2$.

Identification code	(DPB)Fe($COSiMe_3$)$_2$	
Empirical formula	C38 H59 B Fe O2 P2 Si2	
Formula weight	732.63	
Temperature	100(2) K	
Wavelength	0.71073 Å	
Crystal system	Triclinic	
Space group	P-1	
Unit cell dimensions	a = 12.6336(12) Å	α = 90.693(2)°
	b = 18.0101(17) Å	β = 103.060(3)°
	c = 18.2534(13) Å	γ = 90.701(3)°
Volume	4045.0(6) Å^3	
Z	4	
Density (calculated)	1.203 Mg/m^3	
Absorption coefficient	0.541 mm^{-1}	
F(000)	1568	
Crystal size	0.28 x 0.22 x 0.10 mm^3	
Theta range for data collection	1.79 to 37.12°	
Index ranges	-21<=h<=21, -29<=k<=30, -30<=l<=30	
Reflections collected	299923	
Independent reflections	39962 [R(int) = 0.0678]	
Completeness to theta = 25.00°	100.0 %	
Absorption correction	Semi-empirical from equivalents	
Max. and min. transmission	0.9478 and 0.8632	
Refinement method	Full-matrix least-squares on F^2	
Data / restraints / parameters	39962 / 0 / 857	
Goodness-of-fit on F^2	0.948	
Final R indices [I>2sigma(I)]	R1 = 0.0379, wR2 = 0.0907	
R indices (all data)	R1 = 0.0688, wR2 = 0.0984	
Largest diff. peak and hole	1.159 and -0.743 e Å^{-3}	

Table A.24 Crystal data and structure refinement for SOP_2.

Identification code	SOP_2	
Empirical formula	C36 H28 O P2 S	
Formula weight	570.58	
Temperature	100(2) K	
Wavelength	0.71073 Å	
Crystal system	Orthorhombic	
Space group	Pbca	
Unit cell dimensions	a = 10.3898(11) Å	α = 90°
	b = 16.0613(19) Å	β = 90°
	c = 34.037(4) Å	γ = 90°
Volume	5679.9(11) $Å^3$	
Z	8	
Density (calculated)	1.334 Mg/m^3	
Absorption coefficient	0.256 mm^{-1}	
F(000)	2384	
Crystal size	0.30 x 0.30 x 0.20 mm^3	
Theta range for data collection	1.20 to 29.57°	
Index ranges	-14<=h<=14, -22<=k<=22, -47<=l<=47	
Reflections collected	121249	
Independent reflections	7980 [R(int) = 0.0672]	
Completeness to theta = 29.57°	100.0 %	
Absorption correction	Semi-empirical from equivalents	
Max. and min. transmission	0.9506 and 0.9272	
Refinement method	Full-matrix least-squares on F^2	
Data / restraints / parameters	7980 / 0 / 361	
Goodness-of-fit on F^2	1.071	
Final R indices [I>2sigma(I)]	R1 = 0.0421, wR2 = 0.1050	
R indices (all data)	R1 = 0.0540, wR2 = 0.1137	
Absolute structure parameter	-0.014(10)	
Largest diff. peak and hole	0.460 and -0.362 e $Å^{-3}$	

Table A.25 Crystal data and structure refinement for $(SOP_2)RhCl$.

Identification code	$(SOP_2)RhCl$	
Empirical formula	C48 H60 Cl O4 P2 Rh S	
Formula weight	933.32	
Temperature	100(2) K	
Wavelength	0.71073 Å	
Crystal system	Monoclinic	
Space group	P2(1)/n	
Unit cell dimensions	a = 16.9653(17) Å	$\alpha = 90^\circ$
	b = 10.9952(11) Å	$\beta = 108.588(2)^\circ$
	c = 24.222(2) Å	$\gamma = 90^\circ$
Volume	4282.5(7) $Å^3$	
Z	4	
Density (calculated)	1.448 Mg/m^3	
Absorption coefficient	0.629 mm^{-1}	
F(000)	1952	
Crystal size	0.30 x 0.10 x 0.05 mm^3	
Theta range for data collection	1.29 to 29.57°	
Index ranges	-23<=h<=23, -15<=k<=15, -33<=l<=33	
Reflections collected	93917	
Independent reflections	12021 [R(int) = 0.0769]	
Completeness to theta = 29.57°	100.0 %	
Absorption correction	Semi-empirical from equivalents	
Max. and min. transmission	0.9692 and 0.8336	
Refinement method	Full-matrix least-squares on F^2	
Data / restraints / parameters	12021 / 553 / 543	
Goodness-of-fit on F^2	1.048	
Final R indices [I>2sigma(I)]	R1 = 0.0471, wR2 = 0.1200	
R indices (all data)	R1 = 0.0650, wR2 = 0.1335	
Absolute structure parameter	-0.014(10)	
Largest diff. peak and hole	1.622 and -0.925 e $Å^{-3}$	

Table A.26 Crystal data and structure refinement for $(SOP_2)RhN_3$.

Identification code	$(SOP_2)RhN_3$	
Empirical formula	C36 H28 N3 O P2 Rh S	
Formula weight	715.52	
Temperature	100(2) K	
Wavelength	0.71073 Å	
Crystal system	Orthorhombic	
Space group	P2(1)2(1)2(1)	
Unit cell dimensions	a = 12.0674(4) Å	α = 90°
	b = 12.7353(4) Å	β = 90°
	c = 19.5111(6) Å	γ = 90°
Volume	2998.50(17) $Å^3$	
Z	4	
Density (calculated)	1.585 Mg/m^3	
Absorption coefficient	0.782 mm^{-1}	
F(000)	1456	
Crystal size	0.20 x 0.15 x 0.10 mm^3	
Theta range for data collection	1.91 to 36.35°	
Index ranges	-20<=h<=19, -21<=k<=21, -32<=l<=32	
Reflections collected	102598	
Independent reflections	14570 [R(int) = 0.0583]	
Completeness to theta = 36.35°	100.0 %	
Absorption correction	Semi-empirical from equivalents	
Max. and min. transmission	0.9259 and 0.8592	
Refinement method	Full-matrix least-squares on F^2	
Data / restraints / parameters	14570 / 0 / 397	
Goodness-of-fit on F^2	1.031	
Final R indices [I>2sigma(I)]	R1 = 0.0267, wR2 = 0.0527	
R indices (all data)	R1 = 0.0329, wR2 = 0.0551	
Absolute structure parameter	-0.014(10)	
Largest diff. peak and hole	0.545 and -0.603 e $Å^{-3}$	

Table A.27 Crystal data and structure refinement for $[(SOP_2)Rh(CH_3CN)][PF_6]$.

Identification code	$[(SOP_2)Rh(CH_3CN)][PF_6]$	
Empirical formula	C48.50 H43 F6 N O P3 Rh S	
Formula weight	997.72	
Temperature	100(2) K	
Wavelength	0.71073 Å	
Crystal system	Monoclinic	
Space group	C2/c	
Unit cell dimensions	a = 33.188(2) Å	$\alpha = 90^\circ$
	b = 12.5088(7) Å	$\beta = 125.157(2)^\circ$
	c = 27.1062(16) Å	$\gamma = 90^\circ$
Volume	9200.0(9) $Å^3$	
Z	8	
Density (calculated)	1.441 Mg/m^3	
Absorption coefficient	0.582 mm^{-1}	
F(000)	4072	
Crystal size	0.3 x 0.1 x 0.08 mm^3	
Theta range for data collection	1.81 to 34.97°	
Index ranges	-49<=h<=53, -19<=k<=19, -43<=l<=43	
Reflections collected	129317	
Independent reflections	20010 [R(int) = 0.0594]	
Completeness to theta = 34.97°	99.0 %	
Absorption correction	None	
Refinement method	Full-matrix least-squares on F^2	
Data / restraints / parameters	20010 / 508 / 559	
Goodness-of-fit on F^2	1.024	
Final R indices [I>2sigma(I)]	R1 = 0.0356, wR2 = 0.0787	
R indices (all data)	R1 = 0.0586, wR2 = 0.0888	
Absolute structure parameter	1.002(5)	
Extinction coefficient	none	
Largest diff. peak and hole	1.299 and -0.692 e $Å^{-3}$	

Table A.28 Crystal data and structure refinement for $(SOP_2)IrCl(COE)$.

Identification code	$(SOP_2)IrCl(COE)$	
Empirical formula	C52 H58 Cl Ir O3 P2 S	
Formula weight	1052.63	
Temperature	100(2) K	
Wavelength	0.71073 Å	
Crystal system	Triclinic	
Space group	P-1	
Unit cell dimensions	a = 10.8356(9) Å	α = 67.9740(10)°
	b = 14.2555(12) Å	β = 87.4340(10)°
	c = 17.2755(14) Å	γ = 67.8130(10)°
Volume	2275.9(3) $Å^3$	
Z	2	
Density (calculated)	1.536 Mg/m^3	
Absorption coefficient	3.151 mm^{-1}	
F(000)	1068	
Crystal size	0.18 x 0.18 x 0.10 mm^3	
Theta range for data collection	1.28 to 28.70°	
Index ranges	-14<=h<=14, -19<=k<=19, -23<=l<=23	
Reflections collected	48703	
Independent reflections	11715 [R(int) = 0.0648]	
Completeness to theta = 28.70°	99.5 %	
Absorption correction	Semi-empirical from equivalents	
Max. and min. transmission	0.7435 and 0.6008	
Refinement method	Full-matrix least-squares on F^2	
Data / restraints / parameters	11715 / 588 / 578	
Goodness-of-fit on F^2	1.033	
Final R indices [I>2sigma(I)]	R1 = 0.0392, wR2 = 0.0850	
R indices (all data)	R1 = 0.0526, wR2 = 0.0917	
Absolute structure parameter	1.002(5)	
Largest diff. peak and hole	4.086 and -1.163 e $Å^{-3}$	

Table A.29 Crystal data and structure refinement for [(SOP_2)IrCl(H)(CH_3CN)][OTf].

Identification code	[(SOP_2)IrCl(H)(CH_3CN)][OTf]	
Empirical formula	C41 H34 Cl F3 Ir N2 O4 P2 S2	
Formula weight	1029.41	
Temperature	100(2) K	
Wavelength	1.54178 Å	
Crystal system	Monoclinic	
Space group	Pc	
Unit cell dimensions	a = 9.9455(4) Å	$\alpha = 90^\circ$
	b = 13.7424(5) Å	$\beta = 94.950(2)^\circ$
	c = 15.6180(6) Å	$\gamma = 90^\circ$
Volume	2126.63(14) $Å^3$	
Z	2	
Density (calculated)	1.608 Mg/m^3	
Absorption coefficient	8.756 mm^{-1}	
F(000)	1018	
Crystal size	0.41 x 0.25 x 0.16 mm^3	
Theta range for data collection	3.22 to 66.59°	
Index ranges	-11<=h<=11, -16<=k<=15, -18<=l<=18	
Reflections collected	36393	
Independent reflections	7298 [R(int) = 0.0368]	
Completeness to theta = 66.59°	100.0 %	
Absorption correction	Semi-empirical from equivalents	
Max. and min. transmission	0.3348 and 0.1237	
Refinement method	Full-matrix least-squares on F^2	
Data / restraints / parameters	7298 / 446 / 508	
Goodness-of-fit on F^2	1.068	
Final R indices [I>2sigma(I)]	R1 = 0.0202, wR2 = 0.0504	
R indices (all data)	R1 = NaN, wR2 = 0.0505	
Absolute structure parameter	1.002(5)	
Largest diff. peak and hole	0.848 and -0.616 e $Å^{-3}$	

Table A.30 Crystal data and structure refinement for $(SOP_2)IrCl$.

Identification code	$(SOP_2)IrCl$	
Empirical formula	C40 H36 Cl Ir O2 P2 S	
Formula weight	870.34	
Temperature	100(2) K	
Wavelength	0.71073 Å	
Crystal system	Triclinic	
Space group	P-1	
Unit cell dimensions	a = 10.1433(3) Å	α = 94.60°
	b = 10.4097(3) Å	β = 92.44°
	c = 17.6886(4) Å	γ = 113.23°
Volume	1705.13(8) $Å^3$	
Z	2	
Density (calculated)	1.695 Mg/m^3	
Absorption coefficient	4.185 mm^{-1}	
F(000)	864	
Crystal size	0.23 x 0.15 x 0.06 mm^3	
Theta range for data collection	2.14 to 29.13°	
Index ranges	-13<=h<=13, -14<=k<=14, -16<=l<=24	
Reflections collected	34905	
Independent reflections	9155 [R(int) = 0.0320]	
Completeness to theta = 29.13°	99.7 %	
Absorption correction	Semi-empirical from equivalents	
Max. and min. transmission	0.7874 and 0.4461	
Refinement method	Full-matrix least-squares on F^2	
Data / restraints / parameters	9155 / 0 / 424	
Goodness-of-fit on F^2	1.030	
Final R indices [I>2sigma(I)]	R1 = 0.0195, wR2 = 0.0466	
R indices (all data)	R1 = 0.0211, wR2 = 0.0473	
Absolute structure parameter	1.042(12)	
Largest diff. peak and hole	1.303 and -0.791 e $Å^{-3}$	

Table A.31 Crystal data and structure refinement for $(SOP_2)IrCl(O_2)$.

Identification code	$(SOP_2)IrCl(O_2)$	
Empirical formula	C36 H28 Cl Ir O3 P2 S	
Formula weight	830.23	
Temperature	100(2) K	
Wavelength	0.71073 Å	
Crystal system	Monoclinic	
Space group	P2(1)/c	
Unit cell dimensions	a = 17.1826(12) Å	$\alpha = 90^\circ$
	b = 9.3648(7) Å	$\beta = 104.127(2)^\circ$
	c = 19.5299(14) Å	$\gamma = 90^\circ$
Volume	3047.5(4) $Å^3$	
Z	4	
Density (calculated)	1.810 Mg/m^3	
Absorption coefficient	4.680 mm^{-1}	
F(000)	1632	
Crystal size	0.22 x 0.07 x 0.06 mm^3	
Theta range for data collection	2.15 to 37.07°	
Index ranges	-26<=h<=29, -15<=k<=15, -33<=l<=33	
Reflections collected	117710	
Independent reflections	15523 [R(int) = 0.0601]	
Completeness to theta = 37.07°	99.7 %	
Absorption correction	Semi-empirical from equivalents	
Max. and min. transmission	0.7665 and 0.4258	
Refinement method	Full-matrix least-squares on F^2	
Data / restraints / parameters	15523 / 0 / 397	
Goodness-of-fit on F^2	1.032	
Final R indices [I>2sigma(I)]	R1 = 0.0320, wR2 = 0.0688	
R indices (all data)	R1 = 0.0484, wR2 = 0.0747	
Absolute structure parameter	1.042(12)	
Largest diff. peak and hole	7.405 and -2.049 e $Å^{-3}$	

Table A.32 Crystal data and structure refinement for $(SOP_2)Ni(CO)$.

Identification code	$(SOP_2)Ni(CO)$	
Empirical formula	C39 H28 Ni O2.50 P2 S	
Formula weight	689.32	
Temperature	100(2) K	
Wavelength	0.71073 Å	
Crystal system	Monoclinic	
Space group	P2(1)/c	
Unit cell dimensions	a = 10.1778(5) Å	$\alpha = 90^\circ$
	b = 18.3139(9) Å	$\beta = 104.693(3)^\circ$
	c = 18.2294(9) Å	$\gamma = 90^\circ$
Volume	3286.8(3) $Å^3$	
Z	4	
Density (calculated)	1.393 Mg/m^3	
Absorption coefficient	0.787 mm^{-1}	
F(000)	1424	
Crystal size	0.20 x 0.19 x 0.14 mm^3	
Theta range for data collection	2.07 to 26.37°	
Index ranges	-12<=h<=12, -22<=k<=22, -22<=l<=22	
Reflections collected	90737	
Independent reflections	6723 [R(int) = 0.0544]	
Completeness to theta = 26.37°	99.9 %	
Absorption correction	Semi-empirical from equivalents	
Max. and min. transmission	0.8978 and 0.8584	
Refinement method	Full-matrix least-squares on F^2	
Data / restraints / parameters	6723 / 430 / 433	
Goodness-of-fit on F^2	1.326	
Final R indices [I>2sigma(I)]	R1 = 0.0741, wR2 = 0.1778	
R indices (all data)	R1 = 0.0805, wR2 = 0.1807	
Absolute structure parameter	1.042(12)	
Largest diff. peak and hole	1.623 and -0.632 e $Å^{-3}$	

Table A.33 Crystal data and structure refinement for $[(SOP_2)NiCl][PF_6]$.

Identification code	$[(SOP_2)NiCl][PF_6]$	
Empirical formula	C39 H31 Cl F6 Ni O P3 S	
Formula weight	848.77	
Temperature	100(2) K	
Wavelength	1.54178 Å	
Crystal system	Monoclinic	
Space group	P2(1)/c	
Unit cell dimensions	a = 13.3638(2) Å	α = 90°
	b = 15.4106(2) Å	β = 106.0510(10)°
	c = 18.3533(2) Å	γ = 90°
Volume	3632.40(8) $Å^3$	
Z	4	
Density (calculated)	1.552 Mg/m^3	
Absorption coefficient	3.791 mm^{-1}	
F(000)	1732	
Crystal size	0.24 x 0.17 x 0.17 mm^3	
Theta range for data collection	3.44 to 65.08°	
Index ranges	-15<=h<=15, -18<=k<=18, -19<=l<=21	
Reflections collected	68984	
Independent reflections	6189 [R(int) = 0.0320]	
Completeness to theta = 65.08°	100.0 %	
Absorption correction	Semi-empirical from equivalents	
Max. and min. transmission	0.5650 and 0.4631	
Refinement method	Full-matrix least-squares on F^2	
Data / restraints / parameters	6189 / 420 / 469	
Goodness-of-fit on F^2	1.029	
Final R indices [I>2sigma(I)]	R1 = 0.0342, wR2 = 0.0865	
R indices (all data)	R1 = 0.0368, wR2 = 0.0888	
Absolute structure parameter	1.042(12)	
Largest diff. peak and hole	0.817 and -0.643 e $Å^{-3}$	

Table A.34 Crystal data and structure refinement for $(SOP_2)Pd(PPh_3)$.

Identification code	$(SOP_2)Pd(PPh_3)$	
Empirical formula	C54 H43 O P3 Pd S	
Formula weight	939.3	
Temperature	100(2) K	
Wavelength	0.71073 Å	
Crystal system	Monoclinic	
Space group	P2(1)/c	
Unit cell dimensions	a = 20.0444(9) Å	α = 90°
	b = 12.6952(6) Å	β = 99.7570(10)°
	c = 20.6272(9) Å	γ = 90°
Volume	5173.0(4) $Å^3$	
Z	4	
Density (calculated)	1.399 Mg/m^3	
Absorption coefficient	0.538 mm^{-1}	
F(000)	2256	
Crystal size	0.32 x 0.30 x 0.11 mm^3	
Theta range for data collection	1.89 to 33.73°	
Index ranges	-31<=h<=30, -19<=k<=19, -32<=l<=32	
Reflections collected	181033	
Independent reflections	20653 [R(int) = 0.0591]	
Completeness to theta = 33.73°	99.9 %	
Absorption correction	Semi-empirical from equivalents	
Max. and min. transmission	0.9432 and 0.8467	
Refinement method	Full-matrix least-squares on F^2	
Data / restraints / parameters	20653 / 735 / 677	
Goodness-of-fit on F^2	1.071	
Final R indices [I>2sigma(I)]	R1 = 0.0462, wR2 = 0.1039	
R indices (all data)	R1 = 0.0659, wR2 = 0.1152	
Absolute structure parameter	1.042(12)	
Largest diff. peak and hole	1.590 and -1.231 e $Å^{-3}$	

Table A.35 Crystal data and structure refinement for $(SOP_2)Pt(PPh_3)$.

Identification code	$(SOP_2)Pt(PPh_3)$	
Empirical formula	C54.50 H43 Cl O P3 Pt S	
Formula weight	1069.40	
Temperature	100(2) K	
Wavelength	0.71073 Å	
Crystal system	Triclinic	
Space group	P-1	
Unit cell dimensions	a = 11.2946(5) Å	α = 86.456(2)°
	b = 11.4688(5) Å	β = 88.538(2)°
	c = 17.2693(8) Å	γ = 77.085(2)°
Volume	2176.07(17) $Å^3$	
Z	2	
Density (calculated)	1.632 Mg/m^3	
Absorption coefficient	3.486 mm^{-1}	
F(000)	1068	
Crystal size	0.25 x 0.17 x 0.08 mm^3	
Theta range for data collection	1.85 to 36.43°	
Index ranges	-18<=h<=18, -19<=k<=17, -28<=l<=28	
Reflections collected	112644	
Independent reflections	20303 [R(int) = 0.0404]	
Completeness to theta = 36.43°	95.5 %	
Absorption correction	Semi-empirical from equivalents	
Max. and min. transmission	0.7679 and 0.4761	
Refinement method	Full-matrix least-squares on F^2	
Data / restraints / parameters	20303 / 0 / 568	
Goodness-of-fit on F^2	1.041	
Final R indices [I>2sigma(I)]	R1 = 0.0248, wR2 = 0.0545	
R indices (all data)	R1 = 0.0322, wR2 = 0.0566	
Absolute structure parameter	1.042(12)	
Largest diff. peak and hole	1.834 and -1.408 e $Å^{-3}$	

Table A.36 Crystal data and structure refinement for [(SOP_2)PdCl][PF_6].

Identification code	[(SOP_2)PdCl][PF_6]	
Empirical formula	C38 H28 Cl F6 N O P3 Pd S	
Formula weight	895.43	
Temperature	100(2) K	
Wavelength	0.71073 Å	
Crystal system	Monoclinic	
Space group	P2(1)/c	
Unit cell dimensions	a = 13.3148(5) Å	α = 90°
	b = 15.3494(5) Å	β = 105.973(2)°
	c = 18.7144(6) Å	γ = 90°
Volume	3677.1(2) $Å^3$	
Z	4	
Density (calculated)	1.617 Mg/m^3	
Absorption coefficient	0.828 mm^{-1}	
F(000)	1796	
Crystal size	0.22 x 0.20 x 0.11 mm^3	
Theta range for data collection	2.07 to 41.18°	
Index ranges	-24<=h<=22, -28<=k<=28, -34<=l<=34	
Reflections collected	197055	
Independent reflections	24459 [R(int) = 0.0431]	
Completeness to theta = 41.18°	99.9 %	
Absorption correction	Semi-empirical from equivalents	
Max. and min. transmission	0.9144 and 0.8387	
Refinement method	Full-matrix least-squares on F^2	
Data / restraints / parameters	24459 / 588 / 525	
Goodness-of-fit on F^2	1.041	
Final R indices [I>2sigma(I)]	R1 = 0.0356, wR2 = 0.0853	
R indices (all data)	R1 = 0.0518, wR2 = 0.0961	
Absolute structure parameter	1.042(12)	
Largest diff. peak and hole	2.108 and -1.501 e $Å^{-3}$	

Table A.37 Crystal data and structure refinement for $[(SOP_2)PdMe][PF_6]$.

Identification code	$[(SOP_2)PdMe][PF_6]$	
Empirical formula	C39 H34 F6 N O P3 Pd S	
Formula weight	878.04	
Temperature	100(2) K	
Wavelength	0.71073 Å	
Crystal system	Monoclinic	
Space group	P2(1)	
Unit cell dimensions	a = 14.2182(11) Å	α = 90°
	b = 17.0580(13) Å	β = 104.462(2)°
	c = 15.6882(12) Å	γ = 90°
Volume	3684.4(5) $Å^3$	
Z	4	
Density (calculated)	1.583 Mg/m^3	
Absorption coefficient	0.755 mm^{-1}	
F(000)	1776	
Crystal size	0.50 x 0.50 x 0.15 mm^3	
Theta range for data collection	1.34 to 29.62°	
Index ranges	-19<=h<=19, -23<=k<=23, -21<=l<=21	
Reflections collected	68041	
Independent reflections	20594 [R(int) = 0.0514]	
Completeness to theta = 29.62°	99.8 %	
Absorption correction	Semi-empirical from equivalents	
Max. and min. transmission	0.8952 and 0.7040	
Refinement method	Full-matrix least-squares on F^2	
Data / restraints / parameters	20594 / 1 / 979	
Goodness-of-fit on F^2	1.031	
Final R indices [I>2sigma(I)]	R1 = 0.0372, wR2 = 0.0790	
R indices (all data)	R1 = NaN, wR2 = 0.0831	
Absolute structure parameter	1.042(12)	
Largest diff. peak and hole	0.665 and -0.403 e $Å^{-3}$	

Table A.38 Crystal data and structure refinement for $[(SOP_2)PtCl][PF_6]$.

Identification code	$[(SOP_2)PtCl][PF_6]$	
Empirical formula	C38 H31 Cl F6 N O P3 Pt S	
Formula weight	987.15	
Temperature	296(2) K	
Wavelength	0.71073 Å	
Crystal system	Monoclinic	
Space group	P2(1)/c	
Unit cell dimensions	a = 13.3596(6) Å	$\alpha = 90^\circ$
	b = 15.3077(7) Å	$\beta = 106.112(2)^\circ$
	c = 18.7872(9) Å	$\gamma = 90^\circ$
Volume	3691.2(3) $Å^3$	
Z	4	
Density (calculated)	1.776 Mg/m^3	
Absorption coefficient	4.124 mm^{-1}	
F(000)	1936	
Crystal size	0.33 x 0.25 x 0.15 mm^3	
Theta range for data collection	2.07 to 34.98°	
Index ranges	-21<=h<=21, -24<=k<=24, -30<=l<=28	
Reflections collected	143041	
Independent reflections	16228 [R(int) = 0.0371]	
Completeness to theta = 34.98°	99.9 %	
Absorption correction	Semi-empirical from equivalents	
Max. and min. transmission	0.5692 and 0.3466	
Refinement method	Full-matrix least-squares on F^2	
Data / restraints / parameters	16228 / 575 / 507	
Goodness-of-fit on F^2	1.023	
Final R indices [I>2sigma(I)]	R1 = 0.0234, wR2 = 0.0578	
R indices (all data)	R1 = 0.0297, wR2 = 0.0608	
Absolute structure parameter	1.042(12)	
Largest diff. peak and hole	2.825 and -1.569 e $Å^{-3}$	

Table A.39 Crystal data and structure refinement for $[(SOP_2)PtMe][PF_6]$.

Identification code	$[(SOP_2)PtMe][PF_6]$	
Empirical formula	C39 H34 F6 N O P3 Pt S	
Formula weight	966.75	
Temperature	100(2) K	
Wavelength	0.71073 Å	
Crystal system	Monoclinic	
Space group	P2(1)/n	
Unit cell dimensions	a = 8.936(2) Å	α = 90°
	b = 16.722(4) Å	β = 95.722(7)°
	c = 25.078(6) Å	γ = 90°
Volume	3728.4(15) $Å^3$	
Z	4	
Density (calculated)	1.717 Mg/m^3	
Absorption coefficient	4.011 mm^{-1}	
F(000)	1892	
Crystal size	0.45 x 0.45 x 0.25 mm^3	
Theta range for data collection	1.47 to 29.61°	
Index ranges	-12<=h<=12, -23<=k<=23, -34<=l<=34	
Reflections collected	82043	
Independent reflections	10464 [R(int) = 0.0430]	
Completeness to theta = 29.61°	99.7 %	
Absorption correction	Semi-empirical from equivalents	
Max. and min. transmission	0.4337 and 0.2655	
Refinement method	Full-matrix least-squares on F^2	
Data / restraints / parameters	10464 / 0 / 470	
Goodness-of-fit on F^2	1.134	
Final R indices [I>2sigma(I)]	R1 = 0.0276, wR2 = 0.0682	
R indices (all data)	R1 = 0.0302, wR2 = 0.0694	
Absolute structure parameter	0.50(2)	
Largest diff. peak and hole	1.731 and -1.422 e $Å^{-3}$	

Table A.40 Crystal data and structure refinement for $[(SOP_2)Pd]_2[PF_6]_2$.

Identification code	$[(SOP_2)Pd]_2[PF_6]_2$	
Empirical formula	C84 H80 F12 O5 P6 Pd2 S2	
Formula weight	1860.22	
Temperature	100(2) K	
Wavelength	0.71073 Å	
Crystal system	Trigonal	
Space group	P3(2)21	
Unit cell dimensions	a = 14.9538(4) Å	$\alpha = 90^\circ$
	b = 14.9538(4) Å	$\beta = 90^\circ$
	c = 30.2975(9) Å	$\gamma = 120^\circ$
Volume	5867.3(3) $Å^3$	
Z	3	
Density (calculated)	1.579 Mg/m^3	
Absorption coefficient	0.718 mm^{-1}	
F(000)	2838	
Crystal size	0.19 x 0.14 x 0.05 mm^3	
Theta range for data collection	1.71 to 24.11°	
Index ranges	-17<=h<=16, -16<=k<=17, -34<=l<=34	
Reflections collected	45427	
Independent reflections	6173 [R(int) = 0.0489]	
Completeness to theta = 24.11°	99.9 %	
Absorption correction	Semi-empirical from equivalents	
Max. and min. transmission	0.9664 and 0.8757	
Refinement method	Full-matrix least-squares on F^2	
Data / restraints / parameters	6173 / 0 / 502	
Goodness-of-fit on F^2	1.095	
Final R indices [I>2sigma(I)]	R1 = 0.0314, wR2 = 0.0743	
R indices (all data)	R1 = 0.0359, wR2 = 0.0764	
Absolute structure parameter	0.50(2)	
Largest diff. peak and hole	1.367 and -0.275 e $Å^{-3}$	

Table A.41 Crystal data and structure refinement for $[(SOP_2)Pd(CH_3CN)][PF_6]$.

Identification code	$[(SOP_2)Pd(CH_3CN)][PF_6]$	
Empirical formula	C42 H37 F12 N3 O P4 Pd S	
Formula weight	1090.09	
Temperature	100(2) K	
Wavelength	0.71073 Å	
Crystal system	Orthorhombic	
Space group	Pnma	
Unit cell dimensions	a = 17.8021(9) Å	$\alpha = 90^\circ$
	b = 22.4724(12) Å	$\beta = 90^\circ$
	c = 11.0253(5) Å	$\gamma = 90^\circ$
Volume	4410.7(4) $Å^3$	
Z	4	
Density (calculated)	1.642 Mg/m^3	
Absorption coefficient	0.703 mm^{-1}	
F(000)	2192	
Crystal size	0.16 x 0.09 x 0.08 mm^3	
Theta range for data collection	2.06 to 37.80°	
Index ranges	-30<=h<=30, -38<=k<=38, -19<=l<=18	
Reflections collected	181663	
Independent reflections	12056 [R(int) = 0.0717]	
Completeness to theta = 37.80°	99.9 %	
Absorption correction	Semi-empirical from equivalents	
Max. and min. transmission	0.9459 and 0.8959	
Refinement method	Full-matrix least-squares on F^2	
Data / restraints / parameters	12056 / 0 / 310	
Goodness-of-fit on F^2	1.035	
Final R indices [I>2sigma(I)]	R1 = 0.0290, wR2 = 0.0621	
R indices (all data)	R1 = 0.0458, wR2 = 0.0689	
Largest diff. peak and hole	1.125 and -0.787 e $Å^{-3}$	

Table A.42 Crystal data and structure refinement for $L1^{OMe}PdCl$.

Identification code	$L1^{OMe}PdCl$	
Empirical formula	C25 H27 Cl N4 O2 Pd	
Formula weight	557.36	
Temperature	100(2) K	
Wavelength	1.54178 Å	
Crystal system	Monoclinic	
Space group	P2(1)/c	
Unit cell dimensions	a = 5.1225(2) Å	α = 90°
	b = 17.5023(7) Å	β = 90.583(2)°
	c = 24.8571(10) Å	γ = 90°
Volume	2228.46(15) $Å^3$	
Z	4	
Density (calculated)	1.661 Mg/m^3	
Absorption coefficient	8.078 mm^{-1}	
F(000)	1136	
Crystal size	0.25 x 0.15 x 0.12 mm^3	
Theta range for data collection	3.09 to 68.91°	
Index ranges	-4<=h<=5, -21<=k<=21, -30<=l<=30	
Reflections collected	42087	
Independent reflections	3997 [R(int) = 0.0226]	
Completeness to theta = 68.91°	96.5 %	
Absorption correction	Semi-empirical from equivalents	
Max. and min. transmission	0.4440 and 0.2373	
Refinement method	Full-matrix least-squares on F^2	
Data / restraints / parameters	3997 / 0 / 300	
Goodness-of-fit on F^2	1.084	
Final R indices [I>2sigma(I)]	R1 = 0.0215, wR2 = 0.0553	
R indices (all data)	R1 = 0.0216, wR2 = 0.0553	
Largest diff. peak and hole	0.485 and -0.463 e $Å^{-3}$	

Table A.43 Crystal data and structure refinement for [L1^{im}Pd][Cl].

Identification code	[L1^{im}Pd][Cl]	
Empirical formula	C31 H33 Cl7 N8 O2 Pd	
Formula weight	904.20	
Temperature	100(2) K	
Wavelength	0.71073 Å	
Crystal system	Triclinic	
Space group	P-1	
Unit cell dimensions	a = 7.3314(7) Å	α = 84.743(2)°
	b = 13.8105(13) Å	β = 88.483(2)°
	c = 18.3307(18) Å	γ = 82.262(2)°
Volume	1831.2(3) Å^3	
Z	2	
Density (calculated)	1.640 Mg/m^3	
Absorption coefficient	1.060 mm^{-1}	
F(000)	912	
Crystal size	0.28 x 0.20 x 0.05 mm^3	
Theta range for data collection	1.12 to 29.13°	
Index ranges	-10<=h<=10, -18<=k<=18, -25<=l<=25	
Reflections collected	47572	
Independent reflections	9810 [R(int) = 0.0404]	
Completeness to theta = 29.13°	99.7 %	
Absorption correction	Semi-empirical from equivalents	
Max. and min. transmission	0.9489 and 0.7557	
Refinement method	Full-matrix least-squares on F^2	
Data / restraints / parameters	9810 / 490 / 513	
Goodness-of-fit on F^2	1.040	
Final R indices [I>2sigma(I)]	R1 = 0.0341, wR2 = 0.0825	
R indices (all data)	R1 = 0.0414, wR2 = 0.0873	
Largest diff. peak and hole	1.379 and -0.712 e Å^{-3}	

Table A.44 Crystal data and structure refinement for $[L1^{py}(H)PdMe][PF_6]$.

Identification code	$[L1^{py}(H)PdMe][PF_6]$	
Empirical formula	C34 H32 F6 N7 P Pd	
Formula weight	790.04	
Temperature	100(2) K	
Wavelength	0.71073 Å	
Crystal system	Monoclinic	
Space group	P2(1)/c	
Unit cell dimensions	a = 14.6795(13) Å	α = 90°
	b = 13.2225(11) Å	β = 91.096(2)°
	c = 16.7504(14) Å	γ = 90°
Volume	3250.7(5) $Å^3$	
Z	4	
Density (calculated)	1.614 Mg/m^3	
Absorption coefficient	0.692 mm^{-1}	
F(000)	1600	
Crystal size	0.25 x 0.20 x 0.20 mm^3	
Theta range for data collection	1.39 to 30.51°	
Index ranges	-20<=h<=20, -18<=k<=18, -23<=l<=23	
Reflections collected	74757	
Independent reflections	9886 [R(int) = 0.0502]	
Completeness to theta = 30.51°	99.7 %	
Absorption correction	Semi-empirical from equivalents	
Max. and min. transmission	0.8739 and 0.8459	
Refinement method	Full-matrix least-squares on F^2	
Data / restraints / parameters	9886 / 0 / 448	
Goodness-of-fit on F^2	1.023	
Final R indices [I>2sigma(I)]	R1 = 0.0332, wR2 = 0.0767	
R indices (all data)	R1 = 0.0493, wR2 = 0.0861	
Largest diff. peak and hole	0.569 and -0.565 e $Å^{-3}$	

Table A.45 Crystal data and structure refinement for $[L1^{py}(PdCl)PdMe][PF_6]$.

Identification code	$[L1^{py}(PdCl)PdMe][PF_6]$	
Empirical formula	C35 H28 Cl F6 N6 O1.50 P Pd2 S1.50	
Formula weight	997.94	
Temperature	100(2) K	
Wavelength	0.71073 Å	
Crystal system	Monoclinic	
Space group	C2/c	
Unit cell dimensions	a = 16.542(3) Å	α = 90°
	b = 32.618(5) Å	β = 109.131(2)°
	c = 14.722(2) Å	γ = 90°
Volume	7505(2) $Å^3$	
Z	8	
Density (calculated)	1.767 Mg/m^3	
Absorption coefficient	1.226 mm^{-1}	
F(000)	3952	
Crystal size	0.20 x 0.20 x 0.10 mm^3	
Theta range for data collection	1.25 to 26.37°	
Index ranges	-20<=h<=20, -40<=k<=40, -18<=l<=18	
Reflections collected	58464	
Independent reflections	7673 [R(int) = 0.0500]	
Completeness to theta = 26.37°	99.7 %	
Absorption correction	Semi-empirical from equivalents	
Max. and min. transmission	0.8872 and 0.7916	
Refinement method	Full-matrix least-squares on F^2	
Data / restraints / parameters	7673 / 122 / 536	
Goodness-of-fit on F^2	1.081	
Final R indices [I>2sigma(I)]	R1 = 0.0430, wR2 = 0.1070	
R indices (all data)	R1 = 0.0551, wR2 = 0.1182	
Largest diff. peak and hole	1.683 and -0.922 e $Å^{-3}$	

Table A.46 Crystal data and structure refinement for $[L1^{py}(PdCl)PtMe][PF_6]$.

Identification code	$[L1^{py}(PdCl)PtMe][PF_6]$	
Empirical formula	C33 H30 Cl3 F6 N6 P Pd Pt	
Formula weight	1063.44	
Temperature	100(2) K	
Wavelength	1.54178 Å	
Crystal system	Triclinic	
Space group	P-1	
Unit cell dimensions	a = 7.3949(4) Å	α = 70.729(2)°
	b = 15.6616(8) Å	β = 81.541(2)°
	c = 15.8870(9) Å	γ = 86.647(2)°
Volume	1717.88(16) $Å^3$	
Z	2	
Density (calculated)	2.056 Mg/m^3	
Absorption coefficient	14.927 mm^{-1}	
F(000)	1028	
Crystal size	0.25 x 0.20 x 0.04 mm^3	
Theta range for data collection	2.97 to 68.97°	
Index ranges	-8<=h<=8, -18<=k<=18, -19<=l<=17	
Reflections collected	33056	
Independent reflections	6077 [R(int) = 0.0318]	
Completeness to theta = 68.97°	95.4 %	
Absorption correction	Semi-empirical from equivalents	
Max. and min. transmission	0.5866 and 0.1180	
Refinement method	Full-matrix least-squares on F^2	
Data / restraints / parameters	6077 / 0 / 461	
Goodness-of-fit on F^2	1.170	
Final R indices [I>2sigma(I)]	R1 = 0.0232, wR2 = 0.0588	
R indices (all data)	R1 = 0.0234, wR2 = 0.0589	
Largest diff. peak and hole	0.746 and -1.572 e $Å^{-3}$	

Table A.47 Crystal data and structure refinement for $[L2^{py}(PdBr)_3][BF_4]_2$.

Identification code	09413	
Empirical formula	C52 H50 B2 Br3 F8 N13 Pd3	
Formula weight	1589.60	
Temperature	100(2) K	
Wavelength	0.71073 Å	
Crystal system	Orthorhombic	
Space group	Pbca	
Unit cell dimensions	a = 12.8582(13) Å	α = 90°
	b = 19.3783(19) Å	β = 90°
	c = 45.245(4) Å	γ = 90°
Volume	11273.8(19) $Å^3$	
Z	8	
Density (calculated)	1.873 Mg/m^3	
Absorption coefficient	3.150 mm^{-1}	
F(000)	6224	
Crystal size	0.45 x 0.45 x 0.20 mm^3	
Theta range for data collection	0.90 to 29.13°	
Index ranges	-17<=h<=17, -26<=k<=26, -56<=l<=61	
Reflections collected	221928	
Independent reflections	15158 [R(int) = 0.0708]	
Completeness to theta = 29.13°	99.9 %	
Absorption correction	Semi-empirical from equivalents	
Max. and min. transmission	0.5715 and 0.3314	
Refinement method	Full-matrix least-squares on F^2	
Data / restraints / parameters	15158 / 860 / 791	
Goodness-of-fit on F^2	1.258	
Final R indices [I>2sigma(I)]	R1 = 0.0905, wR2 = 0.1983	
R indices (all data)	R1 = 0.1043, wR2 = 0.2045	
Largest diff. peak and hole	1.646 and -2.793 e $Å^{-3}$	